CHAPTER 2

SOLID-STATE CHEMISTRY

Of the three states of matter, solids possess the most structural diversity. Whereas gases and liquids consist of discrete molecules that are randomly distributed due to thermal motion, solids consist of molecules, atoms, or ions that are statically positioned. To fully understand the properties of solid materials, one must have a thorough knowledge of the structural interactions between the subunit atoms, ions, and molecules. This chapter will outline the various types of solids, including structural classifications and nomenclature for both crystalline and amorphous solids. The material in this key chapter will set the groundwork for the rest of this textbook, which describes a variety of materials classes.

2.1. AMORPHOUS *VS*. CRYSTALLINE SOLIDS

A solid is a material that retains both its shape and volume over time. If a solid possesses long range, regularly repeating units, it is classified as a *crystalline* material. Crystalline solids are only produced when the atoms, ions, or molecules have an opportunity to organize themselves into regular arrangements, or *lattices*. For example, crystalline minerals found in nature have been formed through many years of extreme temperature and pressure, or slow evaporation processes. Most naturally occurring crystalline solids comprise an agglomeration of individual microcrystalline units; single crystals without significant defects are extremely rare in nature, and require special growth techniques (see p. 28).

If there is no long-range structural order throughout the solid, the material is best described as *amorphous*. Quite often, these materials possess considerable short-range order over distances of 1–10 nm or so. However, the lack of long-range translational order (periodicity) separates this class of materials from their crystalline counterparts. Since the majority of studies have been addressed to study crystalline solids relative to their amorphous counterparts, there is a common misconception that most solids are crystalline in nature. In fact, a solid product generated from many chemical reactions will be amorphous by default, unless special procedures are used to facilitate molecular ordering (*i.e*., crystal formation). Although the crystalline state is more thermodynamically-favorable than the

Table 2.1. Glass Transition Temperatures

Material	Intermolecular bonding	$T_g(°C)$
SiO_2	Covalent	1,430
Borosilicate glass	Covalent	550
$Pd_{0.4}Ni_{0.4}P_{0.2}$	Metallic	580
BeF_2	Ionic	570
As_2S_3	Covalent	470
Polystyrene	Van der Waal	370
Se_∞	Covalent	310
Poly(vinyl chloride)	Van der Waal	81
Polyethylene	Van der Waal	−30

disordered state, the formation of amorphous materials is favored in kinetically bound processes (*e.g.*, chemical vapor deposition, sol-gel, solid precipitation, *etc.*).[1]

Some materials featuring extended networks of molecules such as glasses may never exist in the crystalline state. In these solids, the molecules are so entangled or structurally complex that crystallization may not occur as the temperature is slowly decreased. Due to the rigidity of the solid, but proclivity to remain in the amorphous state, these compounds have been incorrectly referred to as supercooled liquids. It was even thought that a slow flow of glass over hundreds of years has caused nineteenth century stained glass windows to have a proportionately thicker base.[2] However, it is now well understood that the glass structure remains in tact unless its threshold transition temperature is exceeded. This parameter is known as the glass transition temperature, T_g, and corresponds to the temperature below which molecules have very little mobility.

Other amorphous solids such as polymers, being rigid and brittle below T_g, and elastic above it, also exhibit this behavior. Table 2.1 lists the glass transition temperatures of common solid materials. It should also be noted that whereas crystalline solids exhibit a discrete melting point, amorphous solids undergo a solid–liquid phase transition over a range of temperatures. Although most solid-state textbooks deal almost exclusively with crystalline materials, this text will attempt to address both the crystalline and amorphous states, describing the structure/property relationships of major amorphous classes such as polymers and glasses.

2.2. TYPES OF BONDING IN SOLIDS

Every amorphous and crystalline solid possesses certain types of inter- and intramolecular interactions between its subunits that govern its overall properties. Depending on the nature and strength of these interactions, a variety of physical, optical, and electronic properties are observed. For example, intramolecular forces (*i.e.*, atomic separations/inter-atomic bonding energies) directly influence the conductivity, thermal expansion, and elasticity of a material; in contrast, intermolecular forces will govern the melting/boiling/sublimation point, solubility, and vapor pressure of a

material. As expected, these associations not only govern the behavior of a material in the solid state, but also for the less ordered liquid phase. For example, the hydrogen bonding interactions between neighboring water molecules within an ice lattice are also important in the liquid phase, resulting in high surface tension and finite viscosity. For the gaseous state, intermolecular forces have been overcome, and no longer have an impact on its properties.

2.2.1. Ionic Solids

These solids are characterized by cationic and anionic species that are associated through electrostatic interactions. All predominantly ionic salts possess crystalline structures, as exhibited by common Group 1–17 or 2–17 binary salts such as NaCl and $CaCl_2$ (Figure 2.1). The melting points of these solids are extremely high, as very strong electrostatic attractions between counterions must be overcome. Although oppositely charged ions have attractive interactions, like charges repel one another. In the determination of the lattice energy, U, the sizes and charges of the ions are most important (Eq. 1). That is, the lattice energy for MgO would be much greater than BaO, since the ionic bonding is much stronger for the magnesium salt due to its high charge/small size (large charge density). By contrast, the salt MgN does not exist, even though Mg^{3+} and N^{3-} would be very strongly attracted through electrostatic interactions. The ionization energy required to produce the trivalent magnesium ion is too prohibitive.
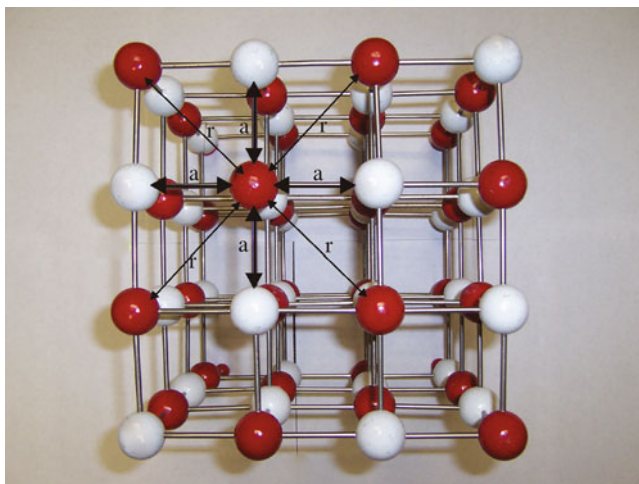

Figure 2.1. Ionic model for sodium chloride. This is a face-centered arrangement of chloride ions (white), with sodium ions occupying the octahedral interstitial sites (red). The attractive electrostatic forces, a, between adjacent Na^+ and Cl^- ions, and repulsive forces, r, between Na^+ ions are indicated.

$$(1) \quad U = \frac{NMZ_{cation}Z_{anion}}{r_o} \left(\frac{e^2}{4\pi\varepsilon_o} \right) \left(1 - \frac{n}{r_o} \right)$$

where: N = Avagadro's number (6.02×10^{23} molecules mol^{-1})

$Z_{cation, anion}$ = magnitude of ionic charges;

r_0 = average ionic bond length

e = electronic charge (1.602×10^{-19} C)

$4\pi\varepsilon_0$ = permittivity of a vacuum (1.11×10^{-10} C^2 J^{-1} m^{-1})

M = the Madelung constant (see text)

n = the Born exponent; related to the corresponding closed-shell electronic configurations of the cations and anions (e.g., [He] = 5; [Ne] = 7; [Ar] or [3d^{10}][Ar] = 9; [Kr] or [4d^{10}][Kr] = 10; [Xe] or [5d^{10}][Xe] = 12)

It is noteworthy that the calculated lattice energy is quite often smaller than the empirical value. Whereas the ions in purely ionic compounds may be accurately treated as hard spheres in the calculation, there is often a degree of covalency in the bonding motif. In particular, Fajans' rules describe the degree of covalency as being related to the charge density of the cation and the polarizability of the anion. In general, polarizability increases down a Periodic Group due to lower electronegativities, and valence electrons being housed in more diffuse orbitals thus experiencing a much less effective nuclear charge. *To wit*, a compound such as LiI would exhibit a significant degree of covalent bonding due to the strong polarizing potential of the very small cation, and high polarizability of iodide. This is reflected in its lower melting point (459°C) relative to a more purely ionic analogue, LiF (m.p. = 848°C).

The Madelung constant appearing in Eq. 1 is related to the specific arrangement of ions in the crystal lattice. The Madelung constant may be considered as a decreasing series, which takes into account the repulsions among ions of similar charge, as well as attractions among oppositely charged ions. For example, in the NaCl lattice illustrated in Figure 2.1, each sodium or chloride ion is surrounded by six ions of opposite charge, which corresponds to a large attractive force. However, farther away there are 12 ions of the same charge that results in a weaker repulsive interaction. As one considers all ions throughout the infinite crystal lattice, the number of possible interactions will increase exponentially, but the magnitudes of these forces diminishes to zero.

Ionic solids are only soluble in extremely polar solvents, due to dipole–dipole interactions between component ions and the solvent. Since the lattice energy of the crystal must be overcome in this process, the solvation of the ions (i.e., formation of [(H$_2$O)$_n$Na]$^+$) represents a significant exothermic process that is the driving force for this to occur.

2.2.2. Metallic Solids

Metallic solids are characterized by physical properties such as high thermal and electrical conductivities, malleability, and ductility (i.e., able to be drawn into a thin wire). Chemically, metals tend to have low ionization energies that often result in

metals being easily oxidized by the surrounding environmental conditions. This explains why metals are found in nature as complex geological formations of oxides, sulfates, silicates, aluminates, *etc*. It should be noted that metals or alloys may also exist as liquids. Mercury represents the only example of a pure metal that exists as a liquid at STP. The liquid state of Hg is a consequence of the electronic configurations of its individual atoms. The 6s valence electrons are shielded from the nuclear charge by a filled shell of 4f electrons. This shielding causes the effective nuclear charge (Z_{eff}) to be higher for these electrons, resulting in less sharing/delocalization of valence electrons relative to other metals. Further, relativistic contraction of the 6s orbital causes these electrons to be situated closer to the nucleus, making them less available to share with neighboring Hg atoms.[3] In fact, mercury is the only metal that does not form diatomic molecules in the gas phase. Energetically, the individual atoms do not pack into a solid lattice since the lattice energy does not compensate for the energy required to remove electrons from the valence shell.

Metallic bonding

The most simplistic model for the bonding in metallic solids is best described via the *free electron model*. This considers the solid as a close-packed array of atoms, with valence electrons completely delocalized throughout the extended structure. Since the delocalization of electrons occurs more readily for valence electrons farther from the nucleus (experiencing a lesser Z_{eff}), metallic character increases going down a Group of the Periodic Table. Perhaps the best example of this phenomenon is observed for the Group 14 congeners. As you move from carbon to lead, the elemental properties vary from insulating to metallic, through a transitional range of semiconducting behavior for Si and Ge.

The close chemical association among neighboring metal atoms in the solid gives rise to physical properties such as high melting points and malleability. The nondirectional bonding in metals allows for two modes of deformation to occur when a metal is bent. Either the atomic spacing between neighboring metal atoms in the crystal lattice may change (*elastic deformation*), or planes of metal atoms may slide past one another (*plastic deformation*). Whereas elastic deformation results in a material with "positional memory" (*e.g.*, springs), plastic deformation results in a material that stays malformed. We will consider the bonding modes of metals and non-metals in more detail later in this chapter.

Although metals are mostly characterized by crystalline structures, amorphous alloys may also be produced, known as metallic glasses. A recent example of such a material is the multicomponent alloy $Zr_{41}Ti_{14}Ni_{12}Cu_{10}Be_{23}$.[4] These materials combine properties of both plastics and metals, and are currently used within electric transformers, armor-piercing projectiles, and even sports equipment. The media has recently been focused on this latter application, for LiquidMetal™ golf clubs, tennis racquets, and baseball bats. Unlike window glass, metallic glass is not brittle. Many traditional metals are relatively easy to deform, or bend permanently out of

shape, because their crystal lattices are riddled with defects. A metallic glass, in contrast, will spring back to its original shape much more readily.

Amorphous metallic materials may be produced through a variety of procedures. Pure individual metal powders may be melted at high temperatures in an arc furnace. Depending on the composition of the melt, supercooling may be possible, resulting in a vitreous solid rather than a crystalline form. Although facile glass-forming solids such as B_2O_3 will form amorphous solids even upon relatively slow cooling (*e.g.*, 1 K s^{-1}), metals generally require very high rates ($> 10^6$ K s^{-1}) to prevent crystal growth. These high rates are accomplished by placing a material with high thermal conductivity (*e.g.*, copper) in contact with a molten metal or alloy. This method is referred to as "melt spinning" or "melt extraction," and results in metallic ribbons up to 15 cm wide and 30 μm thick.

Another common procedure uses a vapor deposition technique to form amorphous metallic thin films (see Chapter 4). Upon thermal annealing, the irregularly deposited atoms in the film have an opportunity to assemble into a crystalline array. A procedure referred to as *ball-milling* may also be used to create amorphous metal alloy powders. This method uses a mixture of crystalline powders that is vigorously agitated with a stainless steel ball within a round vessel. This results in regions of high pressure that cause local melting of the crystalline powders, breaking apart metallic bonds, and facilitating atomic diffusion along preferential crystallite interfaces.

2.2.3. Covalent Network Solids

These solids are characterized by very strong, directional covalent bonds between their constituent atoms. This bonding array generally leads to high melting points and bulk hardness. Due to the arrangement of the atoms comprising these solids, a variety of physical properties may be observed, as evidenced by the very different properties exhibited by the three *allotropes* (*i.e.*, discrete structural forms) of carbon. For instance, diamond is an extremely hard, insulating material that is transparent to light, whereas graphite is a soft, black solid that is capable of conducting electricity along the graphitic layers of the extended solid. Buckminsterfullerene (C_{60}) is very different from either of these carbon forms, being soluble in aromatic solvents, and thereby capable of undergoing chemical reactions. Other examples of covalent network solids are quartz $(SiO_2)_x$, $(BN)_x$, $(ZnS)_x$, $(HgS)_x$, and the two allotropes of selenium – grey (Se_∞) and red $(Se_8)_x$. It should be noted that although the discrete units of the extended solid are covalently bound, there may also be layers that are held together by weaker intermolecular forces such as van der Waal interactions (Figure 2.2).

2.2.4. Molecular Solids

This class of solids features discrete molecules that are held together by rather weak intermolecular forces such as dipole–dipole, London Dispersion, and hydrogen
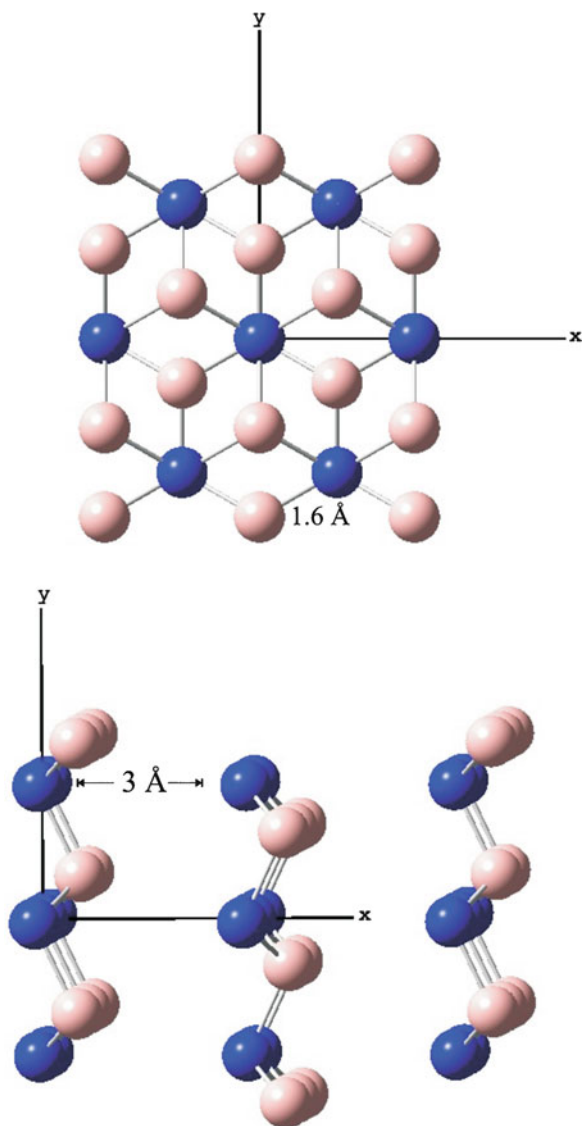
Figure 2.2. Top and side views of hexagonal boron nitride $(BN)_x$, which exhibits the graphitic structure. Shown are the relatively weak van der Waal interactions that hold together adjacent layers/sheets of covalently-bound B-N units.

bonding. Since these forces are much weaker than ionic or metallic bonding interactions, molecular solids are usually characterized by low melting points. Examples include dry ice (CO_2), ice (H_2O), solid methane (CH_4), sugar (comprising various arrangements/conformations of $C_6H_{12}O_6$ molecules), and polymers. For polymeric

materials, the melting points vary significantly depending on the nature of interactions among the polymer subunits. As Chapter 5 will delineate, these interactions also greatly affect many other physical properties of these materials.

Molecular solids may exhibit either crystalline or amorphous structures, depending on the complexity of the individual molecules comprising the bulk material. As with all solids, the more complex the subunits are, the harder it is for them to organize themselves in a repeatable fashion, resulting in an amorphous structure. Unlike purely ionic solids, molecular compounds may be soluble in either nonpolar or polar solvents, as long as the solvent polarity between solute and solvent is matched ("like dissolves like").

Both dipole–dipole and London Dispersion forces are subclasses of van der Waal interactions. When two polar molecules approach one another, a natural attraction known as dipole–dipole forces is created between oppositely charged ends. The relative intensity of dipole–dipole forces may be represented by Eq. 2:

$$(2) \qquad -\frac{2}{3} \left\{ \frac{\mu_1^2 \mu_2^2}{4\pi\varepsilon_o} \right\} \frac{1}{kTr^6}$$

where μ_1 and μ_2 are the molecular dipole moments (Debyes); r, the average distance of separation (Å); T, the temperature (K); and k is the Boltzmann constant $(1.38065 \times 10^{-23} \text{ J K}^{-1})$.

In addition to the mutual attraction between polar molecules, there may also be an interaction between the solute molecules and liquid or gaseous solvent. In highly polar solvents such as water or alcohols, a dense shell of solvent molecules will surround the polar molecules. Although this solute/solvent interaction assists in the solubility of the molecules in the solvent, the dipole–dipole interactions between individual molecules are suppressed.

In contrast to dipole–dipole forces, London Dispersion interactions are much weaker in nature since they involve nonpolar molecules that do not possess permanent dipole moments. The only modes for molecular attraction are through *polarization* of electrons, which leads to the creation of small dipole–dipole interactions and mutual attractive forces. Since electron polarization occurs much more readily for electrons farther from the nucleus, this effect is more pronounced for molecules that are larger with a greater number of electrons, especially positioned on atoms with a high atomic number, consisting of more diffuse orbitals. These "induced dipole" forces are responsible for the liquefaction of gases such as He and Ar at low temperatures and pressures. The relative strength of London Dispersion forces is described by Eq. 3:

$$(3) \qquad -\frac{3}{2} \left\{ \frac{I_1 I_2}{I_1 + I_2} \right\} \frac{\alpha_1 \alpha_2}{r^6}$$

where I_1 *and* I_2 are the ionization potentials of the molecules; and α_1 and α_2 are the polarizabilities of the molecules.

If both polar and nonpolar molecules are present, a dipole-induced dipole interaction may occur. For this situation, the strength of association may be represented by Eq. 4, which is dependent on both the dipole moment of the polar molecule, and

the polarizability of the nonpolar component. Once again, this relation does not include the interactions between the polar molecule and solvent molecules.

$$(4) \quad -2\left\{\frac{\mu_1^2}{4\pi\varepsilon_o}\right\}\frac{\alpha_2}{r^6}$$

Hydrogen bonding may be considered a special case of dipole–dipole forces, where there exist relatively strong interactions between extremely polar molecules. This interaction is often designated by A – H ... B, where the hydrogen bond is formed between a Lewis basic group (B) and the hydrogen covalently bonded to an electronegative group (A). In general, the magnitudes of these interactions (*ca.* 12–30 kJ mol^{-1}) are much less than a covalent bond. However, the linear [F-H—F]$^-$ anion present in concentrated hydrofluoric acid has a bond energy of *ca.* 50 kJ mol^{-1}, representing the strongest hydrogen bond ever discovered. The degree of hydrogen bonding has an influence on many physical properties of a compound such as melting and boiling points, dielectric constants, vapor pressure, thermal conductivity, index of refraction, viscosity, and solubility behavior.

The potential energy between pairs of non-bonded neutral atoms or molecules as a function of internuclear/intermolecular separation may be described as a combination of attraction and repulsion terms – referred to as the *Lennard-Jones potential* (Eq. 5).

$$(5) \quad V(r) = 4\varepsilon\left[\left(\frac{\sigma}{r}\right)^{12} - \left(\frac{\sigma}{r}\right)^6\right]$$

where V(r) is the potential energy as a function of atomic separation, r; σ is the Lennard-Jones size parameter, the intermolecular separation for which the energy is zero ($\sigma = 2^{-1/6}r_o$, where r_o is the intermolecular separation at minimum energy); and ε is the Lennard-Jones energy constant, the minimum energy of the potential energy well.

At farther atomic separations, electron-nuclei attractive forces will dominate; however, as the atoms closely approach one another, there will be increasing mutual repulsion among negatively-charged electrons and positively-charged nuclei, resulting in an exponential increase in the total potential energy (Figure 2.3). However, at an intermediate atomic separation distance, a potential energy well will be generated, corresponding to bond formation between the two atoms. The atomic separation, r_o, at which the force is zero, is referred to as the *equilibrium bond length*. As one would expect, the value of r_o will increase concomitantly with temperature, as atomic motions become greater with increasing thermal energy. The value of the potential energy, V(r_o), at the equilibrium bond length is termed the *binding energy*. For two polar molecules, the long-range electrostatic interactions between molecular dipoles must be accounted for. Hence, another term referred to as the Stockmayer potential must be added to Eq. 5. The δ term in Eq. 6 is the polarity correction term, based on the magnitude and directions of the polar dipoles.

$$(6) \quad V(r) = 4\varepsilon\left[\left(\frac{\sigma}{r}\right)^{12} - \left(\frac{\sigma}{r}\right)^6 + \delta\left(\frac{\sigma}{r}\right)^3\right]$$
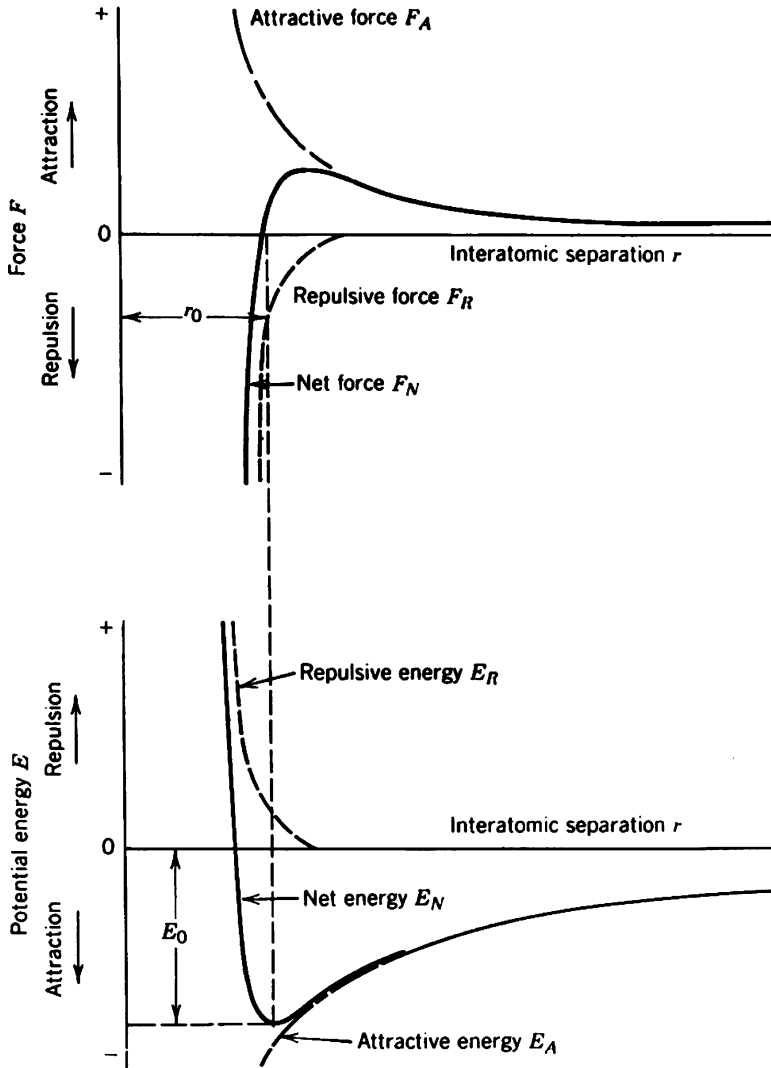
Figure 2.3. Force and potential energy diagrams for a diatomic molecule, with respect to the interatomic separation. The equilibrium bond distance corresponds to the minimum of the potential energy well and the maximum attractive force between the two atoms. As the atoms are brought even closer together, the interatomic bonding becomes less stable due to exponential increases in repulsive forces and potential energy.

2.3. THE CRYSTALLINE STATE

Single crystals comprise an infinite array of ions, atoms, or molecules, known as a *crystal lattice*. The strength of the interactions between the species comprising the crystal is known as the *lattice energy*, and is dependent on the nature and degree of

interactions between adjacent species. For example, the extremely high melting points of salts are directly associated with the strength of the ionic bonds between adjacent ions. For molecular species, it is the degree of intermolecular interactions such as van der Waal and hydrogen bonding forces that controls the lattice energy. Ionic and covalent crystals have similar lattice energies (*ca*. 700–900 kJ mol^{-1}), followed by metallic crystals (*ca*. 400–500 kJ mol^{-1}). By contrast, molecular crystals such as solid carbon dioxide are much more readily broken apart (*ca*. 5–20 kJ mol^{-1}) – a consequence of the weak van der Waal interactions consisting between the discrete molecules that comprise the lattice.

The ions, molecules, or atoms pack in an arrangement that minimizes the total free energy of the crystal lattice. For ionic crystals, there is an overall balance of charge among all ions throughout the lattice. Non-ionic crystals exhibit a greater variety of packing interactions between constituent molecules. One of the most influential forces found in these lattices is hydrogen bonding. The molecules will pack in such a manner to balance the number of hydrogen bond donor and acceptor groups. Often, a residual polar solvent, capable of participating in hydrogen bonding, will play an important role in the observed packing arrangement. Depending on the polarity of the encapsulated solvent, a variety of arrangements of molecules will be observed in the crystal lattice, with hydrophobic and hydrophilic groups being preferentially aligned with respect to each other and the solvent.

Depending on how strongly a solvent is contained within the crystal lattice, sometimes the encapsulated solvent is lost, an occurrence referred to as *efflorescence*. By contrast, if the solid contains ions with a high charge density (high charge/size ratio) and is soluble in water, the crystals will readily adsorb water from the atmosphere and may even be transformed to a solution. An example of such a *deliquescent* crystal is calcium chloride, which is employed as a dehydrating agent for removal of moisture from a flow of inert gases.

The overall shape or form of a crystal is known as the *morphology*. Often, there is more than one crystalline form of the same substance. Each form is known as a *polymorph*, differing in both the arrangement of constituents as well as unit cell dimensions. Although polymorphs differ in both the shape and size of the unit cell, most compounds may exhibit this behavior under appropriate experimental conditions. Common reasons for a varying crystal structure are similar ionic ratios for anions and cations in ionic crystals, or variations in temperature or pressure during crystal growth. These latter effects alter the amount of disorder within the crystal lattice, allowing for the migration of atoms/ions/molecules into lattice positions that are thermodynamically disfavored at lower temperatures and/or pressures.[5]

Most often, the energy for the interconversion between polymorphs is small, resulting in phase changes that occur after only moderate changes in temperature or pressure. In general, exposing a crystal to an applied pressure forces neighboring atoms closer together, causing a decrease in the volume of the unit cell, and an increase in the coordination number of individual atoms. For instance, silicon is transformed from a four-coordinate polymorph at ambient pressure to a variety of higher-coordinate phases at elevated pressures.[6]

If the solid is an element, polymorphs are known as *allotropes*. One of the best-known examples for elemental polymorphism (allotropy) is observed for Group 16 elements (chalcogens). For instance, let's consider the allotropism exhibited by sulfur. The most stable form under ambient conditions is cyclooctasulfur, a yellow powder consisting of arrangements of eight-membered rings (Figure 2.4a). At elevated temperatures, the S_8 rings begin to open and cross-link with one another, resulting in a highly viscous reddish solution (Figure 2.4b). If this solution is quickly quenched by
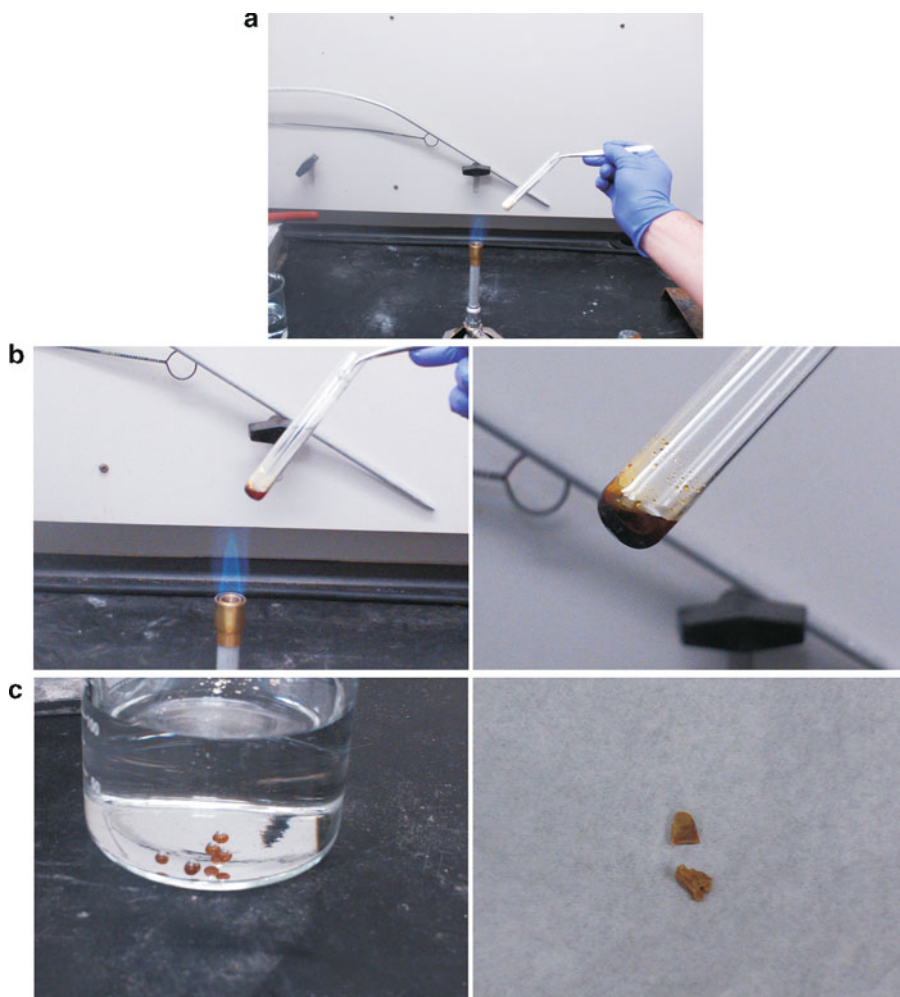
Figure 2.4. Illustration of allotropic transformations exhibited by elemental sulfur. Shown are (a) cyclooctasulfur (S_8) at room temperature/pressure, (b) breaking apart of discrete S_∞ rings at elevated temperature to form a viscous liquid, (c) formation of S_∞ (catenasulfur or "plastic sulfur") via quenching in cold water, and (d) re-conversion of catenasulfur back to the thermodynamic stable S_8 allotrope.

pouring into cold water, a hard, reddish-yellow solid will be formed, comprised of infinite chains of disordered sulfur atoms (Figure 2.4c). This latter form is known as *catenasulfur*, or "plastic sulfur"; however, since it is not thermodynamically stable at room temperature, it will slowly convert back to the powdery S_8 form. The other Group 16 congeners also possess this structural diversity, with the relative thermodynamic stability of a particular allotrope being governed by the structure with the lowest overall free energy.

If the chemical contents of a polymorph are different than other forms, it is designated as a *pseudopolymorph*.[7] This often occurs due to the presence of differing amounts of solvent (*e.g.,* clathrates, host-guest, or inclusion compounds), which will alter physical properties of the crystals such as melting points and solubilities. Polymorphism and pseudopolymorphism may be observed when different experimental conditions are used for synthesis. For example, if crystals are grown by sublimation, changing the temperature will often yield different crystal structures, possibly even metastable phases that are kinetically favored.

When different compounds yield almost identical crystals, the forms are referred to as *isomorphs*. The word "almost" is indicated here, as isomorphs are not exactly the same. Although the arrangement of atoms/ions in the lattices are identical, one or more of the atoms in the lattice have been replaced with another component. For example, alums of the general formula $(M)_2(SO_4) \cdot (M)_2(SO_4)_3 \cdot 24H_2O$ may crystallize as isomorphs where one of the monovalent or trivalent metals is substituted with another.

The conversion between polymorphs may be observed by differential scanning calorimetry (DSC), which shows peaks corresponding to endothermic (melting) or exothermic ((re)crystallization) events associated with structural changes. Figure 2.5 shows the differential scanning calorimetry (DSC) curves of two polymorphs (designated as I_R and II_o) of picryltoluidine, obtained via crystallization from different solvents. Whereas form I_R exhibits an endothermic melting peak at 166°C, form II_o melts at 163°C. Further, the enthalpies of fusion for I_R and II_o forms are 31.3 kJ/mol and 28.6 kJ/mol, respectively. The *heat of fusion rule* states that if the higher melting form has the lower enthalpy of fusion, the two forms are *enantiotropic* (*i.e.,* two forms have differing stabilities at specific temperature ranges). On the other hand, if the lower melting form has the lower enthalpy of fusion (as exhibited here), the two forms are *monotropic* (*i.e.,* one form is more stable at all temperatures).[8]

The rate of a polymorphic phase transition depends on nucleation and growth processes, which are related to the mobility of atoms/molecules in the solid state. The Avrami equation (Eq. 7) may be applied to describe the degree of transformation, X, as a function of time, t:

$$(7) \qquad X(t) = 1 - e^{kt^n},$$

where n and k are constants related to the relative importance of nucleation and growth, respectively.[9]
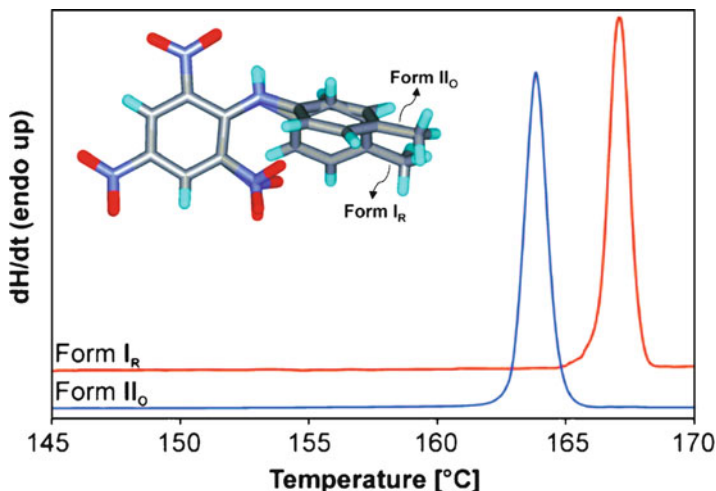
Figure 2.5. Differential scanning calorimetry (DSC) curves of two polymorphs of picryltoluidine. Crystals of form I_R were obtained from methanol, whereas form II_o was obtained from an acetone-water solution. Whereas form I_R exhibits an endothermic melting peak at 166°C, form II_o melts at 163°C. Further, the enthalpies of fusion for I_R and II_o forms are determined as 31.3 and 28.6 kJ/mol, respectively. Reproduced with permission from *Cryst. Growth Des.* **2008**, *8*, 1977. Copyright 2008 American Chemical Society.

External pressure may also be used to convert one form into another. When this medium is used, a polymorph with higher density will typically result due to the local confinement of lattice species through the externally applied pressure. It should be noted that multiple forms of an *amorphous* material (*i.e.*, lacking long-range structural order – see Section 2.4) are denoted as *polyamorphs*, as illustrated by the polyamorphism exhibited by silica at elevated pressures.[10]

2.3.1. Crystal Growth Techniques

Crystal growth involves a phase change from liquid or gas to a solid, such as the precipitation of a solute from solution or the formation of a solid from sublimation of a gas. This occurs through two processes, nucleation and growth, being favored by using supersaturated solutions and/or temperature gradients. When several molecules in the gas phase or in solution approach each other in appropriate orientations, they form a submicroscopic nucleus upon which additional molecules may adsorb *en route* toward an ordered extended crystal structure. The probability that a crystal will form depends on the nature and concentration of the solute (*i.e.*, the distance between solutes), as well as solvent conditions such as temperature, pH, ionic strength, viscosity, polarity, *etc*. To grow single crystals suitable for X-ray

diffraction analysis, relatively few nuclei should be formed rather than multiple sites of nucleation that will yield microcrystalline solids.

High quality crystals may only be obtained when the rate of deposition onto a nucleation site is kept at a rate sufficiently low to allow oriented growth. A high growth rate may lead to defects in the crystal, forming multi-branched or dendritic crystallites through rapid growth in too many directions. As molecules in the gas-phase or solvent interact with the surface of the growing crystal, they may or may not be preferentially adsorbed. That is, a nucleation site that contains steps, ledges, or surface depressions is able to provide more efficient crystal growth due to the prolonged interaction of suspended molecules with a greater surface area.

Experimentally, the successful growth of single crystals on the order of 0.01–0.1 mm^2 is not trivial, and has long been considered as a "black art"! Figure 2.6 illustrates common techniques that may be applied for crystal growth via sublimation or from solution. Perhaps the most important starting point is with a solution that is filtered to remove most suspended nuclei. For air-sensitive solutions, this requires careful manipulation using filtering cannulas and Schlenk techniques. Most of the solvent is then removed to create a nearly supersaturated solution, and then left undisturbed. Another method that is used to grow single crystals from saturated solutions consists of layering a "nonsolvent" onto the top of the saturated solution. Since the compound of interest is not soluble in the layered nonsolvent, crystal formation may begin at the interfacial region. If the nonsolvent is volatile, vapor diffusion may provide another route for the growth of crystals.

Depending on the nature of the suspended molecules, crystal formation may begin immediately, or may even take months to occur. Many organometallic chemists have been surprised to find large crystals at the bottom of flasks placed in the back of the freezer, after months of observation and concluding that no crystals would ever be realized. Sometimes, fortuitous crystal growth may also be realized from unexpected sources. Crystals may be formed from the incorporation of impurities such as dust or vacuum grease, or from surface scratches on the inside walls of the flask. Surprisingly, NMR tubes are notorious for the formation of large crystals, discovered only as the tubes are about to be cleaned! Quite often, chemists set these tubes aside for weeks after the analysis, creating an undisturbed environment for crystal growth. NMR tubes are long and narrow, suppressing convection currents, and solvents very slowly evaporate through the low-permeable cap. Hence, the overall take-home message for crystal growth is to exercise patience; in the process of impatiently checking for crystal growth, additional nucleation sites are often introduced, resulting in the formation of small crystals. Fortunately, many institutions now possess CCD X-ray diffractometers that allow for enough data to be obtained from even microcrystalline solids, in a fraction of the time required for older four-circle instruments.

Although much crystallization from a solution is performed at low temperatures, crystals may also be formed from molten solids. For example, the Czochralski (CZ) method for purification of silicon uses a seed crystal on the surface of the melt maintained slightly above its melting point. As the crystal is slowly pulled from the
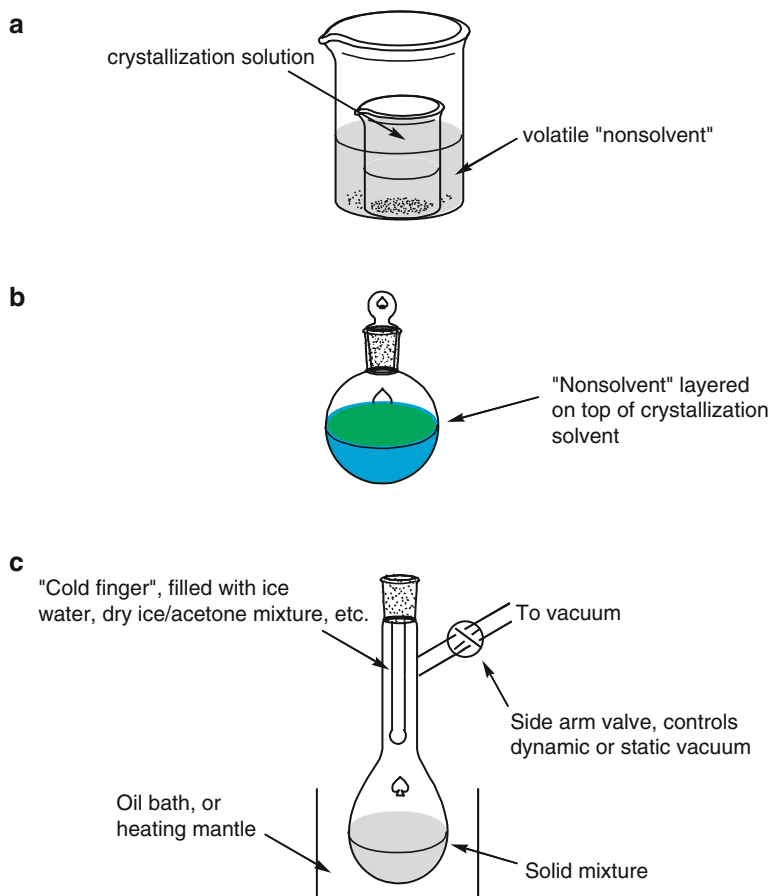
Figure 2.6. Schematic of three common methods used to grow single crystals. Shown is (a) *diffusion* where vapors from a volatile "nonsolvent" meet the crystallization solvent; (b) *interfacial* where the non-solvent is layered on top of the crystallization solvent; (c) *sublimation* where the solid mixture is heated and the vapors form crystallites on the surface of a cold finger. For this latter technique, the crystallization flask may be opened to vacuum throughout the sublimation process (dynamic vacuum), or closed after maintaining initial vacuum to allow slower crystal growth (static vacuum).

melt, there is extension of the crystal due to preferred alignment of other silicon atoms present in the melt (see Chapter 4). The empirical use of seed crystals is frequently used for crystal growth at all temperature regimes. Scratching the inside of the flask, or even using boiling stones has been successful at inducing crystal formation, through the introduction of sites for nucleation. It must be noted that pH is often not an important factor for inorganic or organic crystals; however, for protein crystallization, which is beyond the scope of this book, many such atypical conditions must also be considered.

2.3.2. Crystal Structures

A crystal is comprised of an infinite 3-D lattice of repeating units, of which the smallest building block is known as the *asymmetric unit*. When acted upon by crystal symmetry operations such as rotation axes or mirror planes (see Section 2.3.2), the asymmetric unit is duplicated to produce the contents of a *unit cell* (Figure 2.7). For any crystal lattice, it is possible to define an infinite number of possible unit cells (Figure 2.8). However, by convention, this unit is chosen to be a repeatable unit that
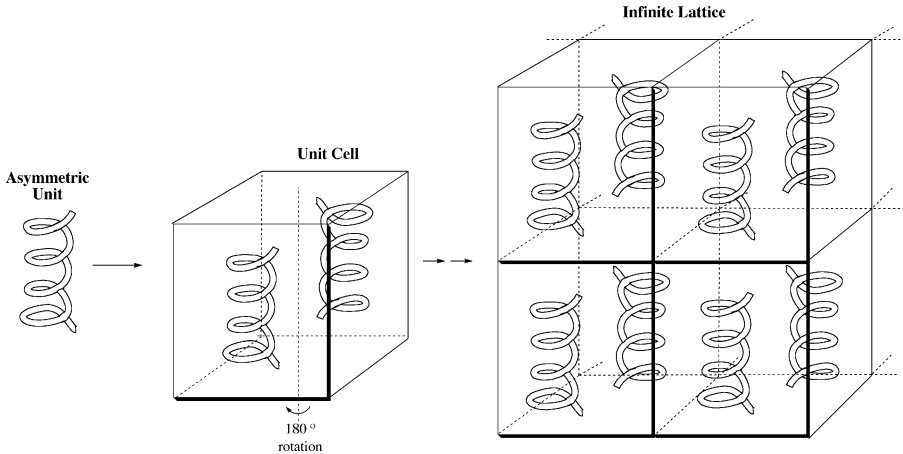
Figure 2.7. Illustration of the asymmetric unit of a unit cell.
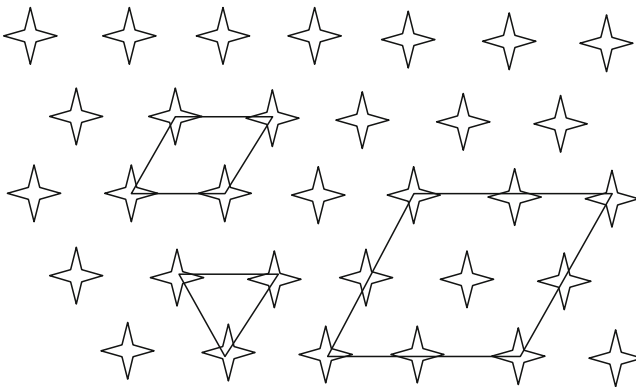
Figure 2.8. Representation of some unit cell selections from a two-dimensional array. The triangle and smaller rhombus selections are known as "primitive" unit cells, as each contains one object per unit cell ($3 \times 1/3$ for the triangle, $4 \times 1/4$ for the rhombus). By contrast, there are four objects per unit cell for the larger rhombus ($4 \times 1/4$ for corner objects; $4 \times 1/2$ for those on the edges; one in the center). When each of these selections is translated along the two-dimensional axes, they reproduce the positions of all objects in the lattice.
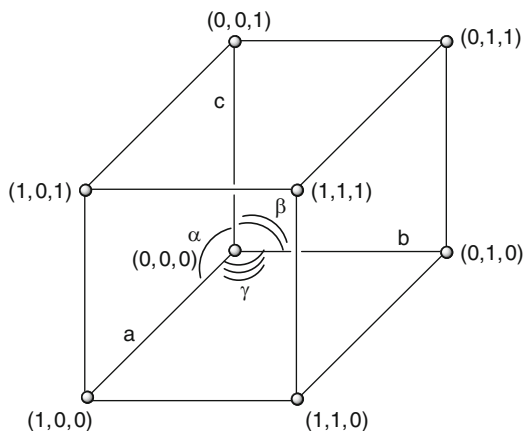
Figure 2.9. Illustration of definitive axes and angles for a unit cell. The angles and side lengths shown above are not representative of all unit cells; seven types of cell dimensions are possible (see text).

Table 2.2. Unit Cell Definitions for the Seven Crystal Systems

Crystal system	Unit cell vector lengths	Unit cell vector angles
Cubic (isometric)	$|a| = |b| = |c|$	$\alpha = \beta = \gamma = 90°$
Tetragonal	$|a| = |b| \neq |c|$	$\alpha = \beta = \gamma = 90°$
Orthorhombic	$|a| \neq |b| \neq |c|$	$\alpha = \beta = \gamma = 90°$
Trigonal (rhombohedral)	$|a| = |b| = |c|$	$\alpha = \beta = \gamma \neq 90°, \gamma < 120°$
Hexagonal	$|a| = |b| \neq |c|$	$\alpha = \beta = 90°, \gamma = 120°$
Monoclinic	$|a| \neq |b| \neq |c|$	$\alpha = \gamma = 90°, \beta \neq 90°$
Triclinic	$|a| \neq |b| \neq |c|$	$\alpha \neq 90°, \beta \neq 90°, \gamma \neq 90°$

possesses the same symmetry elements of the bulk crystal, and will generate the entire extended crystal lattice via translations along the unit cell axes. The structure that exhibits these properties while having the smallest possible volume is referred to as the *primitive* unit cell.

Figure 2.9 provides a schematic of the defining vectors and angles for a unit cell. It is convenient to describe these units as having three vectors (**a**, **b**, and **c**) that may or may not be aligned along the Cartesian axes, based on the values of unit cell angles. Depending on the geometry and volume of the unit cell, there are seven crystal systems that may be generated (Table 2.2).

For simplicity, fractional coordinates are used to describe the lattice positions in terms of crystallographic axes, **a**, **b**, and **c**. For instance, the fractional coordinates are (1/2, 1/2, 1/2) for an object perfectly in the middle of a unit cell, midway between all three crystallographic axes. To characterize crystallographic planes, integers known as *Miller indices* are used. These numbers are in the format (*hkl*), and correspond to the interception of unit cell vectors at (*a*/*h*, *b*/*k*, *c*/*l*). Figure 2.10 illustrates examples of the (001), (011) and (221) planes; since (*hkl*) intercepts the unit cell at {(*a, b, c*) : (1/*h*, 1/*k*, 1/*l*)}, a zero indicates that the plane is parallel to the particular axis, with no interception along $\pm \infty$.[11] A Miller index with capped
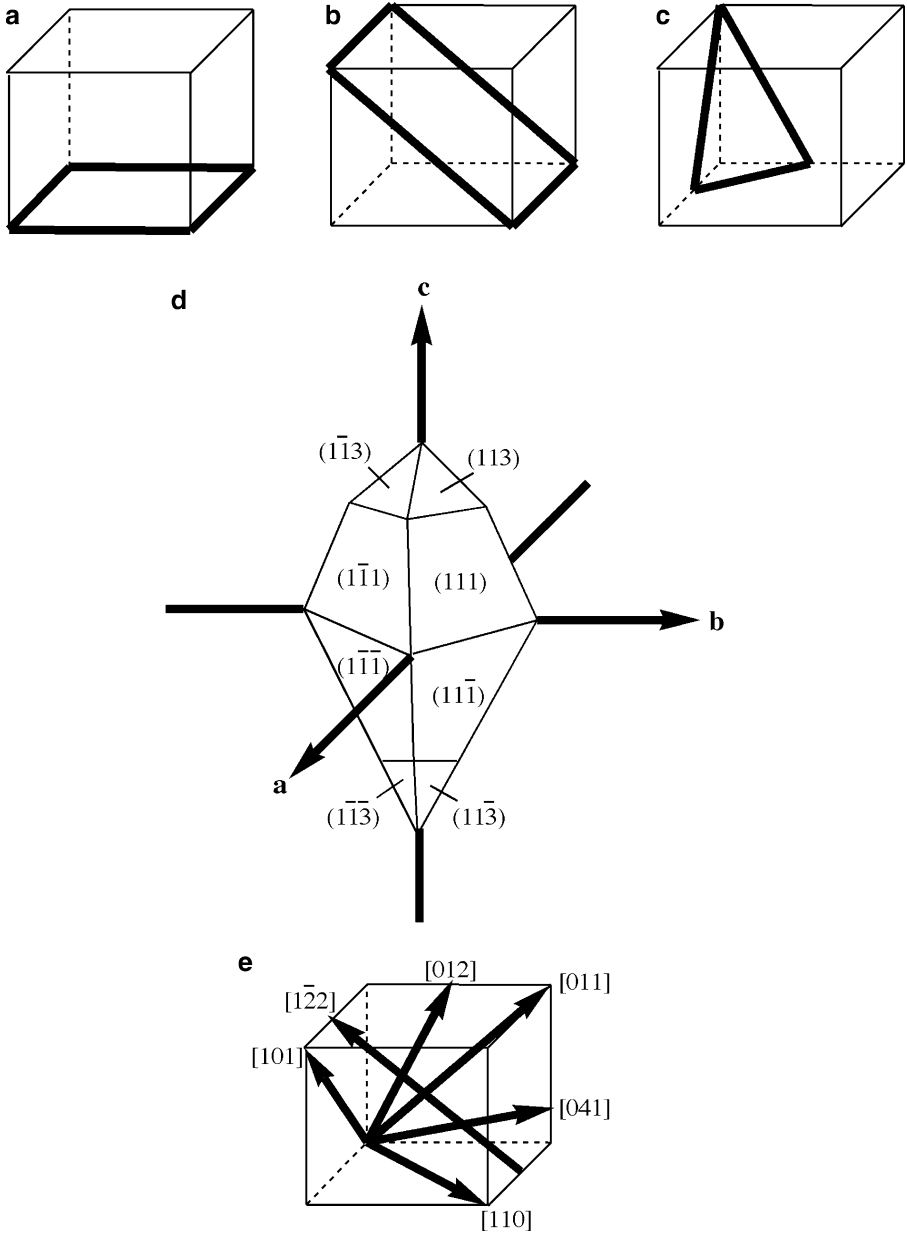
Figure 2.10. Representations of unit cell planes. Shown are: (a) (100), (b) (011), (c) (221), (d) {111} and {113} families of planes. Also illustrated are examples of unit cell directions, (e).

integers such as $(01\bar{1})$ indicates that the crystallographic axis is intercepted in the negative region (interception of the **c** axis at -1, in this case). Symmetry-equivalent planes are indicated by $\{hkl\}$; for example, $\{100\}$ for a cubic unit cell would have six equivalent planes: (100), $(\bar{1}00)$, (010), $(0\bar{1}0)$, (001), and $(00\bar{1})$.

Crystallographic directions correspond to vectors between two lattice points. To properly index directions, the vector should first be (re)positioned so its starting point is at (0,0,0) of the unit cell. The vector is then projected onto each of the three crystallographic axes, multiplying/dividing by a common factor to remove fractional terms. The three terms, expressed as integers, are enclosed within square brackets of the form [abc] (Figure 2.10e). For instance, the [211] direction would correspond to the vector $\mathbf{a} + (1/2)\mathbf{b} + (1/2)\mathbf{c}$. Families of equivalent directions are indicated by <abc>. For example, [100], [100], [010], [010], [001], and [001] directions in a cubic crystal are designated as <100>.

For hexagonal crystal planes, a slightly different indexing nomenclature is used relative to cubic crystals. To index a plane in the hexagonal system, four axes are used, called Miller–Bravais indices. In addition to both **a** and **b** axes, another axis is used, that bisects the γ-angle on the hexagonal *basal plane* – designated as $\mathbf{a_3}$ in Figure 2.11.[12] The use of three axes on the basal plane is required due to the threefold rotation axis present in the lattice. Examples of hexagonal plane indices are shown in Figure 2.11, of the form $(hkil)$, where $i = -h-k$. Lattice directions are indexed analogously to cubic crystals, using only **a**, **b**, and **c** crystallographic axes.

For crystals comprised of metal atoms, the lattice may be simplified as a regular packing of hard spheres. In three dimensions, there are only two ways that spheres may
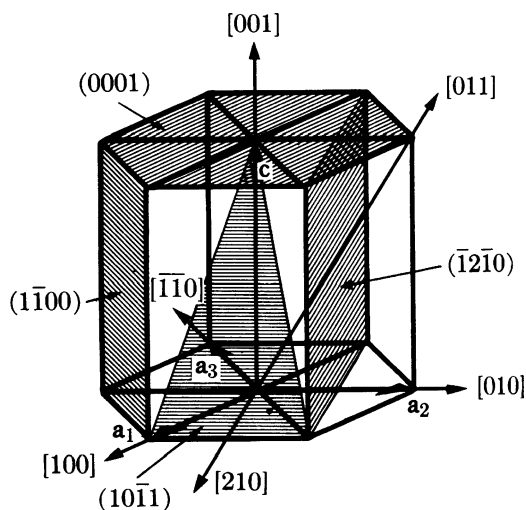

Figure 2.11. Examples of planes (in parentheses) and directions [in brackets] of a hexagonal unit cell. Planes are designated by the $(h\,k\,i\,l)$ designation, where $i = -h-k$. Reproduced with permission from Cullity, B. D. *Elements of X-Ray Diffraction*, 2nd ed., Addison-Wesley: Reading, MA. Copyright 1978 Prentice-Hall.

pack: either simple cubic or close-packed. For example, think about dropping marbles into a large beaker partially filled with water. As the marbles settle to the bottom of the container, they will seek their most stable resting position. These positions will be mostly within the voids formed between three spheres (close-packed), rather than on top of the crests of individual spheres (simple cubic packing). Whereas the coordination number (*i.e.*, number of nearest neighbors) of individual species for simple cubic packing is six, the coordination number for close-packing is 12.

Since a simple cubic arrangement would have a significant amount of excess void-space, this presents a much less efficient manner to pack individual spheres. This larger volume of empty space in simple packing would result in a lower density for the solid relative to its close-packing analog. It should also be noted that the sliding of one layer over another would be more preferred for simple cubic relative to close-packing. This corresponds to a greater degree of crystal defects that are possible for these solids.

Although marble migration is only mentioned as an example, this process is not far removed from the crystallization process. In the formation of single crystals, individual ions/atoms/molecules slowly come into contact with one another, and nucleate from thermodynamically favored positions. Sometimes metastable phases may be obtained if one does not allow such preferential migration to occur, through rapid cooling events, for instance.

Figure 2.12 serves to aid in the visualization of sphere packing sequences in three-dimensions. After a few spheres (in A sites) are arranged in a close-packed
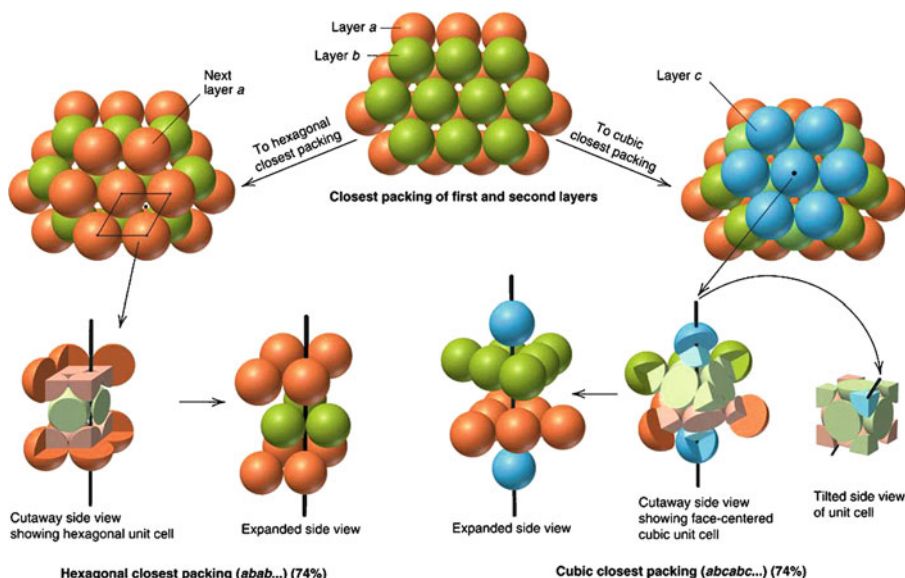

Figure 2.12. Representations of hexagonal close-packing (hcp) and face-centered cubic (fcc) packing. Reproduced with permission from Silberberg, M. S. *Chemistry: The Molecular Nature of Matter*, 2nd ed., McGraw-Hill: New York, 2000.

H hcp																	He hcp
Li bcc	Be hcp											B tetrag	C hcp	N hcp	O cubic	F	Ne fcc
Na bcc	Mg hcp											Al fcc	Si diam	P orthor	S orthor	Cl tetrag	Ar fcc
K bcc	Ca fcc	Sc hcp	Ti hcp	V bcc	Cr bcc	Mn bcc	Fe bcc	Co hcp	Ni fcc	Cu fcc	Zn hcp	Ga orthor	Ge diam	As rhomb	Se hcp	Br orthor	Kr fcc
Rb bcc	Sr fcc	Y hcp	Zr hcp	Nb bcc	Mo bcc	Tc hcp	Ru hcp	Rh fcc	Pd fcc	Ag fcc	Cd hcp	In tetrag	Sn tetrag	Sb rhomb	Te hcp	I orthor	Xe fcc
Cs bcc	Ba bcc	La hcp	Hf hcp	Ta bcc	W bcc	Re hcp	Os hcp	Ir fcc	Pt fcc	Au fcc	Hg rhomb	Tl hcp	Pb fcc	Bi rhomb	Po monoc	At	Rn fcc
Fr bcc	Ra bcc	Ac fcc	Rf	Db	Sg	Bh	Hs	Mt									

Ce fcc	Pr hcp	Nd hcp	Pm	Sm rhomb	Eu bcc	Gd hcp	Tb hcp	Dy hcp	Ho hcp	Er hcp	Tm hcp	Yb fcc	Lu hcp
Th fcc	Pa tetrag	U orthor	Np orthor	Pu monoc	Am hcp	Cm	Bk	Cf	Es	Fm	Md	No	Lr

Figure 2.13. Preferred crystal structures of the elements. Shown are the ordinary forms of each element in its solid state (*e.g.*, graphite, α-iron, *etc.*). The following abbreviations are used: fcc, bcc (body-centered cubic), hcp, cubic (simple cubic), diam (diamond or zinc blende), monoc (monoclinic), rhomb (rhombohedral), tetrag (tetragonal), and orthor (orthorhombic).

arrangement, the next layer packs into B sites, formed as voids above three A spheres. For the third layer of spheres, there are two possibilities that may occur. The atoms/ions in the third layer may sit directly above the spheres in the A layer, or may be placed in C sites. If the packing is described by the former case (ABABAB...), the crystal lattice is described as a hexagonal close-packed (hcp) arrangement. By contrast, if the packing scheme occupies all possible sites (ABCABCABC..., or ACBACBACB...), then the arrangement is termed cubic close-packed, or face-centered cubic (fcc). The Periodic Table shown in Figure 2.13 demonstrates that the close-packing motifs are the most prevalent for natural forms of the elements, which represents the most efficient means to pack multiple layers of hard spheres.

Since hcp crystals have vacant C sites, there are uniaxial channels through the crystalline solid that influences their physical properties. For example, Be, Mg, and Ti alloys that crystallize in hcp arrangements possess extremely low densities, while other hcp metals (*e.g.*, Co) have the possibility for anisotropic magnetic properties.

Although it is easy to visualize a fcc unit cell, with atoms/ions on each corner and on each face of a cube, the ABCABC... packing scheme is more difficult to unravel. Once the unit cell is viewed along the cell corners, parallel to the (111) plane, the packing layers are readily observed (Figure 2.14a). When viewed along a vector perpendicular to the packing planes, the atoms/ions occupying the B and C sites are observed as inverted triangles (Figure 2.14b). Common examples of this packing scheme are diamond, ZnS (zinc blende form), HgS, CuI, AlSb, BeSe, *etc*.
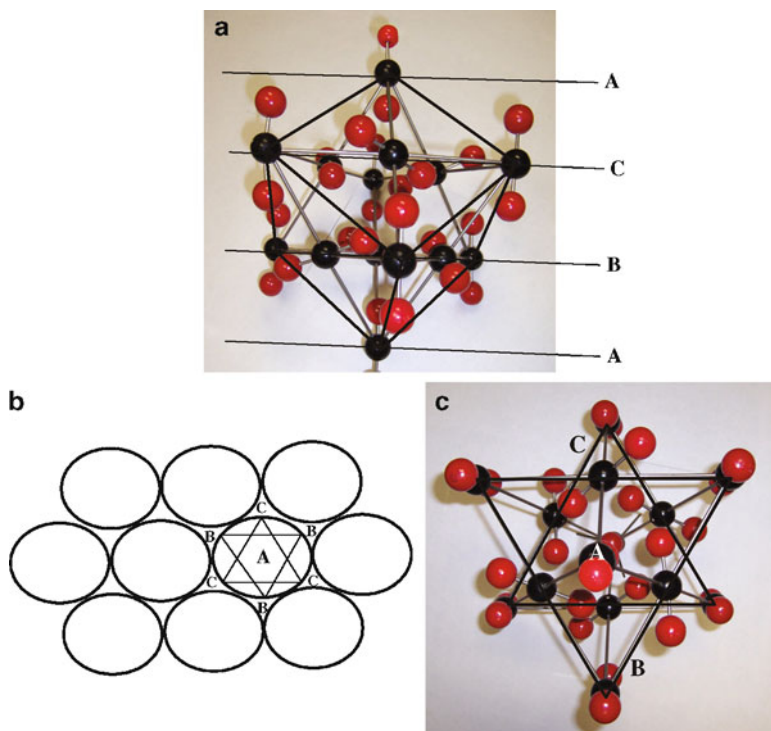
Figure 2.14. Packing model and illustration for cubic close-packed (face-centered cubic, fcc). Shown is solid carbon dioxide (dry ice), that consists of individual CO_2 molecules that pack in an fcc lattice. The *black* carbon atoms shown in (a) illustrate a traditional representation of the lattice, consisting of a cube with atoms on each of the faces. The packing layers are shown from two different views; (a) parallel to the ABC... layers (*i.e.*, (111) planes) and (b) perpendicular to these layers.

Hexagonal close-packing is illustrated in Figure 2.15, showing a unit cell with translation to form a hexagonal arrangement with a sixfold rotation axis. Using simple geometry, it may be proven that the coordinates of the B sites are $\{(a, b, c) = (2/3, 1/3, 1/2)$ or $(1/3, 2/3, 1/2)\}$. There are two possibilities due to lattice equivalency; however, once one of these is designated for B sites, the other positions are designated as C sites and remain vacant in hcp crystal lattices. Although the packing sequence is different between hcp and fcc lattices, there is a similarity between these close-packed structures. The atoms in the (111) planes of B and C layers shown in Figure 2.14 are arranged in a hexagonal pattern, analogous to the stacking planes for hcp shown in Figure 2.12.

Although ccp and hcp arrangements have been shown in detail, there are many other possibilities for the packing of species in a crystal lattice. In 1849, Bravais discovered that there are only 14 possible arrangements of points in three-dimensional space, assuming that each point has an identical environment. Hence, regardless of the identity of the species comprising an infinite crystal lattice, the unit cell must be described by one of these Bravais lattices (Figure 2.16). Other designations that are
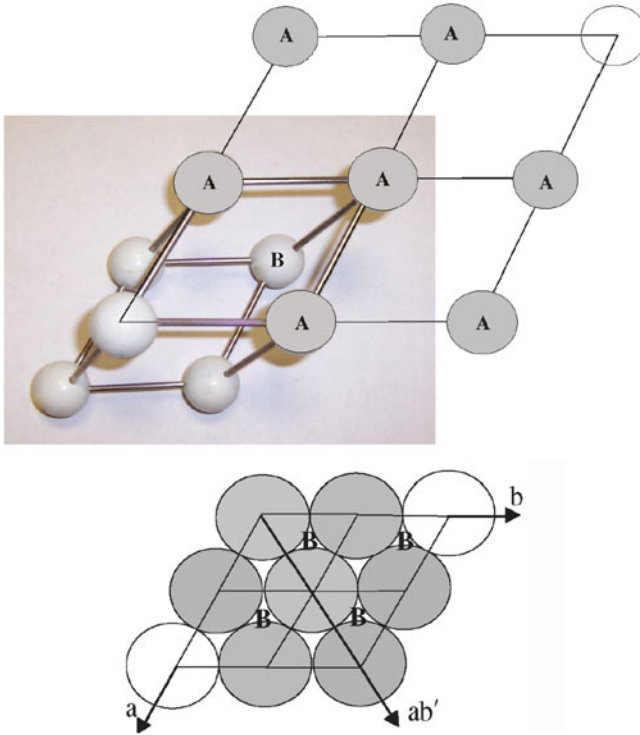
Figure 2.15. Schematic of the packing in an hcp unit cell, showing equivalent close-packed B sites. The hexagon of A atoms is referred to as the basal plane, as this plane marks the top and bottom of a unit cell. The fractional coordinates of each set of B sites are {(a, b, c): (1/3, 2/3, 1/2) shown, or (2/3, 1/3, 1/2)}.

not listed are not oversights, but may be further simplified. For instance, a "base-centered tetragonal" unit cell does not appear as one of the 14 Bravais lattices. As shown in Figure 2.17, a primitive unit cell may be defined from a base-centered tetragonal array – the former is preferentially chosen due to its smaller volume.

A subclass of polymorphism known as *polytypism* is found for one-dimensional close-packed and layered structures such as SiC, CdI_2, ZnS, GaSe, and micas/clay minerals such as kaolins. These crystal structures exhibit differing three-dimensional lattices that vary depending on the stacking order of the two-dimensional sheets that comprise the crystal, known as modular layers. Figure 2.18 illustrates the crystal structures for two common polytypes of SiC, an important material used in ceramic brakes, abrasive machining, and high-temperature electronic applications.[13] Polytypes are defined by the Ramsdell notation <number><letter>, where the number indicates how many planes are stacked in a discrete unit cell, and the letter indicates the crystal lattice type (C = cubic, H = hexagonal, R = rhombohedral). Amazingly, there are over 200 known polytypes of SiC; the most common include 3C (*i.e.,* fcc with ABC... packing), 2H, 4H, 6H, 8H, 9R, 10H, 14H, 15R, 19R, 20H, 21H, and 24R.[14]

Figure 2.16. Models of the 14 Bravais lattices. The various types of Bravais centering are given the symbols *P* (primitive/simple), *F* (face-centered), *I* (body-centered), and *C* (base-centered). The primitive rhombohedral Bravais lattice is often given its own symbol, *R*, and corresponds to a primitive unit cell possessing trigonal symmetry.

Archetypical interstitial crystal lattices

For crystal lattices of ionic solids, the unit cell is best described as one of the 14 Bravais lattices for the larger ion (typically anion), with the smaller ion (cation) occupying vacant sites within the lattice, known as *interstitial sites*. Based on the number of nearest neighbors immediately surrounding these positions, interstitial sites may exist with coordination numbers of 3 (trigonal), 4 (tetrahedral), 6 (octahedral), and 8 (cubic). An example of a cubic site is a species that is housed within the (1/2, 1/2, 1/2) position of a unit cell, surrounded by eight nearest neighbors.

Figure 2.19 provides representations of the interstitial sites within fcc, bcc, and hcp lattices as projected onto the (a, b) plane, with fractional heights along the c-axis indicated. Table 2.3 lists the fractional coordinates of these interstitials for each type of lattice. A fcc unit cell (Figure 2.19a) has a total of eight tetrahedral interstitial sites per unit cell. Each of the tetrahedral interstitial sites has a radius equal to 22.5%

Figure 2.17. Equivalency of a base-centered tetragonal and a primitive tetragonal unit cell.
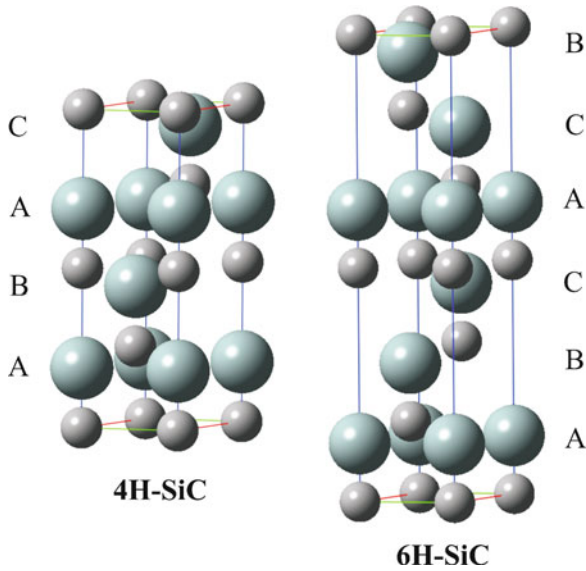
Figure 2.18. Unit cells for the 4H and 6H polytypes of silicon carbide, as viewed along the $(11\bar{2}0)$ plane. Note that each carbon atom is situated in the center of a Si_4 tetrahedron.
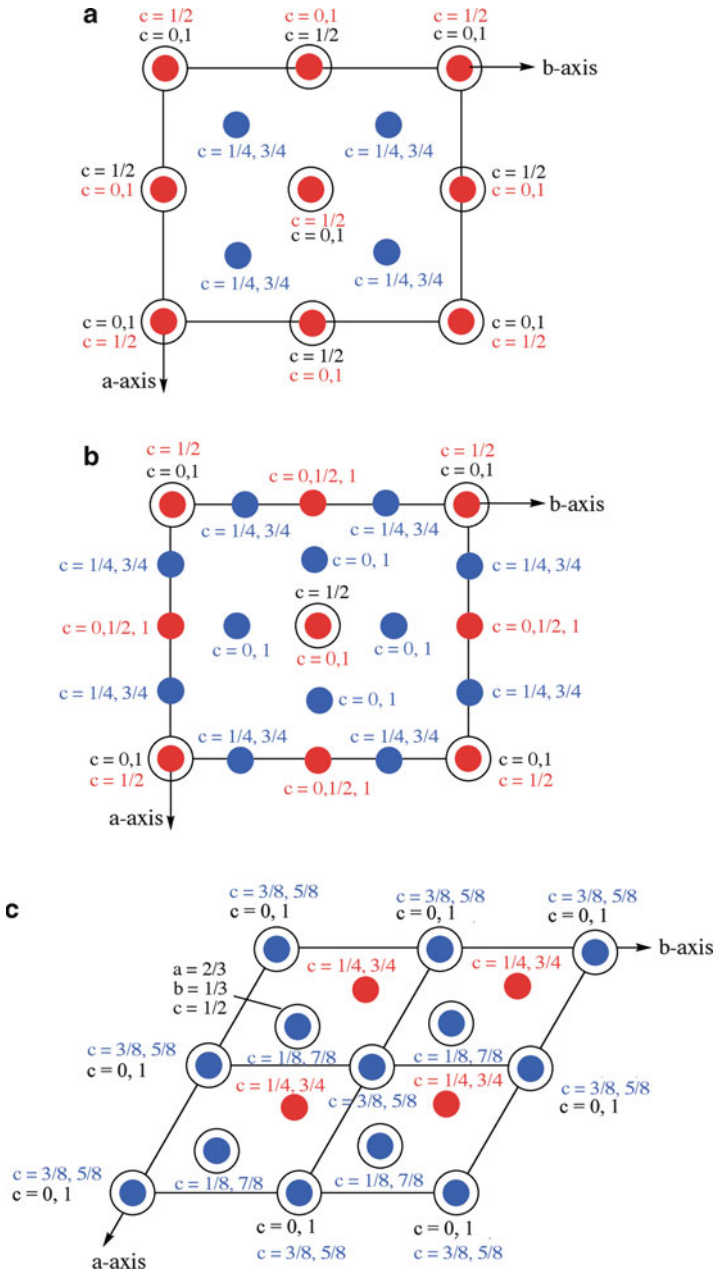
Figure 2.19. Illustrations of the locations of interstitial sites within (a) fcc, (b) bcc, and (c) hcp unit cells. The positions of black spheres are the cubic close-packed lattice positions, whereas red and blue indicate octahedral and tetrahedral interstitial positions, respectively.

Table 2.3. Fractional Unit Cell Coordinates of Interstitial Sites

Crystal system	Octahedral interstitials	Tetrahedral interstitials
FCC	(1/2, 0, 0), (0, 1/2, 0), (1, 1/2, 0), (1/2, 1, 0), (0, 0, 1/2), (0, 1, 1/2), (1, 1, 1/2), (1, 0, 1/2), (1/2, 0, 1), (0, 1/2, 1), (1, 1/2, 1), (1/2, 1, 1), (1/2, 1/2, 1/2)	(1/4, 1/4, 1/4), (1/4, 3/4, 1/4), (3/4, 3/4, 1/4), (3/4, 1/4, 1/4), (1/4, 1/4, 3/4), (1/4, 3/4, 3/4), (3/4, 3/4, 3/4), (3/4, 1/4, 3/4)
BCC	(1/2, 0, 0), (1, 1/2, 0), (1/2, 1/2, 0), (1/2, 1, 0), (0, 1/2, 0), (1, 0, 1/2), (1/2, 0, 1/2), (0, 0, 1/2), (1, 1, 1/2), (0, 1, 1/2), (1, 1/2, 1/2), (1/2, 1, 1/2), (0, 1/2, 1/2), (1/2, 0, 1), (1, 1/2, 1), (1/2, 1, 1), (0, 1/2, 1), (1/2, 1/2, 1)	(1/2, 1/4, 0), (1/2, 3/4, 0), (1/4, 1/2, 0), (3/4, 1/2, 0), (1/2, 1/4, 1), (1/2, 3/4, 1), (1/4, 1/2, 1), (3/4, 1/2, 1), (3/4, 0, 1/4), (3/4, 0, 3/4), (1/4, 0, 1/4), (1/4, 0, 3/4), (1, 1/4, 1/4), (1, 3/4, 1/4), (1, 1/4, 3/4), (1, 3/4, 3/4), (0, 1/4, 1/4), (0, 3/4, 1/4), (0, 1/4, 3/4), (0, 3/4, 3/4), (1/4, 1, 1/4), (1/4, 1, 3/4), (3/4, 1, 1/4), (3/4, 1, 3/4)
HCP	(1/3, 2/3, 1/4), (1/3, 2/3, 3/4)	(0, 0, 3/8), (1, 0, 3/8), (0, 1, 3/8), (1, 1, 3/8), (0, 0, 5/8), (1, 0, 5/8), (0, 1, 5/8), (1, 1, 5/8), (2/3, 1/3, 1/8), (2/3, 1/3, 7/8)

of the host atom/ion radius. The four octahedral sites in fcc are at the edges of the unit cell (*i.e.,* (1/2, 0, 0) and 11 others – each 1/4 inside the unit cell), plus a position in the center (1/2, 1/2, 1/2). The octahedral sites have a radius equal to 41.4% of the host atom/ion radius.

For a bcc unit cell (Figure 2.19b), there are four tetrahedral interstitials on each of the six cell faces (each 1/2 inside the unit cell), giving rise to 12 tetrahedral sites per unit cell. There is one octahedral site on each of the six bcc cell faces (each 1/2 inside the unit cell), as well as one on each of the 12 cell edges (each 1/4 inside the unit cell), totaling six octahedral sites per unit cell. The radii of the tetrahedral and octahedral sites are 29% and 15.5% of the host atom/ion radius, respectively. It should be noted that a simple cubic crystal has a single cubic interstitial site at (1/2, 1/2, 1/2); this has a radius equal to 73% of the size of the host atoms/ions in the unit cell.

Figure 2.19c illustrates a hcp unit cell defined by lattice species at (0, 0, 0) and (2/3, 1/3, 1/2). There are four tetrahedral sites and two octahedral sites per unit cell. The sizes of tetrahedral or octahedral holes within a hcp and fcc array are equivalent, respectively accommodating a sphere with dimensions of 0.225 or 0.414 times (or slightly larger) the size of a close-packed lattice atom/ion.

The nickel arsenide (NiAs) structure (Figure 2.20) is an important hcp example; in this case, the cations form the backbone lattice, and the larger anions occupy both octahedral sites. This structure, also associated with metal chalocogenides such as CoSe, NiTe, $Co_xNi_{1-x}As$, FeS, NiSe, $PtSb_xBi_{1-x}$, and $Pd_xNi_{1-x}Sb$ are only adopted for weakly ionic compounds. Since the octahedral sites are extremely close to one another, purely ionic compounds would be much too unstable due to strong anion-anion repulsions.
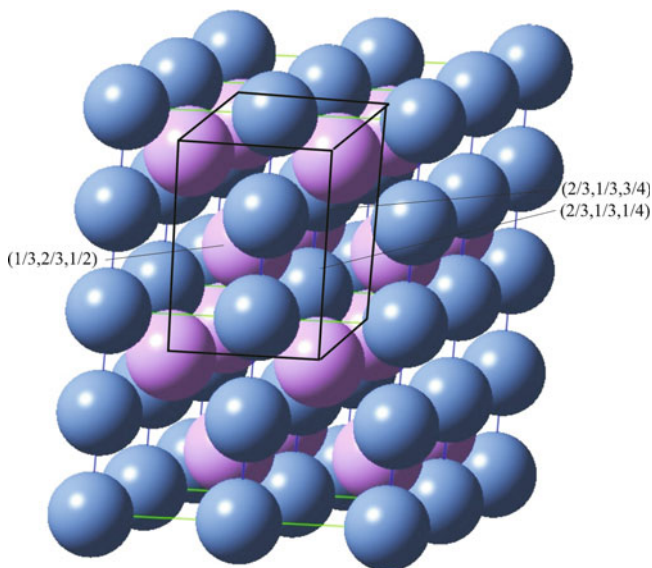
Figure 2.20. Schematic of the NiAs structure. This consists of a hcp array of As^{3-} (purple) ions, with Ni^{3+} (blue) ions occupying all of the available octahedral interstitial sites.

The crystal structure for α-alumina (corundum) is quite similar to NiAs; in this case, 2/3 of the available octahedral interstitial sites are occupied with Al^{3+}, within a hcp framework array of O^{2-} ions (Figure 2.21). Alumina has a diverse range of uses including heterogeneous catalysis supports, aluminum metal production, and as an abrasive refractory ceramic material for grinding/cutting tooling and protective coating applications. Alumina is also used as a polishing agent within CD/DVD repair kits and toothpaste formulations.

Another common hcp-based variety, CdI_2, exhibits partially covalent bonding. This is a very common crystal structure not just for metal (II) halides (*e.g.*, MgI_2, TiI_2, VI_2, MnI_2, FeI_2, CoI_2, PdI_2, $TiCl_2$, VCl_2, $MgBr_2$, $TiBr_2$, $FeBr_2$, $CoBr_2$), but for metal (II) hydroxides (*e.g.*, $Mg(OH)_2$, $Ni(OH)_2$, $Ca(OH)_2$), metal (IV) chalcogenides (*i.e.*, ME_2, M = Grps 4, 5, 9, 10, 14; E = S, Se, Te), and intermetallics (*e.g.*, Cd_2Ce, Cd_2La). This structure is based on a hcp array of the anionic species, with the cation occupying the octahedral sites in alternate layers (Figure 2.22). It should be noted that if the I^- anions are replaced with smaller Cl^- ions, a cubic $CdCl_2$ archetypical structure may result[15] (other examples: $MgCl_2$, $CoCl_2$, $NiCl_2$, $MnCl_2$, NbS_2, TaS_2, NiI_2). This structure consists of a fcc array of Cl^- ions, with the cations occupying octahedral holes in alternate layers.

For ionic crystals, the preference of a cation to occupy a certain interstitial site is primarily governed by the ionic radius ratio of the cation/anion (r_+/r_-).[16] Since anions are most often larger than cations, this ratio is usually less than
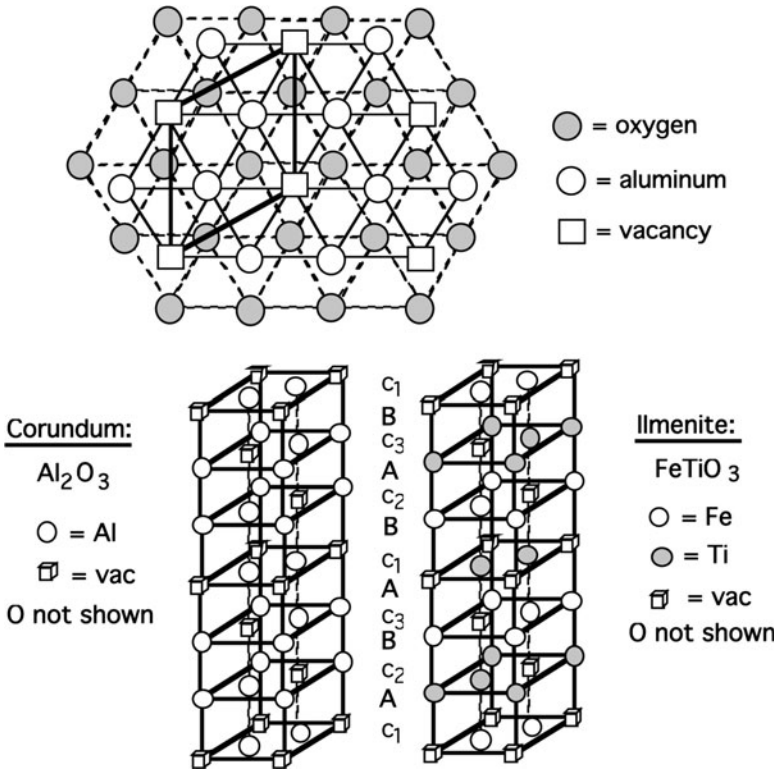
Figure 2.21. Schematic of the a-Al_2O_3 (aluminum oxide, corundum) crystal structure. Shown is the hcp array of O^{2-} ions with Al^{3+} ions and vacancies in the octahedral c-sites above the A plane of the oxide ions. The comparative stacking sequences of Al_2O_3 and $FeTiO_3$ (ilmenite) are also illustrated.

one (Table 2.4). An exception may be found for unusually large cations with small anions such as CsCl ($r_+/r_- = 1.08$). As the value of this ratio decreases, the size of the anions become significantly larger than the cations, and the cation will prefer to occupy a smaller interstitial site. To rationalize this preference, consider a simple cubic arrangement of bowling balls (*cf.* large anions) with a small golf ball (*cf.* small cation) in the middle. Due to the large size difference, this arrangement would not be stable, as the golf ball would rattle around the cubic "cage" formed by the bowling balls. Rather, a smaller close-packed interstitial site such as trigonal or tetrahedral would best contain the smaller golf ball.

For compound unit cells, it is important to point out the occupation of the atoms/ions occupying the Bravais framework and the other species in interstitial sites. For example, the *CsCl structure* is best described as consisting of a simple cubic arrangement of Cl^- ions, and a Cs^+ ion in a cubic interstitial site. Alternatively, one could also designate this structure as having Cs^+ ions at the corners of a cube, and Cl^- in the interstitial cubic site. Even though the overall arrangement of
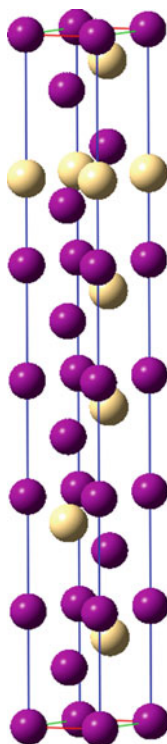
Figure 2.22. Schematic of one common polymorph of the CdI_2 structure. This is based on a hcp array of I^- ions (purple), with Cd^{2+} ions (yellow) occupying octahedral interstitial sites in alternating layers.

Table 2.4. Ionic Radii Ratios Corresponding to Interstitial Sites

Radii ratio range (r_+/r_-)	Geometry of interstitial site (coordination number)
<0.225	Trigonal (3)
<0.414	Tetrahedral (4)
<0.732	Octahedral (6)
>0.732	Cubic (8)

ions in this structure is bcc, such a compound unit cell cannot be assigned to this arrangement since the ions are not equivalent. Many other compounds crystallize in the CsCl structure, such as CsBr, CsI, RbCl (at high temperature/pressure), and intermetallics such as β-AgCd, AgCe, AlFe, AlNd, β-AlNi, AlSc, β-AuCd, AuMg, BaCd, BeCu, BeCo, BePd, CaTi, CdCe, CeMg, CoFe, CoSc, CuEu, β-CuPd, β-CuZn, β-GaNi, GaRh, HgMg, HgSr, HoIn, HoTl, InLn, LiTi, MgPr, MgTi, β-MnPd, β-MnRh, OsTi, RhY, α-RuSi, RuTi, SbTi, ScRh, and SrTi.

It is not immediately apparent why many different values for individual ionic radii appear in reference books. The value for an ionic radius is dependent on its

lattice arrangement, and is determined from electron density maps and empirical X-ray diffraction data. Some general trends for cationic radii are:

1. For a given species and charge, the radius increases as the coordination number increases.
2. For a given charge, the radius decreases with increasing effective nuclear charge, Z_{eff}.[17]
3. For a given species, the radius decreases with increasing ionic charge.
4. For a given species and charge, the radius is larger for high-spin (weak field) ions than for low-spin (strong field) ions.

Most inorganic chemistry texts list cut-off values for the r_+/r_- ratios corresponding to the various geometries of interstitial sites (Table 2.4). For instance, the halite or *rocksalt* structure exhibited by MX (M = Grp I, Mg, Pb, Ag; X = F, Cl, Br, I) are predicted to have occupation of octahedral interstitial sites. Indeed, these structures are described as a fcc array of the halide ion (except for v. small F^-), with the cation occupying all of the octahedral interstitial sites (*i.e.*, 4 MX units per unit cell).

However, it should also be pointed out that deviations in these predictions are found for many crystals due to covalent bonding character. In fact, the bonding character for compounds is rarely 100% covalent or ionic in nature, especially for inorganic species. For instance, consider the zinc sulfide (ZnS) crystal structure. The ionic radius ratio for this structure is 0.52, which indicates that the cations should occupy octahedral interstitial sites. However, due to partial covalent bonding character, the anions are closer together than would occur from purely electrostatic attraction. This results in an "effective radius ratio" that is decreased, and a cation preference for tetrahedral sites rather than octahedral. One crystal structure for this complex lattice (α-ZnS, Wurtzite structure – also found for β-AgI, ZnO, α-CdS, CdSe, α-SiC, GaN, AlN, ωBN, and BeO) is shown in Figure 2.23. This is best described as a hcp lattice of sulfide ions, with zinc ions occupying one-half of the available tetrahedral interstitial sites. As you might expect, a hybrid of ionic/covalent bonding will greatly affect the physical properties of the solid; for instance, the hardness of ZnS is significantly greater than what would be expected for a purely ionic solid.

Interestingly, zinc sulfide (β-ZnS) may also crystallize in a cubic lattice, which consists of a fcc array of S^{2-}, with Zn occupying 1/2 of the available tetrahedral sites. This structure is known as *sphalerite* or *zincblende*, and is shared with other compounds such as α-AgI, β-BN, CuBr, and β-CdS. When the same atom occupies both the fcc and tetrahedral interstitials of the sphalerite structure, it is described as the *diamond lattice*, shared with elemental forms (allotropes) of silicon, germanium, and tin, as well as alloys thereof. Important semiconductors such as GaAs, β-SiC, and InSb also adopt the sphalerite crystal structure.

If the cation in the crystal lattice exhibits a cubic environment (coordination number of 8), the *fluorite* structure is commonly observed (Figure 2.24). Lattices of this variety consist of an fcc arrangement of cations, with all eight tetrahedral interstitial sites (*e.g.*, (1/4, 1/4, 1/4), *etc.*) occupied by the anionic species. Of course, this will only be prevalent when the size of the anion is much smaller than the cation,
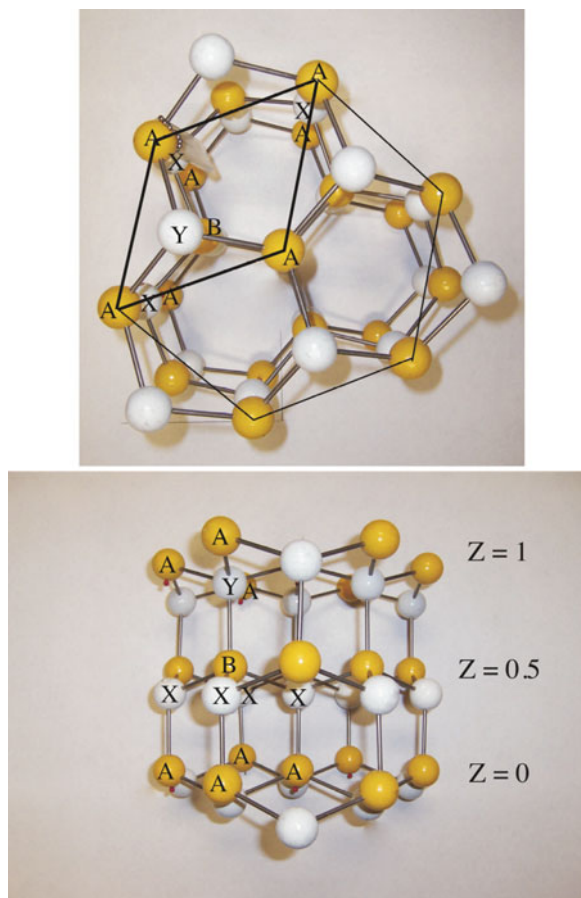
Figure 2.23. Model of the wurtzite (ZnS) crystal structure. The framework is based on an hcp lattice of S^{2-} anions (yellow; the unit cell consists of A and B ions) with zinc ions occupying tetrahedral interstitial sites (white, labeled as X and Y ions).

such as CaF_2. Other examples of fluorite lattices include intermetallics (*e.g.*, $PtGa_2$, $SnMg_2$, LiMgP, HoOF, $GeLi_5P_3$, $AuIn_2$), oxides (*e.g.*, ZrO_2 (cubic zirconia), CeO_2, UO_2), hydrides (*e.g.*, CeH_2, NbH_2), and nitrides (*e.g.*, UN_2). For structures with relatively smaller cations, the anions will form the fcc lattice, with cations situated within the interstitials. Since the relative positions of cations and anions are reversed in the latter case, the *anti* prefix is used, designating the structure as *antifluorite* (*e.g.*, alkali metal oxides, Li_2O). For intermetallic compounds of stoichiometry AB_2, which differ significantly in electronegativity, either the pyrite (FeS_2) structure (*e.g.,* $AuSb_2$, $PdAs_2$, $PdBi_2$, $PdSb_2$, $PtAs_2$, $PtBi_2$, $PtSb_2$, and $RuSn_2$), or CaC_2 structure (*e.g.,* Ag_2Er, Ag_2Ho, Ag_2Yb, $AlCr_2$, $AuEr_2$, $AuHo_2$, Au_2Yb, Hg_2MgSi_2W, $MoSi_2$, and $ReSi_2$) is favored.
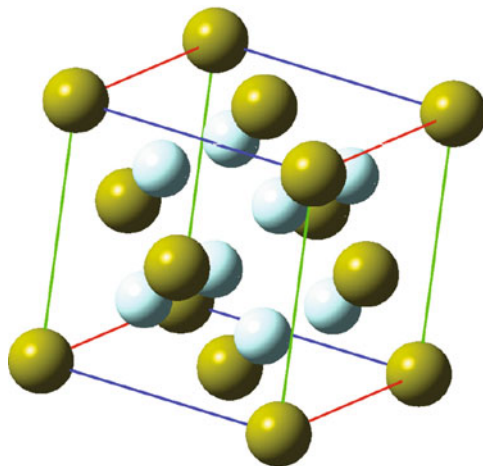
Figure 2.24. Unit cell representation for the fluorite structure of CaF_2.

Metal oxide lattices

The vast majority of catalysts used in heterogeneous catalytic processes are based on metal oxides, either as the catalytically active species (*e.g.*, TiO_2) or as a high surface area support material (*e.g.*, MgO). There is ongoing interest in the preparation of these catalysts with specific reproducible properties; a challenge that has been possible through increasing knowledge regarding the structure/property relationships of these materials.

In this section, we will describe a number of important crystals that are comprised of a close-packed array of oxide anions, with cations situated in vacant interstitial sites. Often, there are two or more different types of cations that occupy the vacancies. One example is the *normal spinel* structure consisting of a fcc array of oxide ions (as well as S^{2-} (*e.g.*, $FeCr_2S_4$, $CuCr_2S_4$, Fe_3S_4) or Se^{2-} (*e.g.*, $ZnCr_2Se_4$)), with 1/8 of the tetrahedral holes occupied by M^{2+} ions, and 1/2 of the octahedral holes occupied with M^{3+} ions. The *inverse spinel* structure features the divalent cations switching places with half of the trivalent ions (*i.e.*, M^{3+} positioned within tetrahedral sites and M^{2+} within octahedral sites).

The complicated unit cell for normal spinel is shown in Figure 2.25, which is comprised of a large fcc array of tetrahedrally-coordinated cations, and eight octant sub-units that contain O^{2-} and M^{2+}/M^{3+} cations. The ionic count per unit cell (u.c.) is as follows:

M^{2+}: fcc array (four ions/u.c.) + one ion in the center of 4/8 octant sub-units = 8/u.c.

M^{3+}: four ions at alternating corners of 4/8 octant sub-units = 16/u.c.

O^{2-}: four ions at alternating corners in all octant sub-units = 32/u.c.

Hence, the normal spinel structure may also be described as $[M^{2+}]_8(M^{3+})_{16}O_{32}$ or $[M^{2+}_{8/3}M^{3+}_{16/3}](M^{2+}_{16/3}M^{3+}_{32/3})O_{32}$, where brackets and parentheses indicate
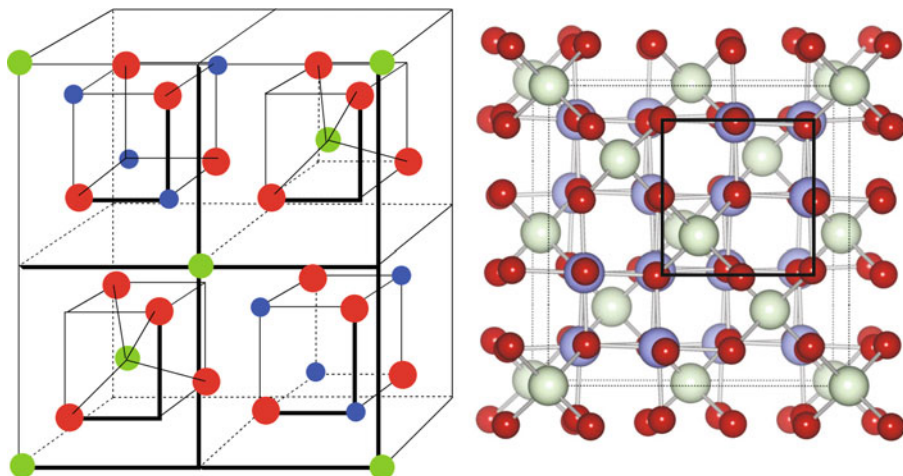
Figure 2.25. Illustrations of the AB_2O_4 (binary: A = B; ternary: A $\neq$ B) normal spinel lattice. For clarity the representation on the left shows the front half of the unit cell. The A ions (green), generally in the +2 oxidation state, occupy 1/8 of the available tetrahedral sites; the B ions (blue), generally in the +3 oxidation state, occupy 1/2 of the available octahedral sites within a fcc oxygen (red) sublattice. Reproduced with permission from *Phys. Rev. B* **2007**, *76*, 165119. Copyright 2007 The American Physical Society.

ions in tetrahedral and octahedral sites, respectively. More simply, one can describe the AB_2O_4 stoichiometry of the spinel structure as a fcc of O^{2-} ions, with A^{2+} occupying 1/8 of the tetrahedral sites and B^{3+} occupying 1/2 of the octahedral sites (Figure 2.25).

Magnetic tape has long employed the inverse spinel magnetite, Fe_3O_4, which contains iron cations in mixed oxidation states $[Fe^{3+}](Fe^{2+}/Fe^{3+})O_4$. Another magnetic iron oxide used for these applications is known as maghemite, which has the structure $[Fe^{3+}]_8(Fe_{40/3}{}^{3+}\square_{8/3})O_{32}$. The $\square$ symbol indicates a vacancy; hence, this structure is considered Fe^{2+}-deficient magnetite, a defect inverse spinel structure. Since these magnetic ferrites (and others such as Co_3O_4) contain only one metal in two oxidation states of the general form M_3O_4, they are referred to as binary spinels.

In addition to the above ferrites that contain M^{2+}/M^{3+} cations, there are other common types of ternary spinels, such as $M_2{}^+M^{6+}O_4$ (*e.g.*, Na_2MoO_4, Ag_2MoO_4) and $M^{4+}M_2{}^{2+}O_4$ (*e.g.*, $TiZn_2O_4$, $SnCo_2O_4$). One interesting spinel of the form $LiMn_2O_4$ is used as a cathode (reduction site) material for lithium-ion batteries.[18] Based on the chemical formula, Mn ions within MnO_2 sub-units exhibit an average oxidation state of 3.5 (experimentally: 3.55, due to lithium oxides on the surface[19]); the variation between stable Mn^{3+}/Mn^{4+} oxidation states allows for electron transfer to occur in the solid state.[20] It should be noted that structures such as $BaFe_2O_4$, as well as oxygen-deficient analogues such as $BaFe_{12}O_{19}$ or $Ba_2Mn_2Fe_{12}O_{22}$, used in magnetic stripe cards are not spinel lattices. Rather, these structures consist of a hcp array of oxide anions, with some of the oxides replaced with Ba^{2+}.

The equilibrium distribution of cations in tetrahedral and octahedral sites within the spinel lattice depends on the size of the ionic radii, electrostatic energies, and polarization effects. As one would expect, the degree of cation disorder will significantly influence the magnetic properties of magnetic ferrite spinels.[21] One may intentionally prepare spinels containing nonequilibrium cation distributions through rapid quenching of sintered powders. For instance, when ground mixtures of MnO and Al_2O_3 powders are sintered and quenched the resulting $(Mn_xAl_{1-x})_3O_4$ spinel has an oxygen-deficient metal:oxygen ratio of 3:3.7.[22] Another mixed ternary system, $Mn_{1.5-0.5x}Co_{1+0.5x}Ni_{0.5}O_4$ $(0 \leq x \leq 1.0)$, is used in negative temperature coefficient (NTC) thermistors[23] for applications in a variety of electrical products, communication and industrial equipment, and automobiles.

The Boltzmann distribution (Eq. 8) relates the dependence of temperature on the amount of cation disorder in spinels, where E_i is the activation energy required to exchange interstitial sites of M^{2+} and M^{3+} cations (*i.e.*, between tetrahedral and octahedral sites, respectively). Energy values for these interchanges generally fall in the range 0.11–0.14 eV.

$$(8) \qquad \frac{i(1+i)}{(1-i)^2} = e^{\frac{-E_i}{kT}},$$

where: i = degree of inversion; normal spinel = 0 and inverse spinel = 1.

Another important oxide lattice is the *rutile* structure, common for both oxides and fluorides with the general formula MO_2 (M = Ti, Cr, Ge, Ir, Mo, Nb, Os, Pb, Ru, Sn, Te) and $M'F_2$ (M' = Co, Zn, Fe, Mg, Mn, Ni, Pd). This structure (Figure 2.26)
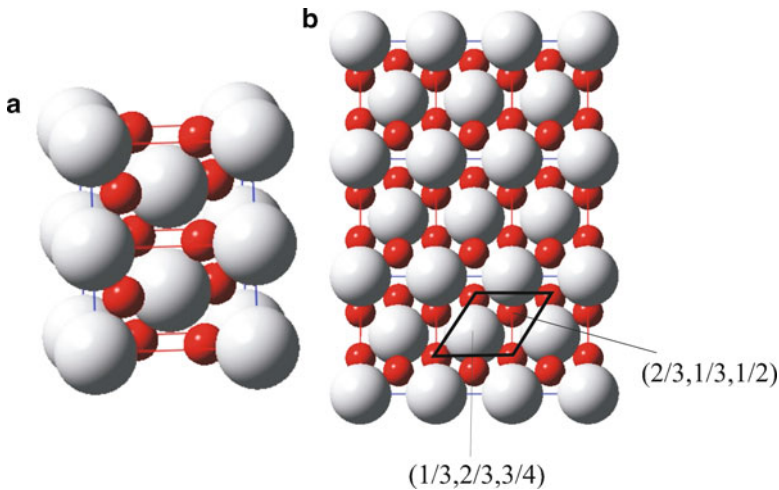
Figure 2.26. Schematic of the rutile structure. This consists of a hcp array of O^{2-} (red) ions, with Ti^{4+} (white) ions occupying 1/2 of the available octahedral interstitial sites. The representation shown in (a) is a common illustration along the [100] direction, that illustrates the octahedral coordination of Ti^{4+} ions; (b) shows the structure along the [110] direction, illustrating the hcp array of oxide ions.
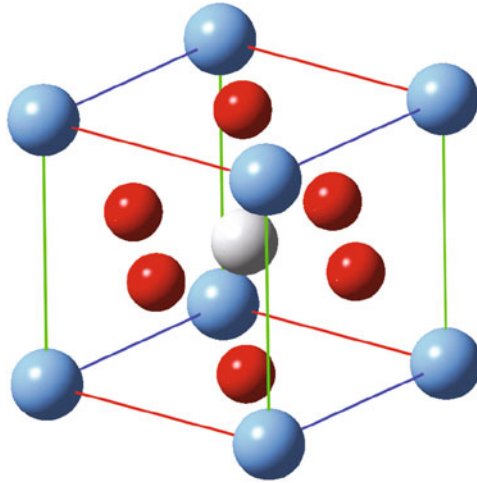
Figure 2.27. Unit cell illustration of the perovskite $BaTiO_3$, illustrating the ABO_3 stoichiometry.

consists of a (distorted) hcp arrangement of anions, with metal cations occupying ½ of the available octahedral holes. In a space-filling view of the lattice, the metal occupation causes the structure to expand so that the oxide ions are no longer in contact with one another. There is one nitride with this structure (ε-Ti_2N), which is known as *antirutile*, since the position of nitride and titanium ions are reversed.

The largest category of metal oxide crystals is the *perovskites*. These oxides have the general formula ABO_3, where A is a cation of larger size than B. These lattices consist of a ccp arrangement of both oxide anions and the larger cation (Figure 2.27). The smaller cation occupies the octahedral hole at the position (1/2, 1/2, 1/2). It should be noted that most perovskite lattices are comprised of distorted cubic unit cells. The degree of structural distortion, d, may be predicted by Eq. 9:

$$(9) \qquad d = \frac{r_A + r_o}{\sqrt{2}(r_B + r_o)},$$

where: r_A, r_B, and r_o are the ionic radii of A and B cations, and O anions, respectively.

As the value of d approaches 1.0, the perovskite will become more perfectly cubic; however, if d $\leq$ 0.81, the ionic radius of the A site will be smaller than ideal, resulting in BO_6 octahedra becoming tilted to fill the available volume. Stable perovskites are predicted to have values in the range 0.78 $\leq$ d $\leq$ 1.05. However, it should be noted that values outside of this range may also yield stable structures, as the above formula does not consider the influence of bond covalency within the perovskite lattice.

Approximately 90% of the metallic elements of the Periodic Table are known to form stable oxides with the perovskite structure. Further, it is possible to partially substitute A and B cations to yield a perovskite of the formula $A_{1-x}A'_xB_{1-y}B'_yO_3$.

It should be noted that the perovskite structure is not only obtained for oxides, but also for some nitrides (*e.g.*, Ca_3GeN), halides (*e.g.*, $KMgF_3$), hydrides (*e.g.*, $BaLiH_3$), and carbides (*e.g.*, $MgCNi_3$). Recently, oxynitride perovskites (*e.g.*, $BaTaO_2N$) have received considerable attention due to their potential applications for nontoxic inorganic pigments and photocatalysts.[24] The reduced electronegativity of the nitride ion, relative to the oxide anion, increases the covalency of the cation-anion bonds thus affecting its overall structure and physical/optical properties. The ability of inducing structural distortions by cationic substitution results in a diverse range of applications for perovskites. In addition to numerous applications in catalysis, sensors, and electronics,[25] the perovskite backbone is a key component in modern *high-temperature superconductive* (HTS) materials.

Superconductivity of perovskites: toward a room-temperature superconductor

By definition, a superconductor exhibits no resistance to electrical conductivity. Further, when a superconductor is placed in a weak external magnetic field, **H**, and cooled below its transition temperature, the magnetic field is repelled. This phenomenon is referred to as the Meissner effect, and is the most intriguing property of superconductors – the ability to levitate on top of a magnetic surface (Figure 2.28a).
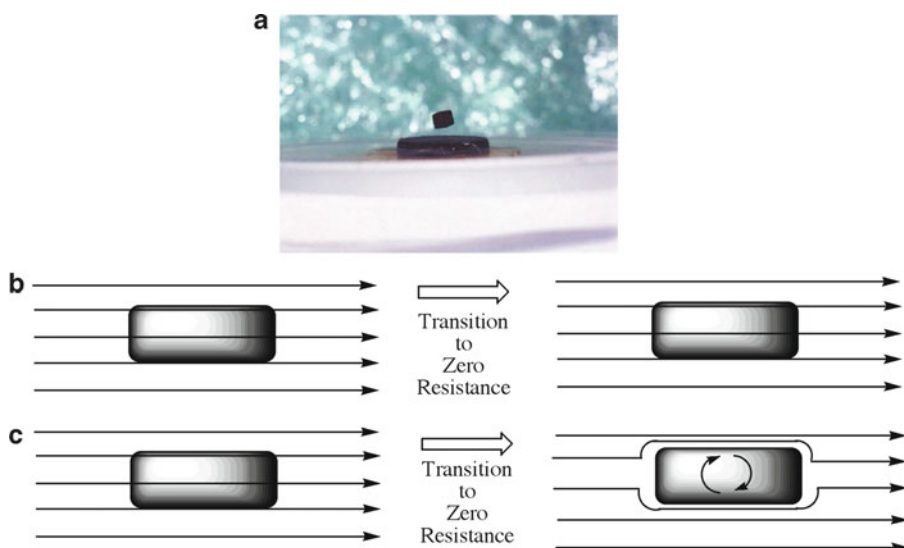
Figure 2.28. (a) Photograph of the Meissner effect for a rare-earth magnet above a sample of YBCO immersed in liquid nitrogen (From http://www.physics.brown.edu/physics/demopages/Demo/em/demo/5G5050.htm). The onset of strong diamagnetism ("superdiamagnetism," as observed by the repulsion of an external magnetic field) is the most reliable method to determine superconductive behavior. The schematic illustrates the different behavior toward an applied external magnetic field for a perfect conductor, (b), and a superconductor, (c).

It should be noted that the Miessner effect does not completely repel **H**; that is, the field is able to penetrate the surface of the superconductor to a depth known as the *London penetration depth*, λ. For most superconductors, λ is on the order of 100 nm decaying exponentially beyond this region toward the bulk of the superconductor structure.

The Meissner effect should be distinguished from the diamagnetism exhibited by a perfect electrical conductor (Figure 2.28b). According to Lenz's Law, when a magnetic field is applied to a conductor, it will induce an electrical current in the conductor that creates an opposing magnetic field. In a perfect conductor, a large current can be induced; however, the resulting magnetic field will exactly cancel the applied field. In contrast, the Meissner effect is the spontaneous repulsion of the applied magnetic field that occurs only once the transition to superconductivity has been achieved.

Many pure transition metals (*e.g.*, Ti, Zr, Hf, Mo, W, Ru, Os, Ir, Zn, Cd, Hg) and main group metals (*e.g.*, Al, Ga, In, Sn, Pb) exhibit superconductivity, many only when exposed to high-pressure conditions. These materials are referred to as Type I or *soft superconductors*.

Binary and ternary alloys and oxides of these elements, as well as pure V, Nb, Gd, and T_c are referred to as Type II or *high-field superconductors*. In contrast to Type I, these materials exhibit conductive characteristics varying from normal metallic to superconductive, depending on the magnitude of the external magnetic field. It is noteworthy to point out that metals with the highest electrical conductivity (*e.g.*, Cu, Au) do not naturally possess superconductivity.

Although superconductivity was first discovered in 1911 for supercooled liquid mercury, it was not until 1957 that a theory was developed for this phenomenon.[26] Proposed by Bardeen, Cooper and Schrieffer, the *BCS theory* purports that at a certain critical temperature, T_c, the electrons within thermal energy (kT_c) of the Fermi level are able to correlate their motion in pairs, referred to as *Cooper pairs*. It is not readily apparent why this should occur, since electrons are mutually repulsive due to like negative charges. The formation of Cooper pairs is thought to result from electron–phonon (*i.e.,* lattice vibration) coupling. That is, an electron moving through the lattice attracts the positively-charged nuclei of the lattice atoms, causing them to be distorted from their original position. This creates a small attractive force toward another electron of opposite spin, whose motion becomes correlated with that of the original electron (Figure 2.29a). The primary experimental evidence that supports the concept of phonon-facilitated Cooper pair formation is known as the isotope effect (Figure 2.29b). That is, the linear inverse relationship of critical temperature and mass of lattice atoms suggests that electron/lattice coupling interactions are a key component to superconductivity.

Whereas individual electrons are fermions (1/2 spin) and must obey the Pauli exclusion principle, Cooper pairs exhibit boson-like properties and are hence able to condense into the same energy level. At absolute zero, the condensed Cooper pairs form a single energy state that lies kT_c below the Fermi level (Figure 2.30). As a consequence of condensation, a number of forbidden energy levels appear
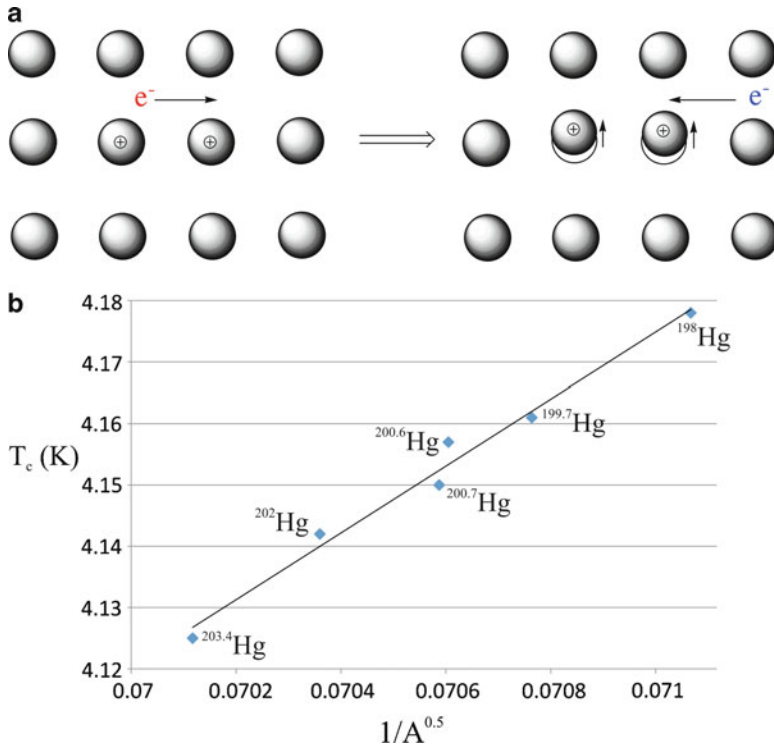
Figure 2.29. Illustration of Cooper pair formation by electron–phonon coupling, and experimental evidence for their formation ("the isotope effect"). Data taken from Maxwell, E. *Phys. Rev.* **1950**, *78*, 477, and Reynolds, C. A. *et al. Phys. Rev.* **1950**, *78*, 487.

within the conduction band, centered about the Fermi level. The energy of this bandgap (*ca.* 7/2 kT_c) corresponds to the minimum energy required to break up a Cooper pair and release the electrons into the vacant quantum levels. The energy gap may be measured by microwave absorption spectroscopy, and represents another key experimental finding that supports the BCS theory. As the critical temperature is approached, the energy gap decreases; at $0 < T < T_c$, the superconductor metal is in an excited state, wherein a number of electrons, primarily from broken Cooper pairs, have been promoted across the bandgap into vacant energy states. This indicates that the binding energy of the Cooper pairs is decreased as the temperature increases, caused by greater phonon vibrations that interrupt electron correlation. At $T > T_c$, the binding energy of the Cooper pairs has been exceeded and the electrons behave as discrete carriers, resulting in bulk resistivity due to e^-/e^- collisions. According to this theory, a superconductor's electrical resistance will be zero because the Cooper pair condensate moves as a coherent quantum mechanical entity, which lattice
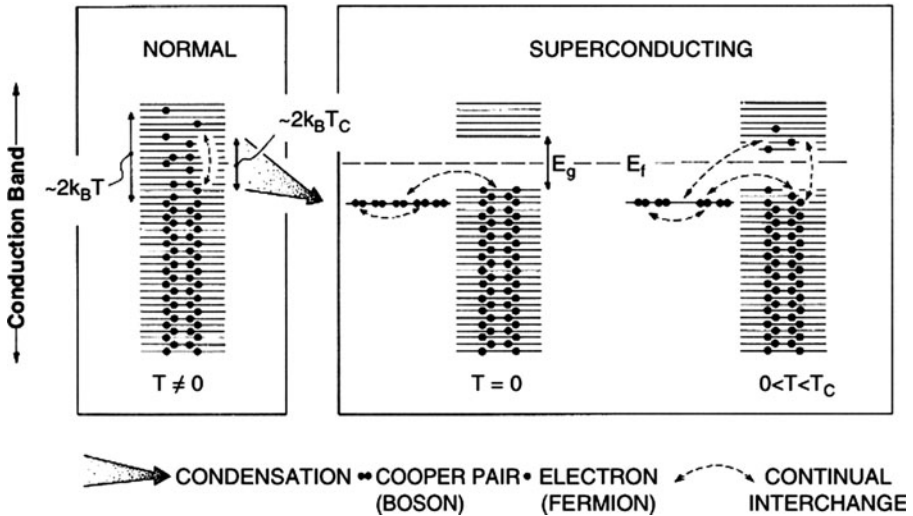
Figure 2.30. Schematic of Cooper pair formation for a metallic superconductor. At a certain critical temperature, T_c, the electrons within thermal energy (kT_c) of the Fermi level are able to correlate their motion in pairs (Cooper pairs). This process is referred to as condensation. At absolute zero, the condensed Cooper pairs form a single energy state that lies kT_c below the Fermi level. As a consequence of condensation, a number of forbidden energy levels (bandgap, E_g) appear within the conduction band, centered about the Fermi level. The energy of this bandgap corresponds to the minimum energy required to break up a Cooper pair and release the electrons into the vacant quantum levels. At $0 < T < T_c$, the superconductor metal is in an excited state, wherein a number of electrons, primarily from broken Cooper pairs, have been promoted across the bandgap into vacant energy states. Reproduced with permission from Hurd, C. M. *Electrons in Metals*, Wiley: New York, 1975. Copyright John Wiley & Sons Limited.

vibrations and impurities cannot disrupt by scattering in the same manner as individual conduction electrons.

In order to exhibit superconductive behavior, early Type I and II materials needed to be cooled below a critical temperature (T_c) ranging from 0.015 (for W) to 23 K (for Nb_3Ge). An intriguing goal of current research is to increase the T_c to room temperature (*high-temperature superconductors*, HTS), which would trivialize resistance-free applications such as power grid lines and widespread levitated trains. In 1986, Muller and Bednorz at IBM made an important discovery toward this goal – the first high-temperature superconductor, $La_{2-x}Sr_xCuO_4$ (LSCO), with a critical temperature of 35 K. A year later, the first material with a critical point above the boiling point of nitrogen (77 K) was discovered, known as $YBa_2Cu_3O_{7-\delta}$ (YBCO), with a critical point of 92 K. In more recent years, the highest-temperature cuprate based superconductors have been synthesized with a general formula $M_uN_wCa_{x-}Cu_yO_z$ (where M = Y, Bi, Tl, or Hg; N = Ba or Sr; u = 1 or 2; w = 2 or 4; x = 0, 1, or 2; y = 1, 2, or 3; z = 3, 4, 6, 7, 9, 10, or 15). To date, the highest-temperature superconductive materials are thallium (*e.g.*, $TlBa_2Ca_2Cu_3O_9$, T_c = 133 K),
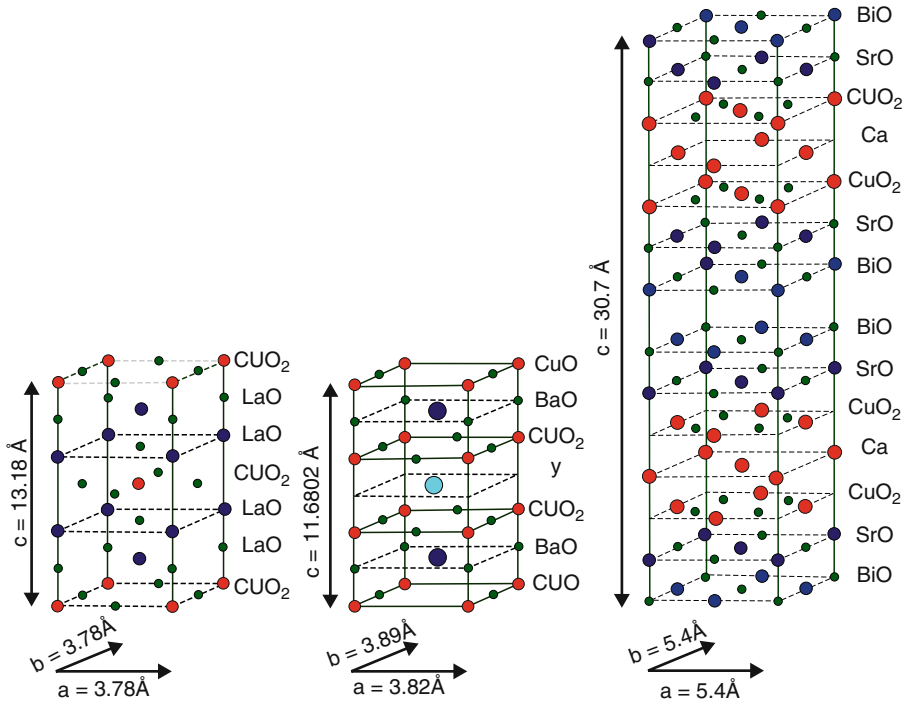
Figure 2.31. Comparison of the crystal structures of (left–right) LSCO, YBCO, and BSCCO superconductors, respectively. Reproduced with permission from Prof. Hoffman's webpage at Harvard University: http://hoffman.physics.harvard.edu/research/SCmaterials.php.

mercury (*e.g.*, $Hg_{0.8}Tl_{0.2}Ba_2Ca_2Cu_3O_{8.33}$, $T_c = 138$ K), or lead-doped (*e.g.*, $(Hg_{0.75}Pb_{0.15}Tl_{0.1})Ba_2Ca_2Cu_3O_{8+}$, $T_c = 142$ K).[27]

Figure 2.31 shows a comparison between the major stacked cuprates that have played an important role in the ongoing development of a room-temperature superconductor. The presence of three or four metals in the crystal structure is referred to as a ternary or quaternary metal oxide, respectively. Unlike the BCS theory for type-I superconductors, there is no prevailing theory to explain high-temperature superconductivity. The lattices for these compounds are distorted perovskites, where "CuO_2" layers are thought to be responsible for the superconductive behavior, and the other metal and metal oxide layers act as charge reservoirs, inducing redox behavior in the copper oxide layers. The Cu^{2+} ion is square planar with an electronic configuration of $[Ar]3d^9$ (one unpaired electron, $S = 1/2$).

For $YBa_2Cu_3O_{7-\delta}$ at an oxygen concentration corresponding to $\delta \geq 0.7$, the solid is insulating. This is due to effective antiferromagnetic ordering of the unpaired electron spins among neighboring Cu^{2+} ions in the CuO_2 layer. However, as additional O is added to the lattice, YBCO undergoes the *Mott transition* of insulating to metallic conductivity – thought to result from a change in the crystal

symmetry from tetragonal to orthorhombic. The additional electronegative O atoms in the lattice serve to inject excess "holes" via oxidation of some Cu^{2+} centers to Cu^{3+}; hence, at $T < T_c$, the system is *perfectly diamagnetic* as the unpaired electrons condense into Cooper pairs and Cu^{3+} ions are formally d^8 (low-spin, diamagnetic). In these structures, the holes are also found to segregate themselves into stripes that alternate with antiferromagnetic regions in the material, widely referred to as a "stripe phase" – thought to be important in the mechanism for high-T_c superconductivity.[28] Others have shown that lattice vibrations (phonons) play an unconventional role in superconductivity – in particular, electron–phonon coupling interactions.[29] As you can see, there is no unifying theory that has yet been adopted to explain the superconductivity of high-T_c materials.

In terms of formal charges on the ions, p-type (or hole-doped) YBCO may be written as: $Y^{3+}(Ba^{2+})_2(Cu^{2+})_2Cu^{3+}(O^{2-})_{7-\delta}$. YBCO becomes superconductive at $\delta \le 0.4$, with its most pronounced superconductivity at $\delta = 0.05$.[30] It should be noted that there are other examples of p-type superconductors that involve metal doping rather than varying oxygen content, such as $La_{2-x}Sr_xCuO_4$ ($T_c = 34$ K at x = 0.15).[31] Similarly, electron-doped (n-type) superconductors may be synthesized such as $Nd_{2-x}Ce_xCuO_4$ ($T_c = 20$ K), written formally as $Nd_{2-x}^{3+}Ce_x^{4+}(e^-)_xCu^{2+}O_4$.

A new class of superconductors that contain iron have been synthesized only within the last few years.[32] The compound LaFePO was discovered in 2006, with a critical temperature of 4 K; fluorine doping to yield $LaFe[O_{1-x}F_x]$ increases the T_c to 26 K. Since 2008, analogous compounds of general formula (Ln)FeAs(O, F) (Ln = Ce, Sm, Nd, Pr) have been prepared that exhibit superconductivity at temperatures up to 56 K. Other compounds such as $(Ba, K)Fe_2As_2$ have T_c values up to 38 K, and MFeAs (M = Li, Na) have a T_c around 20 K.[33] What is most intriguing about iron-based superconductors is that *ferromagnetism* (see Chapter 3) directly competes against Cooper pair formation. Interestingly, these structures exhibit tetragonal-orthorhombic transitions, analogous to cuprate superconductors; however, there appears to be participation of all five 3d orbitals in the Fermi level, relative to just the d_{x2-y2} in the cuprates. Not only will further discoveries in this field be important in developing a unifying theory for HTS, but the physical properties of alternative HTS materials may be more conducive for applications; that is, cuprates suffer from a high degree of brittleness that precludes the facile production of superconductive power lines.[34]

There are already commercial applications that employ superconductive materials; for example, MAGLEV trains have been operable for many years in Japan and England. However, reports of deleterious effects of radio waves may slow the widespread use of this technology. In 2001, three 400-foot HTS cables (Figure 2.32) were installed at the Frisbie Substation of Detroit Edison, capable of delivering 100 million watts of power. This marked the first time commercial power has been delivered to customers of a U.S. power utility through superconducting wire. Similar plans are underway to install an underground HTS power cable in Albany, New York, in Niagara Mohawk Power Corporation's power grid. The 350-m cable,
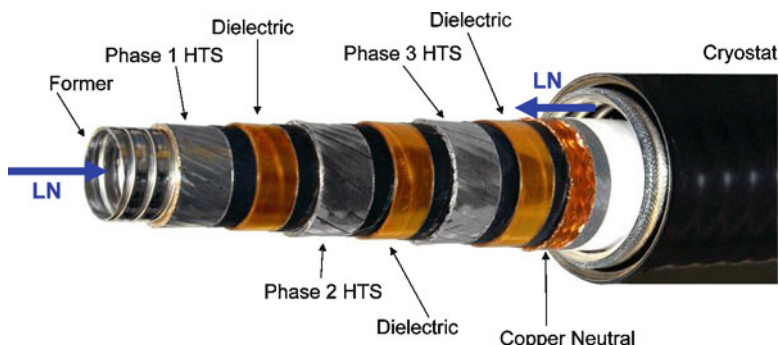
Figure 2.32. Photograph of a high-temperature superconductor (HTS) wire used for electrical power applications. LN refers to the flow direction of the liquid nitrogen cryogenic cooling fluid. Photograph courtesy of Southwire Company (http://www.southwire.com).

believed to be four times the length of any previously installed HTS cable, will be designed to provide more power and operate at significantly lower loss levels than other HTS installations. In order to develop a widespread resilient and ultra-efficient electric grid, many U.S. government agencies such as the Department of Energy (DoE) and Homeland Security have recently established priorities to develop HTS wires and novel cryogenic dielectric materials, as well as associated electrical applications such as cables, fault current limiters, and transformers.[35]

2.3.3. Crystal Symmetry and Space Groups

Crystallography employs two terms to describe the symmetry of the crystal lattice: *point groups* and *space groups*. Chemists should be quite familiar with the notion of point groups, as this designation is used to predict molecular reactivities and IR/Raman absorption bands. A flowchart for the assignment of a molecular point group is shown in Figure 2.33. Examples of this notation, given by Schoenflies symbols, are C_{3v} for ammonia and $Os_3(CO)_9(C_6H_6)$, O_h for $[CoF_6]^{3-}$, and D_{3h} for $(CH_3)_8Si_5O_6$ molecules (Figure 2.34).

By definition, a symmetry operation is an event that results in the transposing of one item into another that is indistinguishable from the original. This operation may take place about a point, line, or plane of symmetry. When a set of symmetry operations is applied to components of the unit cell of a crystal lattice, the resulting symmetry is designated as a *crystallographic point group*. Whereas a molecular point group operation will reproduce an individual molecule, a crystallographic point group operation must leave the entire crystal unchanged.

Illustrative examples of crystallographic symmetry operations are shown in Figure 2.35. An integer label, n, indicates the regeneration of an equivalent lattice point when an object in the crystal lattice is rotated $360°/n$ about an axis. A rotation-inversion axis is designated by $\bar{n}$, featuring rotation about an axis ($360°/n$), followed

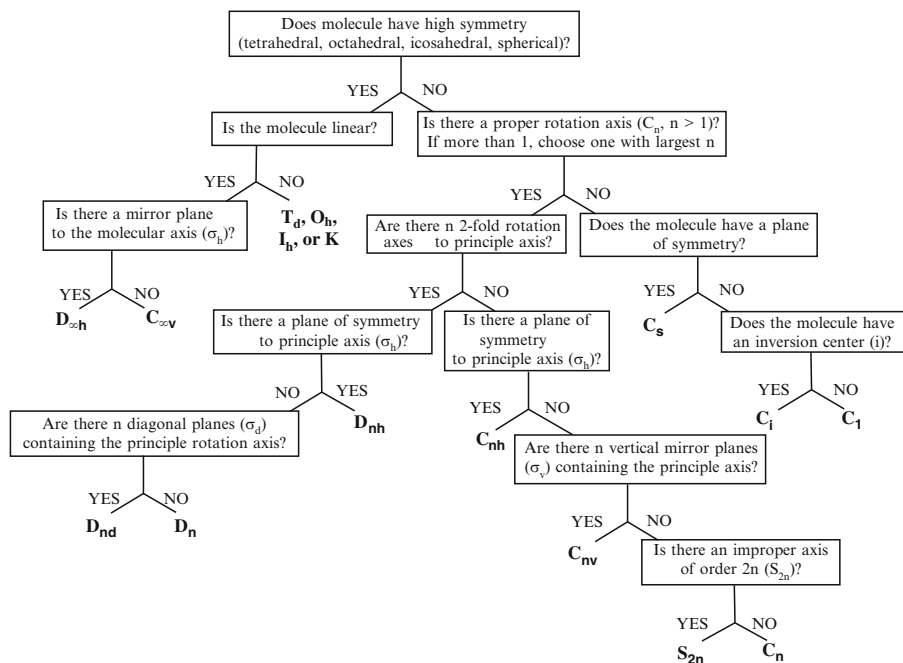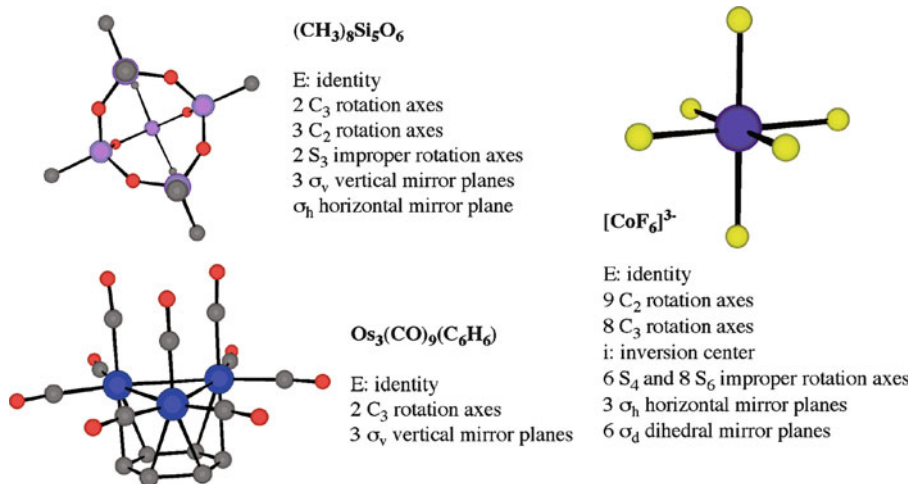*Figure 2.33.* Scheme for determining the point group symmetry of a molecule.

$(CH_3)_8Si_5O_6$

E: identity
2 C_3 rotation axes
3 C_2 rotation axes
2 S_3 improper rotation axes
3 σ_v vertical mirror planes
σ_h horizontal mirror plane

$[CoF_6]^{3-}$

E: identity
9 C_2 rotation axes
8 C_3 rotation axes
i: inversion center
6 S_4 and 8 S_6 improper rotation axes
3 σ_h horizontal mirror planes
6 σ_d dihedral mirror planes

$Os_3(CO)_9(C_6H_6)$

E: identity
2 C_3 rotation axes
3 σ_v vertical mirror planes

Figure 2.34. Examples of symmetry group elements and molecular point group assignments.
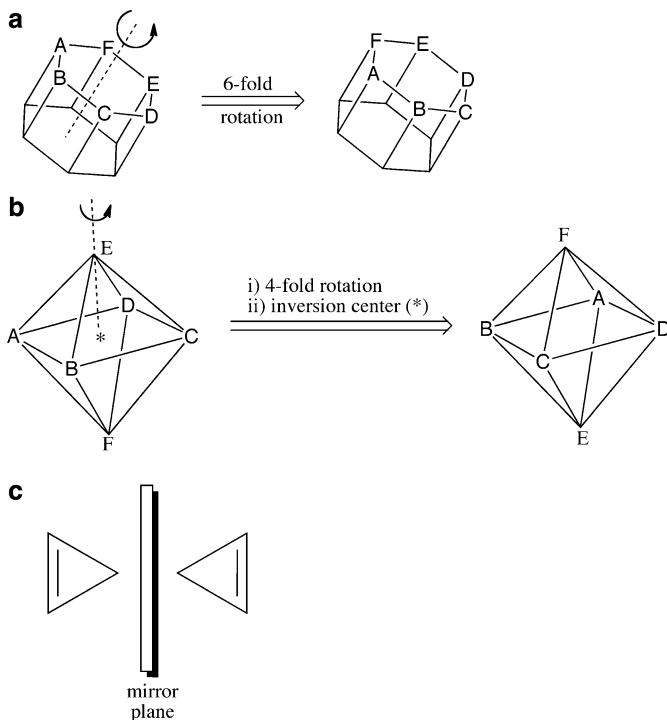
Figure 2.35. Illustrations of: (a) 6, (b) $\bar{4}$, and (c) m crystallographic symmetry operations.

by reflection through a center of symmetry. If individual lattice points are simply reflected through a plane of symmetry, the operation is symbolized by m, denoting the presence of a mirror plane. Although individual atomic and ionic lattice points are not affected by n and m operations, molecular lattice points exhibit a change in handedness following these operations (see Figure 2.35b, c). Point groups that include these operations, known as *improper symmetry operations*, must exclude all chiral molecules, as they would then be superimposible on their mirror images. Two important restrictions apply to crystallographic point group symmetry operations:

1. The symmetry operations must be compatible with infinite translational repeats in a crystal lattice;
2. A symmetry operation cannot induce a higher symmetry than the unit cell possesses.

The point group symmetry describes the non-translational symmetry of the crystal; however, the infinite crystal lattice is generated by translational symmetry (see below). Only two, three, four and sixfold rotation axes are compatible with translational symmetry, so point groups containing other types of rotation
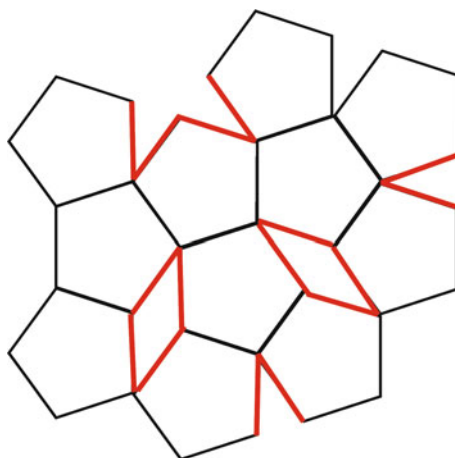
Figure 2.36. The translational incompatibility of a fivefold rotation axis, which leaves voidspaces (red) among the lattice objects.

Table 2.5. The 32 Crystallographic Point Groups

Crystal system (Bravais lattices) {defining symmetry elements}	Crystallographic point groups[a] (molecular point groups[b])
Cubic (*P, I, F*) {Four ⊥ threefold rotation axes}	23, $m\bar{3}$, 432, $\bar{4}3m$, $m\bar{3}m$ (T, T_h, O, T_d, O_h)
Tetragonal (*P, I*) {One fourfold rotation axis}	4, $\bar{4}$, 4/*m*, 422, 4*mm*, $\bar{4}2m$, 4/*mmm* ($C_4, S_4, C_{4h}, D_4, C_{4v}, D_{2d}, D_{4h}$)
Orthorhombic (*P, C, I, F*) {Three ⊥ twofold rotation axes or three ⊥ m's}	222, *mm*2, *mmm* (D_2, C_{2v}, D_{2h})
Trigonal/Rhombohedral (*P*) {One threefold rotation axis}	3, $\bar{3}$, 32, 3*m*, $\bar{3}m$ ($C_3, C_{3i}, D_3, C_{3v}, D_{3d}$)
Hexagonal (*P*) {One sixfold rotation axis}	6, $\bar{6}$, 6/*m*, 622, 6*mm*, $\bar{6}m2$, 6/*mmm* ($C_6, C_{3h}, C_{6h}, D_6, C_{6v}, D_{3h}, D_{6h}$)
Monoclinic (*P, C*) {One twofold rotation axis}	2, *m*, 2/*m* (C_2, C_s, C_{2h})
Triclinic (*P*) {N/A}	1, $\bar{1}$ (C_1, C_i)

[a] The H–M symbolism derived from crystal symmetry operations. For image and movie representations of each point group, see the website: http://cst-www.nrl.navy.mil/lattice/spcgrp/index.html
[b] The analogous Schoenflies symbolism derived from molecular symmetry operations.

axes (*i.e.*, 5 or $\bar{5}$) are not relevant (Figure 2.36).[36] Furthermore, since there is no such thing as a linear 3-D crystal, the linear point groups are also irrelevant. The remaining point group symmetry operations yield a total of 32 crystallographic point groups, designated by Hermann-Mauguin symbols (Table 2.5). As they can be deduced from the macroscopic crystal symmetry, they are also referred to as the *32 crystal classes*. For the same reason, the symmetry elements that give rise to the crystal classes are sometimes referred to as external symmetry elements.

One way to visualize the 32 crystallographic point groups is to use stereographic projections (Figure 2.37). The symbolism used to illustrate rotation axes are as follows:

Twofold (diad):
Threefold (triad): ▲
Fourfold (tetrad): ◆
Sixfold (hexad): ⬣

Mirror planes are indicated as solid lines, and may be positioned perpendicular or parallel to the plane of the paper.

As illustrated by the stereographic projections in Figure 2.37, the 6mm crystallographic point group is observed to have a primary sixfold axis of rotation, with two
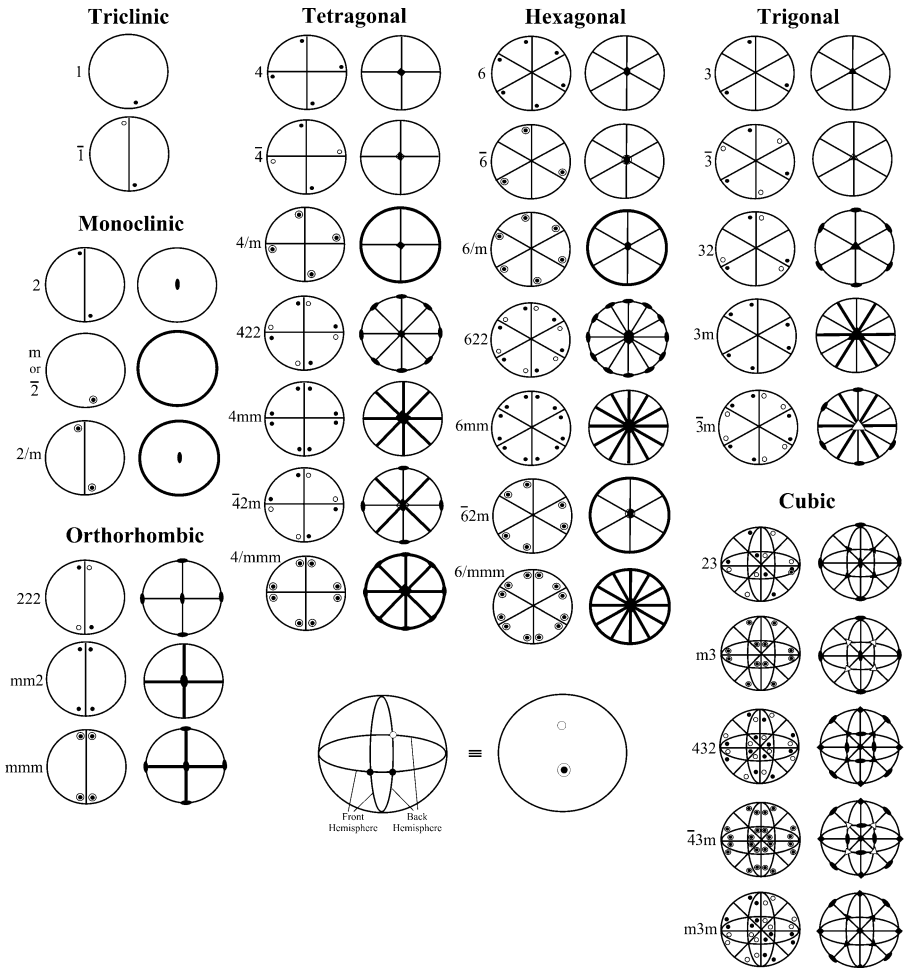
Figure 2.37. Stereographic projections illustrating both general positions and symmetry operations for the 32 crystallographic point groups. Shaded and open circles indicate a general position on the front and back hemispheres, respectively.

mirror planes that are parallel to the rotation axis. In contrast the 6/mmm point group
has a mirror plane perpendicular to the rotation axis (in the plane of the paper), as
well as other mirror planes that lie parallel to the primary rotation axis. Carrying out
the first two symmetry operations automatically generates the third term of the point
group symbol, if present. For instance, for the mm2 point group, the twofold rotation
axis is generated by the presence of two mutually perpendicular mirror planes.

The 32 crystallographic point groups are useful to define the contents of a discrete
unit cell; however, there must be additional symmetry elements that take into
account the translational symmetry of an extended periodic lattice. Accordingly,
both *glide planes* and *screw axes* feature translation in addition to mirror and
rotation operations, respectively (Figure 2.38). For glide planes, the translation is
designated as *a*, *b*, or *c* if movement is halfway along the **a**, **b**, or **c** unit cell axes,
respectively. If the translation is along the diagonals 1/2 (**a** + **b**), 1/2 (**a** + **c**), or
1/2 (**b** + **c**), the glide plane is designated as *n*. Lastly, if the translation is along 1/4
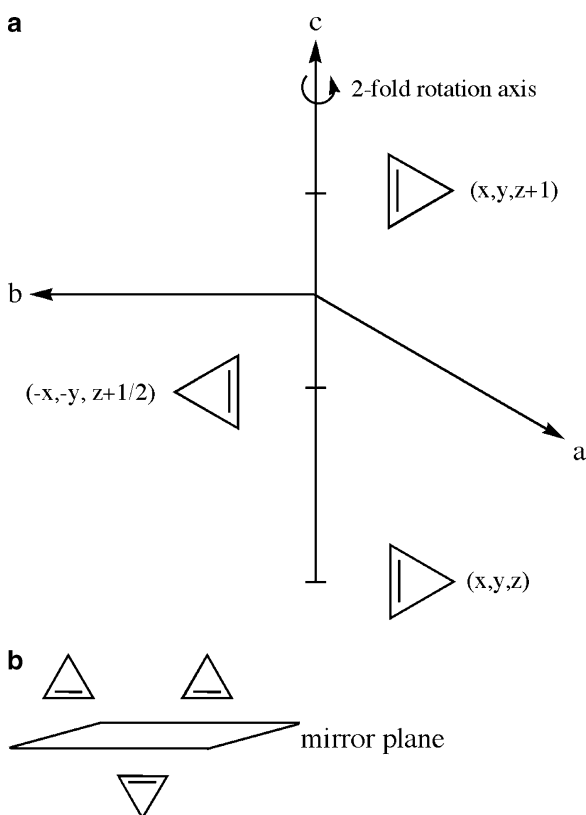(**a** + **b**), 1/4 (**a** + **c**), or 1/4 (**b** + **c**), the glide plane is given the symbol *d*.[37]

Figure 2.38. Illustrations of: (a) 2_1 screw axis (twofold rotation axis and 1/2 translation), listing the
orientations and (x, y, z) coordinates for the original/translated object, (b) glide plane.

For screw axes, the nomenclature is of the form n_x, indicating a 360°/n rotation, followed by a x/n translation along one of the unit cell vectors, **a**, **b**, or **c**. For example, the 6_1 and 6_3 screw axes would imply sixfold axes of rotation followed by $1/6$ and $1/2$ translations, respectively.

It is noteworthy to point out that two sequential screw-axis or glide-plane operations will yield the original object that has been translated along one of the unit cell vectors. For example, a 6_3 axis yields an identical orientation of the molecule only after 6 repeated applications – 3 unit cells away (*i.e.*, $6 \times 1/2 = 3$). Since glide planes feature a mirror plane prior to translation, the first operation will cause a change in handedness of the molecule. By contrast, screw axis operations do not alter the stereoisomerism of the molecule.

Both glide and screw axes are not point group operations because they involve translations. That is, one cannot distinguish between analogous rotation and screw axes, or between glide and mirror planes, by simply looking at the crystal faces. You may notice that of the symmetry elements discussed, both glide planes and screw axes are absent from the list of point group symbols, listed in Table 2.5. For the purposes of determining the crystallographic point group, screw axes are treated as rotation axes (*e.g.*, $6_3 \equiv 6$), and glide planes treated as mirror planes (*e.g.*, b $\equiv$ m).

When the symmetry elements are applied to species arranged periodically on a crystal lattice, the result is a *space group*. The combination of the 32 crystallographic point groups with the 14 Bravais lattices yields a total of 230 possible space groups for crystals, designated by the Hermann-Mauguin (H-M) space group symbol. The 73 different space groups that can be generated from point groups only, without using glide planes and/or screw axes, are called *symmorphic* space groups.

The first letter of the H-M symbol is a single letter that refers to the Bravais centering, L. The letters used are P (primitive), A ((100) face centered), B ((010) face centered), C ((001) face centered), F (face centered), and I (body centered). The remaining three letters refer to the crystal system as well as symmetry elements contained in the lattice. Table 2.6 lists the symmetry elements corresponding to each of the primary, secondary and tertiary terms of the space group symbol, L(1°)(2°)(3°). Both rotation and screw axes are parallel, whereas mirror/glide planes are perpendicular, to the directions listed in Table 2.6. Note that the only space groups

Table 2.6. Space Group Symmetry Element Symbolism

Crystal system	Symmetry direction[a] (symbol: L 1° 2° 3°)[b]		
	1°	2°	3°
Triclinic	N/A	N/A	N/A
Monoclinic	[010] (b-unique)	N/A	N/A
Orthorhombic	[100]	[010]	[001]
Tetragonal	[001]	[100]/[010]	[110]
Hexagonal/Trigonal	[001]	[100]/[010]	[120]/[110]
Cubic	[100]/[010]/[001]	[111]	[110]

[a] Mirror and glide planes will be perpendicular to the indicated directions, whereas rotation and screw axes will be aligned parallel to the directions.
[b] L refers to the Bravais lattice centering (*i.e.*, P = primitive, I = body-centered, F = face-centered, C = c-centered).

possible for a triclinic crystal are P1 and P$\bar{1}$. For monoclinic crystals, there are three possible crystallographic point groups (2, m, and 2/m), which are combined with varying combinations of lattice centering and glide planes/screw axes to yield 13 possible space groups: P2, P2$_1$, C2, Pm, Pc, Cm, Cc, P2/m, P2$_1$/m, C2/m (or B2/m), P2/c, P2$_1$/c, and C2/c (or B2/b). More explicitly, the P2 space group would represent a primitive monoclinic unit cell, with a twofold rotation axis parallel to **b** ([010] direction). In comparison, the Cm space group indicates a C-centered unit cell with a mirror plane perpendicular to **b**. There are 59 orthorhombic, 68 tetragonal, 25 trigonal, 27 hexagonal, and 36 cubic space groups for a total of 230.

In order to extract the relevant symmetry elements from a space group symbol, the following procedure should be followed. First, the centering is readily determined from the first term of the symbol. The relevant crystal system may be determined by comparing the remaining terms with the 32 crystallographic point groups (Table 2.5), treating screw axes and glide planes as rotation axes and mirror planes, respectively. For instance, the Pmmm space group implies that it is a primitive unit cell; the mmm is found in Table 2.5 for an orthorhombic unit cell. Hence, this would translate to a primitive orthorhombic unit cell. Next, using Table 2.6 for an orthorhombic system, the Pmmm space group would be defined by mirror planes perpendicular to each of the **a**, **b**, and **c** axes. As another example, let's consider a very common space group, P2$_1$/c. This can be simplified to the 2/m crystallographic point group, which is in the monoclinic crystal system. Hence, this space group consists of a primitive monoclinic unit cell, with a twofold screw axis parallel to **b** (rotation of 180° about **b**, followed by translation along **b** of 1/2 the unit cell distance). In addition, a c-glide plane is perpendicular to the screw axis (**ab** mirror plane, with 1/2 translation along **c**). For a crystal classified within the F432 space group (*e.g.*, sodium phosphate, Na$_3$PO$_4$), we can determine this is comprised of a fcc unit cell, with a fourfold rotation axis parallel to **a**, **b**, and **c**, a threefold rotation axis parallel to the cube diagonal [111], and a twofold rotation axis parallel to the **ab** plane [110].

Table 2.7 lists the various symbols that are used to graphically describe space groups. As an example, consider the representation below, which describes general positions of atoms/ions/molecules within a unit cell, projected onto the **ab** plane:
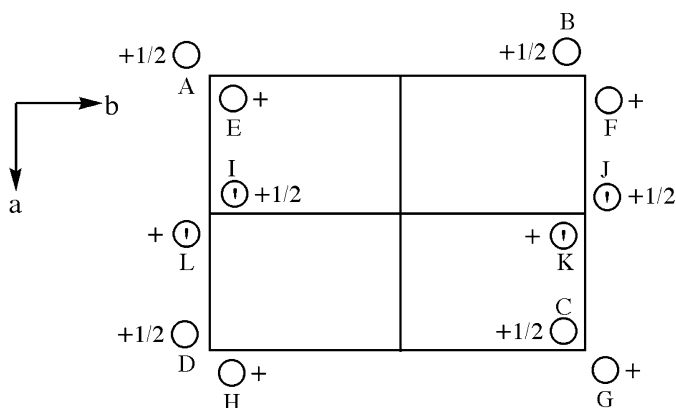
Table 2.7. Common Symbols Used for Space Group Representations

Symmetry operation	Symbols
Mirror plane (m) ⊥ plane of projection	————————
Glide plane (a, b, c) ⊥ plane of projection	- - - - - - - - - - -
Glide plane (n) ⊥ plane of projection	– · – · – · – · –
Mirror plane (m) // plane of projection	
Glide plane (a, b, c) // plane of projection (translation of 1/2 in the direction of the arrow)	
Glide plane (n) // plane of projection (translation of 1/2 in the direction of the arrow)	
Rotation axes ⊥ plane of projection	2 3 4 6
Screw axes ⊥ plane of projection	2_1 3_1 3_2 4_1 4_2 4_3 6_1 6_2 6_3 6_4 6_5
Rotation axes // plane of projection	2 4
Screw axes // plane of projection	2_1 4_1
Center of symmetry (inversion center: i)	○
Rotation axis ⊥ plane of projection with center of symmetry	2/m 3/m 4/m 6/m

Points A–D, E–H, I/J, and K/L are equivalent positions in the unit cell, as they are duplicated by translations of one full unit along **a** or **b**. The relationship between points A and E looks like a simple twofold rotation axis; however, these points differ by 1/2 a unit cell length in the **c**-direction. Next, let's consider the relationship between points E and I. The apostrophe symbol indicates these points are mirror images of each other, suggesting that a mirror plane passes between them. However, these points also vary in their position along **c**, which implies the presence of a c-glide plane. Lastly, let's consider the relationship between points A and I (or E and L), which are located at the same position along **c**. To generate position I, one could mirror point A across the **a**-axis, followed by translation of 1/2 along **a** – an a-glide

plane. Since we have a twofold rotation axis and two glide planes, the crystal system is likely orthorhombic (Table 2.5 – defined by 3 twofold rotation axes/mirror planes). To summarize, we would have a primitive orthorhombic unit cell, with a c-glide ⊥ **a**, an a-glide ⊥ **b**, and a 2_1 screw axis // **c**. Hence, the space group symbol is Pca2_1, and would be illustrated by the following symmetry operations:
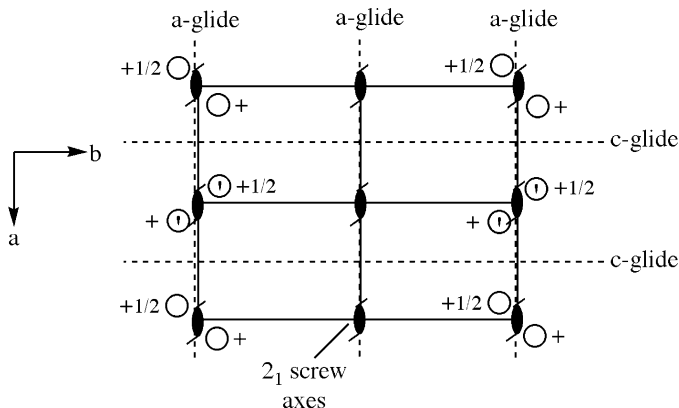
There are four general positions (E, C, I, and K) that lie within the unit cell, which is defined as: $0 \leq x \leq 1; 0 \leq y \leq 1; 0 \leq z \leq 1$. The asymmetric unit for this unit cell is defined as: $0 \leq x \leq 1/4; 0 \leq y \leq 1; 0 \leq z \leq 1$. The coordinates of the four general positions are as follows: $(x, y, z), (-x, -y, z + 1/2), (x + 1/2, -y, z)$, and $(-x + 1/2, y, z + 1/2)$. A position lying exactly on a glide plane or the screw axis is called a special point, which always decreases the overall multiplicity (number of equivalent positions generated from the symmetry operation). For instance, if we had a molecule located at $(1/2, 1/2, z)$, directly on the 2_1 screw axis, the ensuing symmetry operation would not generate another equivalent molecule – a multiplicity of 1 rather than 2.

The effect of Bravais centering is illustrated in Figure 2.39. As the degree of centering increases, so will the number of general positions within the unit cell. For instance, a primitive orthorhombic cell of the Pmm2 space group contains four atoms/ions/molecules per unit cell. By adding either an A-centered, C-centered, or body-centered units, there are now eight species per unit cell. That is, for a C-centered unit cell, there are four general positions for each of the (0, 0, 0) and (1/2, 1/2, 0) sets. For a face-centered unit cell, there are four times the number of general positions since, by definition, a fcc array contains four components/unit cell relative to primitive (1/u.c.) and A, C, I cells (2/u.c.).

2.3.4. X-Ray Diffraction from Crystalline Solids

In order to experimentally ascertain the space group and ultimate 3-D structure of a crystalline solid, one must impinge the crystal with high-energy electromagnetic radiation. For instance, when X-rays interact with a crystalline solid, the incoming
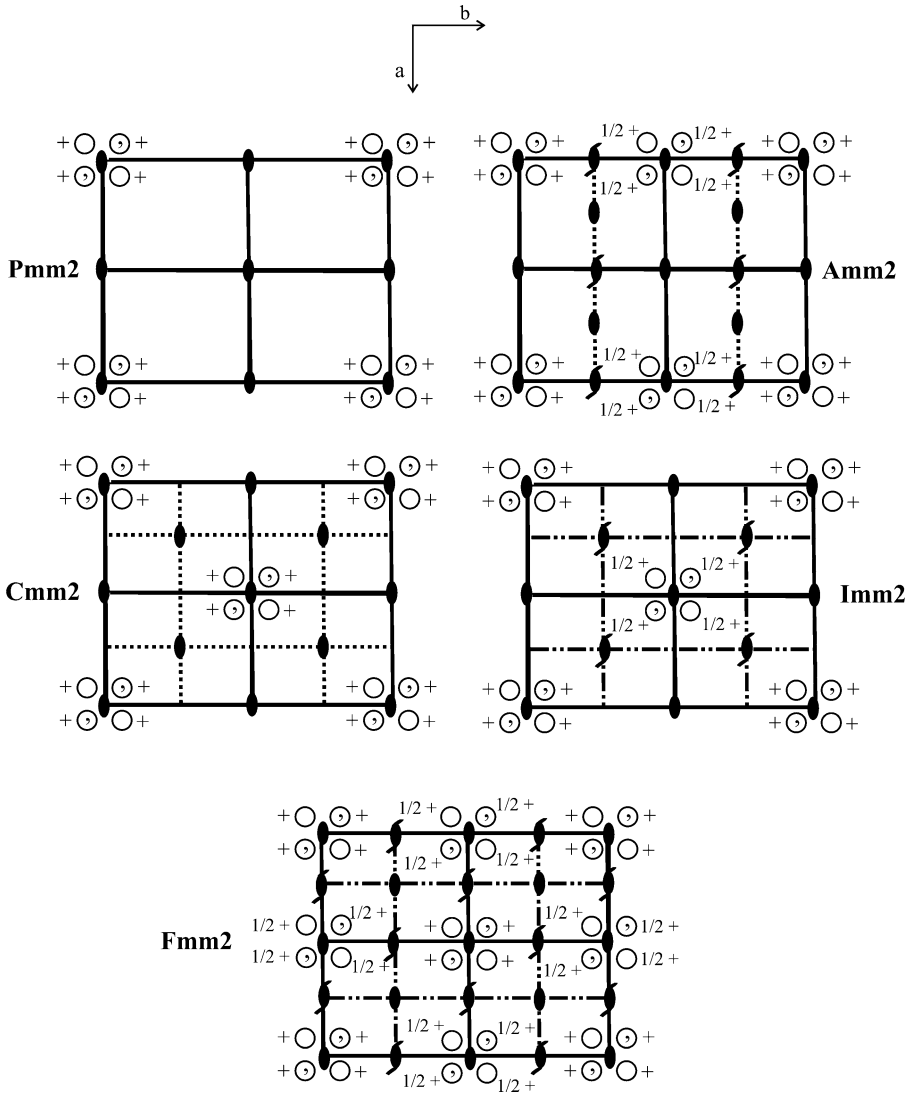
Figure 2.39. 2-D representations of the Pmm2, Amm2, Cmm2, Imm2 and Fmm2 space groups, showing general positions and symmetry elements.

beam will be diffracted by the 3-D periodic array of atoms/ions to yield a characteristic diffraction pattern on a photographic film or area detector/CCD camera (Figure 2.40). As first presented in the early 1900s the most intense diffraction peaks correspond to scattered waves that are in-phase with one another (*i.e.,* constructive interference), which will occur only when the conditions of the Bragg equation are satisfied (Eq. 10 and Figure 2.41).
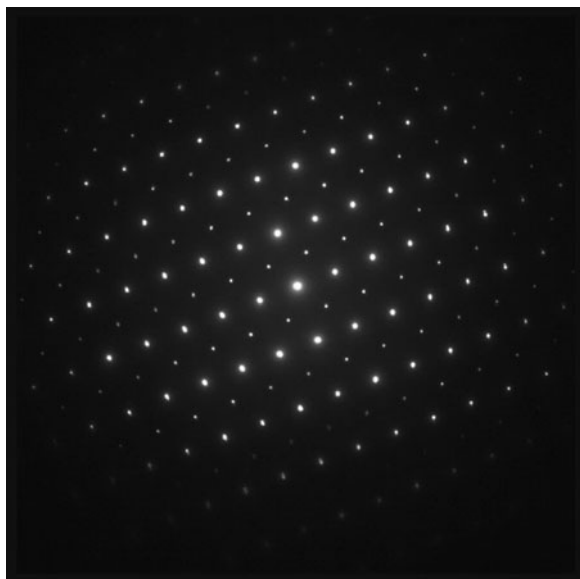
Figure 2.40. Example of diffraction spots from a charge-couple device (CCD) detector, from the single crystal x-ray diffraction analysis of corundum.

$$d \sin \theta = AB$$
$$d \sin \theta = BC$$

$$AB + BC = 2d \sin \theta = n\lambda$$
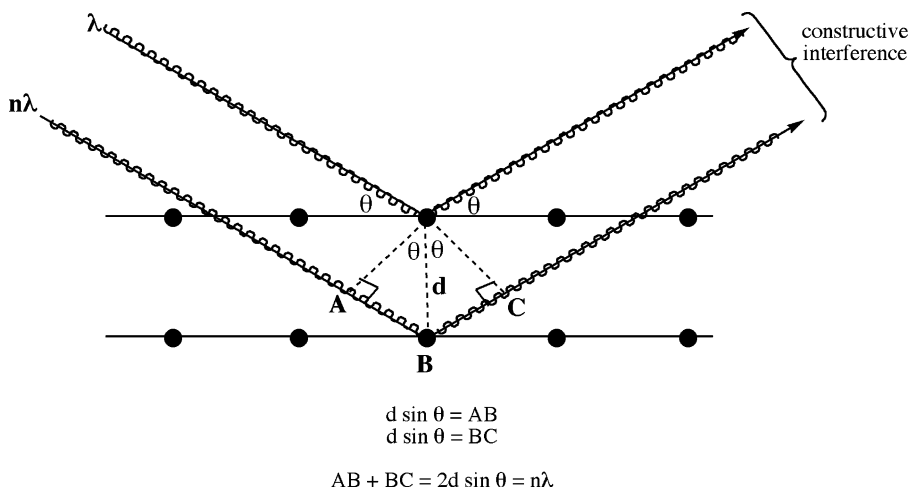
Figure 2.41. Schematic of Bragg's Law, which governs the conditions required for the constructive interference of waves.

(10)   nλ = 2d sin θ,

where: d = lattice spacing of the crystal planes (*e.g.*, d_{111} would indicate the spacing
     between neighboring 111 planes)
     λ = wavelength of the incoming beam
     θ = angle of the incident and diffracted beams (*i.e.*, $\theta_{in} = \theta_{out}$)

Illustrated another way, if two waves differ by one whole wavelength, they will
differ in phase by 360° or 2π radians. For instance, the phase difference, ϕ, of the
(hkl) reflection resulting from a wave scattered by an arbitrary lattice atom at
position(x, y, z), and another scattered from an atom at position (0, 0, 0) is:

(11) $\phi = 2\pi(hu + kv + lw)$,

where the vector (**uvw**) corresponds to fractional coordinates of (x/**a**, y/**b**, z/**c**).

The two waves may differ in amplitude as well as phase if the two atoms are different.
In particular, for scattering in the $2\theta = 0°$ (forward) direction of a wave by an atom
comprised of Z electrons, the waves scattered from all of the electrons in the atom will
be in-phase.[38] Accordingly, the amplitude of the scattered wave is simply Z times the
amplitude of the wave scattered by a single electron. The atomic scattering factor, *f*, is
used to describe the scattering by an atom in a given direction (Eq. 12). As just described,
f = Z (atomic number) for forward scattering; however, as (sin θ)/λ increases, *f* will
decrease due to more destructive interference among the scattered waves.

(12) $f = \dfrac{\text{amplitude of wave scattered by one atom}}{\text{amplitude of wave scattered by one electron}}$

A description of the scattered wavefront resulting from diffraction by a unit cell of
the crystal lattice is significantly more complex. That is, one would need to include
the contribution of waves scattered by all atoms of the unit cell, each with differing
phases and amplitudes in various directions. In order to simplify the trigonometry
associated with adding two waves of varying phases/amplitudes, it is best to
represent individual waves as vectors.[39] Instead of using **x** and **y** components for
the vectors in 2-D real space, one may represent the vectors in *complex space*, with
real and imaginary components. This greatly simplifies the system; that is, the
addition of scattered waves is simply the addition of complex numbers, which
completely removes trigonometry from the determination.

Complex numbers are often expressed as the sum of a real and an imaginary
number of the form a + *i*b (Figure 2.42). It should be noted that the vector length
represents the wave amplitude, A; the angle the vector makes with the horizontal
(real) axis represents its phase, ϕ (Eq. 13 – Euler's equation). The intensity of a
wave is proportional to the square of its amplitude, which may be represented by
Eq. 14 – obtained by multiplying the complex exponential function by its complex
conjugate (replacing *i* with − *i*).

(13) $Ae^{i\phi} = A\cos\phi + Ai\sin\phi$

(14) $\left| Ae^{i\phi} \right|^2 = Ae^{i\phi}Ae^{-i\phi}$

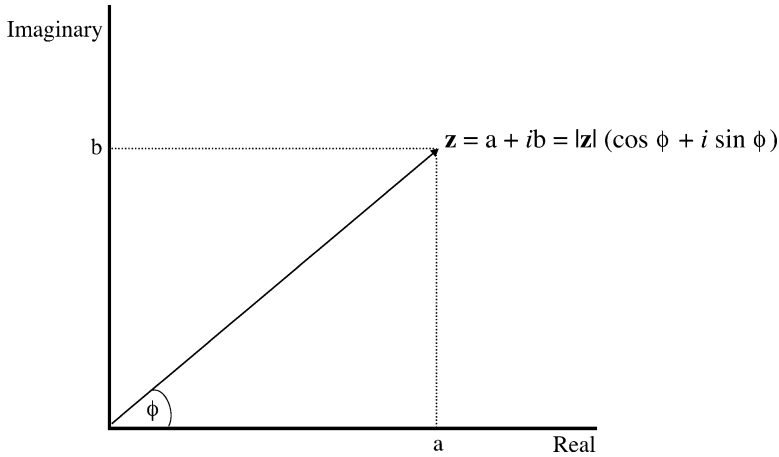*Figure 2.42.* The expression of a vector, **z**, in terms of a complex number.

If we now include the phase and scattering factor expressions we used in Eqs. 11 and 12, we will obtain an equation that fully describes the scattering of the wave from a lattice atom, in complex exponential form (Eq. 15):

$$(15) \qquad Ae^{i\phi} = fe^{2\pi i(hu+kv+lw)}$$

If we want to describe the resultant wave scattered by all atoms of the unit cell, we will need to replace the atomic scattering factor with the *structure factor*, F. This factor describes how the atomic arrangement affects the scattered beam, and is obtained by adding together all waves scattered by the discrete atoms. Hence, if a unit cell contains N atoms with fractional coordinates ($\mathbf{u}_n$, $\mathbf{v}_n$, $\mathbf{w}_n$), and atomic scattering factors, f_n, the structure factor for the *hkl* reflection would be given by:

$$(16) \qquad F_{hkl} = \sum_{n=1}^{N} f_n e^{2\pi i(hu_n+kv_n+lw_n)}$$

The intensity of the diffracted beam by all atoms of the unit cell in which Bragg's Law is upheld is proportional to $|F|^2$, which is obtained by multiplying the expression given by Eq. 16 by its complex conjugate. Hence, this equation is invaluable for diffraction studies, as it allows one to directly calculate the intensity of any *hkl* reflection, if one knows the atomic positions within the unit cell. For instance, let's consider the structure factor for a bcc unit cell, with atoms at (0, 0, 0) and (1/2, 1/2, 1/2). The expression for the bcc structure factor is given by Eq. 17:

$$(17) \qquad F_{hkl}=fe^{2\pi i(0)} + fe^{2\pi i(h/2+k/2+l/2)} = f\left[1 + e^{\pi i(h+k+l)}\right]$$

Since $e^{n\pi i} = -1$ or $+1$, where n = odd integer or even integer, respectively, $|F|^2 = (2f)^2$ when $(h + k + l)$ is even, and $|F|^2 = 0$ when $(h + k + l)$ is odd. That is, for a bcc unit cell, all reflections with $(h + k + l) = 2n + 1$, where n = 0, 1, 2, ... such as (100), (111), (120), *etc.* will be absent from the diffraction pattern, whereas reflections with $(h + k + l) = 2n$ such as (110), (121), *etc.* may be present if the diffraction satisfies Bragg's Law. Such missing reflections are referred to as *systematic absences*, and are extremely diagnostic regarding the centering present in the unit cell, as well as the presence of translational symmetry elements such as screw axes or glide planes (Table 2.8).

Table 2.8. Systematic Absences for X-Ray and Electron Diffraction

Cause of absence	Symbol	Absences[a]
Body-centering	I	$h + k + l = 2n + 1$ (odd)
A centering	A	$l + k = 2n + 1$
B centering	B	$h + l = 2n + 1$
C centering	C	$h + k = 2n + 1$
Face centering	F	*hkl* mixed (not all even or all odd)
Glide plane $\perp$ (100) (0*kl*)	b	$k = 2n + 1$
	c	$l = 2n + 1$
	n	$k + l = 2n + 1$
	d	$k + l = 4n + 1$
Glide plane $\perp$ (010) (*h0l*)	a	$h = 2n + 1$
	c	$l = 2n + 1$
	n	$h + l = 2n + 1$
	d	$h + l = 4n + 1$
Glide plane $\perp$ (001) (*hk0*)	a	$h = 2n + 1$
	b	$k = 2n + 1$
	n	$h + k = 2n + 1$
	d	$h + k = 4n + 1$
Glide plane $\perp$ (110) (*hhl*)	b	$h = 2n + 1$
	n	$h + l = 2n + 1$
	d	$h + k + l = 4n + 1$
Screw axis // **a** (*h00*)	2_1 or 4_2	$h = 2n + 1$
	4_1 or 4_3	$h = 4n + 1$
Screw axis // **b** (0*k0*)	2_1 or 4_2	$k = 2n + 1$
	4_1 or 4_3	$k = 4n + 1$
Screw axis // **c** (00*l*)	2_1 or 4_2 or 6_3	$l = 2n + 1$
	$3_1, 3_2, 6_2$ or 6_4	$l = 3n + 1$
	4_1 or 4_3	$l = 4n + 1$
	6_1 or 6_5	$l = 6n + 1$
Screw axis // (110)	2_1	$h = 2n + 1$

[a]Refers to the Miller indices ((*hkl*) values) that are absent from the diffraction pattern. For instance, a body-centered cubic lattice with no other screw axes and glide planes will have a zero intensity for all reflections where the sum of $(h + k + l)$ yields an odd #, such as (100), (111), etc.; other reflections from planes in which the sum of their Miller indices are even, such as (110), (200), (211), etc. will be present in the diffraction pattern. As these values indicate, there are three types of systematic absences: 3-D absences (true for all *hkl*) resulting from pure translations (cell centering), 2-D absences from glide planes, and 1-D absences from screw axes.[40]

Another way to represent the structure factor is shown in Eq. 18, where $\rho(\mathbf{r})$ is the electron density of the atoms in the unit cell ($\mathbf{r}$ = the coordinates of each point in vector notation). As you may recall, this is in the form of a Fourier transform; that is, the structure factor and electron density are related to each other by Fourier/inverse Fourier transforms (Eq. 19). Accordingly, this relation is paramount for the determination of crystal structures using X-ray diffraction analysis. That is, this equation enables one to prepare a 3-D electron density map for the entire unit cell, in which maxima represent the positions of individual atoms.[41]

(18) $F_{hkl} = \int_V \rho(r) e^{2\pi i(hu+kv+lw)} dV$

(19) $\rho(r) = \int_V F_{hkl} e^{-2\pi i(hu+kv+lw)} \, dV = \frac{1}{V} \sum_h \sum_k \sum_l F_{hkl} e^{-2\pi i(hu+kv+lw)}$

It is noteworthy that the units of functions related by a Fourier transform are reciprocals of one another. For instance, consider the reciprocal relationship between the period and frequency of a wave. Whereas the former is the time required for a complete wave to pass a fixed point (units of sec), the latter is the number of waves passing the point per unit time (units of s^{-1}). Similarly, the unit of the structure factor (Å) is the inverse of the electron density (Å^{-1}). Since the experimental diffraction pattern yields intensity data (equal to $|F|^2$), the spatial dimensions represented by the diffraction pattern will be inversely related to the original crystal lattice.

Accordingly, the observed diffraction pattern represents a mapping of a secondary lattice known as a *reciprocal lattice*; conversely, the "real" crystal lattice may only be directly mapped if one could obtain high enough resolution for an imaging device such as an electron microscope. The reciprocal lattice is related to the real crystalline lattice by the following (as illustrated in Figure 2.43):

(i) For a 3-D lattice defined by vectors **a**, **b**, and **c**, the reciprocal lattice is defined by vectors **a***, **b***, and **c*** such that **a*** $\perp$ **b** and **c**, **b*** $\perp$ **a** and **c**, and **c*** $\perp$ **a** and **b**:

(20) $a^* = \dfrac{b \times c}{[a \bullet (b \times c)]}$ $b^* = \dfrac{a \times c}{[a \bullet (b \times c)]}$ $c^* = \dfrac{a \times b}{[a \bullet (b \times c)]}$

Recall that the cross-product of two vectors separated by θ results in a third vector that is aligned in a perpendicular direction as the original vectors. For instance, for **b** $\times$ **c**, the magnitude of the resultant vector would be |**b**||**c**| sin θ, and would be aligned along the **a** axis. This is in contrast to the dot-product of two vectors, which results in the scalar projection of one vector onto the other, of magnitude |**b**||**c**| cos θ for **b** • **c**. For instance, for a cubic unit cell, the denominator terms in Eq. 20, [**a** • (**b** $\times$ **c**)], would simplify to:

b $\times$ **c** = |**b**||**c**| sin 90° = |**b**||**c**|, aligned along the **a** axis;
∴ [**a** • **b** $\times$ **c**] = |**a**||**b**||**c**| cos 0° = |**a**||**b**||**c**|, or the *volume of the unit cell*

As you might have noticed, the magnitude of a reciprocal lattice vector is in units of [1/distance], relative to the basis vectors in real space that have units of distance.
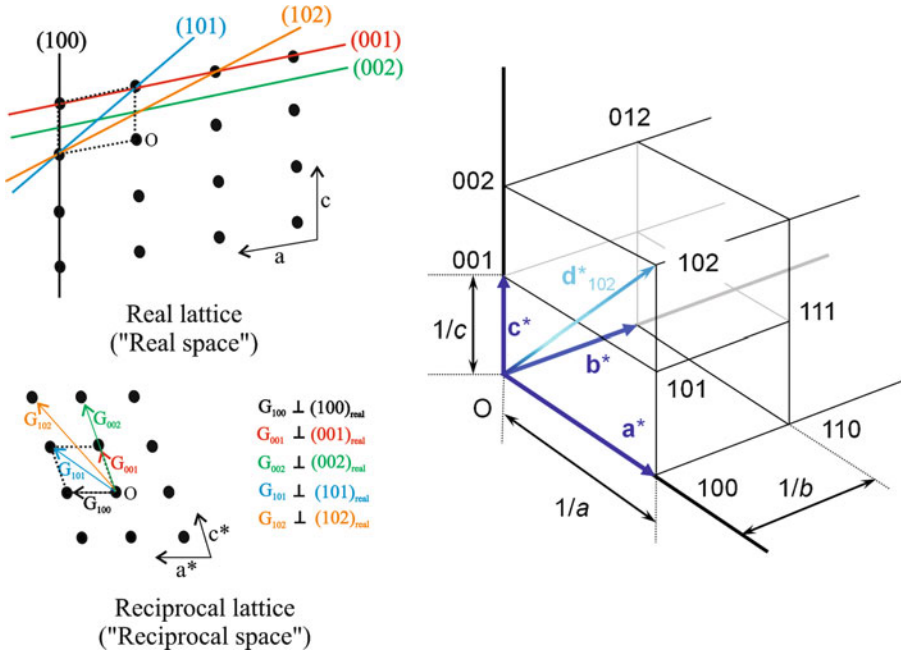
Figure 2.43. Comparison between a real monoclinic crystal lattice (a = b $\neq$ c) and the corresponding reciprocal lattice. Dashed lines indicate the unit cell of each lattice. The magnitudes of the reciprocal lattice vectors are not in scale; for example, |a*| = $1/d_{100}$, |c*| = $1/d_{001}$, |G_{101}| = d_{101}, etc. Note that for orthogonal unit cells (cubic, tetragonal, orthorhombic), the reciprocal lattice vectors will be aligned parallel to the real lattice vectors. © 2009 From *Biomolecular Crystallography: Principles, Practice, and Application to Structural Biology* by Bernard Rupp. Reproduced by permission of Garland Science/ Taylor & Francis Group LLC.

(ii) A vector joining two points of the reciprocal lattice, **G**, is perpendicular to the corresponding plane of the real lattice (Figure 2.38). For instance, a vector joining points (1, 1, 1) and (0, 0, 0) in reciprocal space will be perpendicular to the {111} planes in real space, with a magnitude of $1/d_{111}$. As you might expect, one may easily determine the interplanar spacing for sets of real lattice planes by taking the inverse of that represented in Eq. 20 – *e.g.*, the distance between adjacent planes of {100} in the real lattice is:

$$(21) \quad \frac{[a \bullet (b \times c)]}{|b \times c|}$$

In order to more completely understand reciprocal space relative to "real" space defined by Cartesian coordinates, we need to first recall the deBroglie relationship that describes the wave-particle duality of matter:

$$(22) \quad \lambda = \frac{h}{p}, \text{ or } p = \frac{h}{\lambda},$$

where: h = Planck's constant (6.626×10^{-34} J·s); p = momentum
Accordingly, if we represent a wave as a vector as described previously, the *wavevector*, **k**, will have a magnitude of:

$$(23) \qquad |k| = \frac{|p|}{\hbar} = \frac{2\pi}{\lambda},$$

where: $\hbar$ = the reduced Planck's constant ($h/2\pi$)

As one can see from Eq. 23, the magnitude of the wavevector, **k**, will have units proportional to [1/distance] – analogous to reciprocal lattice vectors. This is no accident; in fact, solid-state physicists refer to reciprocal space as *momentum space* (or *k-space*), where long wavevectors correspond to large momenta and energy, but small wavelengths. This definition is paramount to understanding the propagation of electrons through solids, as will be described later.

In order to determine which lattice planes give rise to Bragg diffraction, a geometrical construct known as an *Ewald sphere* is used. This is simply an application of the law of conservation of momentum, in which an incident wave, **k**, impinges on the crystal. The Ewald sphere (or circle in two-dimensional) shows which reciprocal lattice points, (each denoting a set of planes) which satisfy Bragg's Law for diffraction of the incident beam. A specific diffraction pattern is recorded for any **k** vector and lattice orientation – usually projected onto a two-dimensional film or CCD camera. One may construct an Ewald sphere as follows (Figure 2.44):

  (i) Draw the reciprocal lattice from the real lattice points/spacings.
 (ii) Draw a vector, **k**, which represents the incident beam. The end of this vector should touch one reciprocal lattice point, which is labeled as the origin (0, 0, 0).
(iii) Draw a sphere (circle in 2-D) of radius |**k**| = $2\pi/\lambda$, centered at the start of the incident beam vector.
 (iv) Draw a scattered reciprocal lattice vector, **k'**, from the center of the Ewald sphere to any point where the sphere and reciprocal lattice points intersect.
  (v) Diffraction will result for any reciprocal lattice point that crosses the Ewald sphere such that **k'** = **k** + **g**, where **g** is the scattering vector. Stated more succinctly, Bragg's Law will be satisfied when **g** is equivalent to a reciprocal lattice vector. Since the energy is conserved for elastic scattering of a photon, the magnitudes of **k'** and **k** will be equivalent. Hence, using the Pythagorean theorem, we can re-write the diffraction condition as:

$$(24) \qquad (k+g)^2 = |k|^2 \Rightarrow 2k \bullet g + g^2 = 0$$

Since **g** = h**a*** + k**b*** + l**c***, with a magnitude of $2\pi/d_{hkl}$ for the (hkl) reflection, Eq. 24 can be re-written in terms that will yield Bragg's Law in more familiar terms (*c.f.* Eq. 1):

$$(25) \qquad 2\left(\frac{2\pi}{\lambda}\right)\left(\frac{2\pi}{d_{hkl}}\right)\sin\theta = \frac{4\pi^2}{d_{hkl}{}^2} \Rightarrow \frac{2\sin\theta}{\lambda} = \frac{1}{d_{hkl}}$$
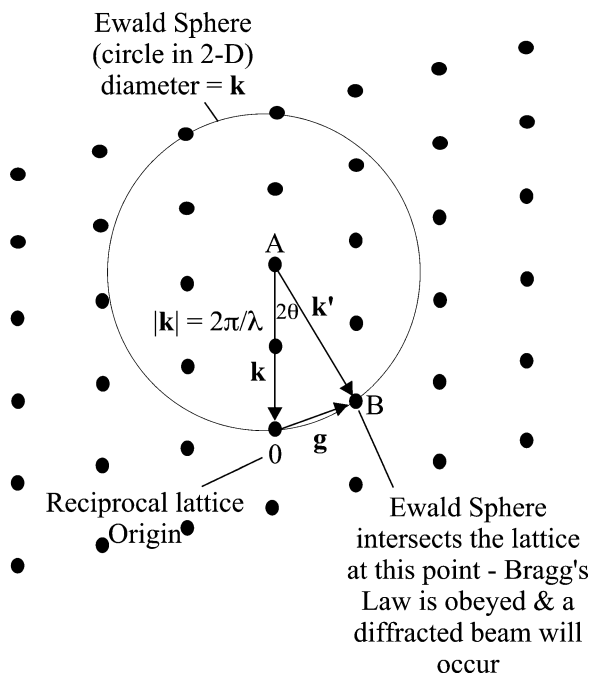
Figure 2.44. Illustration of Ewald sphere construction, and diffraction from reciprocal lattice points. This holds for both electron and X-ray diffraction methods. The vectors AO, AB, and OB are designated as an incident beam, a diffracted beam, and a diffraction vector, respectively.

In general, very few reciprocal lattice points will be intersected by the Ewald sphere,[42] which results in few sets of planes that give rise to diffracted beams. As a result, a single crystal will usually yield only a few diffraction spots. As illustrated in Figure 2.45, a single-crystalline specimen will yield sharp diffraction spots (also see Figure 2.40). In contrast, a polycrystalline sample will yield many closely spaced diffraction spots, whereas an amorphous sample will give rise to diffuse rings. Since the wavelength of an electron is much smaller than an X-ray beam, the Ewald sphere (radius: $2\pi/\lambda$) is significantly larger for electron diffraction relative to X-ray diffraction studies. As a result, electron diffraction yields much more detailed structural information of the crystal lattice (see Chapter 7 for more details regarding selected area electron diffraction (SAED)).

2.3.5. Crystal Imperfections

All crystals will possess a variety of defects in isolated or more extensive areas of their extended lattice. Surprisingly, even in solids with a purity of 99.9999%, there are on the order of 6×10^{16} impurities per cm^3! Such impurities are not always a disadvantage. Often, these impurities are added deliberately to solids in order to improve its physical, electrical, or optical properties.
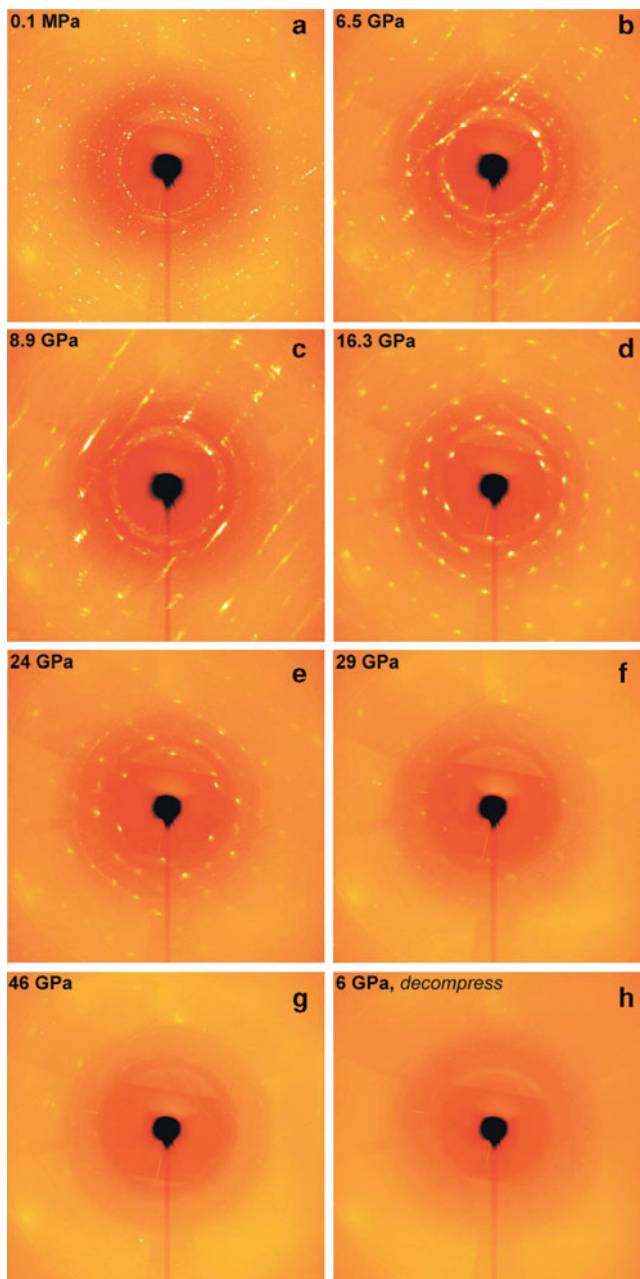
Figure 2.45. Diffraction patterns collected from the tridymite phase of SiO_2 compressed to different pressures at room temperature. The polycrystalline sample at ambient pressure (a–c) gradually transforms to a single crystal at a pressure of 16 GPa (d). Further compression results in disordering of the crystal lattice (e,f), eventually resulting in diffuse scattering rings, characteristic of an amorphous morphology at pressures of 46 GPa and higher (g,h). Reproduced with permission from *J. Synchrotron Rad.* **2005**, *12*, 560. Copyright 2005, International Union of Crystallography.

There are four main classifications of crystalline imperfections that exist in crystalline solids:

(a) *Point defects* – interstitial/substitutional dopants, Schottky/Frenkel defects, voids (vacancies)
(b) *Linear defects* – edge and screw dislocations
(c) *Planar defects* – grain boundaries, surfaces
(d) *Bulk defects* – pores, cracks

Of these four types, point/linear defects may only be observed at the atomic level, requiring sophisticated electron microscopy. In contrast, planar defects are often visible using a light microscope, and bulk defects are easily observed by the naked eye.

Although a solution is typically thought of as a solid solute dissolved in a liquid solvent (*e.g.*, sugar dissolved in water), *solid solutions* are formed upon the placement of foreign atoms/molecules within a host crystal lattice. If the regular crystal lattice comprises metal atoms, then this solution is referred to as an *alloy*. Solutions that contain two or more species in their crystal lattice may either be *substitutional* or *interstitial* in nature (Figure 2.46), corresponding to shared occupancy of regular lattice sites or vacancies between lattice sites, respectively.

Substitutional solid solutions feature the actual replacement of solvent atoms/ions that comprise the regular lattice with solute species, known as *dopants*. The dopant species is typically arranged in a random fashion among the various unit cells of the extended lattice. Examples of these types of lattices are illustrated by metal-doped aluminum oxide, constituting gemstones such as emeralds and rubies (both due to Cr-doping). For these solids, small numbers of formal Al^{3+} lattice sites are replaced with solute metal ions. We will describe how this relates to the color of crystalline gemstones in Section 2.3.6.

In general, the constituent atoms of substitutional solid solutions will be randomly positioned at any site in the lattice. However, as the temperature is lowered, each lattice position may no longer be equivalent, and ordered arrays known as *superlattices* may be formed. Examples of superlattice behavior are found for Au–Cu alloys used in jewelry, gold fillings, and other applications (Figure 2.47).
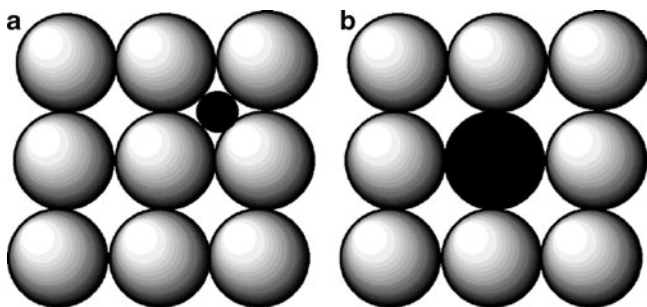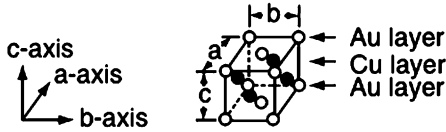

Figure 2.46. Illustration of the difference between (a) interstitial and (b) substitutional defects in crystalline solids.

a The unit cell of the AuCu I superlattice
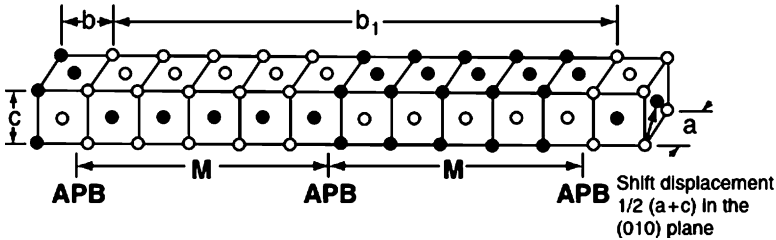

b The unit cell of the AuCu II superlattice

Figure 2.47. Unit cell representations of two varieties of AuCu superlattices. For the AuCu II superlattice, M refers to the length of repeat unit, and APB indicates the antiphase boundaries between adjacent periodic arrays. Republished with the permission of the International and American Associations for Dental Research, from "Determination of the AuCu Superlattice Formation Region in Gold–Copper–Silver Ternary System", Uzuka, T.; Kanzawa, Y.; Yasuda, K. *J. Dent. Res.* **1981**, *60*, 883; permission conveyed through Copyright Clearance Center, Inc.

For an 18-karat Au/Cu dental alloy, a superlattice will be present at temperatures below 350°C; at higher temperatures, a random substitutional alloy is formed. The AuCu I superlattice (Figure 2.47a) consists of alternate planes of copper and gold atoms, resulting in a tetragonal unit cell that has been elongated along both *a* and *b* axes. This is analogous to the hardening mechanism we will see in Ch. 3 for the austenite to martensite transformation, which also involves a tetragonal unit cell. In fact, the hardening of gold alloys is thought to arise from the superlattice ordering and precipitation hardening mechanisms. A more complex superlattice is also observed in Au/Cu alloys (Figure 2.47b) consisting of a periodic array of multiple unit cells, with Cu and Au atoms exchanging positions between corners and faces. In this case, hardening is thought to occur from the existence of relatively high-energy antiphase boundaries (APBs) between adjacent arrays.[43]

As we will see more in Chapter 7, the resolution of electron microscopes is now suitable for the easy visualization of small atomic cluster arrays. Figure 2.48 illustrates a well-ordered array of Fe–Pd alloy nanoparticles. Interestingly, even though Fe (bcc) and Pd (fcc) do not share the same crystal structure, each nanoparticle crystallite comprises only one lattice, indicating that the Fe and Pd metals form a solid solution. Interestingly, it is common for the bcc lattice of iron to change to fcc when alloyed with metals such as Pt, Pd, Cu, or Ni.[44]

In order to form a stable substitutional solid solution of appreciable solubility, the following *Hume-Rothery* rules, must be satisfied. Though these requirements are
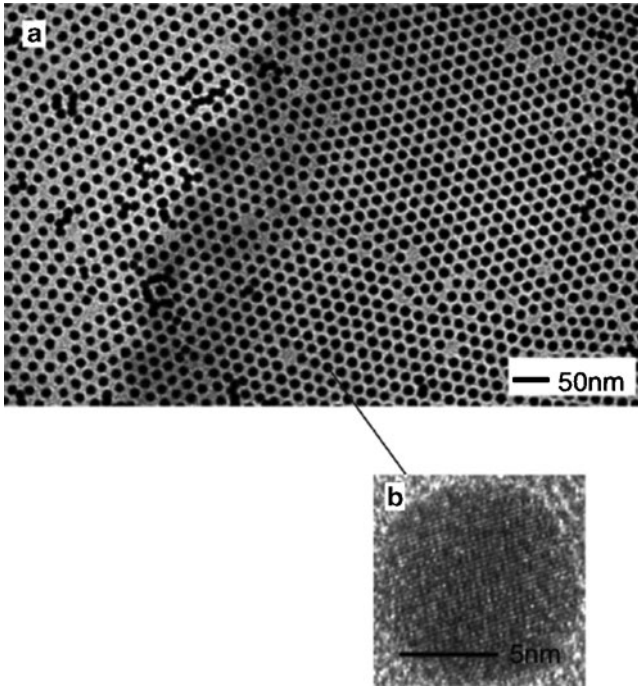
Figure 2.48. Transmission electron microscope image showing a 2D hexagonal superlattice of Fe–Pd alloy nanoparticles. Image (b) confirms that each nanoparticle consists of only one type of crystal lattice. Reproduced with permission from *Chem. Mater.* **2004**, *16*, 5149. Copyright 2004 American Chemical Society.

often cited for metallic alloys, they are relevant for any solid solution including ceramic lattices:

1. The percentage difference between solute and solvent atomic radii should be less than 15% (Eq. 26). If there were a larger mismatch between the dopant and solvent atomic radii, the rate of diffusion would either be too slow (for large r_{solute}), or the dopant would position itself in an interstitial site rather than replacing a solvent atom (for small r_{solute}). For instance, although most gemstones feature the replacement of formally Al^{3+} ions in an aluminum oxide (alumina) based crystal with M^{3+} ions (M = Cr, Ti, Fe), the substitution of aluminum ions with Li^+ or W^{3+} ions would cause too drastic a perturbation of the crystal structure. Whereas small lithium atoms/ions would have an opportunity to diffuse into the lattice forming interstitial solutions, the large tungsten ions would only adsorb to the surface of individual crystals.

$$(26) \quad \left| \frac{r_{solute}}{r_{solvent}} \right| \times 100\% \leqslant 15\%$$

2. The crystal structures of the dopant and solvent atoms must be matched. That is, the density of the host solvent unit cell must be voluminous enough to accommodate the solute atoms.

3. In order for dopant atoms to be stabilized within a host lattice, both solvent/solute species must have similar electronegativities. If this prerequisite were not met, electron density would transfer to the more electronegative atoms, forming a compound with an entirely new lattice structure and distinct properties. For instance, the reaction of metallic aluminum and nickel results in nickel aluminide, Ni_3Al, a compound with both ceramic and metallic properties. Such *transformational alloys* are in contrast to interstitial and substitutional alloys, in which the original solvent lattice framework is not significantly altered.

4. The solute and solvent atoms should have similar valences in order for maximum solubility, rather than compound formation. In general, a greater solubility will result from the dissolution of a higher-valence solute species in a lower-valence solvent lattice, than vice versa. For instance, the solubility limit of Zn in Cu is 38.4 at.% Zn, but only 2.3 at.% Cu for Cu in Zn. Solubilities also decrease with an increase in periodic separation; for example, the solubility maximum is 38.4% Zn in Cu, 19.9% Ga in Cu, 11.8% Ge in Cu, and only 6.9% As in Cu.

In contrast to substitutional solid solutions, there must be a significant size difference between solute and solvent species for appreciable interstitial solubility (Eq. 27). Accordingly, the most common interstitial solutes are hydrogen, carbon, nitrogen, and oxygen. If the dopant species is identical to the lattice atoms, the occupancy is referred to as *self-interstitial*. This will result in a large local distortion of the lattice since the lattice atom is significantly larger than intersitial sites. Consequently, the energy of self-interstitial formation is *ca.* three times greater than that required to form vacancies, resulting in a very low concentration (*i.e.,* $<1/cm^3$ at room temperature).

$$(27) \quad \text{Interstitial solubility} = \frac{r_{solute}}{r_{solvent}} \leqslant 0.59$$

As one would expect, smaller atoms diffuse more readily than larger ones. For instance, the interdiffusion of a carbon impurity atom within an α-Fe lattice at 500°C is 2.4×10^{-12} m^2/s, relative to 3.0×10^{-21} m^2/s for self-diffusion of Fe atoms within the iron lattice. Whereas carbon is able to migrate via *interstitial diffusion* requiring minimal lattice distortion, Fe diffusion occurs via *vacancy diffusion*, which necessitates a much greater perturbation of the lattice since strong Fe-Fe metallic bonds must first be broken.

The migration of a lattice atom/ion into an available interstitial site will leave behind a vacancy (Figure 2.49); the formation of such an interstitial/vacancy pair is known as a *Frenkel defect*. In contrast, *Schottky defects* are formed through the migration of a cation–anion pair from the crystal lattice framework, leaving behind two vacant lattice sites. For ionic crystals, the overall charge of the crystal must be charge-balanced. That is, if trivalent ions such as La^{3+} are substituted with divalent cations such as Ca^{2+}, there must be concomitant placements of divalent anions
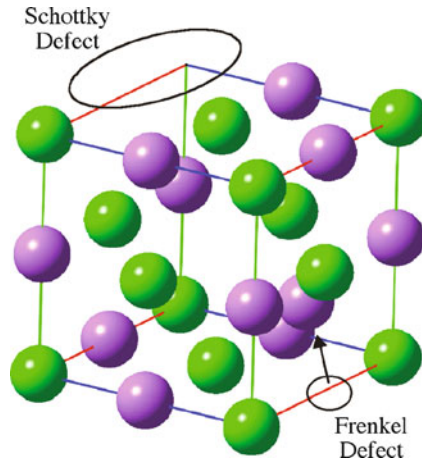
Figure 2.49. Illustration of a unit cell of an ionic crystal with Frenkel and Schottky defects.

(e.g., O^{2-}) to balance the crystal charge. This is the mode of activity for solid electrolytes used for fuel cell, supercapacitor, battery, and sensory applications – the topic of this end-of-chapter "Important Materials Application."

When the composition of a crystal is defined by a distinct chemical formula (e.g., SiO_2), it is known as a *stoichiometric compound*. If the composition of the crystal is altered upon doping or thermal treatment, the resulting solid may deviate from the original chemical formula, forming a *nonstoichiometric* solid. Nonstoichiometry and the existence of point defects in a solid are often closely related, and are prevalent for transition metal (e.g., W, Zn, Fe) and main group (e.g., Si, Al) oxides. For instance, the formation of x anion vacancies per each quartz (SiO_2) unit cell will result in the nonstoichiometric compound SiO_{2-x}.

Bulk defects are produced through the propagation of the microscopic flaws in the lattice. For crystals with a planar defect such as polycrystalline solids, the *grain boundary* marks the interface between two misaligned portions of the bulk crystal (Figure 2.50). The size of the individual microcrystals (or grains) that comprise a larger aggregate greatly affects many properties of the bulk crystal. Both optical microscopy and X-ray diffraction are used to determine the grain sizes; most commercial metals and alloys consist of individual crystallites with diameters ranging from 10 to 100 μm, each corresponding to millions of individual metal atoms. Since energy is required to form a surface, grains tend to grow in size at the expense of smaller grains to minimize energy. This growth process occurs by diffusion, which is accelerated at high temperatures.

A decrease in the size of these microscopic grains or crystallites results in an increase in both strength and hardness of the bulk material, due to closer packing among neighboring grains. The density of atoms at a solid surface, or in the region surrounding a grain boundary is always smaller than the bulk value. This is due to atoms at these regions containing dangling bonds, known as coordinatively
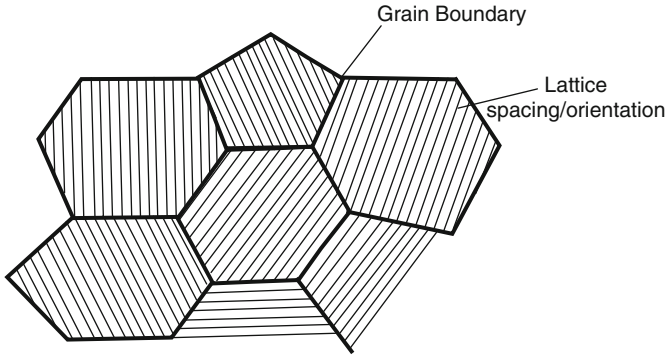
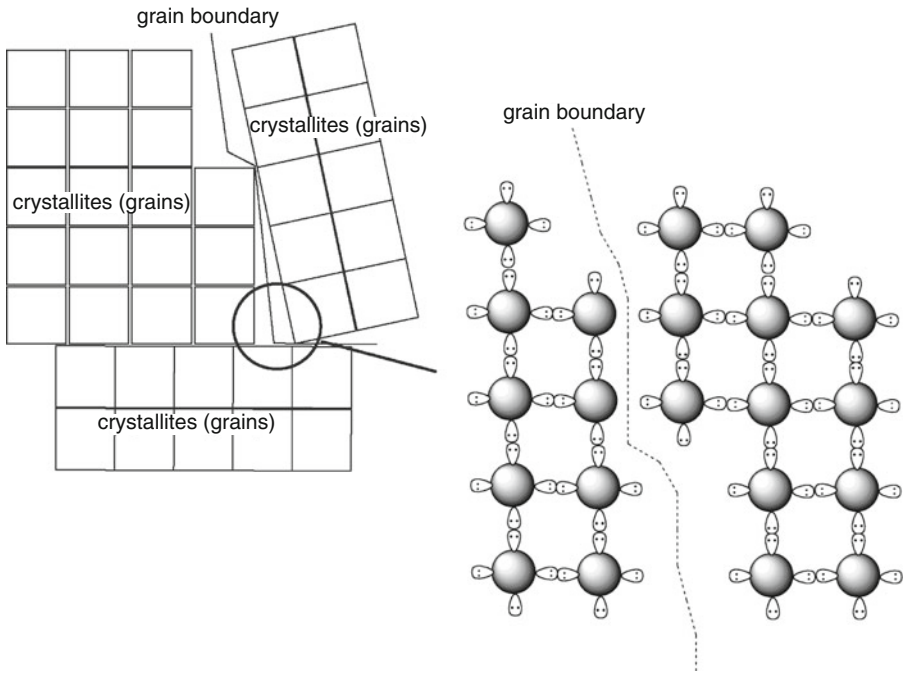*Figure 2.50.* Illustration of grain boundaries between individual crystalline domains.

Figure 2.51. Schematic of a polycrystalline solid, with grain boundaries formed from dangling bonds between neighboring metal atoms.

unsaturated (Figure 2.51). Hence, surfaces and interfaces are very reactive, often resulting in the concentration of impurities in these regions.

A special type of grain boundary, known as *crystal twinning*, occurs when two crystals of the same type intergrow, so that only a slight misorientation exists between them. Twinned crystals may form by inducing alterations in the lattice

during nucleation/growth (*e.g.,* impurity incorporation during slow cooling) or from the application of an external force (*stress*). The twin boundary is a highly symmetrical interface, often with the crystal pairs related to one another by a mirror plane or rotation axis. Accordingly, twinning poses a problem in determining the correct crystal structure via X-ray diffraction due to the complexity created by overlapping reciprocal lattices.[45] Due to the symmetric equivalence of the polycrystals, twin boundaries represent a much lower-energy interface than typical grain boundaries formed when crystals of arbitrary orientation grow together.

A stress exerted on a material results in a structural deformation referred to as *strain*, whose magnitude is related to the bonding interactions among the atoms comprising the solid. For example, a rubbery material will exhibit a greater strain than a covalently bound solid such as diamond. Since steels contain similar atoms, most will behave similarly as a result of an applied stress. There are four modes of applying a load, referred to as tension, compression, shear, and torsional stresses (Figure 2.52). Both tension and compression stresses are applied parallel to the long axis of the material, resulting in elongation or contraction of the material along the direction of the stress, respectively. In contrast, shear stress is applied at some angle with respect to the long axis, and will cause the material to bend. The resultant flex is referred to as *shear strain*.

For small stresses, a material will generally deform elastically, involving no permanent displacement of atoms and reversal of the deformation upon removal of the shear stress. The linear relationship between stress and strain in these systems is governed by Hooke's law (Eq. 28). The stiffer the material, the greater will be its *Young's modulus*, or slope of the stress *vs.* strain curve. It should be noted that some materials such as concrete do not exhibit a linear stress/strain relationship during elastic deformation. In these cases, the modulus is determined by taking the slope of a tangential line drawn at a specific level of stress.

$$(28) \qquad \sigma = E\varepsilon,$$

where: σ = tensile stress, in units of force per unit area (S.I. unit: 1 Pa = 1 N/m^2);
$\quad\quad\quad$ E = Young's modulus, or modulus of elasticity (*e.g.,* 3 GPa for Nylon, 69 GPa for aluminum, and 407 GPa for W)
$\quad\quad\quad$ ε = strain, defined as the geometrical change in shape of an object in response to an applied stress

Poisson's ratio is used to describe the lateral distortion that is generated in response to a tensile strain. The values for elastomeric polymers are *ca.* 0.5, metals 0.25–0.35, polymeric foams 0.1–0.4, and cork is near zero. Interestingly, *auxetic* materials exhibit a negative Poisson's ratio, becoming thicker under tension (Figure 2.53). Though this phenomenon was first discovered for foam-like structures,[46] there are now many classes of materials such as bcc metals, silicates, and polymers[47] that exhibit this property. Such materials exhibit interesting mechanical properties such as high-energy absorption and fracture resistance, which may prove useful for applications such as packing material, personal protective gear, and body armor. The waterproof/breathable fabric Gore-Tex® is an auxetic material, comprised of a fluorinated polymeric structure (see Chapter 5).
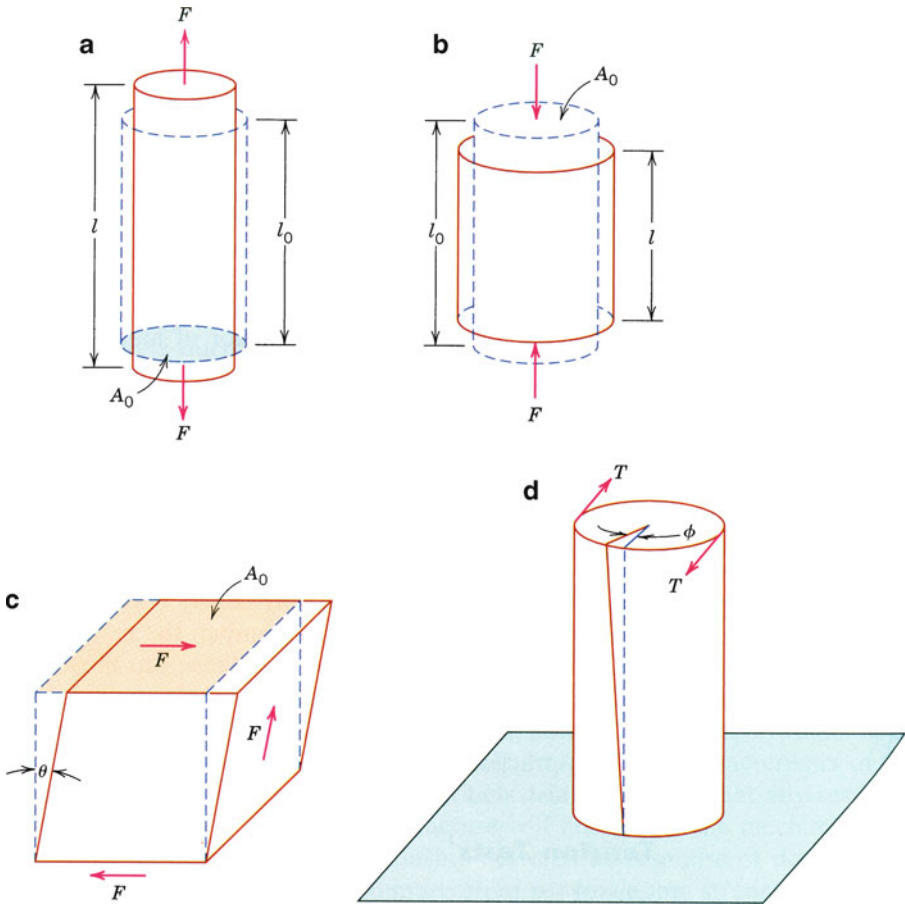
Figure 2.52. Illustration of various types of loads (stresses), which result in material strain. Shown are (a) tensile stress, (b) compressive stress, (c) shear stress, and (d) tortional stress. Reproduced with permission from Callister, W. D. *Materials Science and Engineering: An Introduction*, 7th ed., Wiley: New York, 2007. Copyright 2007 John Wiley & Sons, Inc.

For large stresses, a material will deform plastically, involving the permanent displacement of atoms. The onset of plastic deformation is referred to as the *yield point* (or *yield strength*) of the material. For most metals, there is a gradual transition from elastic to plastic deformation; however, some steels exhibit very sharp transitions. After the yield point is reached, plastic deformation continues until the material reaches its fracture point. Accordingly, the *tensile strength* represents the maximum strain in the stress *vs.* strain curve (Figure 2.54); this property with respect to its weight is referred to as the *specific strength*:

(29)   specific strength $= \dfrac{\text{tensile strength}}{\text{specific gravity}}$
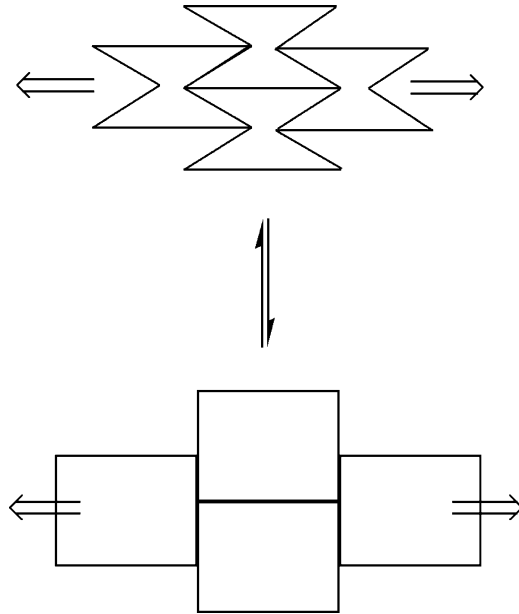
Figure 2.53. Illustration of the deformation modes exhibited by an auxetic material. These materials possess hinge-like structures that flex upon elongation.

In Chapter 3, we will discuss some strategies used to increase the yield and tensile strengths of metallic alloys – of extreme importance for structural engineering applications.

Plastic deformation of crystalline solids is referred to as *slip*, and involves the formation and movement of *dislocations*. Edge and screw dislocations are abrupt changes in the regular ordering of atoms along an axis in the crystal, resulting from breaking/reforming large numbers of interatomic bonds (Figure 2.55). Dislocations may be created by shear force acting along a line in the crystal lattice. As one would expect, the stress required to induce such dislocations is extremely high – of the same magnitude as the strength of the crystal. Accordingly, it is more likely that dislocations arise from irregularities (*e.g.*, steps, ledges) at grain boundaries or crystal surfaces for poly- and single crystals, respectively, which may then propagate throughout the crystal lattice.

During plastic deformation, existing dislocations serve as nucleation sites for new dislocations to form; hence, the dislocation density of the material increases significantly. Whereas the dislocation density (in units of dislocation distance per unit volume; mm/mm^3 or mm^{-2}) of pure metallic crystals is on the order of 10^3 mm^{-2}, the density may reach 10^{10} mm^{-2} in heavily deformed metals. It should be noted that line defects may not always be detrimental. As we will see in Chapter 3, the interactions among neighboring dislocations are responsible for work hardening of metals.
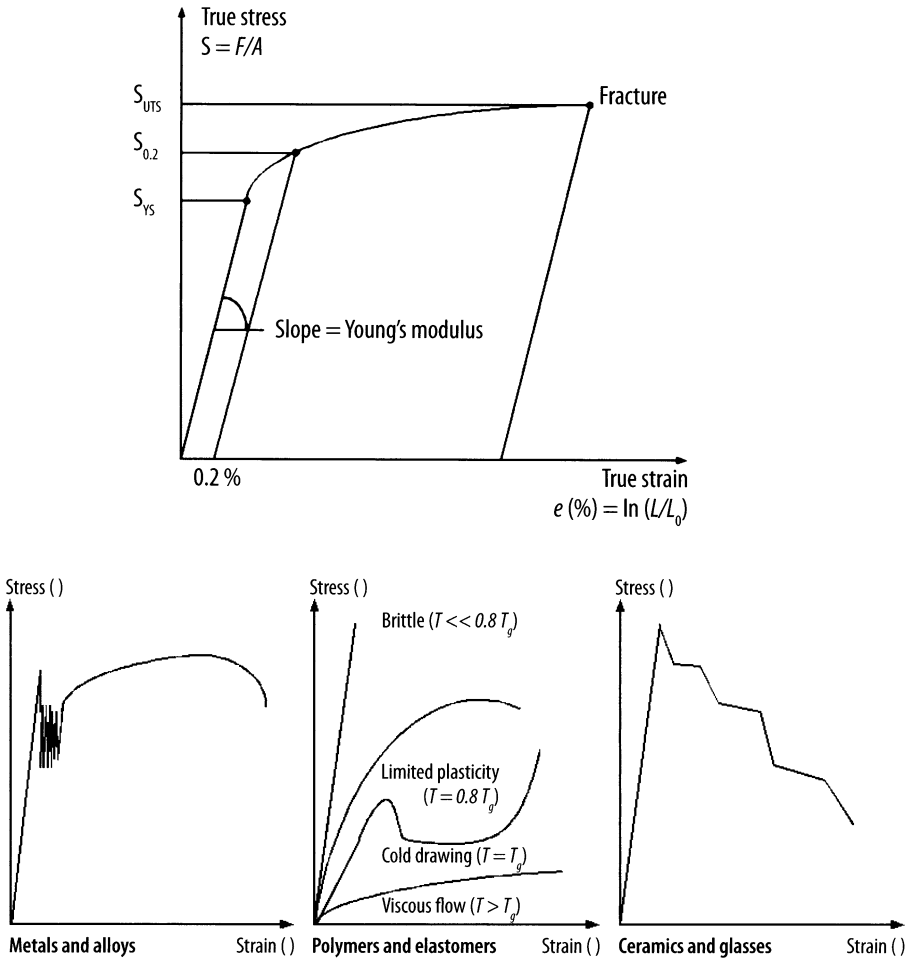
True stress
$S = F/A$

S_{UTS} Fracture

$S_{0.2}$

S_{YS}

Slope = Young's modulus

0.2 %   True strain
$e\ (\%) = \ln(L/L_0)$

Stress ( )   Stress ( )   Stress ( )

Brittle ($T \ll 0.8\,T_g$)

Limited plasticity
($T = 0.8\,T_g$)

Cold drawing ($T = T_g$)

Viscous flow ($T > T_g$)

Metals and alloys   Strain ( ) **Polymers and elastomers**   Strain ( ) **Ceramics and glasses**   Strain ( )

Figure 2.54. Illustration of a true stress *vs.* strain curve and comparison of stress–strain curves for various materials. UTS = ultimate strength, and YS = yield strength. The tensile strength is the point of rupture, and the offset strain is typically 0.2% – used to determine the yield strength for metals without a well-defined yield point.[48] Reproduced with permission from Cardarelli, F. *Materials Handbook*, 2nd ed., Springer: New York, 2008. Copyright 2008 Springer Science & Business Media.

In single crystals, there are preferred planes where dislocations may propagate, referred to as *slip planes*. For a particular crystal system, the planes with the greatest atomic density will exhibit the most pronounced slip. For example, slip planes for bcc and fcc crystals are {110} and {111}, respectively; other planes, along with those present in hcp crystals, are listed in Table 2.9. Metals with bcc or fcc lattices have significantly larger numbers of slip systems (planes/directions) relative to hcp. For example, fcc metals have 12 slip systems: four unique {111} planes, each
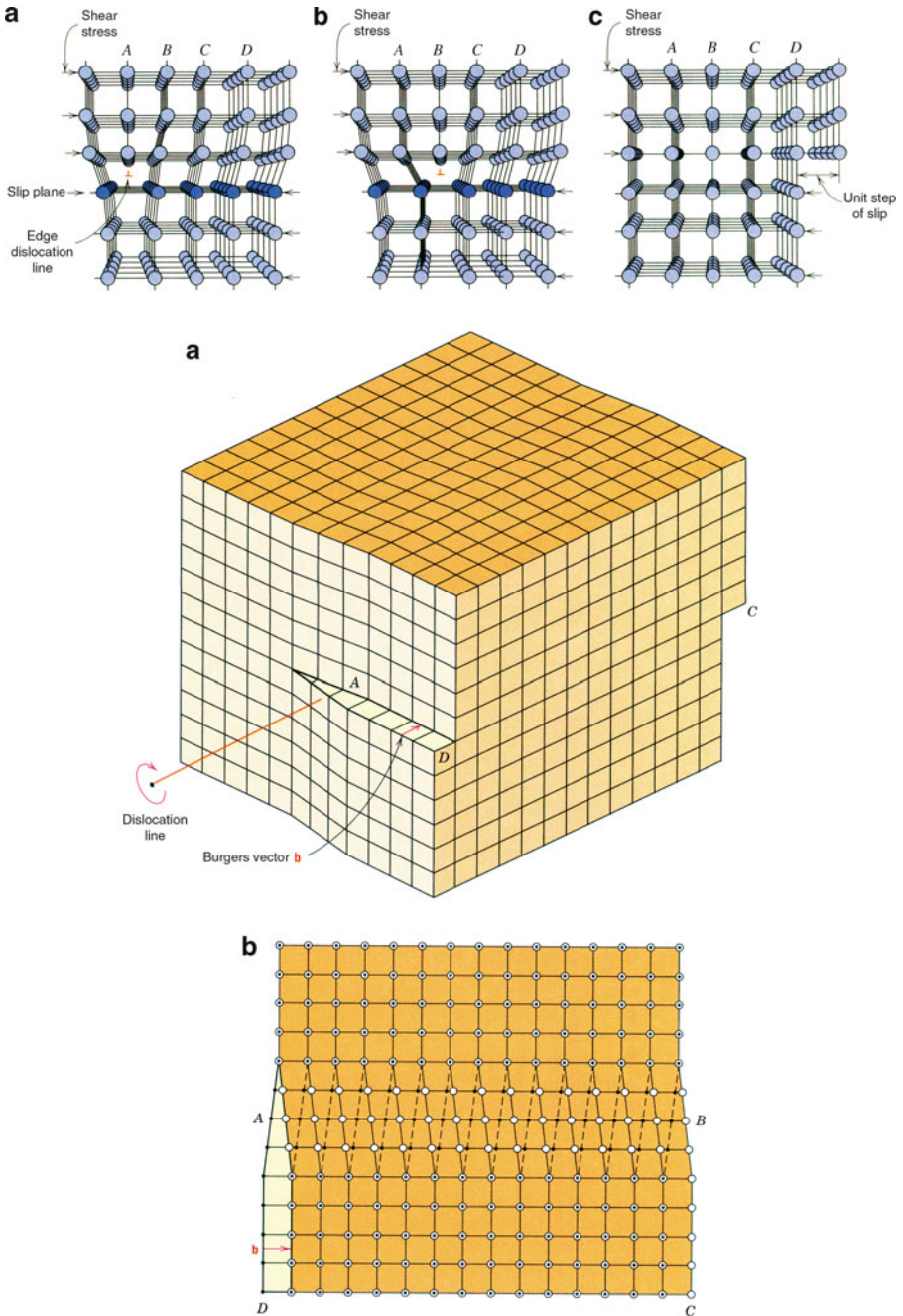
Figure 2.55. Illustration of dislocations. Shown are (top) edge dislocations and (bottom) screw dislocations. Reproduced with permission from Callister, W. D. *Materials Science and Engineering: An Introduction*, 7th ed., Wiley: New York, 2007. Copyright 2007 John Wiley & Sons, Inc.

Table 2.9. Slip Systems for BCC, HCP and FCC Crystals

Crystal	Slip plane	Slip direction
Body-centered cubic (BCC)	{110}	<111>
	{211}	<111>
	{321}	<111>
Hexagonal close-packed (HCP)	{0001}	<1120>
	{1010}	<1120>
	{1011}	<1120>
Face-centered cubic (FCC)	{111}	<110>
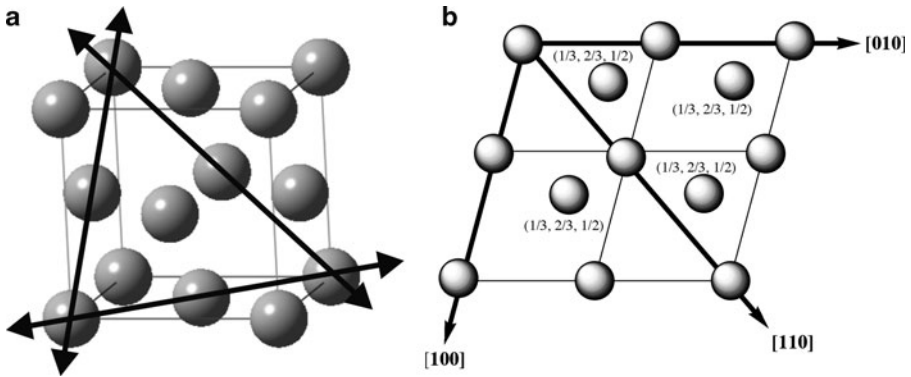
Figure 2.56. (a) The {111}<110> slip system for a face-centered cubic crystal. Note that there are 3 unique {111} planes, giving rise to 12 total slip systems for fcc. (b) The {001}<100> slip system for a hexagonal close-packed crystal. Shown is a 2×2 array of unit cells projected onto the (001) plane. Bold arrows indicate the three slip directions lying in each of the planes.

containing three <110> slip directions. In contrast, hcp metals only have three to six slip systems (Figure 2.56). Consequently, fcc metals are generally more ductile due to greater varieties of routes for plastic deformation along these directions, whereas hcp metals are relatively brittle.

In contrast to the aforementioned bulk, planar, and linear classes of crystalline imperfections that involve perturbations of large groups of lattice atoms, point defects refer to individual atomic displacements. As the temperature of the crystal is increased, the atoms in the crystal vibrate about their equilibrium positions generating vacancies or voids in the lattice. The Arrhenius equation (Eq. 30) is used to calculate the equilibrium number of vacancies or voids in the crystal lattice at a specific temperature. Since the activation energy (Figure 2.57) is often signifi-cantly greater than the thermally-induced kinetic energy of lattice atoms, the most pronounced atomic migration occurs along dislocations and voids in the crystal, since fewer atoms are involved in the atomic displacement (i.e., E_a is much lower). For a typical solid, there is one vacancy per 10^{15} lattice atoms at room temperature; however, at a temperature just below the melting point, there will be one vacancy per ca. 10,000 lattice atoms.
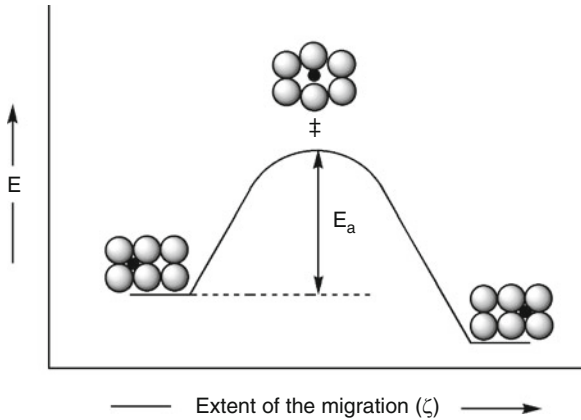
Figure 2.57. Illustration of the energetics involved for the atomic diffusion of interstitial impurities.

$$(30) \qquad \frac{N_v}{N_T} = e^{-(E_a/kT)},$$

where: N_v is the number of vacancies; N_T, the total number of atoms in the crystal lattice; E_a, the activation energy for the diffusion process; k, the Boltzmann constant $(1.38 \times 10^{-23}$ J atom^{-1} K$^{-1})$; and T is the temperature (K).

2.3.6. Physical Properties of Crystals

Hardness

Thus far, we have examined the 3-D arrangements of atoms, ions, or molecules comprising a crystal lattice. The macroscopic physical properties of crystalline materials are directly related to these arrangements. For instance, the overall hardness of a crystal depends on the nature of the interactions among the discrete components of the crystal lattice. Those crystals possessing covalent interactions (*e.g.*, diamond) will have a high hardness, whereas those containing only van der Waals forces will be soft (*e.g.*, talc). A variety of scales (Table 2.10) may be used to assign the relative hardness of a material. The Mohs scale is generated by a qualitative assessment of how easily a surface is scratched by harder materials, with the hardest material (diamond) given a value of ten. The hardness of a material is directly proportional to its tensile strength; depending on which method is used, proportionality factors may be calculated. For instance, if the Brinell hardness value is known, the tensile strength is simply 500 times that value.

Tests such as Vickers, Knoop, and Brinell use an indentation technique that impinges a hard tip (*e.g.*, diamond) into the sample with a known load (Figure 2.58a). After a designated period of time, the load is removed, and the indentation area is measured. The hardness, *H*, is defined as the maximum load, *L*, divided by the

Table 2.10. Hardness Scales

Solid	Mohs	Vickers	Knoop
Talc	1	27	N/A
Graphite	1.5	37	N/A
Gypsum	2	61	N/A
Fingernail	2.5	102	117
Calcite	3	157	169
Fluorite	4	315	327
Apatite	5	535	564
Knife blade	5.5	669	705
Feldspar	6	817	839
Pyrex glass	6.5	982	929
Quartz	7	1,161	N/A
Topaz/Porcelain	8	1,567	N/A
Sapphire/Corundum	9	2,035	N/A
Diamond	10	N/A	N/A

N/A indicates the hardness value is above/below the acceptable range of the particular hardness scale. Values were obtained from the conversion site: http://www.efunda.com/units/hardness/convert_hardness. cfm?HD=HM&Cat=Steel#ConvInto.

residual indentation area, A_r (Eq. 31). The coefficient, F, varies depending on which indentation method is used. This value (14.229 for Knoop and 1.854 for Vickers) is related to the geometry of the pyramidal probe, which will affect the penetration depth under the same load. Since a spherical probe is used for the Brinell test, a more complex formula is used to calculate the hardness (Eq. 32), where D is the diameter of the spherical indentor, and D_i is the diameter of the indentor impression (both in mm):

$$(31) \quad H = F \left(\frac{L}{A_r} \right)$$

$$(32) \quad H = \frac{L}{\frac{\pi}{2} D \left(D - \sqrt{D^2 - D_i^2} \right)}$$

Quite often, an indentation is so small that it is difficult to resolve with a normal light microscope. To circumvent these problems, software is now capable of monitoring the load and displacement of the probe during the measurement, and relating this to the contact area. Such an analysis without the need for visual confirmation is necessary for *nanoindentation* techniques for thin films and other surface hardness applications. As its name implies, the hardness of a material is evaluated by the depth and symmetry of the cavity created from controlled perforation of a surface with a nanosized tip (Figure 2.58b). It should be pointed out that although we have discussed crystalline solids in great detail thus far, hardness measurements are also easily performed on amorphous solids such as glasses.

Cleavage and fracturing

The intermolecular forces in a crystal lattice are often not homogeneous in all directions. If the solid consists of strong interactions among neighbors in specific
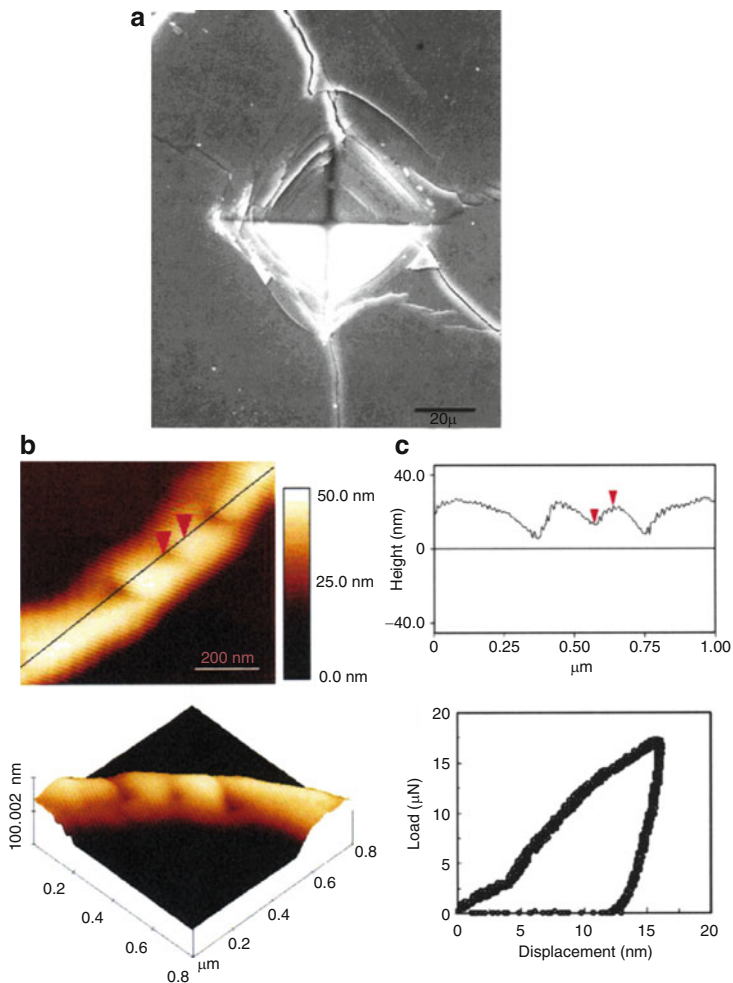
Figure 2.58. Examples of indentation processes to determine surface hardness. Shown are (a) Vickers indentation on a SiC–BN composite, (b) atomic force microscope images of the nanoindentation of a silver nanowire, and (c) height profile and load–displacement curve for an indent on the nanowire. Reproduced with permission from *Nano Lett.* **2003**, 3(11), 1495. Copyright 2003 American Chemical Society.

layers, and weak interactions among molecules in neighboring layers (*e.g.*, graphite), a *cleavage plane* (*c.f.* slip planes, discussed earlier) is created where little force is needed to separate the crystal into two units (Figure 2.59a, b). Since the cleavage planes are parallel to crystal faces, the fragments formed upon cleavage will retain the symmetry exhibited by the bulk crystal. Whereas *cleavage* describes the formation of a smooth piece of the original crystal when subjected to an external stress,
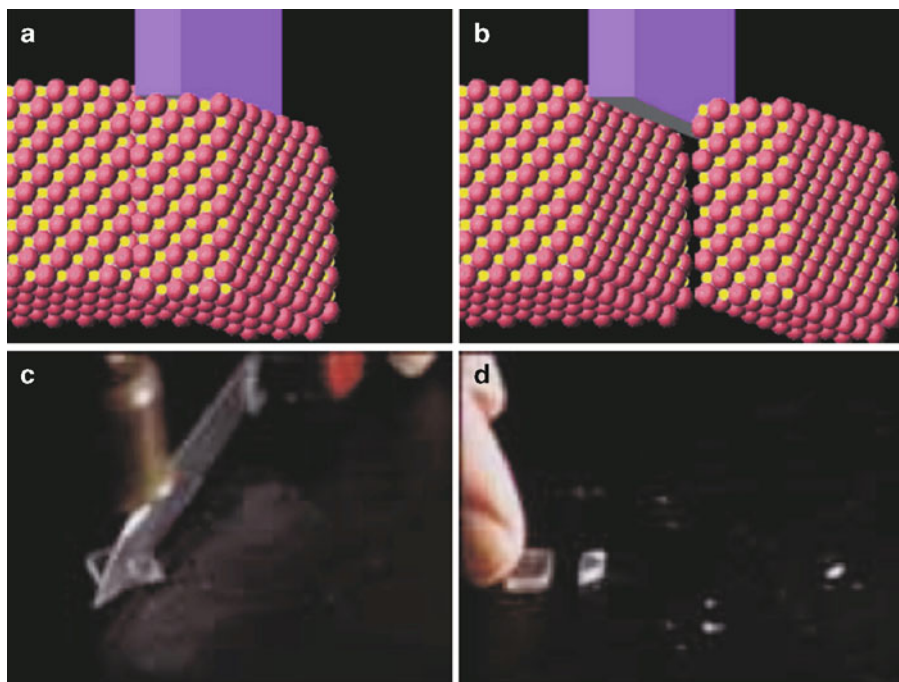
Figure 2.59. Example of cleavage and fracture at the atomic (a, b) and macroscopic (c, d) levels. In images (c, d), a crystal of NaCl is exposed to a stress along an oblique angle to the cleavage plane, resulting in both cleavage and fracturing. Images taken with permission from the Journal of Chemical Education online: http://jchemed.chem.wisc.edu/JCESoft/CCA/CCA2/SMHTM/CLEAVE.HTM.

a *fracture* refers to chipping a crystal into rough, jagged pieces. Figure 2.59c, d show photos of cleavage and fracture of a NaCl crystal subjected to stress at oblique angles to the cleavage plane. Although preferential cracking will occur along the cleavage plane, smaller fractured pieces will also be formed. In general, as one increases both the magnitude and obliqueness of the applied stress, the amount of fracturing will increase, relative to cleavage.

On occasion, the cleavage plane may be easily observed due to a fibrous network lattice. One example of such a crystal is ulexite, sodium calcium borate of the chemical formula $NaCa(B_5O_6)(OH)_6 \cdot 5H_2O$. Upon visual inspection, it is quite obvious that upon external stress, the crystal will preferentially cleave in directions parallel to the crystallite fibers (Figure 2.60a). However, more intriguing is the interesting optical properties exhibited by this crystal, commonly designated as the "T.V. rock" (Figure 2.60b, c). If the crystal is surrounded by a medium of a lower refractive index (*e.g.*, air), light is propagated through the individual fibers by internal reflection. This is analogous to fiber optic cables that will be described a bit later in this chapter. Figure 2.60b shows that light passing through the crystal will exhibit concentric circles. This is due to the difference in the effective path lengths
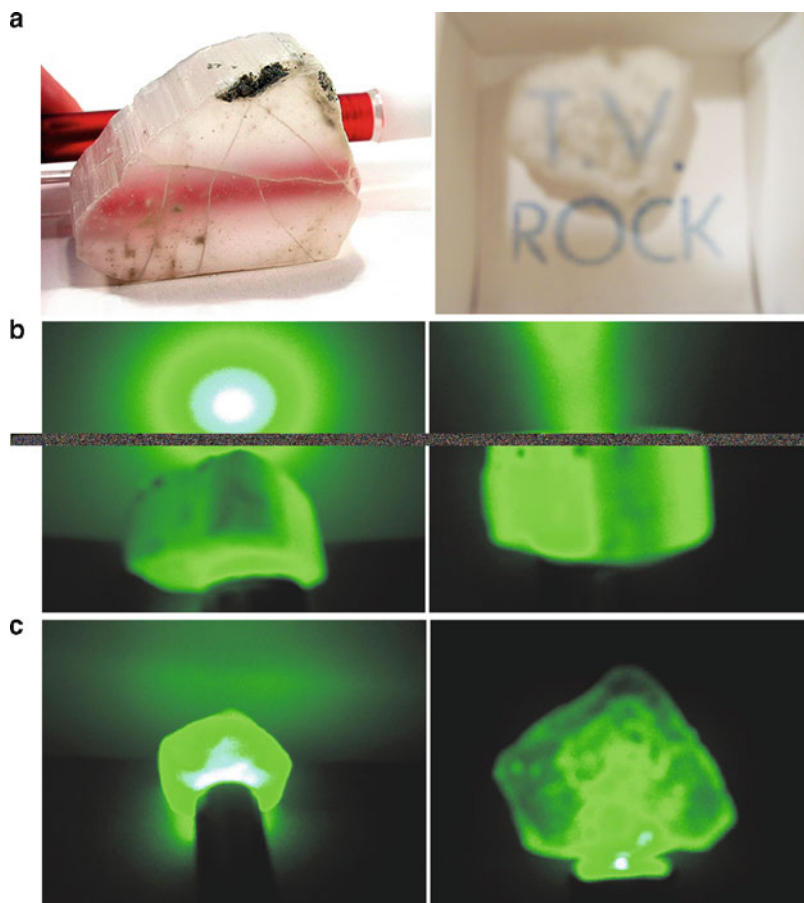
Figure 2.60. Optical properties of ulexite, the "T.V. rock." Shown are (a) the fibrous morphology of the crystal, and projection onto the surface of the rock from transmission through parallel fibers, (b) passage, and (c) blockage of a green laser beam when impinged on the crystal at angles parallel and perpendicular to the fibers, respectively.

of light passing either directly through individual fibers, or crossing grain boundaries *en route* through the crystal via adjacent fibers.[49]

Color

In a previous section, we discussed substitutional impurities within crystal lattices without mentioning the changes in physical properties that this creates. Perhaps the most obvious outcome of a crystal impurity is the resultant color. In this section, we will answer the common question: "why are some crystals colorless, and others colored?"

Many crystals such as diamonds, quartz and corundum are normally colorless upon inspection. In these crystals, the constituent atoms form a rigid, regular

framework of covalent or ionic interactions. Since visible light (350–700 nm) is not energetically sufficient to cause bond rupturing and/or electronic transitions of the constituent metal atoms/ions, this energy is not absorbed by pure crystals, giving rise to a colorless state. However, when an impurity is added to the lattice, visible radiation may be suitably energetic to cause lattice alterations and/or electronic transitions, yielding an observable color change.

Colored crystals need not be gemstones; in fact, a colorless crystal of potassium chloride may be suitably altered to exhibit color. When solid KCl is heated to 500°C in the presence of potassium vapor, the crystal becomes a violet color. This occurs due to the ionization of gaseous potassium atoms that abstract a Cl^- anion from the crystal lattice. The electron formed in the oxidation process becomes trapped in the anion vacancy, as this will rebalance the overall charge of the crystal (Eq. 33):

(33) $\quad [(KCl)_n(KCl)]_{(s)} + K_{(g)} \rightarrow [(KCl)_n(K)(e^-)]_{(s)} + KCl_{(s)}$
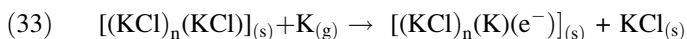
Another process that may be used to generate an anion vacancy is through irradiation of the crystal with ionizing radiation such as X-rays. This high-energy radiation will cause the removal of a halide ion from the lattice and will excite some of the lattice electrons from valence to conduction bands (see Section 2.3.7). At this point, the electrons are free to diffuse through the crystal, where they remain mobile until they find an anion vacancy site. At low temperatures (*e.g.*, in liquid nitrogen), electrons may even become localized by polarizing their surroundings; that is, displacing the surrounding ions, to give self-trapped electrons. For each type of electron trap, there is a characteristic activation energy that must be overcome for the release of the electron. As an irradiated crystal is heated, electrons are released from their traps by thermal activation, leading to a change in the observed color. The free electrons are able to migrate once again through the crystal until they recombine with an anion hole. This phenomenon has been studied in detail for aptly named "chameleon diamonds", which undergo color changes from greyish-green to yellow when they are heated/cooled (*thermochromic* behavior) or kept in the dark (*photochromic* behavior). In these diamonds, the color change is thought to arise from electron traps created by the complexation of H, N, and Ni impurities.[50]

Everyone is familiar with the coloration phenomenon of gemstones such as ruby. In these crystals, the brilliant colors are due to the presence of transition metal dopants. Table 2.11 lists some common gemstones, and the respective host crystal

Table 2.11. Active Dopants in Gemstone Crystals

Gemstone	Color	Host crystal	Impurity ion(s)
Ruby	Red	Aluminum oxide	Cr^{3+}
Sapphire	Blue	Aluminum oxide	Fe^{2+}, Ti^{4+}
Emerald	Green	Beryllium aluminosilicate	Cr^{3+}
Aquamarine	Blue-green	Beryllium aluminosilicate	Fe^{2+}
Garnet	Red	Calcium aluminosilicate	Fe^{3+}
Topaz	Yellow	Aluminum fluorosilicate	Fe^{3+}
Tourmaline	Pink/red	Calcium lithium boroaluminosilicate	Mn^{2+}
Turquoise	Blue-green	Copper phosphoaluminate	Cu^{2+}

and dopants that give rise to their characteristic colors. Whereas crystals of pure corundum (α-alumina) are colorless, a small amount (<1%) of chromium doping yields the familiar reddish/pink color. This color change is only possible if the periodic framework of the crystal is altered, through the incorporation of additional dopant atoms/ions or vacancies in the lattice. For ruby, a transition metal ion, Cr^{3+}, replaces Al^{3+} yielding electronic d–d transitions that were unattainable for the original main-group ion.

In a pure crystal of Al_2O_3 (as well as Fe_2O_3 and Cr_2O_3 that share the *corundum* structure) the oxide ions form an hcp array with the metal ions filling in 2/3 of the available octahedral intersitial sites (Figure 2.61). The formal electronic configuration of Al^{3+} ions is [Ne], indicating that all electrons are paired. Since the irradiation of the crystal with visible light is not energetic enough to cause promotion of electrons into empty excited-state orbitals, the crystal appears colorless. If Al^{3+} ions are replaced with Cr^{3+} at a concentration of only 0.05 wt% (*i.e.*, 1.58×10^{19} Cr^{3+} ions/cm^3), the crystal will appear brilliantly red. In these *ruby* crystals, each of the Cr^{3+} ions have a configuration of $[Ar]3d^3$. Although general chemistry tends to simplify the d-orbitals as being a set of five degenerate orbitals, transition metal complexes exhibit splitting of the d-orbital energy levels. This results in facile electronic transitions upon exposure to visible light, explaining the bright colors exhibited by many transition metal compounds.

A simple theory, referred to as *crystal field theory*,[51] is often used to account for the colors and magnetic properties of transition metal complexes. This theory is based on the electrostatic repulsions that occur between electrons in d-orbitals of a transition metal, and electrons contained in ligand orbitals. Figure 2.62 shows the splitting of the d-orbitals resulting from the electrostatic repulsions between
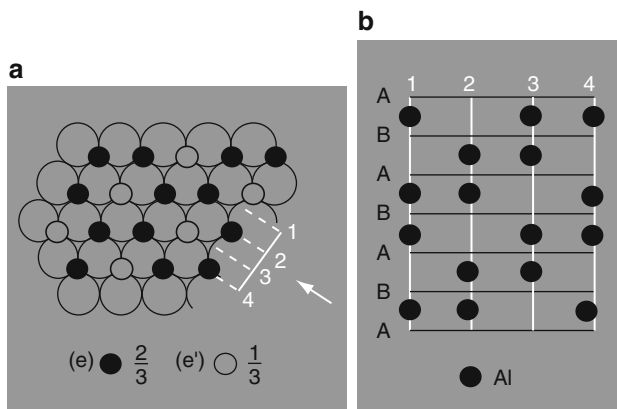

Figure 2.61. Representation of the structure of α-alumina (corundum). (a) Al^{3+} ions (filled circle) are shown to occupy the octahedral sites between the hcp layers of O^{2-} ions (open circle). (b) The stacking sequence of Al^{3+} ions as viewed in the direction of the arrow in (a). Reprinted from Greenwood, N. N.; Earnshaw, A. *Chemistry of the Elements*, 2nd ed., Copyright 1998, with permission from Elsevier.

Figure 2.62. Top: Energy splitting diagram for an octahedral Cr^{3+} ion in the ruby lattice. Bottom: The Tanabe-Saguno diagram for a d^3 transition metal (the parity subscript g has been omitted from the term symbols for clarity) along with an illustration of the transitions responsible for the absorption and luminescence of Cr^{3+} in ruby. Reproduced from Atkins, P. et al. *Inorganic Chemistry*, 4th ed., W. H. Freeman: New York, 2006.

the metal and ligand electrons for an octahedral Cr^{3+} complex. Since the d_{z2} and d_{x2-y2} orbitals are located directly along the internuclear bond axes, a greater electrostatic repulsion will occur resulting in an increase in energy. The energy gap between the two sets of d-orbitals is designated as 10 Dq or Δ_o (o = octahedral complex; Δ_t refers to a tetrahedral complex, *etc.*). Visible light is capable of being absorbed by the complex, causing the excitation of electrons into empty d_{z2} or d_{x2-y2} orbitals. As you are well aware, the color we observe will be the reflected, or complementary, color of that being absorbed. For instance, absorbed wavelengths in the 490–560 nm regime (green) will appear red, whereas absorption of 560–580 nm (yellow) radiation will appear blue/violet, and so on.

Figure 2.62 also illustrates the Tanabe-Saguno diagram for the d^3 Cr^{3+} ion of ruby, showing the ground state molecular term symbol as $^4A_{2g}$ (g = gerade, since an octahedral ligand field has a center of symmetry), with two spin-allowed transitions to $^4T_{2g}$ (green, 550 nm) and $^4T_{1g}$ (blue, 420 nm); the transition from $^4A_{2g} \rightarrow {}^2E_g$ is spin-forbidden.[52] It should be noted that the Laporte selection rule disfavors electronic transitions between the ground $^4A_{2g}$ and excited ^4T states since they both exhibit even parity. However, the absorption of energy and electronic excitation occurs because Cr^{3+} doping distorts the perfect octahedral environment of the corundum host, mixing in states of odd parity. Rather than simple relaxation back to the ground state and accompanying fluorescent emission, there is a fast (10^7 s^{-1}) *intersystem crossing* (ISC) into the metastable doublet state, ^2E_g. Even though this non-radiative decay process[53] is spin-forbidden, it is driven by *spin-orbit coupling*, which becomes more pronounced with increasing nuclear charge (*i.e.*, Z^4). Since the transition from the ^2E_g intermediate state to the ground state is also spin-forbidden, the electrons experience a finite lifetime in the doublet intermediate state before relaxing to the ground state, with emission of red light (λ = 694 nm). The relatively long lifetime of an excited state (*ca.* 3 ms for ruby) is characteristic of *phosphorescence*, relative to *fluorescence* in which electrons exhibit fast relaxation (*ca.* 5 ps–20 ns) from excited to ground states.

Interestingly, if Cr^{3+} is substituted for Al^{3+} in the *beryl* ($Be_2Al_2Si_6O_{18}$, Figure 2.63) base lattice of *emerald* gemstones, the crystal appears green rather than red. Since the coordination spheres about the Cr^{3+} centers for both ruby and emerald are distorted octahedra, the shift in the absorption wavelength must result from the lattice structure. In the beryl lattice, the Be^{2+} ions pull electron density away from the oxygen ions, which will cause less electron–electron repulsions between the Cr^{3+} d-orbitals and lone pairs of the oxygen ligands. This will correspond to a decrease in the Δ_o value, the absorption of lower-energy wavelengths, and a shift of the reflected color from red to green. It should be noted that red phosphorescence is also present in emerald; however, this is outweighed by the strong yellow/red absorption that yields the familiar green color.

Not only does the observed color depend on the nature of the transition metal impurity, but on the oxidation state of the dopant. For instance, the color of a beryl-based crystal changes from blue to yellow, upon doping with Fe^{2+} and Fe^{3+} (Aquamarine and Heliodor), respectively. For Mn^{2+} and Mn^{3+} impurities

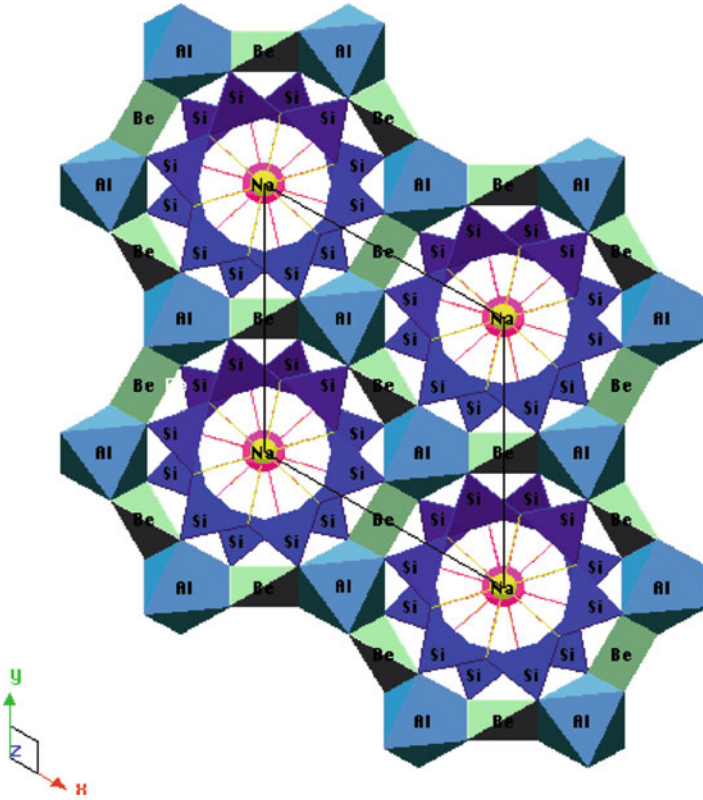*Figure 2.63.* Crystal structure of the beryl lattice, showing the location of Al octahedra. Reproduced with permission from http://www.seismo.berkeley.edu/~jill/wisc/Lect9.html.

(Morganite and Red Beryl), the color changes from pink to red, respectively. As a general rule, as the oxidation state of the transition metal ion increases, the ligand ions are drawn in closer to the metal center. This will result in more electron–electron repulsions between the metal and ligand, and a larger Δ_o. The increase in the energy gap between d-orbitals causes the absorption of higher energy wavelengths, and a corresponding red shift for the observed/transmitted color. As you might expect, it should be possible to change the color of such a crystal through heating in an oxidizing or reducing environment. This is precisely the operating principle of "mood rings" that respond to differences in body temperature. The color change resulting from a temperature fluctuation is referred to as *thermochromism*. When the application of an external pressure causes a color change, the term *piezochromism* is used.

Another factor that must be mentioned relative to our discussion of color is the wavelength of light used to irradiate the crystal. Alexandrite, Cr^{3+}-doped chysoberyl ($BeAl_2O_4$), has two equivalent transmission windows at the red and blue-green
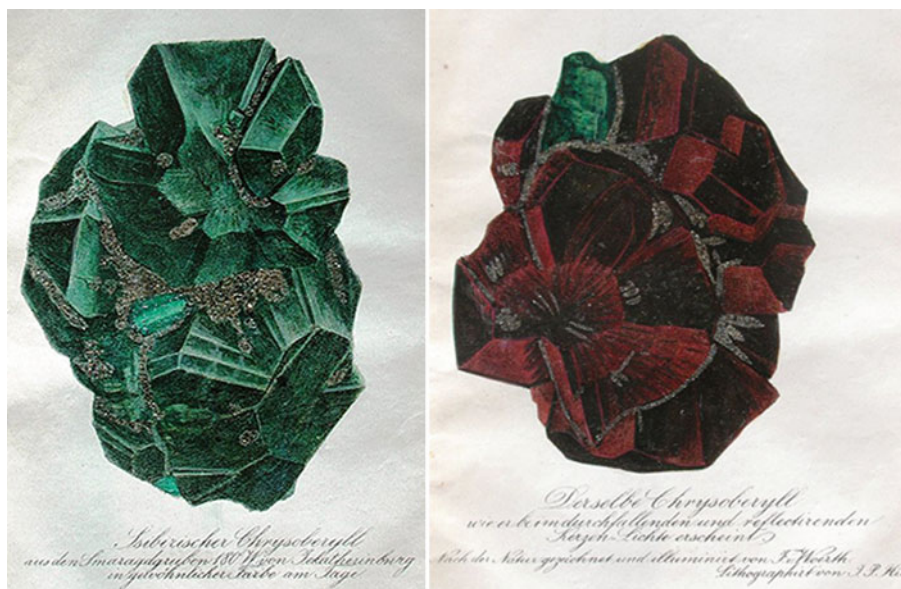
Figure 2.64. Photographs of chrysoberyl/alexandrite in daylight (left) and under incandescent light (right). Images taken from http://www.nordskip.com/alexandrite.html.

regions. As illustrated in Figure 2.64, alexandrite appears brilliantly red upon exposure to incandescent lamplight (reddish) and bright green upon exposure to sunlight or fluorescent light (greenish). Exposure to white light will also yield a purple color (blue + red), depending on the viewing angle and illumination source. The dramatic color intensity is due to the internal reflection of the incident light from the multifaceted crystal faces. Interestingly, in addition to its use as an expensive decorative gemstone, alexandrite may also be employed as a tunable solid-state laser, with $\lambda_{laser} = 750 \pm 50$ nm.[54]

Thus far, we have only considered the colors responsible for doping a crystal with one type of metal ion. However, crystals such as blue sapphire contain two metal dopants that yield the desirable deep blue color due to charge-transfer effects. If two adjacent Al^{3+} sites in alumina are replaced with Fe^{2+} and Ti^{4+}, an internal redox reaction may occur, where the iron is oxidized and the titanium is reduced (Eq. 34):

$$(34) \qquad Fe^{2+} + Ti^{4+} \rightarrow Fe^{3+} + Ti^{3+}$$
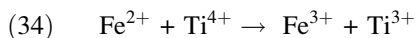
As this process requires energy corresponding to orange/yellow wavelengths of visible light, the complementary color of blue is reflected. Although blue sapphire is an example of heteronuclear charge transfer involving two different transition metal ions, there are also precedents for homonuclear charge transfers involving two oxidation states of the same metal (*e.g.*, Fe^{2+} and Fe^{3+} in magnetite, Fe_3O_4). Lastly, it should be noted that charge transfer may also occur between the

metal and ligands. For instance, the blue color of the gemstone lapis lazuli (*i.e.*, $(Na, Ca)_8(Al, Si)_{12}O_{24}(S, SO_4)$), is due to ligand-metal charge transfer (LMCT) initiating from the sulfur atoms in the ligand.[55]

Properties resulting from crystal anisotropy

Crystals are classified as being either *isotropic* or *anisotropic* depending on the equivalency of their crystallographic axes. All crystals that do not belong to the cubic crystal system possess anisotropic symmetry. Since electromagnetic radiation partially comprises an electrical component, the velocity of light passing through a material is partially dependent upon the electrical conductivity of the material. The relative speed at which electrical signals travel through a material varies with the type of signal and its interaction with the electronic structure of the solid, referred to as its *dielectric constant* (ε or κ).

   Anisotropic crystals are composed of a complex crystal lattice orientation that has varying electrical properties depending upon the direction of the impinging light ray. As a result, the refractive index will vary with direction when light passes through an anisotropic crystal, giving rise to direction-specific trajectories and velocities. This effect is most easily observed in crystals when there are large differences in the refractive indices of the crystallographic axes. This phenomenon is referred to as *birefringence* and is illustrated by the double refraction exhibited by optical calcite shown in Figure 2.65. Examples of the two distinct refractive indices for representative crystals are calcite (1.6584 and 1.4864), tourmaline (1.669 and 1.638), and rutile (2.616 and 2.903). The birefringence exhibited by a crystal is dependant on the difference in the refractive indices experienced by the extraordinary and ordinary rays as they propagate through a crystal.

   If birefringence occurs in a colored crystal, the observed color is often dependent on the viewing angle, as already discussed above for alexandrite. This phenomenon is known as *pleochroism*, and is caused by the incident light beam following different paths within the crystal, with each path absorbing different colors of light. Whereas tetragonal, trigonal, and hexagonal crystals often show two colors (*dichroic*, Figure 2.66a), orthorhombic, monoclinic, and triclinic crystals may
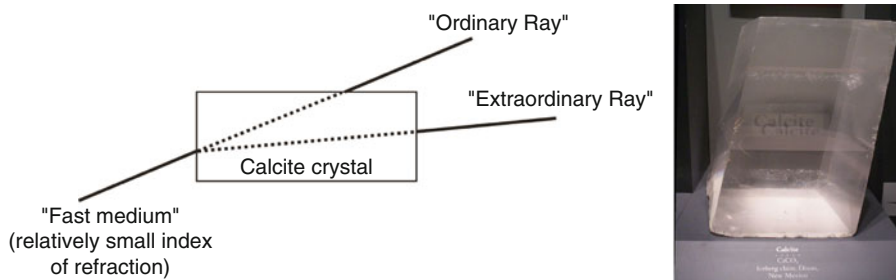

Figure 2.65. Illustration of the double refraction phenomenon exhibited by calcite crystals.

Figure 2.66. Dichroscope images of (a) dichroism exhibited by tourmaline; (b) trichroism exhibited by iolite. Images taken from http://www.nordskip.com/pleochroism.html.[56]

display three colors (*trichroic*, Figure 2.66b). It should be noted that cubic crystals do not exhibit pleochroism, since all unit cell axes are equivalent.

Crystals that do not possess a center of symmetry (*i.e.*, noncentrosymmetric) exhibit interesting properties when exposed to pressure – a phenomenon known as *piezoelectricity*, from the Greek word *piezein* (to squeeze). As pressure is applied, the crystal changes shape slightly by the movement of ions. The ionic migration causes some of the positive and negative ions to move in opposite directions, causing a polarization of charge. Conversely, if a piezoelectric crystal is placed in an electric field, the ions move toward opposite electrodes, thereby changing the shape of the crystal. All noncentrosymmetric crystallographic point groups will exhibit piezoelectricity. It should be noted that 432 is also noncentrosymmetric, but does not exhibit piezoelectricity.

At a temperature greater than the Curie temperature, T_c, the lattice atoms can migrate and cancel the effects of an external stress. However, at $T < T_c$, the cubic perovskite crystal becomes tetragonal; therefore the central cation (*e.g.,* Ti^{4+} in $BaTiO_3$) becomes displaced, resulting in a net dipole moment and breaking the charge symmetry of the crystal. The magnitude of the piezoelectric effect is not trivial; for a 1 cm^3 quartz crystal exposed to a 2 kN (450 lb-force) external force will generate 12 kV!

Piezoelectricity is the operating principle of quartz watches. In these devices, a tiny crystal of quartz oscillates at a frequency of 32 kHz in response to an electrical charge generated from the battery. In general, the overall size and composition of a piezoelectric crystal will affect its oscillation frequency. Since quartz loses very little energy upon vibration, the integrated circuit (IC, see Chapter 4) within a watch is used to reduce the repeatable oscillations into electric pulses, which are displayed as hours, minutes, and seconds on the watch face. The loud pop one hears when the ignition button is pressed on a gas grill is the sound generated by a small spring-loaded hammer hitting a piezoelectric crystal, generating thousands of volts across the faces of the crystal – actually comparable to the voltage generated by an automotive spark plug! Room humidifiers also operate via the induction of *ca.* 2,000,000 vibrations/s of a piezoelectric crystal, which is strong enough to cause atomization of water molecules.

In a microphone, as one speaks, small changes in air pressure surrounding the piezoelectric crystal cause tiny structural distortions that generate a very small voltage. Upon amplification, these voltage changes are used to transmit sounds; this principle has also been exploited for SONAR applications ("SOund Navigation And Ranging"). The military has also investigated piezoelectric crystals mounted in the boots of soldiers, whereby simple walking/running would provide current to power electronic devices embedded in warfighter uniforms such as sensors, IR shields, artificial muscles, *etc*.

Natural crystals that exhibit piezoelectricity include quartz (point group: 32), Rochelle salt (potassium sodium tartrate; orthorhombic space group, 222), berlinite

(AlPO$_4$), cane sugar, topaz (Al$_2$SiO$_4$(F, OH)$_2$), tourmaline group minerals (Ca, K, Na)(Al, Fe, Li, Mn)$_3$(Al, Cr, Fe, V)$_6$(BO$_3$)$_3$(Si, Al, B)$_6$O$_{18}$(OH, F)$_4$, and even bone! Synthetic examples include perovskites (*e.g.*, BaTiO$_3$, PbTiO$_3$, Pb(Zr$_x$Ti$_{1-x}$)O$_3$ – PZT, KNbO$_3$, LiTaO$_3$, BiFeO$_3$) and polyvinylidene fluoride – PVDF. The latter structure is not crystalline, but is comprised of a polymeric array of intertwined chains that attract/repel one another when an electrical field is applied. This results in a much greater piezoelectric effect than quartz.

Other noncentrosymmetric crystals that alter their shape in response to changes in temperature are referred to as *pyroelectric*. These crystals are used in infrared detectors; as an intruder passes the detector, the body warmth raises the temperature of the crystal, resulting in a voltage that actuates the alarm. Even for such miniscule temperature changes of a thousandth of a degree, a voltage on the order of 15 mV may result, which is readily measured by electronic components. Crystals that exhibit this effect are BaTiO$_3$ (barium titanate), PbTi$_{1-x}$Zr$_x$O$_3$ (lead zirconate titanate, PZT), and PVDF (polyvinylidene fluoride). Of the 32 crystallographic point groups discussed earlier, 20 are piezoelectric and ten are pyroelectric (Table 2.12).

The pyroelectric crystal classes are denoted as *polar*, each possessing a spontaneous polarization that gives rise to a permanent dipole moment in their unit cells. If this dipole can be reversed by the application of an external electric field (generating a hysteresis loop), the crystal is referred to as *ferroelectric*. These crystals will exhibit a permanent polarization even in the absence of an applied electrical field. As an example, let us consider the pyroelectric crystal BaTiO$_3$. Above the Curie temperature (T_c) of 130°C, BaTiO$_3$ is cubic (recall Figure 2.27). Since the positions of the positive and negative charges balance one another, there is no net polarization. However, as the crystal is cooled to temperatures below T_c, the unit cell becomes distorted into a tetragonal array where the Ti^{4+} ion is moved from its central position. This yields a finite polarization vector, resulting in ferroelectricity. It should be noted that all ferroelectric crystals are *both* piezoelectric and pyroelectric, but the reverse is not necessarily true.

Table 2.12. Piezoelectric and Pyroelectric Crystal Systems

Crystal system	Crystallographic point group		
	Centrosymmetric	Non-centrosymmetric Piezoelectric	Non-centrosymmetric Pyroelectric
Triclinic	$\bar{1}$	1	1
Monoclinic	2/m	2, m	2, m
Orthorhombic	mmm	222, mm2	mm2
Tetragonal	4/m, 4/mmm	4, $\bar{4}$, 422, 4mm, 42m	4, 4mm
Trigonal	$\bar{3}$, $\bar{3}$m	3, 32, 3m	3, 3m
Hexagonal	6/m, 6/mmm	6, $\bar{6}$, 622, 6mm, 6m2	6, 6mm
Cubic	m$\bar{3}$, m$\bar{3}$m	23, $\bar{4}$3m	N/A

2.3.7. Bonding in Crystalline Solids: Introduction to Band Theory

Building on the concept of 'reciprocal space' and appreciation of some physical properties of crystals, we are now in a position to discuss how the bonding motif of a metallic or semiconductor crystal affects its electrical conductivity. Chemists are familiar with traditional molecular orbital diagrams that are comprised of linear combinations of atomic orbitals (L.C.A.O. – M.O. theory). For diatomic molecules, the overlap of two energetically-similar s-orbitals results in σ (bonding) and σ^* (antibonding) molecular orbitals. The overlap of p-orbitals may result in σ/σ^* (via overlap of p_z atomic orbitals), as well as π/π^* orbitals via p_x and p_y interactions. The overlap for metals containing d-orbitals is more complex, which gives rise to σ, π and δ bonding/antibonding molecular orbitals (Figure 2.67).

A key concept in LCAO-MO bonding theory is the formation of the same number of molecular orbitals as the number of atomic orbitals that are combined (*e.g.*, there are 12 M.O.s formed when 4s and 3d atomic orbitals combine in the Ti_2 molecule, see Figure 2.68a). As the number of atoms increases to infinity within a crystal lattice, the $\Delta E \approx 0$ between energy levels within bonding and antibonding regions (Figure 2.68b). This is an application of the Pauli exclusion principle, which states for N electrons, there must be N/2 available states to house the electron density.[57]

The electron-occupied band is known as the *valence band*, whereas the unfilled band is referred to as the *conduction band*. The energy gap, if present, between these
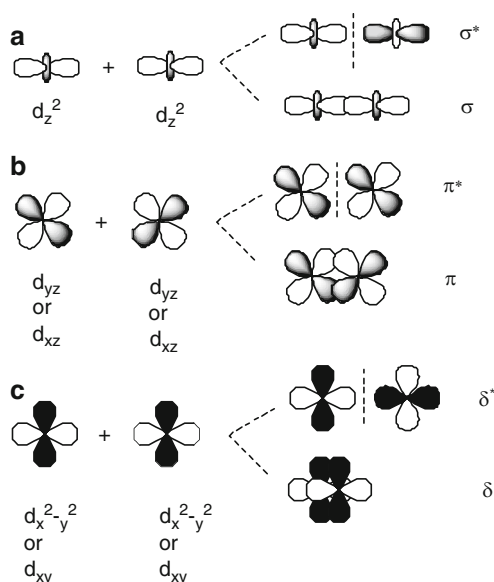
Figure 2.67. Illustration of d-orbital overlap between adjacent metal atoms in an extended metallic network.
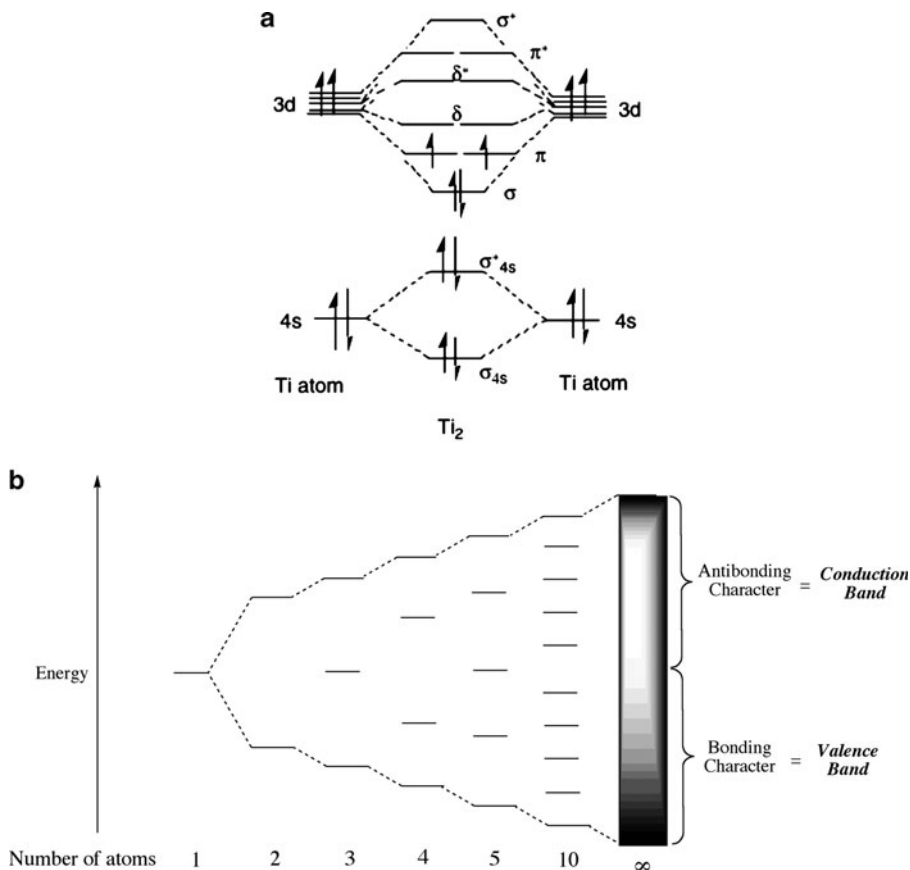
Figure 2.68. Molecular orbital (MO) diagram for the homonuclear diatomic molecule Ti$_2$ showing a discrete bandgap between filled and empty MOs. Also shown is the band diagram for a metallic solid, illustrating the continuum between valence and conduction bands (i.e., no bandgap) for increasingly larger numbers of atoms.

levels is known as the *band gap*, E$_g$ (Figure 2.69a). For metals with a partially-filled valence band (*e.g.*, Li, Na, Fe, *etc.*), or overlapping filled valence and empty conduction bands (*e.g.*, Mg, Ca, Zn, *etc.* – Figure 2.69b), there is no bandgap. Since electrical conductivity corresponds to promotion of electrons from valence to conduction bands, this corresponds to metals being conductive even at absolute zero. In contrast, the bandgaps for semiconductors and insulators are on the order of 190 kJ.mol^{-1} and > 290 kJ.mol^{-1}, respectively. Whereas semiconductors become conductive at elevated temperatures due to thermal promotion of electrons between valence and conduction bands, insulators remain non-conductive due to the overwhelming energy gap that must be overcome by valence electrons.
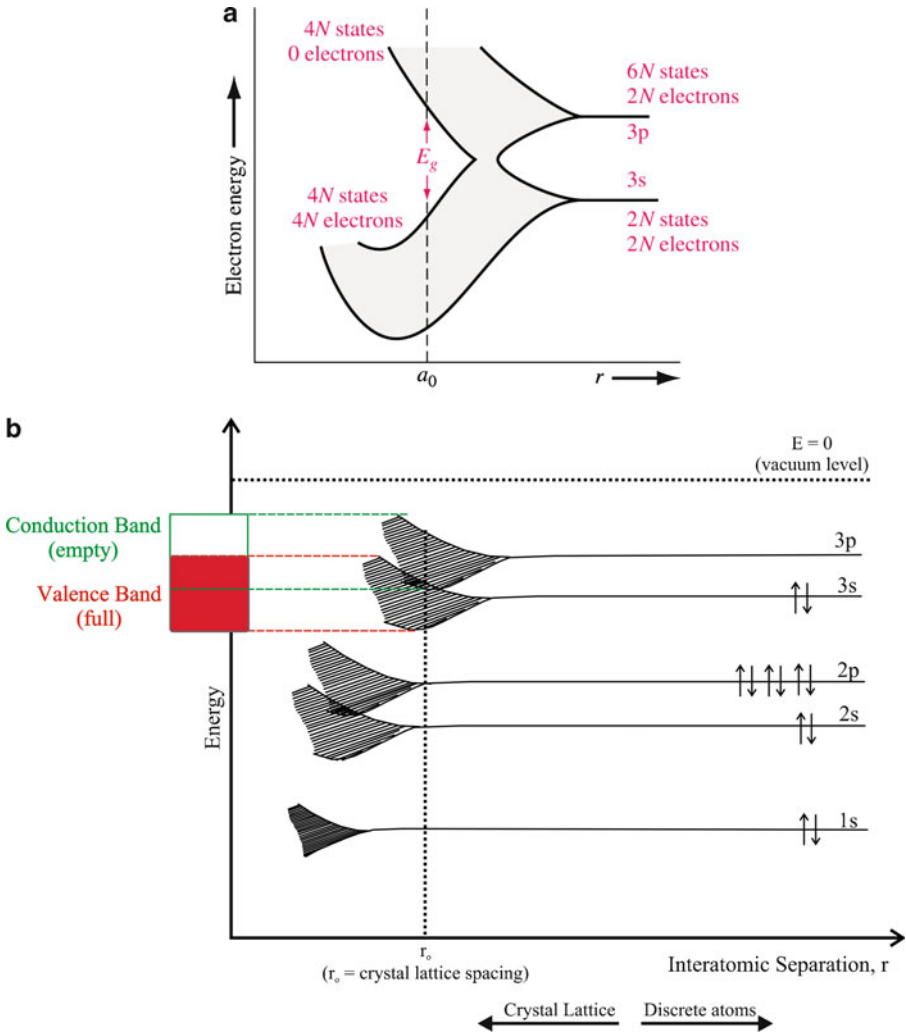
Figure 2.69. Top: The splitting of 3s and 3p atomic orbitals of Si_x into bands, showing the presence of a bandgap at the equilibrium bond distance, a_o. Reproduced with permission from Neamen, D. A. *Semiconductor Physics and Devices*, 3rd ed., McGraw-Hill: New York, 2003. Copyright 2003 McGraw-Hill. Bottom: The band diagram for Mg metal, showing the formation of valence/conduction bands and zero bandgap through overlap of 3s/3p atomic orbitals on neighboring Mg atoms.

At extremely high temperatures, electrons may be removed entirely from the crystalline lattice, referred to as *thermionic emission*. The minimum energy required to remove an electron from the Fermi level to the vacuum level (a position outside of the solid – Figure 2.69b) is referred to as its *work function*,[58] and varies depending on the composition and crystallographic orientation of the solid. For instance, some

representative work functions for metals and semiconductors are Li: 2.93 eV, Na: 2.36 eV, Al: 4.1 eV, Ag(110): 4.64 eV, Ag(111): 4.74 eV, W: 4.35 eV, Si: 4.7 eV, Ge: 5 eV.

At absolute zero, the highest occupied energy level is referred to as the *Fermi level* (in 3-D: Fermi surface), derived from Fermi-Dirac statistics.[59] The Fermi-Dirac distribution function, *f(E)*, describes the probability that a given available energy state will be occupied at a given temperature:

(35) $f(E) = \dfrac{1}{e^{(E-E_F)/kT} + 1}$

where: k = Boltzmann's constant (1.38×10^{-23} J/K)
       E = available energy state
       E_F = Fermi level

At absolute zero, electrons will fill up all available energy states below a level called the *Fermi level*, E_F. At low temperatures, all energy states below the Fermi level will have a electron occupation probability of one, and those above E_F will essentially be zero. However, at elevated temperatures, the probability of having electron density in energy levels above E_F increases (Figure 2.70).

In metals, the position of the Fermi level provides information regarding the thermal motion of conduction electrons, known as *electron velocity* v, through the extended crystal lattice (Eq. 36; m_e = electron mass: 9.1066×10^{-28} g). For instance, the Fermi energies for copper (7 eV) and gold (5.5 eV) correspond to velocities of 1.6×10^6 m/s and 1.4×10^6 m/s, respectively. However, it should be noted that the average speed of electron flow, known as the *drift velocity,* within electrical wires is much less, typically on the order of 100 µm/s (*i.e.,* 6 mm/min) for DC voltage – much slower than one would think![60]
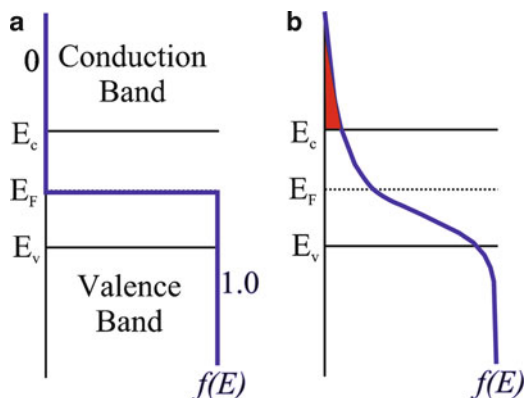
Figure 2.70. Schematic of the Fermi-Dirac probability function at 0 K (left), and at T > 0 K (right) showing the promotion of electron density from the valence to conduction bands.
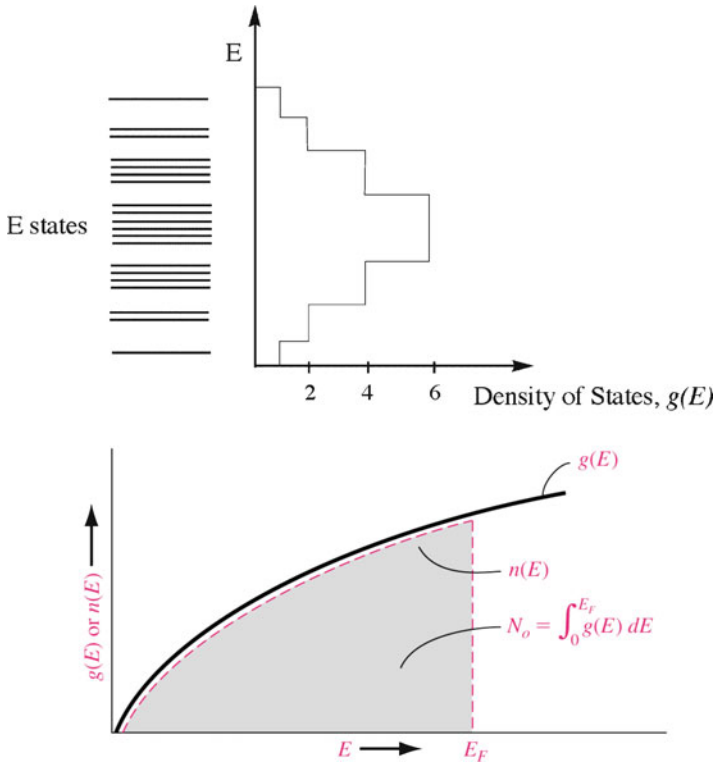
Figure 2.71. Top: Schematic of the density of states (DOS) – the number of available energy states per unit volume in an energy interval. Bottom: Density of states and electrons in a continuous energy system at T = 0 K. Reproduced with permission from Neamen, D. A. *Semiconductor Physics and Devices*, 3rd ed., McGraw-Hill: New York, 2003. Copyright 2003 McGraw-Hill.

$$(36) \qquad v = \sqrt{\frac{2E_F}{m_e}}$$

As one might imagine, though the Fermi function, $f(E)$, may predict a finite probability for electrons to populate the conduction band, there may not be available empty energy levels to accommodate the electrons. Hence, one must also consider the *density of states* (DOS), or the number of available energy states per unit volume in an energy interval (Figure 2.71). In order to determine the conduction electron population of a solid, one would simply multiply $f(E)$ by the density of states, $g(E)$. For a metal, the DOS starts at the bottom of the valence band and fills to the Fermi level; since the valence and conduction bands overlap, the Fermi level lies within the conduction band and there is electrical conductivity at 0 K (Figure 2.72a). In contrast, the DOS for conduction electrons in semiconductors begins at the top of the bandgap (Figure 2.72b), resulting in appreciable electrical conductivity only at
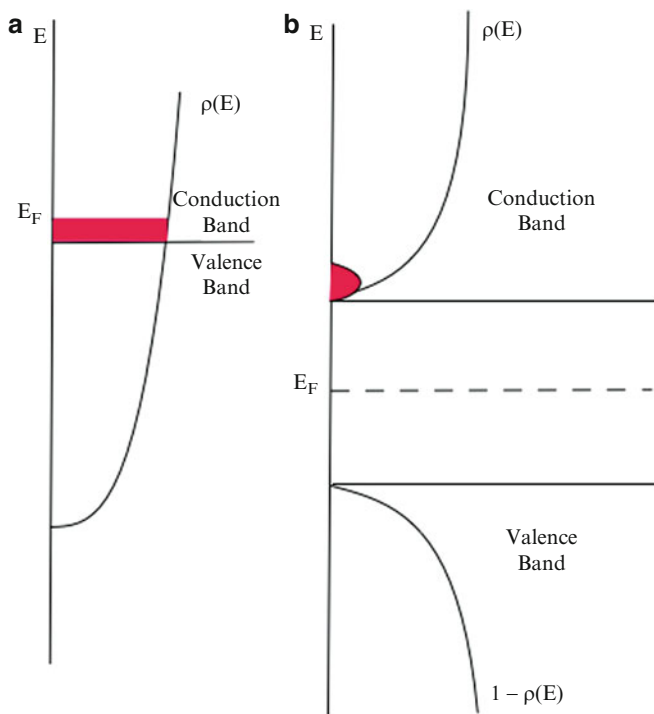
Figure 2.72. DOS and Fermi level, E_F, for a metal (a), and semiconductor (b)

elevated temperatures. It should be noted that although the Fermi level of metals is on the order of 2–11 eV, thermal energy (kT) is only 0.026 eV at 300K. Hence, only a tiny fraction of electrons ($<0.5\%$) that are positioned at energy levels within kT of the Fermi level may participate in electrical or thermal conductivity of the solid.

The origin of energy gaps in momentum space

The potential energy of an electron in a crystal lattice depends on its location, which will be periodic due to the regular array of lattice atoms. The periodic wavefunctions that result from solving the Schrödinger equation are referred to as *Bloch wavefunctions* (Eq. 37).[61]

$$(37) \quad \psi_k(r) = Ae^{ik \bullet r},$$

where: A = amplitude; a function that describes the periodicity of the real lattice, described by $\mathbf{r} = h\mathbf{u} + k\mathbf{v} + l\mathbf{w}$ – *i.e.,* see Eq. 11.

Once the electron is confined to a periodic lattice, certain values of $\mathbf{k}$ will cause the electron waves to be diffracted from lattice atoms, preventing the electron wave from propagating through the solid. For simplicity, let's consider an electron traversing from left to right through a linear array of atoms, of lattice constant *a*.
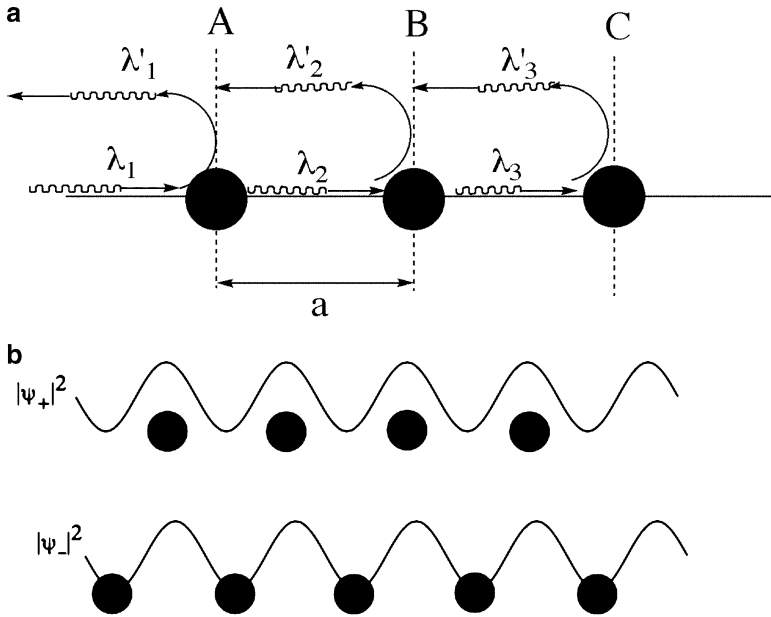
Figure 2.73. Illustration of electron wave propagation through a linear array of atoms, showing the constructive interference of forward/reverse wavefronts to form standing waves.

As the electron interacts with each atom, partial reflection will occur (Figure 2.73a). When these reflected electron waves interfere constructively, a traveling wave is produced that moves in the opposite direction (right-left). As we have seen from Bragg's Law, constructive interference will only take place when the path difference between two waves (2a in this 1-D array example) is equal to nλ. Substituting Eq. 23, we arrive at:

$$(38) \qquad |k| = \frac{\pm n\pi}{a}$$

Whenever Eq. 38 is satisfied, traveling electron waves cannot propagate through the crystal. That is, the Bragg-reflected waves traveling in opposite directions will give rise to *standing waves* at each lattice point, exhibiting no lateral motion:

$$\psi_+ = e^{i\pi\frac{x}{a}} + e^{-i\pi\frac{x}{a}} = A_+ \cos\left(\frac{n\pi x}{a}\right)$$

$$(39)$$

$$\psi_- = e^{i\pi\frac{x}{a}} - e^{-i\pi\frac{x}{a}} = A_- \cos\left(\frac{n\pi x}{a}\right)$$

The maximum of the probability functions, $\left|\psi_{+/-}\right|^2$, reside either directly upon the lattice atoms, or between the atoms (Figure 2.73b). As negatively-charged electrons

approach the positively-charged nuclei of the lattice atoms, their electrostatic potential energy will decrease by $e^2/4\pi\varepsilon_o r$. Hence, the energy of an electron in ψ_+ will be lower than an electron in ψ_-, or $E_+ < E_-$

$$E_+ = \frac{(\hbar k)^2}{2m_e} - V_n$$

(40)

$$E_- = \frac{(\hbar k)^2}{2m_e} + V_n$$

The first terms of Eq. 40 correspond to the energy of a free electron as a traveling wave (*i.e.*, away from $k = \pm n\pi/a$), obtained from solving the familiar "particle in a box" problem. The term V_n corresponds to the electrostatic potential energy resulting from electron-nuclei interactions. As one can see from Figure 2.74, the E *vs.* **k** plot for an electron wave in the 1-D lattice will result in a parabolic increase in energy with **k** until $k = \pm \pi/a$ is reached, at which point a sharp discontinuity is found. Another parabolic increase in energy is then followed until $k = \pm 2\pi/a$ is reached, and so on.

The range of **k**-values between $-\pi/a < k < \pi/a$ is known as the first *Brillouin zone* (BZ). The first BZ is also defined as the *Wigner-Seitz primitive cell* of the reciprocal lattice, whose construction is illustrated in Figure 2.75. First, an arbitrary point in the reciprocal lattice is chosen and vectors are drawn to all nearest-neighbor points. Perpendicular bisector lines are then drawn to each of these vectors; the enclosed area corresponds to the primitive unit cell, which is also referred to as the first *Brillouin zone*.

Extending the number of reciprocal lattice vectors and perpendicular bisectors results in the 2nd, 3rd, ..., nth BZs, which become increasingly less useful to
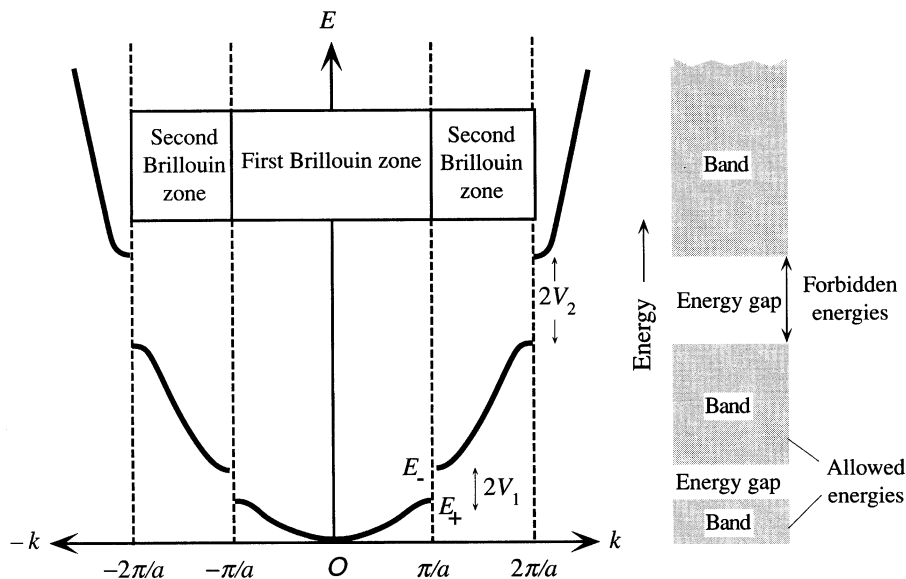
Figure 2.74. The energy of an electron as a function of its wavevector, **k**, inside a 1-D crystal, showing energy discontinuities at $k = \pm n\pi/a$. Reproduced with permission from Kasap, S. O. *Principles of Electronic Materials and Devices*, 3rd ed., McGraw-Hill: New York, 2006.
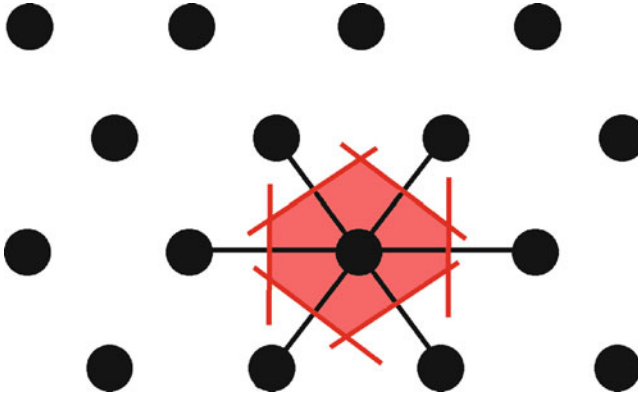
Figure 2.75. The Wigner-Seitz construction of a primitive unit cell for a 2-D lattice.
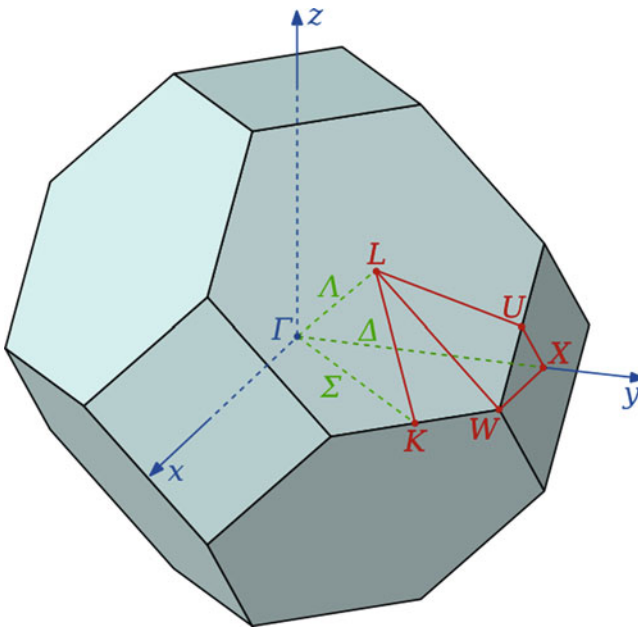

Figure 2.76. The first Brillouin zone of a fcc lattice, showing symmetry labels for high-symmetry lines and points.

describe the electronic properties of crystalline solids. The BZ boundaries identify where energy gaps occur along the **k**-axis. These are due to the finite lattice potential that alters the energy-state continuum of the free-electron model to one in which there are regions that have no energy states at all. It should be noted that for 3-D arrays, the BZs are complex polyhedra; Figure 2.76 illustrates the Brillouin zone for a fcc lattice, showing symmetry labels for relevant lines and points.

Figure 2.77 illustrates diffraction of an electron in a 2-D lattice, along with the E-**k** relationship. When $k_x = \pm\, n\pi/a$, the electron wave will be diffracted by

Figure 2.77. Diffraction of an electron in a 2-D crystal. Adapted with permission from Kasap, S. O. *Principles of Electronic Materials and Devices*, 3rd ed., McGraw-Hill: New York, 2006.
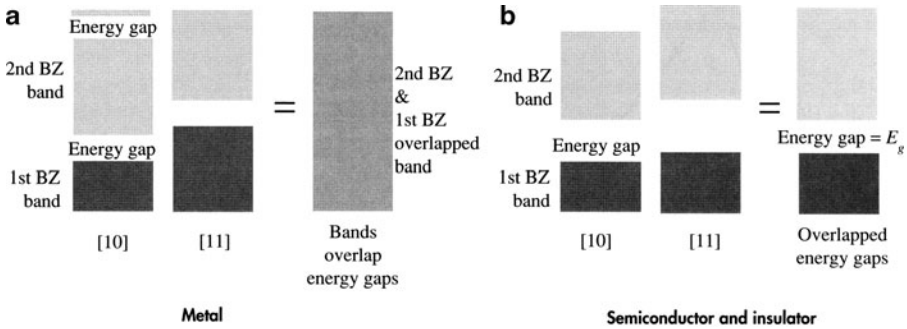
Figure 2.78. Comparison of 2-D bands for a metal and semiconductor, showing the overlap of Brillouin zones along [10] and [11] directions. Reproduced with permission from Kasap, S. O. *Principles of Electronic Materials and Devices*, 3rd ed., McGraw-Hill: New York, 2006.

the {10} planes. Conversely, when $k_y = \pm\, n\pi/b$, the electron will be diffracted by the {01} planes. The electron wave may also be diffracted from the {11} planes when:

$$(41) \qquad k_{xy} = \frac{\pm n\pi}{\sqrt{b^2 - \frac{a^2+b^2}{4}}}$$

The first energy gap along the [11] direction given by Eq. 41 will occur farther away than those in [10] or [01] directions. Hence, when considering the propagation of electrons through a crystal lattice, one must consider all possible directions since these will correspond to varying degrees of electron wave diffraction. In the case of a metal, there will be overlap between the 1st and 2nd BZ in [01] or [10] directions with those in the [11] direction (Figure 2.78a). However, for an insulator or semiconductor, the BZs do not overlap, resulting in a bandgap, E_g (Figure 2.78b); the 1st and 2nd Brillouin zones are thus referred to as valence and conduction bands, respectively. Qualitatively, one can say that in a metal the electron may populate any energy level by simply varying its direction, whereas there exist finite energy levels in a semiconductor/insulator that are forbidden to house electrons. We will consider a variety of E-**k** diagrams for 3-D lattices in Chapters 4 and 6, when we describe the conductivity of bulk semiconductors and nanomaterials, respectively.

2.4. THE AMORPHOUS STATE

Thus far, we have focused on solids that have a well-ordered crystalline structure. It is now time to turn our attention to some examples of amorphous solids. We already discussed the synthesis of amorphous metals; those obtained through fast nonequilibrium conditions. However, there is a more pervasive class of

materials that exhibits an amorphous structure, which our society is indebted to for countless applications: silica-based glasses. Further, although the majority of ceramic materials exhibit a crystalline structure, these materials are typically comprised of polycrystals alongside embedded amorphous structures. In fact, ceramics may also have amorphous structures when synthesized at low temperatures, with the conversion to crystalline phases as their temperature is increased, a process referred to as *sintering*, *firing*, or *annealing*. This results in the familiar properties of ceramics such as significant hardness and high melting point, desirable for structural applications or those occurring within extreme environments such as high temperatures and/or pressures. In this section, we will describe the structure and properties of some important classes of amorphous glasses, as well as partially-amorphous and/or polycrystalline ceramics and cementitious materials.

2.4.1. Sol-Gel Processing

The sol-gel (solution–gelation) process is a versatile solution-based process for making ceramic and glassy materials. In general, the sol-gel process involves the formation of a *sol* (colloidal suspension of *ca.* $\geq$ 200 nm solid particles) and subsequent crosslinking to form a viscous *gel*. Though this technique has been in practice since the 1930s, until only recently have the complex mechanisms involved in sol-gel been investigated.[62] The most common starting materials, or *precursors*, used in the preparation of the sol are water-sensitive metal alkoxide complexes, $M(OR)_x$, where R = alkyl group (*e.g.*, CH_3, C_2H_5, CF_3, *etc.*). Although original formulations used sodium silicates, the use of alkoxide precursors avoids undesirable salt byproducts that may only be removed through long, repetitive washing procedures. In addition, the nature of the metal and associated R groups may be altered to affect the rate and properties of the ultimate oxide material.

Sol-gel syntheses are typically carried out in the presence of polar solvents such as alcohol or water media, which facilitate the two primary reactions of *hydrolysis* and *condensation* (Eqs. 42 and 43, respectively). During the sol-gel process, the molecular weight of the oxide product continuously increases, eventually forming a highly viscous three-dimensional network (step-growth polymerization – Chapter 5).

(42) $M - OR + H_2O \rightarrow M - OH + ROH$

(43) $M - OR + M - OH \rightarrow [M - O - M]_n + ROH$
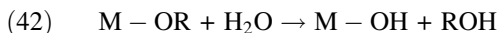
The most widely used metal alkoxides are $Si(OR)_4$ compounds, such as tetramethoxysilane (TMOS) and tetraethoxysilane (TEOS). However, other alkoxides of Al, Ti, and B are also commonly used in the sol-gel process, often mixed with TEOS. For instance, aluminum silicates may be generated through hydrolysis/condensation of siloxides (Eq. 44), which proceed through an intermediate Al–O–Al network known

as *alumoxanes*. Alumoxanes are important for applications in antiperspirants, catalysts, and paint additives. Their structure is best described as Al(O)(OH) particles with a core structure analogous to the minerals boehmite and diaspore (Figure 2.79), and organic substituents on the surface.

$$Al(OSiR_3)_3 + H_2O \rightarrow \left[Al(O)(OH)_x - (OSiR_3)_{1-x}\right]_{n \text{ (gel)}}$$

$$(44) \quad \xrightarrow{\Delta} (Al_2O_3)_m (SiO_2)_n$$
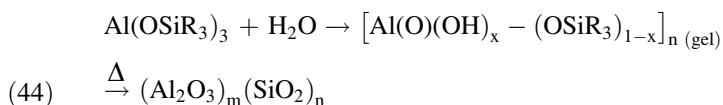
As one would expect from the similar electronegativities of Si and O, the hydrolysis of silicon alkoxides are significantly slower than other metal analogues. For identical metal coordination spheres and reaction conditions, the general order or reactivity for some common alkoxides is: $Si(OR)_4 \ll Sn(OR)_4 \sim Al(OR)_3 < Zr(OR)_4 < Ti(OR)_4$. That is, larger and more electropositive metals are more susceptible to nucleophilic attack by water. As a result, the hydrolysis of most metal alkoxides is too rapid, leading to uncontrolled precipitation. Although the ratio of $H_2O/M(OR)_n$ may be tuned to control the hydrolysis rate, the nature of the metal alkoxide (*e.g.*, altering the OR groups or metal coordination number) is the most powerful way to control the rate of hydrolysis. It is also possible to control the stepwise hydrolytic pathway, which governs the ultimate three-dimensional structure of the gel (Figure 2.80).

It should be noted that a sol-gel process may also take place through nonhydrolytic pathways. In these systems, a metal halide reacts with an oxygen donor such as ethers, alkoxides, *etc.* to yield a crosslinked metal oxide product (Eq. 45).

$$(45) \quad M - OR + MX \rightarrow [M - O - M]_n + RX$$
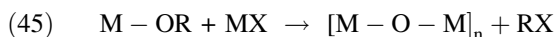
In stark contrast to other metal alkoxides, the kinetics for the hydrolysis of $Si(OR)_4$ compounds often require several days for completion. As a result, acid (*e.g.*, HCl, HF) or base (*e.g.*, KOH, amines, NH_3) catalysts are generally added to the mixture, which also greatly affects the physical properties of the final product. Under most conditions, condensation reactions begin while the hydrolytic processes are underway. However, altering the pH, $[H_2O/M(OR)_n]$ molar ratio, and catalyst may force the completion of hydrolysis prior to condensation.

A likely mechanism for an acid-catalyzed system is shown in Figure 2.81. The protonation of the alkoxide group causes electron density to be withdrawn from Si, allowing the nucleophilic attack from water. In contrast, the base-catalyzed hydrolysis of silicon alkoxides proceeds through the attack of a nucleophilic deprotonated silanol on a neutral silicic acid (Figure 2.82). In general, silicon oxide networks obtained via acid-catalyzed conditions consist of linear or randomly branched polymers; by contrast, base-catalyzed systems result in highly branched clusters (Figure 2.83).

As condensation reactions progress, the sol will set into a rigid gel. Since the reactions occur within a liquid alcoholic solvent, condensation reactions result in a three-dimensional oxide network $[M-O-M]_n$ that contains solvent molecules within
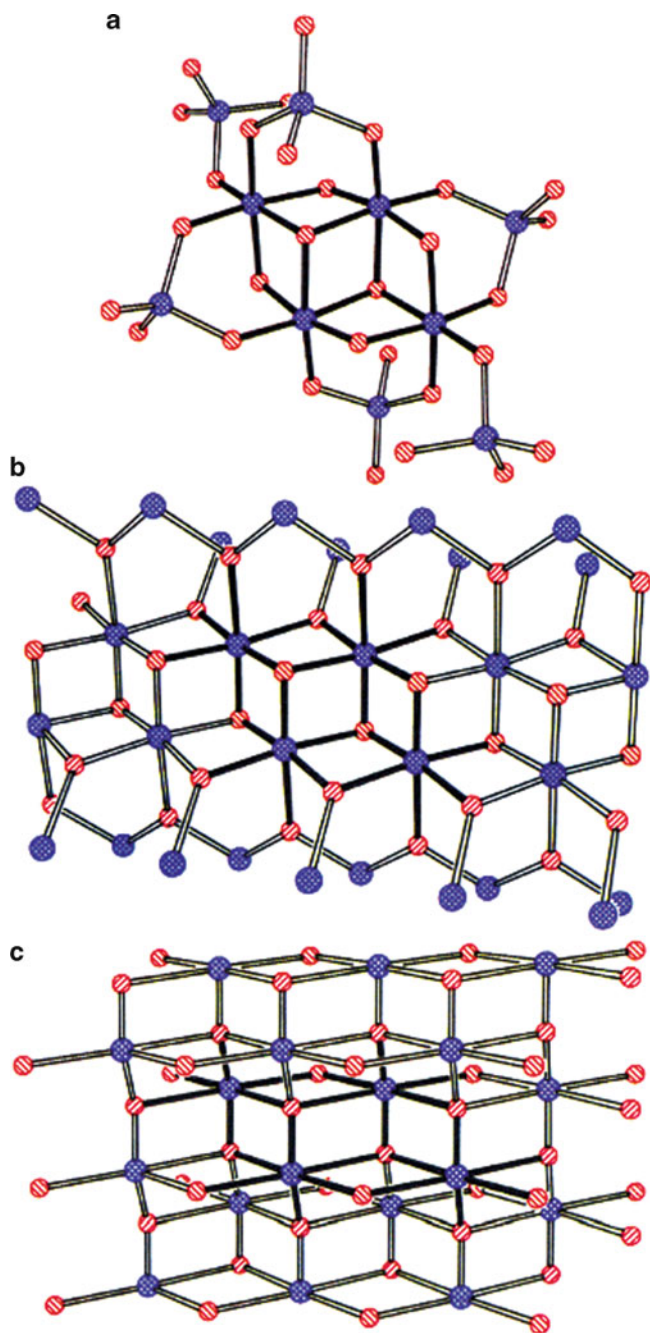
Figure 2.79. Comparison of the core structure of (a) siloxy- substituted alumoxane gels with (b) diaspore, and (c) boehmite minerals. The aluminum and oxygen atoms are shown in blue and red, respectively. Reproduced with permission from *Chem. Mater.* **1992**, 4, 167. Copyright 1992 American Chemical Society.
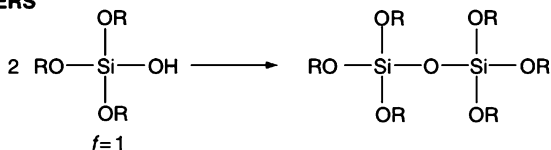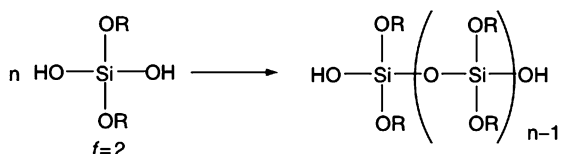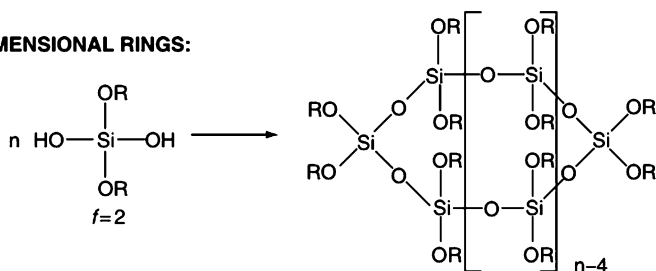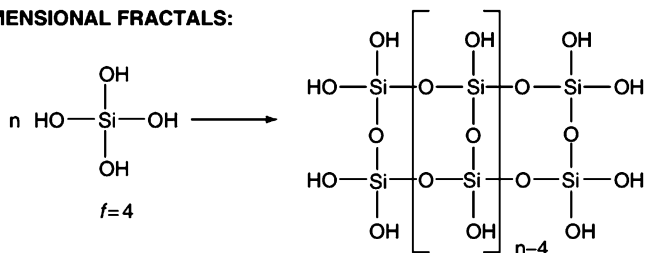
Figure 2.80. Relationship between a siloxy precursor and its control over the three-dimensional shape of a gel. Reproduced with permission from *Chem. Rev.* **2004**, 104, 3893. Copyright 2004 American Chemical Society.

its pores. The product at its gel point is often termed an *alcogel*, recognizing the trapped solvent. At this stage, the gel is typically removed from its original container, but remains saturated with the solvent to prevent damage to the gel through evaporation. It is worthwhile to note that at the gel point, the –O–Si–O– framework still contains a number of unreacted alkoxide moieties. Hence, sufficient time (typically 48 h+) must be allotted to allow for complete hydrolysis and polycondensation, so the network is suitably strengthened to prevent cracking – a process referred to as *aging*, or *syneresis*.
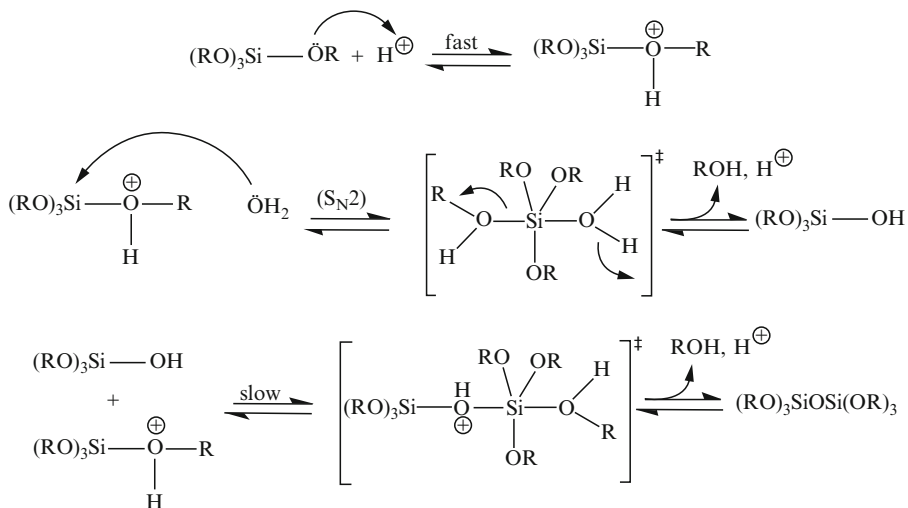
Figure 2.81. Reaction schemes for the acid-catalyzed hydrolysis and condensation of a silicon alkoxide precursor.
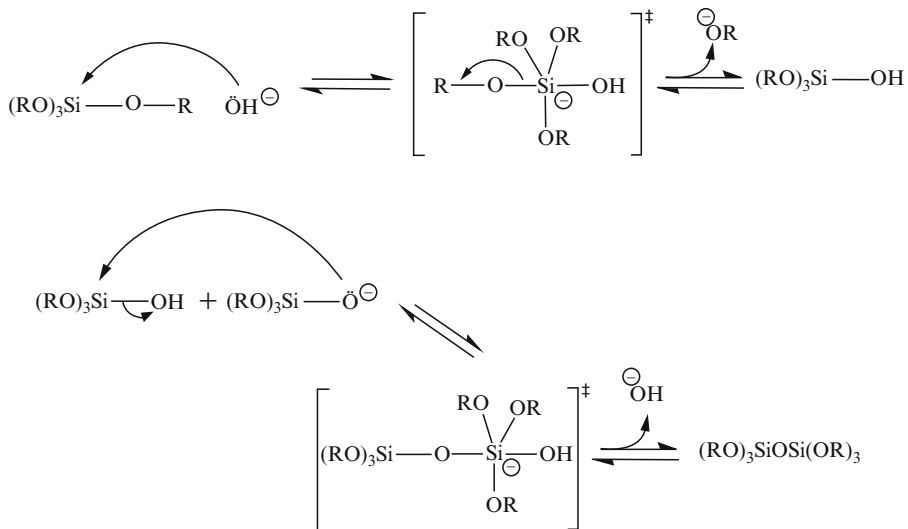

Figure 2.82. Reaction schemes for the base-catalyzed hydrolysis and condensation of a silicon alkoxide precursor.

Depending on the post-treatment used for the sol, a wide variety of materials may be synthesized: ultra-fine powders, thin film coatings, ceramic fibers, microporous inorganic membranes, ceramics and glasses, or extremely porous materials (Figure 2.84). Thin films are easily generated on a substrate through simple spincoating or
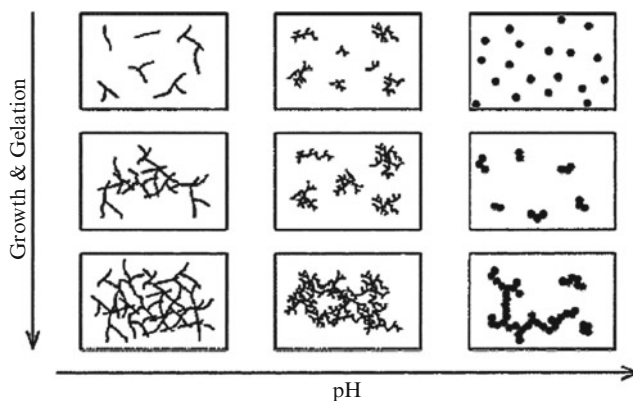
Figure 2.83. Comparison of the morphology with the pH of the sol-gel process. Reproduced with permission from *Chem. Rev.* **2004**, 104, 3893. Copyright 2004 American Chemical Society.

dip-coating of the gel, followed by slow evaporation to prevent extensive cracking. Alternatively, the gel may be retained in a mold and heat-treated to convert the material into a dense ceramic or glass. If the solvent of an alcogel is removed through slow evaporation, a porous material known as a *xerogel* is formed. By contrast, if supercritical CO_2[63] is used to remove the solvent, a highly foam-like, porous, transparent material called an *aerogel* is formed. Silica aerogels consist of 99.8% air, and have a density of 1.9 g L^{-1} and a thermal conductivity of 1.7 × 10^{-2} W m^{-1} K^{-1}. The properties of aerogels afford a range of applications, among which include sound dampening, catalysis, desiccation, and thermal insulating (*e.g.*, windows, refrigerators, walls).[64] Due to the complex, crosslinked structure of aerogels, the insulating ability is an order of magnitude greater than commonly used fiberglass. As a testament to the unique properties of silica aerogels, the Guinness Book of World Records recognizes this material as the best insulator and least-dense solid.

Aerogels retain the original shape and volume of the alcogel – typically > 85% of the original volume. By contrast, xerogels exhibit significant shrinking and cracking during drying, even under room-temperature conditions (Figure 2.85). It is important that the water be removed prior to the drying event. This is easily accomplished through soaking the alcogel in pure alcohol. The soaking time is dependent on the thickness of the gel. Any water left in the gel will not be removed by supercritical drying, and will lead to a dense, opaque aerogel. Similarly, water will not be removed as readily as alcohol by simple evaporation; hence, water-containing gels will result in heavily cracked and heterogeneous xerogels.

Inorganic gels are rarely used in their as-dried state. The gel is first dehydrated through thermal removal of surface –OH groups, thus preventing rehydration
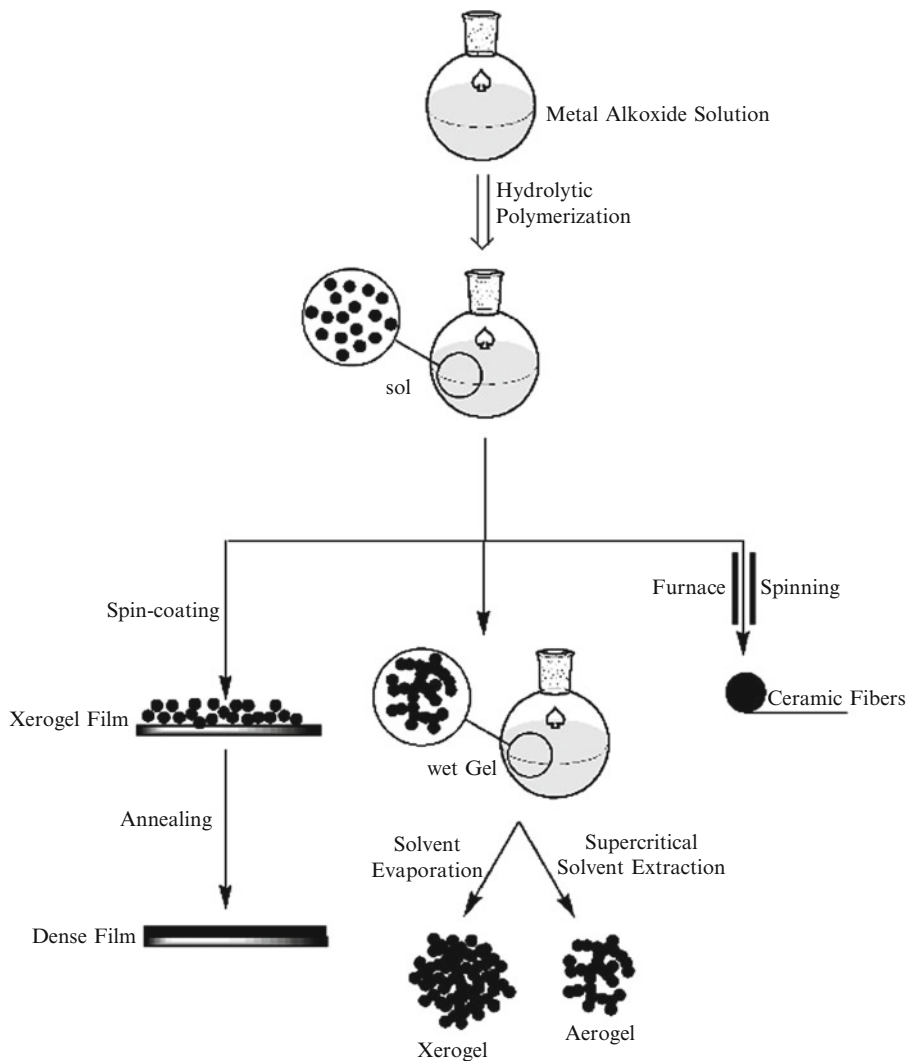
Figure 2.84. Illustration of the products obtained through sol-gel processing.

reactions. Most often, this step is followed by high-temperature annealing ($T > 800$ °C), in order to convert the amorphous material into a desired crystalline phase. As an example for alumoxanes, it has been shown that the gel is initially transformed to γ-Al$_2$O$_3$, *en route* to its highest crystalline form, α-Al$_2$O$_3$.[65] During the sintering (or firing) process, the pore size is also diminished and organic moieties are removed. Hence, this results in significantly better mechanical properties, as desired for dense ceramics and glasses.
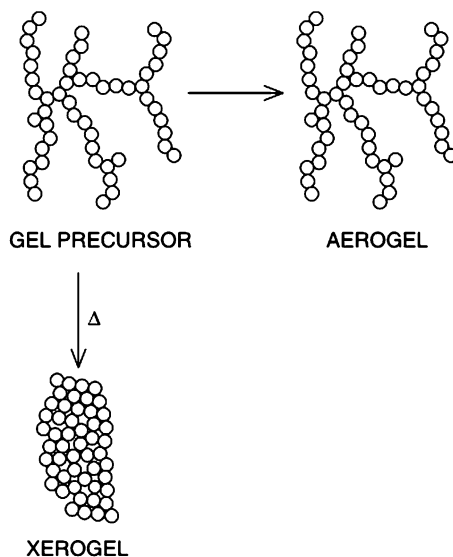
Figure 2.85. Comparison of the three-dimensional shape of an aerogel and xerogel formed from a gel. Reproduced with permission from *Chem. Rev.* **2004**, 104, 3893. Copyright 2004 American Chemical Society.

An extremely useful class of sol–gel synthesized porous materials is called *zeolites*. These materials are best described as hydrated aluminosilicate minerals that consist of interlocking SiO_4^{4-} and AlO_4^{5-} tetrahedra, of general formula $M_{x/n}[(AlO_2)_x (SiO_2)_y] \cdot zH_2O$ (M = cation of valence n). By definition, the (Si + Al)/O ratio in zeolites must equal 0.5, resulting in a negatively charged polyhedron structure. Therefore, other cations (*e.g.*, M = Na^+, K^+, Ca^{2+}, Mg^{2+}, *etc.*) must occupy the large spaces or cages of the zeolite structure in order to maintain overall charge neutrality. Though not immediately apparent from their general formulae, zeolites contain a number of reactive Brønsted acidic (*e.g.,* aluminol (–AlOH), silanol (–SiOH), and bridging Si–O(H)—Al groups), Lewis acidic (*e.g.,* framework Al^{3+} ions, charge-balancing cations), and Lewis basic (*e.g.,* framework oxygen) sites that have important consequences in catalytic reactions. In general, the number of Brønsted acid sites increases linearly with the charge density of the charge-balancing cation(s), due to a greater polarization of adsorbed water. Increasing strength of Lewis acidity is inversely proportional to the Si/Al ratio of the zeolite framework.

There are 48 naturally occurring zeolites (even found on Mars!), and more than 150 synthetic varieties (Figure 2.86).[66] The natural varieties are mostly used in applications such as concrete, soil treatment ("zeoponics" – *e.g.*, controlled release of fertilizer or nutrients such as K^+ or N_2), and even kitty litter that are not affected by their high levels of compositional and structural heterogeneity. However, synthetic zeolites possess a uniform and precise composition and structure, which
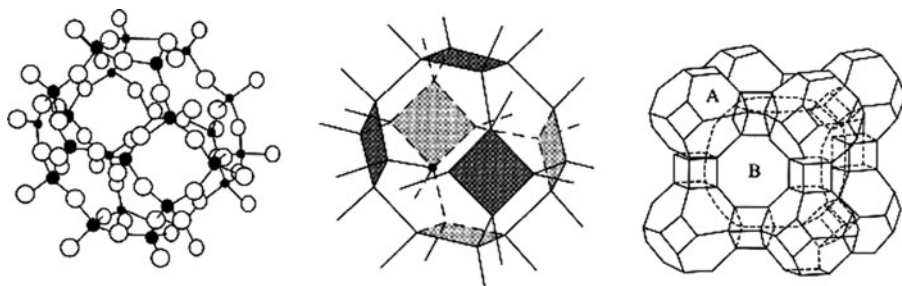
Figure 2.86. Representations of zeolite structures. Shown are molecular and crystal representations of a polyhedron (a) formed from 24 SiO$_4$ tetrahedra. Also shown is the three- dimensional array of LTA, Linde A: [Na$_{12}$(Al$_{12}$Si$_{12}$O$_{48}$)]·27H$_2$O formed from interlocking SiO$_4$ and AlO$_4$ polyhedra of (pore size, B: 4.1 Å). Reprinted from Greenwood, N. N.; Earnshaw, A. *Chemistry of the Elements*, 2nd ed., Copyright 1998, with permission from Elsevier.

is suited for applications such as catalysis, molecular sieves, photovoltaics, sensors, laundry detergents, and water purification. Both natural and synthetic zeolites are being explored for an intriguing adsorptive application as a blood clotting facilitator (*e.g.*, QuikClot™ and Hemosorb™). More recently, there is interest in exploiting zeolite thin films as low-dielectric constant (low-κ) materials for future computer chips and biocompatible/antifouling coatings for fuel cells and water desalination, to name only a few of the plethora of possible applications.[67]

The three-dimensional structure of zeolites is characterized by a complex system of interconnected channels, resulting in low density.[68] The structural rigidity and channel system of zeolites allow allows facile movement of ions and molecules into and out of the structure. Hence, zeolites are able to adsorb and desorb water without damage to the crystal structure, and ion-exchange takes place readily among the chelated cations. The pervasive use of zeolites in the petrochemical industry for oil refining and organic syntheses is related to their very high surface area and tunable hydrophobicity/hydrophilicity, which govern their adsorption capacity. Further, the tunable sizes and geometry of the channels and cavities provide efficient sequestering of guest molecules, facilitating shape-selectivity of catalytic reactions to increase the residence time of reactants and improve the overall yield/efficiency. Depending on the type of zeolite, the interior voidspaces may also be large enough to accommodate larger molecular species such as organic molecules, water, ammonia, and anions such as CO_3^{2-} and NO_3^{-}. By definition, *microporous* materials have pore diameters of less than 2 nm and *macroporous* materials have pore diameters >50 nm. *Mesoporous* materials have intermediate pore diameters of 2–50 nm, Whereas the earliest examples of zeolites featured pore sizes in the 2–15 Å, more recent precedents have been focused on mesoporous structures with pore sizes up to 200 Å (*e.g.,* M41S) that extend the range of applications for chemical syntheses, electronic arrays, and biomaterials.[69]

Zeolites are usually synthesized under *hydrothermal* conditions, from alkaline solutions of sodium aluminate and sodium silicate at temperatures between *ca.* 80–200°C (Figure 2.87).[70] The zeolitic structure that is formed will vary depending
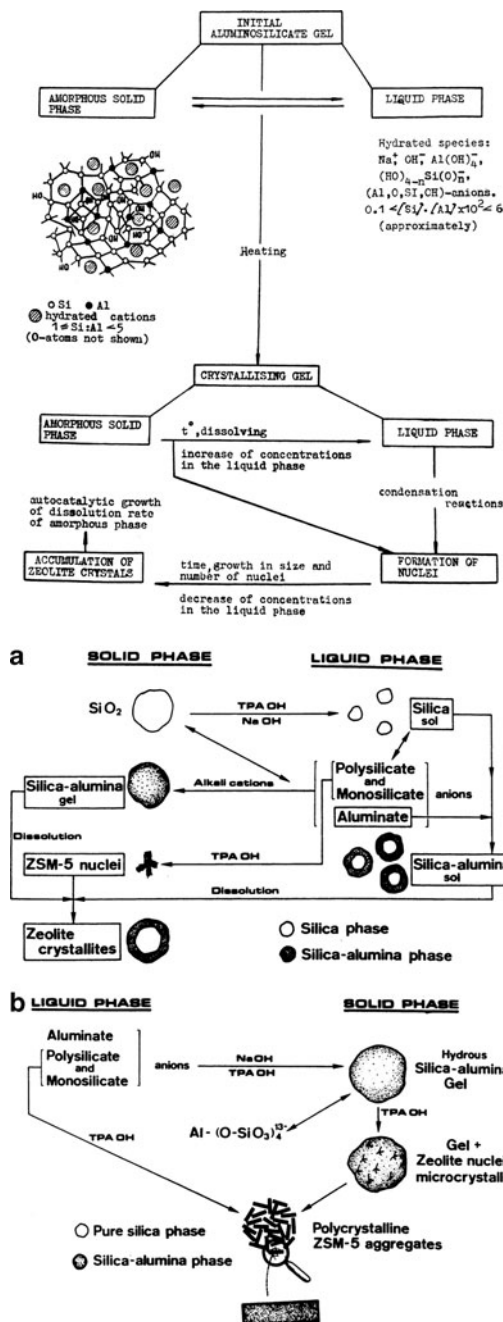
Figure 2.87. Top: Schematic of aluminosilica gel crystallization. Reproduced with permission from *ACS Adv. Chem. Ser.* **1971**, *101*, 20. Copyright 1971 American Chemical Society. Bottom: Two synthetic routes for ZSM-5 zeolites. Reproduced with permission from *ACS Symp. Ser.* **1984**, *248*, 219. Copyright 1984 American Chemical Society.
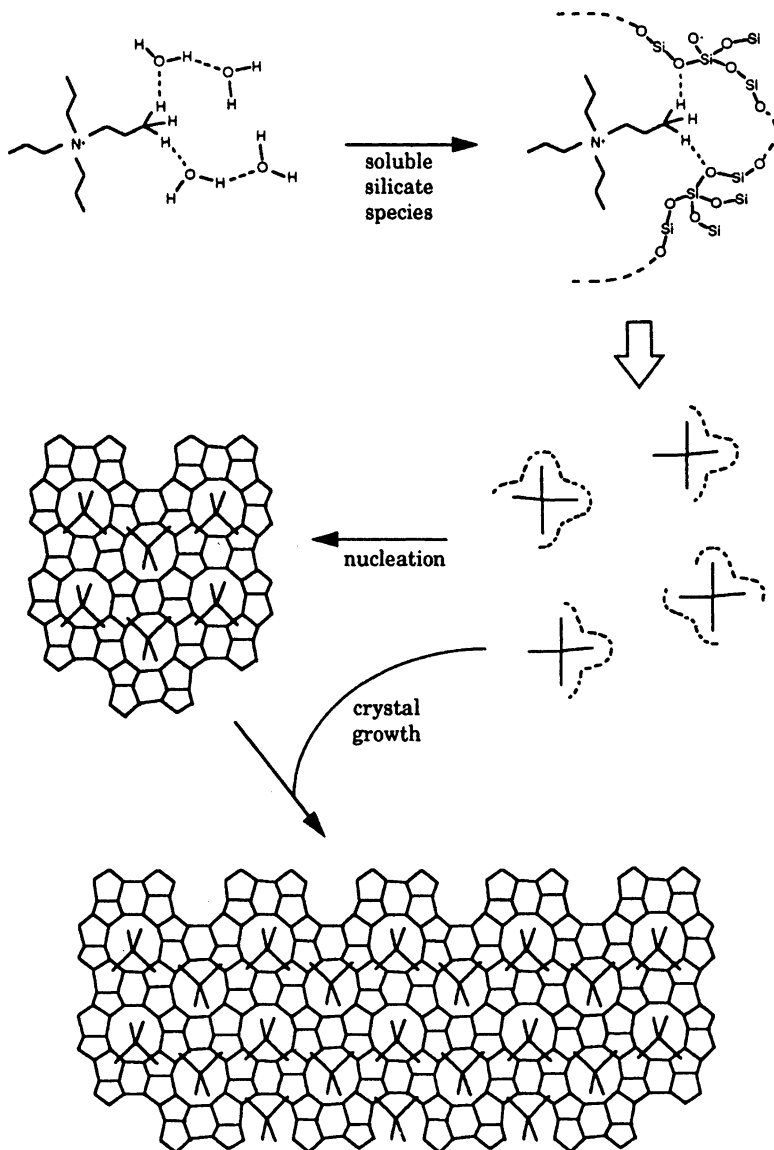
Figure 2.88. Mechanism of template-directed crystal growth for the synthesis of a zeolite. Reproduced with permission from *J. Phys. Chem.* **1994**, *98*, 4647. Copyright 1994 American Chemical Society.

on the reactants used and the experimental conditions (*i.e.*, temperature, time, and pH). Particularly important is the presence of a templating ion, which directs the 3-D structure of the aluminosilicate lattice (Figure 2.88). In alkaline media, an organic ammonium cation is used (*e.g.,* propylammonium); neutral framework zeolites such

as $AlPO_4$ require the use of amines rather than quaternary salts. Both require the removal of the organic template via calcination in order to yield open-pore zeolitic structures.

Synthesis may also be carried out at a lower pH using fluoride-containing media, wherein F^- ions are thought to act as structure directors via strong interactions with framework Si atoms. Consequently, the nucleation rate is decreased, which yields larger crystals relative to standard alkaline hydrothermal routes.[71] The fluoride route under neutral/acidic pH conditions is also extremely useful to synthesize zeolite-like materials called *zeotypes*, which contain elements other than silicon and aluminum (*e.g.*, titanosilicates, zirconosilicates, *etc.*).[72] Under alkaline conditions, the precursors would be preferentially precipitated as hydroxide species rather than ordered arrays.

2.4.2. Glasses

From drinking vessels and windows to eyeglass lenses, materials comprising glass have long played an important role in our society. In fact, it is estimated that applications for glass date back to Egypt in *ca*. 3,500 B.C. Though we are most familiar with transparent silica-based (SiO_2) glass (Figure 2.89), there are many other types of glass that may be fabricated for various applications. For instance, infrared-transmitting chalcogenide glasses such as As_2E_3 (E = S, Se, Te) are suitable for specialized applications such as optical storage, sensors, and infrared lasers. As we have already seen, even metals may be suitably synthesized to possess a bulk-disordered glassy structure. By definition, the term *glass* is actually not a specific material, but a general architectural type – an amorphous solid that has cooled to rigidity without crystallizing. Glasses are most commonly made by rapidly
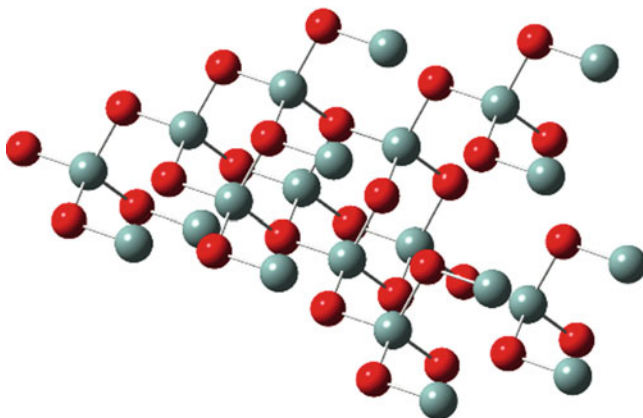

Figure 2.89. Molecular structure of amorphous SiO_2, comprising randomly corner-linked SiO_4 tetrahedra.

quenching a melt; accordingly, the constituent atoms are not allowed to migrate into regular crystalline lattice positions.[73]

It is noteworthy to point out why a material as disordered as glass is transparent. That is, one would think that the amorphous structure of glass should facilitate *opacity*, which is the extent to which visible radiation is blocked by the material it is passing through. There are two primary reasons for the transparency of glass – electronic and structural. First, as we will see shortly, glass may contain a variety of dopants that will afford particular colors (via electronic transitions) or physical properties (*e.g.,* enhanced hardness, thermal/electrical conductivity, reflectivity, *etc*.). However, these impurities are only present in sufficient quantity to cause only partial absorption of the electromagnetic spectrum, resulting in observable transparency – though less pronounced relative to undoped glass.

Second, unlike metals, glasses are held together by covalent/ionic bonding, and do not contain free electrons in their structure. Accordingly, the incident wave-lengths are not perturbed into destructive waves and are free to transmit through the material. Additionally, the degree of disorder within glasses is of the same order of magnitude as the incident radiation, allowing the light to pass through relatively unattenuated.[74] However, it should be noted that if glass contains imperfections, and/or inclusions of metals or larger particles with dimensions greater than the wavelength of indicent light, the material will become increasingly opaque due to *Rayleigh scattering* – Eq. 46.[75]

$$(46) \qquad scattering \; \alpha \; \frac{(\Delta\eta)(d^3)}{\lambda^4},$$

where $\Delta\eta$ is the change in the refractive index and d is the spatial distance covered by the disorder.

Glasses and ceramics are largely based on a covalently bound network that is comprised of an infinite array of silicate (SiO_4^{4-}) tetrahedra.[76] As shown in Figure 2.90, a variety of structures are possible by Si-O-Si linkages among adjacent tetrahedra. Since the silicate sub-units carry an overall -4 charge, alkali or alkaline earth metal ions are commonly present in order to afford charge neutrality, and link adjacent silicate tetrahedra via ionic bonding (Figure 2.91). In addition to random or crystalline 3-D structures, silicates may also assemble into chain-like arrays; for instance, the large family of hydrous magnesium silicates (*e.g.,* chrysotile, pyroxene, Figure 2.92a), better known as *asbestos*. Layered-sheet arrays are also well known, especially in combination with aluminum oxide such as aluminosilicate clays (Figure 2.92b). For these latter structures, there is only weak van der Waal attraction between adjacent layers, which governs their overall physical properties. For instance, talc ($Mg_3Si_4O_{10}(OH)_2$) is one of the softest minerals (Mohs hardness of 1) and may be used as a lubricant, due to facile slippage of neighboring layers.

The most straightforward method to make silica (SiO_2) glass, known as *fused silica* or *quartz glass*, is through melting sand at a temperature of 1,800–2,000°C followed by very slow cooling. Unlike other glasses, that require a rapid quenching event, quartz will automatically form a glassy solid at all but the slowest cooling
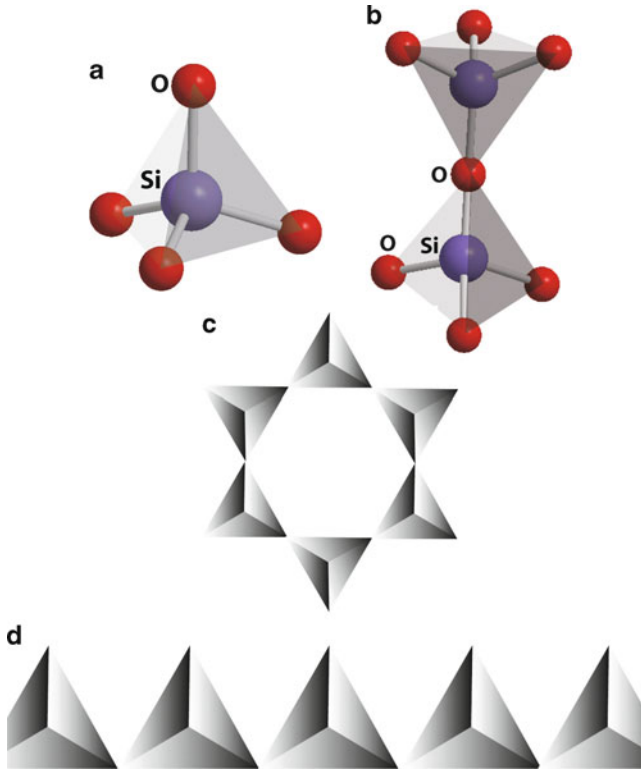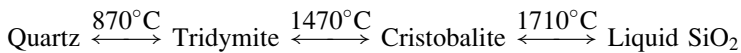
Figure 2.90. Molecular structures of common silicate anions. Shown are (a) SiO_4^{4-}, (b) $Si_2O_7^{6-}$, (c) $Si_6O_{18}^{12-}$, and (d) a chain metasilicate polymer $\{SiO_3^{2-}\}_\infty$.

rates – a consequence of its complex crystal structure (Figure 2.93). For example, it is estimated to have taken 100,000 years to form natural crystalline quartz! Actually, crystalline silica exists as three varieties, with each form having slightly differing crystal structures and physical properties[77]:

$$\text{Quartz} \xleftrightarrow{870°C} \text{Tridymite} \xleftrightarrow{1470°C} \text{Cristobalite} \xleftrightarrow{1710°C} \text{Liquid SiO}_2$$

Two methods commonly used to synthesize quartz are hydrothermal (autoclave at high temperature/pressure, containing water and seed crystals) and flux growth. For this latter technique, LiO, MoO, PbF_2 and silica powders are added to a crucible; the ionic compounds serve as a molten solvent to dissolve materials with a high melting point, facilitating crystallization at lower pressures/temperatures. Fused silica is thermally stable at temperatures up to *ca.* 1,665°C. Further, the coefficient of linear expansion is 5.5×10^{-7} cm cm^{-1} K^{-1}; by comparison, the softening point and coefficient of linear expansion for normal window pane glass are *ca.* 500°C and 9.0×10^{-6} cm cm^{-1} K^{-1}, respectively.
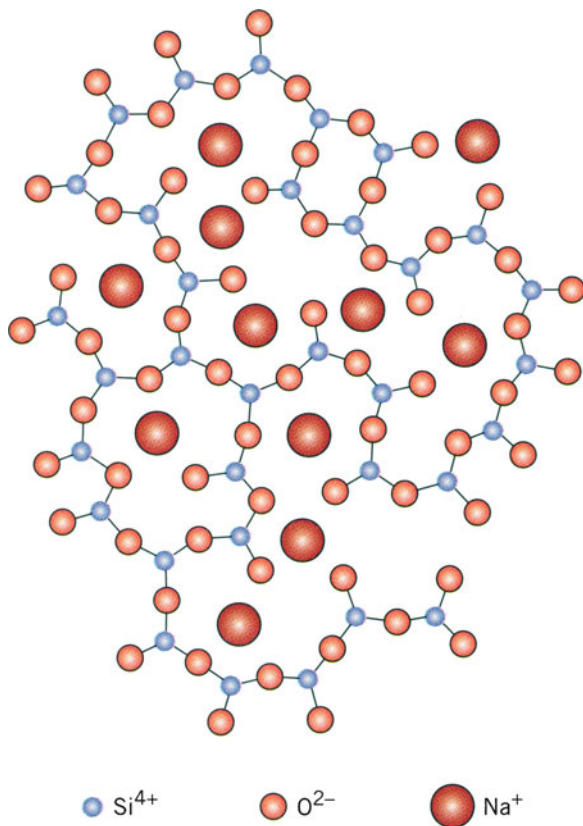
Figure 2.91. Schematic representation of ionic positions within soda glass. Reproduced with permission from Callister, W. D. *Materials Science and Engineering: An Introduction*, 7th ed., Wiley: New York, 2007. Copyright 2007 John Wiley & Sons, Inc.

Although the mechanical properties of quartz are desirable for high-temperature applications, this glass is relatively difficult to mold into desired shapes through conventional glass-blowing techniques. Quartz glass is transparent toward ultraviolet radiation ($\lambda = ca$. 190–300 nm), indicating that the spatial range of structural disorder is less relative to other glasses that contain additional additives (*vide infra*). As a result, quartz windows are used for ultraviolet lamps that are employed in a number of important applications in chemistry, biology, engineering, and materials science.

The chemistry of glass making is now a mature field, with many types available for a variety of applications. In order to decrease the prohibitively high melting point of SiO_2, *ca*. 18% of sodium carbonate ("soda," Na_2CO_3) is often added to sand, resulting in a silica framework doped with Na^+ ions.[78] The resultant glass is more easily workable than fused silica due to interruption of the silicate network.

a

Silicate chains

Mg^{2+}

OH⁻

Silicate chains

Mg^{2+}

b

A

B

C

Oxygen cross-links

R
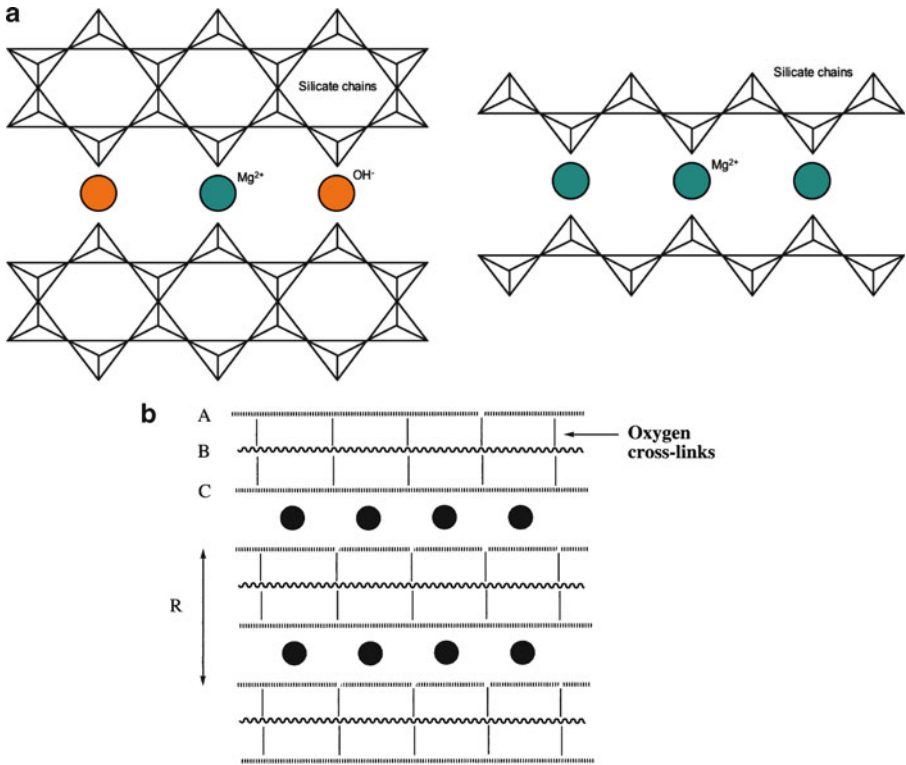
Kaolinite
A and C = aluminate layer with exposed Al-OH groups
B = silicate layer
● = water molecules associated with Al-OH groups that line the galleries
Repeating distance (R) = 7.15 A

Montmorillonite
A and C = silicate layer with no free Si-OH groups
B = Magnesium aluminosilicate layer with OH groups and negative charges
● = water molecules or labile cations in the galleries
Repeating distance (R) = 15 A

Mica
A and C = aluminosilicate layer [(Si$_{1.5}$Al$_{0.5}$)O$_5$]$_n$
B = aluminate layer with hydroxyl groups
● = potassium ions in the galleries
Repeating distance (R) = 9.9 A

Vermiculite
A and C = aluminosilicate layer [(Si$_{1.5}$Al$_{0.5}$)O$_5$]$_n$
B = [Mg$_3$(OH)$_2$]$_n$ layer
● = water molecules and Mg^{2+} ions in the galleries
Repeating distance (R) = 14 A

Talc
A and C = silicate sheets
B = magnesium oxide layer,
● = potassium ions in the galleries

Figure 2.92. Molecular structures of silicate-based minerals. Shown are (a) chain structures of chrysotile (Mg$_3$Si$_2$O$_5$(OH)$_2$ – a common member of the asbestos family) and pyroxene (XSiO$_3$, X = Mg, Na, etc.), and (b) sheet/layered structures exhibited by various clays. Reproduced with permission from Allcock, H. R. *Introduction to Materials Chemistry*, Wiley: New York, 2008. Copyright 2008 John Wiley and Sons, Inc.
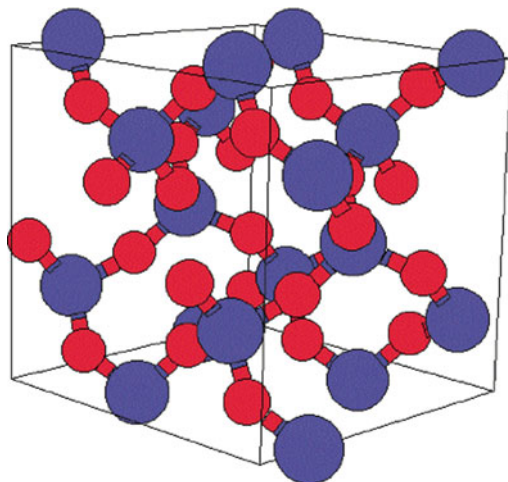
Figure 2.93. Unit cell of the α-quartz crystal lattice. Reproduced with permission from the Naval Research Laboratory – Center for Computational Materials Science website: http://cst-www.nrl.navy. mil/lattice/struk.picts/sio2a.s.png.

However, the sodium ions are detrimental since they are easily solvated by water, which leads to corrosion. To prevent such weathering, *ca.* 10% of limestone ($CaCO_3$) is added to effectively replace the Na^+ ions with Ca^{2+}. When this mixture is heated to its melting point (*ca.* 1,000°C), a mixture of calcium silicate ($CaSiO_3$) and sodium silicate (Na_2SiO_3) results. Upon cooling, the most prevalent type of glass, called "crown glass" or *soda–lime* glass, is generated. This type of glass accounts for over 90% of the glass used worldwide. Interestingly, our current synthetic procedure has not deviated from the earliest glassmakers' recipes, dating back to *ca.* 1450 in Venice, which also used white stone pebbles (quartz, SiO_2) and plant ash containing sodium- and calcium-based additives (Na_2O and lime (CaO)). It should be noted that a glass with a molar concentration of $Na_2O:CaO:SiO_2 =$ 16:10:74 can form crystals of *devitrite* ($Na_2O \cdot 3CaO \cdot 6SiO_2$), at a rate of 17 µm/min at a temperature of 995°C – especially if the molten glass is cooled too slowly.[79] Such devitrification will alter the physical properties of glass (*e.g.,* transparency, strength) in the area surrounding crystal growth; this occurs much less readily in ancient glasses due to their very complex compositions.

There are a number of other glass recipe variations that may be used to yield desired properties. Most likely, these formulations were discovered by accident or in a trial-and-error manner, using materials from their locale and measuring the resultant properties. For instance, the Europeans were the first to discover that K_2O, obtained locally from plant ash, could also be combined with lime and quartz to yield a potash-lime glass, later exploited for stained-glass windows. Another popular variation substitutes boric oxide (B_2O_3) for lime and soda to yield

borosilicate glass. The physical properties of this glass resemble fused silica (*e.g.*, coefficient of thermal expansion: 3.3×10^{-7} cm cm^{-1} K^{-1}), except that its softening temperature is only *ca.* 700°C. Borosilicate glass is the variety that is sold in stores as Pyrex™ cookware and laboratory equipment. These applications demand a glass that resists thermal expansion (*i.e.*, cracking) as a result of significant changes in temperature.

It was not until the late seventeenth century that PbO was substituted for lime in glass formulations. This "soda–lead" glass is what we know as *crystal* (referred to as *flint glass* in pre-Civil War America), and has always been a symbol of wealth and extravagance such as expensive glassware and chandeliers. In order for crystal to be legally given the "full lead" designation, at least 24% of lead oxide must be present in its structure. The addition of the heavy element lead adds significant weight to the glass, while increasing its refractive index. This latter property results in the familiar clear, sparkling appearance of crystal glassware. The presence of lead also makes the glass softer than regular types that must be cut with a diamond saw. Black crystal is truly one of the most fabulous materials for modern artistic design. The lack of transparency is caused by a combination of additives – typically Fe_2O_3, CuO, MnO_2, and Co_2O_3.

Colored glass has been used since the construction of the first churches, prior to the tenth century. Although decorative applications represent the majority of uses for colored glass, there are some other recent functional applications such as traffic light signals. The colors imparted by glass are a result of dopant species that are added during its fabrication (Table 2.13). Both transition metal ions and colloidal suspensions yield an observable color, with the hue dependent on the concentration used. Variation of the color and intensity is also extremely sensitive toward the heating regime (both temperatures and exposure times) used during the glassmaking

Table 2.13. Colors of Glass Resulting from Doping

Additive	Color
Co_2O_3	Blue
Fe_2O_3	Yellow-green
FeO	Bluish-green
Colloidal Se[a]	Red
Colloidal Au[a]	Red
Colloidal Cu[a]	Red
CuO	Turquoise
NiO	Blue/violet/black
SnO_2	White
Sb_2O_3, As_2O_3	White; oxidizing agents
TiO_2	Yellow-brown
UO_2	Fluorescent yellow/green
$AgNO_3$	Orange-red
PbO/Sb_2O_3	Yellow (opaque); oxidizing agents
$K_2Cr_2O_7$	Dark green/black
Mn_2O_3	Purple

[a]With average particle diameters of *ca.* 50–100 nm.

process. In general, the observed color is the complement of the color that is absorbed by the ion. That is, the absorption of short wavelengths will result in an observable red color. Decolorizing agents may also be added; for instance, to remove a yellowish color (*e.g.,* from the presence of Fe^{3+} impurities), a slight excess of manganese may be added that will yield the complementary color of pale purple, effectively neutralizing the glass to a colorless state.

For colloidal dopants, the particle size must be smaller than a wavelength of visible light, or an opaque glass will result. If one would prefer a cloudy glass, a number of additives (*e.g.*, SnO_2, TiO_2, CaF_2) may be used that result in a suspension that changes the overall index of refraction. Colloidal metals yield a deep red color, with colloidal gold first used in the late seventeenth century. Alternatively, a metal salt such as $AuCl_3$ may be added to glass followed by thermal or chemical (*e.g.*, using $NaBH_4$) reduction to metallic Au. It is important to note that a red color will only result if an agent is also added to prevent particle agglomeration. In general, the observed color will shift toward the blue portion of the spectrum as the average particle size decreases (*e.g.*, blue color results from diameters of <50 nm). Chapter 6 will provide more details related to the scattering properties and other applications of nanoparticles.

In comparison, transition metals are added to a molten glass matrix as soluble oxides. As you may see from Table 2.13, the observed color is a consequence of the metal ion type/concentration, as well as its oxidation state. To obtain a desired color, oxidizing agents such as $NaNO_3$, or reducing agents such as carbon powder may be added to afford the desired oxidation state. An intriguing form of glass, referred to as *vaseline glass* contains UO_2 and is slightly radioactive. Since UV radiation is sufficient to excite the weakly bound outer electrons of U, this additive results in a fluorescent green color. Although this is observable under normal light, it is most pronounced upon irradiation with a UV lamp. Interestingly, UO_2 was also added to ceramic glaze to yield bright orange dinner plates and tableware in the 1930s. However, it was later discovered that heat and acidic foods caused uranium to leach from the glaze, resulting in an immediate disband of this application. As one might expect, UO_2-doped materials are not currently manufactured for decorative applications, making such acquisitions a collector's item.[80]

In order to achieve opacity, tiny bubbles may be purposely introduced within the viscous melt – a process that dates back to ancient preparations. The resultant dispersion of light gives rise to an opalescent glass; however, it is now more prevalent to use *opalizing agents*. Earliest examples, dating back to 1,400 B.C., used $M_2Sb_2O_7$ (M = Pb, Ca) for opaque white glass; mixtures of Cu/Cu_2O are used to yield opaque red glass, and opaque white/blue glass often uses $CaF/CaF_3 + NaF/SnO_2$ combinations.

Thus far, we have considered the varying chemical compositions and properties of glasses. In this last section, we will examine an important architecture – glass fibers, of paramount importance in our society. The synthesis of glass fibers dates back to the early eighteenth century, and applications for surgical lamps were prevalent as early as the nineteenth century. We are all familiar with the bright pink bags of
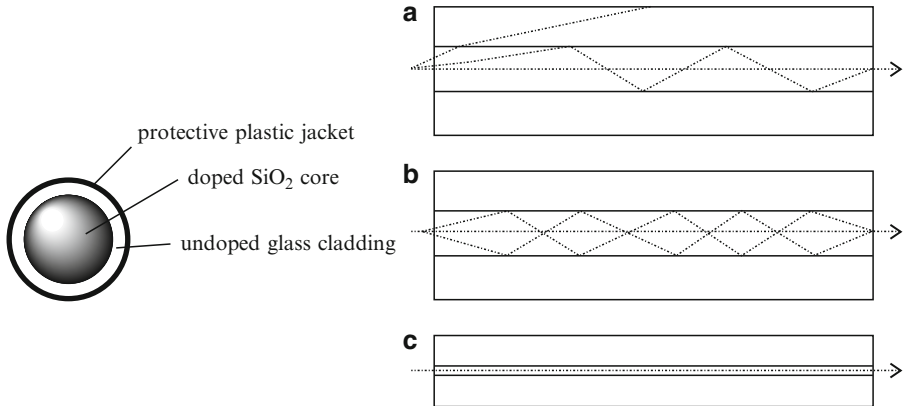
Figure 2.94. Cross-section image of an optical fiber. Shown is the propagation of light waves through an (a) step-index multimode fiber, (b) graded-index multimode fiber, and (c) single-mode fiber.

fiberglass insulation that may be purchased from home improvement stores. In fact, insulation represents the leading application for fibrous glass materials.

In contrast to fiberglass, which consists of a disordered array of needle-like fibers, extremely long, one-dimensional cylindrical glass structures may be carefully fabricated to allow the transmission of light from one end to the other. Although the diameters of optical fibers are less than a human hair (*i.e.*, 8–10 μm), these fibers are stronger than steel and are able to withstand being buried underground. The fiber consists of a *core* surrounded by a *cladding* layer (Figure 2.94). The silica core is doped with other oxides such as B_2O_3, GeO_2, and P_2O_5, resulting in a slightly higher (*ca.* 0.4%) refractive index than the cladding. The boundary between the core and cladding may either be abrupt (*step-index fiber*), or gradual (*graded-index fiber*).

There are two types of optical fibers: single-mode or multiple-mode, referring to the simultaneous transmission of single or multiple light rays, respectively. Single-mode fibers have much smaller diameters than multimode analogues (Figure 2.94a–c), resulting in a simpler pathway for light through the fiber. Whereas multimode fibers are used to transmit information short distances (*e.g.*, LAN applications), single-mode fibers are used for the long-distance transmission of cable television and telephone signals. It is not hard to see why fiber optics are desirable for transmission applications. The amount of information transmitted through 0.25 lb of optical fiber would take 33 t of copper wire! Further, optical fibers are able to transmit signals at lightning speeds – unmatched by any other material. For example, three half-hour T.V. episodes may be transmitted in 1 s.

In a step-index fiber, wavelengths of light are transmitted through the fiber core by total internal reflection (Figure 2.94a). Depending on the angle of incidence of the light, the rays may either be transmitted through the fiber to the detector, or refracted from the core into the cladding resulting in signal loss. The desired angle (*acceptance angle*) required for total internal reflection is determined by the

difference in index of refraction between the core and cladding materials. In a graded-index fiber, the refractive index in the core decreases continuously between the axis and the cladding. This causes the light rays to bend smoothly as they approach the cladding, rather than reflect abruptly from the core-cladding boundary. Light may be lost by attenuation due to absorption by impurities and scattering from microscopic density variations in the glass. In order to achieve sufficient transparency, the concentration of impurities such as iron and hydroxyl ions (OH^-) must be reduced to less than 1 and 10 ppb, respectively.

A fiber optic system typically consists of a transmitting device that generates the light signal, a fiber cable that transmits the light, and a receiver. The information (voice, data, or video) is encoded into electrical signals. At the light source, these electrical signals are converted into either digital or analog light signals. Once the signals are converted to light, they travel down the fiber until they reach a detector, which changes the light signals back into electrical signals. Finally, the electrical signals are decoded into the original voice, data, and/or video information.

The most common method to make optical fibers is heating a rod (preform), of the desired refractive index, to temperatures of *ca.* 2,000°C. The preform is made from the high-temperature (2,000–2,300°C) reaction of $SiCl_4$ in the presence of dopant gases such as BCl_3, $GeCl_4$.[81] Once the tip of the preform is melted, it falls by gravity to form a thin strand. This wire is threaded through a coating reel, and then pulled into an optical fiber of the desired diameter. The draw towers used for this process are impressive buildings, often 8–10 stories in height. The speed of the pulling process (typically 10–20 m s^{-1}) governs the ultimate diameter of the fibers. For subsequent applications, the fiber is spooled onto shipping reels and cut to the desired length.

Another interesting application for glasses is for light control, referred to as "smart glass." We are all familiar with movie scenes where a top-secret meeting takes place, and a flip of the switch instantly darkens the windows. More routinely, it is now commonplace to have self-dimming mirrors that react to trailing vehicle headlights. Three main technologies are responsible for these intriguing materials applications: *photochromic glasses*, *electrochromic devices* (ECDs) and *suspended-particle devices* (SPDs).

Photochromic glasses exhibit a darkening effect upon exposure to particular wavelengths (usually in the UV regime) of light, and date back to the work of Corning in the 1960s. *Transitions*^{TM} *Lenses*[82] that have appeared in television commercials use this technology, effectively protecting eyes from harmful UV irradiation. The darkening effect results from redox reactions (*e.g.,* Eq. 47) involving microcrystalline metal halides (*e.g.,* AgCl,[83] CuCl[84]) that are present within the glass. As one would expect, the size of these dopants must be controlled to prevent reduced transmittance due to scattering before photochromic darkening may take place. However, it has been proposed that the photo-induced formation of *nanoparticles* (see Chapter 6) may also contribute to the observable darkening effect.

(47) $Cu^+ \xrightarrow{h\nu} Cu^{2+} + Cu^0{}_{(nanoparticle)}$
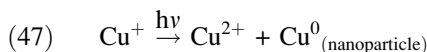
To synthesize photochromic glass, silica and metal halide powders are placed into a platinum crucible and heated in air to 1,400°C, followed by pouring into slabs and annealing at *ca.* 400°C overnight. Another heat treatment at a temperature around 600–650°C (*ca.* 1 h) is then performed to control the size of the inclusions, required for high transmittance and spectral response. We will see examples of organic molecules that also give rise to photochromism in Chapter 5 for plastic lenses, CD-R memory, and molecular switch applications.

The composition of the glass is directly related to the observed photochromic response. In general, as the silica concentration is increased, the maximum photochromic response is observed as the alkali:B_2O_3 ratio is decreased (where alkali = Na_2O:Li_2O:K_2O ratio). Likely, this delicate balance is related to governing the necessary oxidation state of the metal, and size of metal halide and/or colloidal metals precipitates formed during heat treatment. That is, metal halide solubility is related to the number of non-bridging oxygens present in the host glass, which is influenced by the concentrations of B and alkali metal ions, via formation of M^+—O—B bonds during heating. Salts containing fluoride, tungstate or molybdate anions are also often added to alter the photochromic response. These additives likely serve as effective nucleation agents that facilitate precipitation of metal halide crystallites of the appropriate size during the heat treatment.

As their name implies, electrochromic materials change color as a result of an injection of electrons. The typical ECD has a number of layers, sandwiched between glass (Figure 2.95a). When no voltage is applied to the device, the incoming light will pass through undisturbed (*ca.* 70–80% transmittance). However, when a negative voltage is applied, the positive Li^+ ions are injected into the WO_3 layer of the distorted perovskite structure. A redox reaction takes place, where some of the tungsten sites are reduced from W^{6+} to W^{5+} and an electron is placed into the
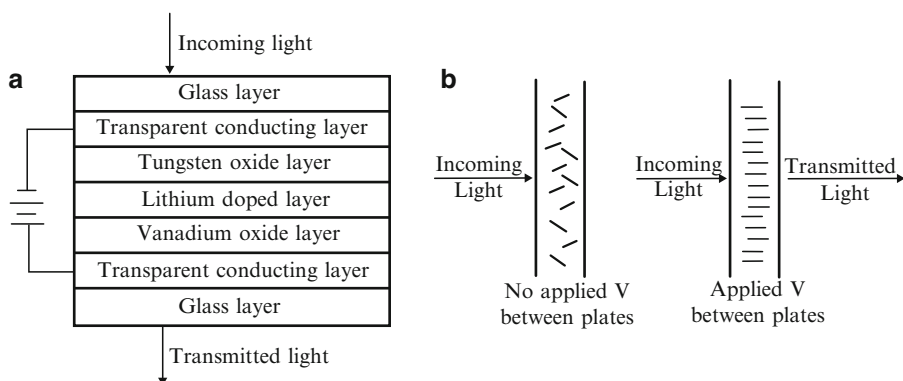

Figure 2.95. Cross-section schematic of an (a) electrochromic device and (b) suspended-particle device.

conduction band. Charge balance is maintained through the interstitial placement of Li^+ ions in the lattice. Since the electron becomes delocalized, metallic behavior is induced in the tungsten oxide layer changing the transparent layer to a dark reflective color (*ca.* 10% transmittance of incoming light through the device). The dark color will remain even if the applied voltage is removed, since the reverse reactions are not spontaneous. If the reverse bias is applied to the device, lithium ions flow from the WO_3 layer reoxidizing the W^{5+} ions and restoring transparency. We will discuss more details regarding the electrical properties and band structure of semi-conductive oxides such as TiO_2, SnO_2, and WO_3 in Chapter 4.

More recently, thin films of Ni/Mg hydride alloys have also been developed for light attenuation using electrochromic or gas-chromic (injection of H_2 and O_2 gases) technology.[85] Although they can technically be classified as electrochromic materials, the new reflective hydrides that are being developed behave in a noticeably different way. Instead of absorbing light, they reflect it. Thin films made of nickel–magnesium alloy are able to switch back and forth from a transparent to a reflective state. The switch can be powered by low voltage electricity (electrochromic technology) or by the injection of hydrogen and oxygen gases (gas-chromic technology). Furthermore, this material has the potential to be even more energy efficient than other electrochromic materials.

By comparison, SPDs operate through the behavior of rod-like particles (*e.g.*, liquid crystals, see Appendix C.3) toward an applied voltage (Figure 2.95b). When no voltage is applied, the particles are randomly aligned, and do not allow light to pass through the device. However, an electric charge will polarize the particles to align with the field. We will describe the molecular behavior of polarizable particles in more detail later (Chapter 4), related to dielectric materials placed in a parallel plate capacitor.

2.4.3. Cementitious Materials

The use of cementitious materials for structural applications dates back to ancient Egypt. A type of cement was used to hold together the limestone blocks of the great pyramids that still stand today. During the time of the Roman Empire, an improvement of the cement formulation was developed, which used a fine, volcanic ash known as Pozzolana found in various parts of Italy. Although they did not realize it at the time, the hardening process occurred due to the reaction of the aluminosilicate-based ash with $Ca(OH)_2$ in the presence of water to yield a calcium–silicate–hydrate (CSH) rigid gel. Amazingly, thousands of years later, the CSH structure is not yet completely understood – it is likely a disordered form of the hydrated calcium silicate mineral tobermorite (Figure 2.96).

The last major development in cement technology occurred in the early nineteenth century in England. Bricklayer Joseph Aspdin first made a variety of cement known as *Portland cement* – not in a laboratory, but on his kitchen stove! His patent in 1824 changed the world forever, as this form of cement is the basic ingredient in concrete – essential for the erection of virtually all buildings and many roads
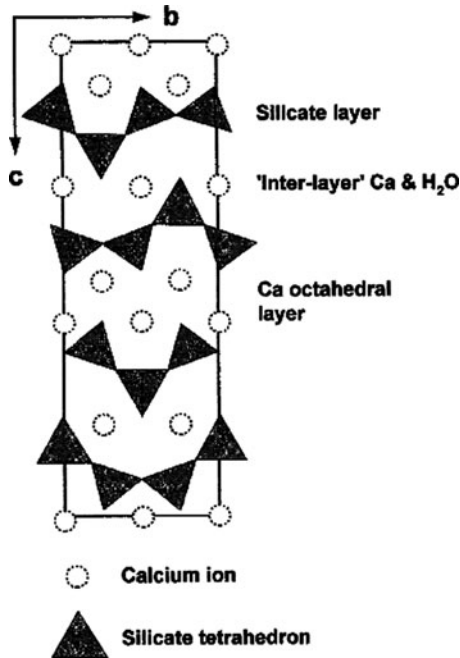
Figure 2.96. The crystal structure of tobermorite, viewed along the bc plane. The amorphous gel produced during cement formation likely contains defects such as missing/disordered silicate tetrahedra and/or water sites. Reprinted from *Chem. Geol.* **2000**, 167, 129, Copyright 2000, with permission from Elsevier.

throughout the world. In fact, concrete is the most heavily used man-made material in our world – in 2005, it was estimated that the worldwide annual production of concrete amounts to 1 ton for every man, woman, and child on earth!

It is interesting to note the development timeline for cement/concrete, which has addressed many important societal needs. For example, if we consider road construction, stones were used as early as 4,000 B.C., and were still prevalent in early America – still evident in some historical cities such as Boston, MA. As motorcars became more abundant and faster in the early twentieth century, replacements were sought for dirt, gravel, and stone roads. Asphalt[86] and simple road tarring were the first alternatives that addressed the environmental problem of dust as well as road smoothness, and the majority of highways across North America still comprise asphalt pavement. Comparatively, a large proportion of city streets and highways, especially in the warmer locales, are made from concrete. Since concrete is more apt to crack relative to asphalt under significant temperature changes, this material is not greatly used to construct roadways in northern climates (*e.g.*, North Dakota, Montana, Minnesota, Michigan, Canadian Provinces).

Portland cement is produced from the sintering of minerals containing $CaCO_3$, SiO_2, Al_2O_3, Fe_2O_3, and MgO in a ceramic kiln, held at a temperature of *ca.*
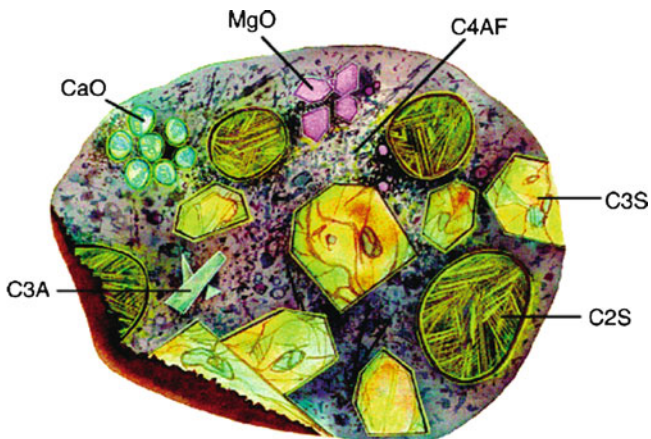
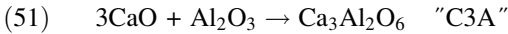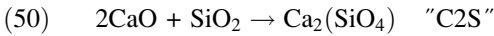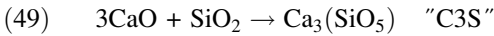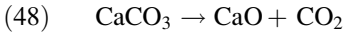*Figure 2.97.* Cross-section representation of a powdered cement particle. Dicalcium silicate (Ca_2SiO_4), tricalcium silicate (Ca_3SiO_5), tricalcium aluminate ($Ca_3Al_2O_6$), and tetracalcium aluminoferrite ($Ca_4Al_nFe_{(2-n)}O_7$) crystallites are abbreviated as C2S, C3S, C3A, and C4AF, respectively. Reproduced with permission from *Chem. Mater.* **2003**, 15, 3074. Copyright 2003 American Chemical Society.

1,500°C. Equations 48–52 show the reactions that occur during the processing of cement. The resulting complex material is referred to as *clinker* (Figure 2.97), and may be stored for many years under anhydrous conditions before its use in concrete. As one can see from Eq. 48, this process releases the greenhouse gas CO_2, causing environmental concerns over the world's increasing production of cement. It is estimated that Portland cement manufacturing accounts for over 10% of the world's total emission of CO_2. As a result, there is an increasing focus on cements fabricated with fly ash (*e.g.*, by-product from coal-fired power plants), that possess the same qualities as Portland cement clinker without the need for the calcination step (Eq. 48). When water is mixed with Portland cement, the product sets in a few hours and hardens over a period of 3–4 weeks. The initial setting reaction is caused through reaction between water, gypsum ($CaSO_4 \cdot 2H_2O$ – added to clinker to control the hardening rate), and C3A forming calcium and aluminum hydroxides. The crystallization of these hydroxides results in an observable hardening within the first 24 h. The subsequent reactions between the formed hydroxides and C3S result in formation of a crosslinked CSH gel (*vide supra*); this provides further strengthening over the first week. The reaction between hydroxides and C2S proceed the slowest, and result in hardening/strengthening of the material in latter stages of setting.[87] The hardening of concrete is actually a consequence of individual grains of *aggregates* being cemented together by the clinker–water byproducts. Aggregates that are present in concrete are of two or more size distributions – typically coarse gravel/stones and fine sand. As a general rule, 1 m^3 of concrete contains over 4,400 lb of gravel and sand.

(48) $CaCO_3 \rightarrow CaO + CO_2$

(49) $3CaO + SiO_2 \rightarrow Ca_3(SiO_5)$ "C3S"

(50) $2CaO + SiO_2 \rightarrow Ca_2(SiO_4)$ "C2S"

(51) $3CaO + Al_2O_3 \rightarrow Ca_3Al_2O_6$ "C3A"

(52) $4CaO + Al_2O_3 + Fe_2O_3 \rightarrow Ca_4Al_2Fe_2O_{10}$ "C4AF"
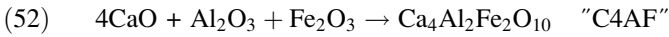
2.4.4. Ceramics

Ceramics refer to a broad category of inorganic materials that possess a high hardness (close to diamond on the Moh's scale) and brittleness, pronounced resistance to heat and corrosion, and are electrically/thermally insulating. Though amorphous glasses may often be classified within the ceramic umbrella, it is generally accepted to include only inorganic materials with at least some degree of crystallinity. Most often, these materials possess both amorphous and polycrystalline regions, with the latter exhibiting abrupt changes in crystal orientation across individual grain boundaries in the extended lattice.

There are three categories of ceramics: oxides (e.g., alumina, zirconia), non-oxides (carbides, borides, nitrides, silicides), and composites of oxides/non-oxides. The two common approaches to synthesize ceramics include a low-temperature sol-gel route (*vide supra*), and a high-temperature multi-step process involving[88]:

  (i) *Grinding/milling* – silicate/aluminosilicate minerals (*e.g.,* various clays, silica) and bauxite (hydrous aluminum oxide ore) are among the most abundant materials in the Earth's crust, constituting the most common raw materials for ceramics processing. These minerals are pulverized into a fine powder, often alongside *calcination* – thermal treatment to remove volatile impurities (*e.g.,* organics, waters of hydration, CO_2 from carbonates, etc.).

 (ii) *Mixing and forming* – the powder is mixed with water to semi-bind the particles together, and is cast, pressed, or extruded into the desired shape. Sometimes, an organic polymer binder such as polyvinyl alcohol, $(—CH_2—CH(OH)—)_n$, is added to enhance the adhesion of the granules; these additives are then burnt out during the firing (at $T > 200°C$). Organic lubricants may also be added during pressing to increase densification.

(iii) *Drying* – the material is heated to remove the water or organic binder(s) and lubricant(s) from the formed material, known as a *green body*. Care must be used to prevent rapid heating, to prevent cracking and other surface defects. During heating, shrinkage will occur resulting in a material that is denser (by a factor of 2–3) than the green precursor – especially for syntheses using polymeric precursors (*e.g.,* organosilicon polymers for SiC or Si_3N_4 ceramics). Gas evolution may also occur that will introduce porosity into the ceramic.
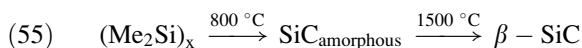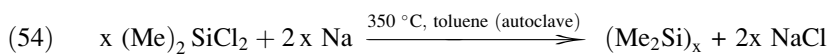
(iv) *Firing/sintering* – quite often, precursor compounds at earlier stages of ceramic processing are at least partially amorphous. The final firing/sintering stage is used to fuse the particles together and convert the material into a (poly) crystalline product, which has the bulk form and physical properties desired for a particular application. Firing is usually performed at a temperature below the melting point of the ceramic. Most importantly, as we will see in the next chapter (powder metallurgy), the microstructure of the final product is strongly related to the morphology of the green body.

Porcelain, used for applications that range from toilets to decorative plates, is formed by firing the green ceramic comprised of the clay mineral *kaolinite* ($Al_2Si_2O_5(OH)_4$), and a variety of other crystalline and amorphous materials such as *feldspars* ($KAlSi_3O_8/NaAlSi_3O_8/CaAl_2Si_2O_8$), glass, ash, and quartz. At a temperature of *ca.* 1,200–1,400°C, glass and an aluminosilicate mineral known as *mullite* (or porcelainite) are formed, resulting in the familiar high strength and translucence of porcelain.

Non-oxide ceramics are typically synthesized via high-temperature routes, which convert molecular precursors into the desired structures. For instance, SiC (carborundum) may be produced from the direct reaction of silica sand with carbon in an electric furnace (Eq. 53). Industrially, a mixture of 50 wt% SiO2, 40 wt% coke, 7 wt % sawdust, and 3 wt% NaCl is heated together at ca. 2,700°C – known as the *Acheson process*. The purpose of the salt is to remove metallic impurities via formation of volatile metal chlorides (*e.g.,* $FeCl_3$, $MgCl_2$, etc.). To yield highly crystalline SiC, the *Lely process* uses the sublimation of SiC powder or lumps at 2,500°C under argon at atmospheric pressure.

$$(53) \quad SiO_2 + 2\,C \xrightarrow[\text{(electric furnace)}]{\text{2000–2500 °C}} SiC + CO_2$$

A lower-temperature route involves the reduction of dichlorodimethylsilane with Na or Na/K alloys in an organic solvent (Eqs. 54 and 55):

$$(54) \quad x\,(Me)_2\,SiCl_2 + 2\,x\,Na \xrightarrow{\text{350 °C, toluene (autoclave)}} (Me_2Si)_x + 2x\,NaCl$$

$$(55) \quad (Me_2Si)_x \xrightarrow{800\,°C} SiC_{amorphous} \xrightarrow{1500\,°C} \beta - SiC$$

Chlorinated silanes may also be used to synthesize silicon nitride (Si_3N_4) ceramics, via reaction with an amine (Eq. 56):

$$(56) \quad x\,MeSiCl_3 + 3x\,NH_3 \xrightarrow{500\,°C} (MeSiN_3)_x + 3x\,HCl$$
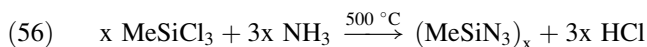
Of course, the "brute force" method of reacting silica with ammonia or N_2/H_2 gases at temperatures in excess of 1,200°C will also yield crystalline silicon nitride ceramics. Another route that does not involve chlorinated precursors consists of sintering a polymeric precursor such as poly[(methylvinyl)silazane]$-$ $[(CH_3SiHNH)_{0.8}(CH_3SiCH = CH_2NH)_{0.2}]_n$.

Biomaterials applications

The applications for ceramics span virtually every commercial sector, from porcelain dishes and sinks to uses in cutting tools, ball bearings, electronics (*e.g.,* capacitors, insulators, integrated circuit packaging, piezoelectrics, super-conductors), coatings (*e.g.,* engine components, drill bits), filters, membranes, and catalyst support materials. It is estimated that the current annual world demand for advanced ceramics is over $50 billion. One interesting futuristic application for ceramics is a "smart ski" that uses a piezoceramic material embedded in the ski to reduce vibrations and increase stability and control at higher speeds. An emerging area for ceramic applications is the field of *biomaterials*, a $12 billion industry.

By definition, a biomaterial is a biocompatible material or device that is placed within a living creature in order to perform, augment, or replace a natural function. Throughout this textbook, we will discuss a variety of such materials, which span applications from dentistry (*e.g.,* implants such as crowns and dentures), orthopedic (*e.g.,* artificial limbs, joint and bone repair/replacement), optometric (contact lenses), and medicinal (*e.g.,* soluble sutures, coronary stents, artificial organs, *drug delivery agents* used to deliver a chemical compound directly to the site of treatment – *e.g.,* glass microspheres to deliver radioactive therapeutic agents). Such medical breakthroughs have not only extended the life expectancy of humans (currently 78 years in the U.S.), but have resulted in a way of life that would have seemed impossible just a few decades ago.

Ceramics and glasses are generally used to repair or replace joints or tissue, as well as a coating to improve the biocompatibility of metallic-based implants. Before placing a biomaterial within a body, it must be non-toxic, bioinert (*i.e.,* able to withstand corrosion in a biological environment without causing damage to surrounding tissues), bioactive (*i.e.,* able to undergo interfacial interactions with surrounding tissues), and biodegradable/resorbable (*i.e.,* eventually replaced or incorporated within growing tissue). For instance, when a bioactive glass is placed in a physiological environment, there is an ion exchange among cations in the glass and hydronium ions within the surrounding solution. Hydrolysis then takes place, wherein the glass network is disrupted, changing its morphology to a porous, gel-like surface layer. Precipitation of a calcium phosphate mineral ensues, followed by further mineralization to a crystalline substance that mimics the structure of bone.

Placing a biomaterial within living tissue will always render a tissue response at the implant/tissue interface. In particular, the following four responses may result from implantation, which govern the degree of medical complications and ultimate lifetime of an implant[89]:

(i) *The surrounding tissue will die if the material is toxic;*

(ii) *A fibrous tissue of varying thickness will form if the material is nontoxic and biologically inert;*

(iii) *An interfacial bond will form if the material is nontoxic and biologically active; or,*

(iv) *The surrounding tissue will replace the implant if the material is nontoxic and soluble*

The encapsulation of soft tissue (ii above), causes deleterious wear and abrasion in metallic implants. Other contributing factors in decreasing the lifetime of an implant include infection, inflammation, and lack of prolonged bonding between the implant and surrounding bone. Consequently, the current average lifetime of a titanium orthopedic implant is on the order of 10–15 years. However, there are many efforts devoted to improving the longevity of implants. One such approach features modifying the titanium surface via *anodization* (see Chapter 3), to increase the surface area and mimic the roughness of natural bone, which facilitates the adsorption of a larger number of bone-forming cells known as *osteoblasts*. To address the other factors, this approach also features coating the implant with anti-infection and anti-inflammation drugs (penicillin/streptomycin and dexamethasome, respectively).[90]

There are three primary methods used for bone substitution, required for applications such as spinal deformities and "non-unions" (fractures that do not heal within 9 months). *Autografting* consists of transplanting a bone from one region of the patient's body (usually the pelvic region) to the desired location. This procedure is often preferred, as it precludes immunogenicity problems; however, there may be complications and additional pain at the harvesting site, as well as the additional surgical costs for the combined harvesting/transplanting procedures. In contrast, *allografting* consists of harvesting bone from a live or deceased donor for the transplanting procedure. These implants are much less successful than autograft implants due to immuogenicity, transmitted diseases, and the absence of viable osteoblasts. Due to these limitations, it is becoming increasingly more popular to use synthetic materials as bone substitutes. Whereas refractory ceramics such as alumina (Al_2O_3) and zirconia (ZrO_2) are used in high-wear applications such as joint replacements, calcium phosphate/sulfate based ceramics are used for bone regeneration applications.

The most common synthetic bone grafting ceramic is $Ca_{10}(PO_4)_6(OH)_2$, known as *hydroxyapatite* (Figure 2.98). Unlike other calcium phosphates, hydroxyapatite is stable under physiological conditions, which features a pH range of 5.5–7.2. Hydroxyapatite serves as an osteoconductive scaffold to which proteins and cells may nucleate, and within which bone-forming cells known as *osteoblasts* are generated (Figure 2.99). In addition to using hydroxyapatite as a filler material, it may also be used as a coating material. That is, while its mechanical properties are too brittle to withstand load-bearing applications, hydroxyapatite may be used as a coating on metallic alloys to impart a greater biocompatibility of joint replacements, while reducing the release of metallic ions from the implant.

Interestingly, the composition, phase, morphology, and placement of hydroxyapatite will influence the speed and extent of bone growth. Since the resorption process is surface-driven by the adsorption of osteoblasts, the ultimate solubility of a ceramic will be directly related to its surface area – *i.e.,* crystal size and density. In addition, careful control of processing parameters is necessary to prevent thermal decomposition of hydroxyapatite into other soluble calcium phosphate phases (*e.g.,* tricalcium phosphate, $Ca_3(PO_4)_2$, tetracalcium phosphate, $Ca_4(PO_4)_2O$, and CaO), which
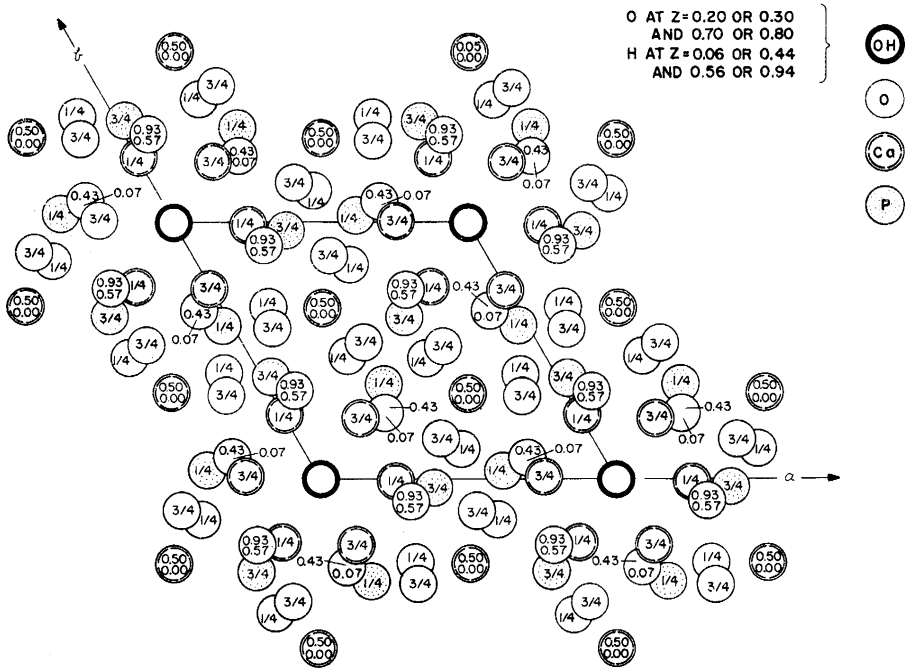
Figure 2.98. Crystal structure of hydroxyapatite, projected on the (x,y) plane. Reproduced with permission from *Nature*, **1964**, *204*, 1050.
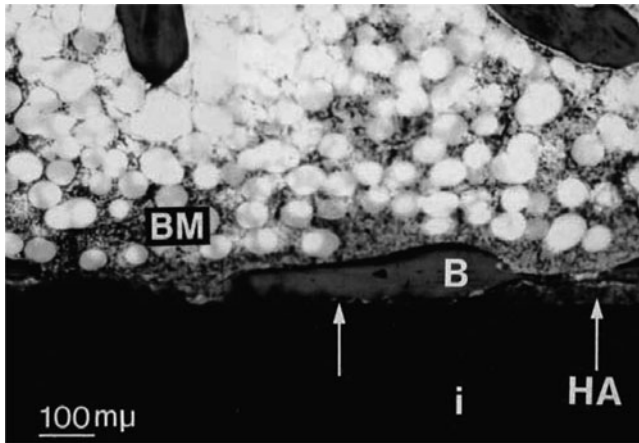

Figure 2.99. Photomicrograph of an HA-coated implant. Areas with complete resorption of the coating (arrow) were covered by bone marrow (BM) and bone (B) ongrowth (Light Green and basic fuchsin ×75). Reproduced with permission from *J. Bone Joint Surg.* **1997**, *79-B*, 654. Copyright 1997 British Editorial Society of Bone and Joint Surgery.

dissolve more rapidly in body fluid than crystalline hydroxyapatite.[91] It has been shown that the plasma spraying procedure used to deposit hydroxyapatite coatings onto orthopedic and dental implants may also result in co-deposits of amorphous calcium phosphate and other resorbable phosphates. Increased concentrations of these other phosphates are thought to result in premature resorption of the coating before the bone may attach to the implant, drastically shortening its lifetime.[92]

Due to its inherent brittleness, hydroxyapatite is often combined with calcium sulfate ($CaSO_4 \cdot 2H_2O$, denoted as *plaster of Paris*) to form a more durable ceramic material. Calcium sulfate is biocompatible and bioactive, being resorbed after 30–60 days. Calcium sulfate is mostly used in its partially hydrated form; when mixed with water, an exothermic reaction leads to recrystallization into the dihydrate final form shared by the mineral *gypsum* (Eq. 57):

(57) $CaSO_4 \bullet (1/2 \ H_2O) + 3/2 \ H_2O \ \rightarrow \ CaSO_4 \bullet 2 \ H_2O \ + \ heat$
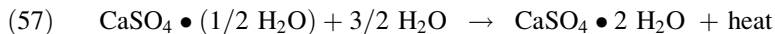
Analogous to cement, plaster is used as a building material by hydrating a finely-divided powder. However, unlike cement, plaster remains relatively soft following drying, which limits its utility for structural applications. The hardening mechanism of plaster is due to the recrystallization process. That is, when the hemihydrate powder is mixed with water, the evolved heat evaporates the water, forming a network of interlocked dihydrate needle-like crystals. For identical chemical compositions, the size and morphology of the starting powder will determine the amount of water required to make a sufficiently strong ceramic material. Whereas plaster crystals are irregular in size/morphology, formed by heating gypsum in air at 115°C, stone crystals feature a much greater uniformity – a consequence of being fabricated by heating gypsum under an applied pressure. The less uniform crystals of plaster will pack relatively inefficiently, requiring more water for mixing relative to stone. As a result, the evaporation of larger volumes of water will result in a greater porosity, causing the hardness of set plaster to be much less than dried stone.

IMPORTANT MATERIALS APPLICATIONS I: FUEL CELLS

By definition, a *fuel cell* is any device that generates electricity by chemical reactions that occur at the cathode (positively charged) and anode (negatively charged). Figure 2.100 illustrates the general operating principle of fuel cells. As opposed to batteries that store a limited amount of energy, fuel cells operate with a continuous fuel flow that allows prolonged periods of electricity generation. In addition, these systems may be easily scaled-up to power large electrical grids.

An electrolyte is an essential component within fuel cells, used to facilitate the selective migration of ions between the electrodes. Fuel cells are typically classified according to the electrolytes used: alkaline fuel cell (AFC), polymer electrolyte (or proton exchange membrane) fuel cell (PEMFC), phosphoric acid fuel cell (PAFC), molten carbonate fuel cell (MCFC), and solid oxide fuel cell (SOFC). Typical efficiencies, operating temperatures and output voltage for the various types of fuel cells are shown in Table 2.14. It should be noted that none of these fuel cells
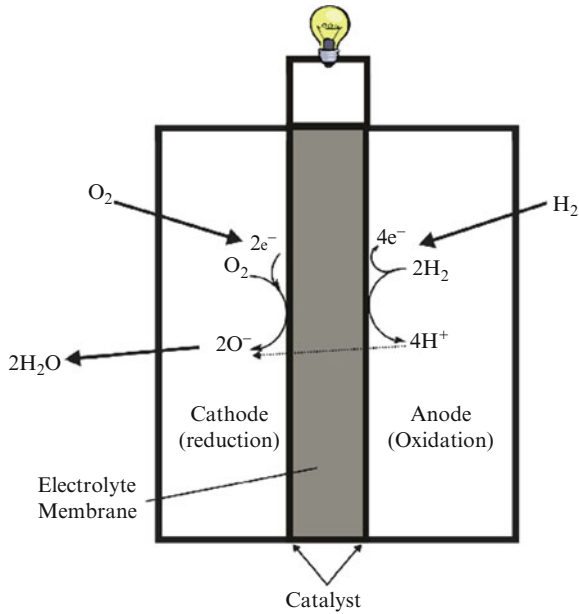
Figure 2.100. Illustration of the operation of *proton exchange membrane* (PEM) fuel cell. In this design, the electrolyte facilitates the transfer of protons across its membrane.

Table 2.14. Comparative Data for Fuel Cells

Fuel cell	Operating temperature (°C)	Efficiency (%)	Output current (kW)
Alkaline	100–200	70	0.3–5
Polymer	80	40–50	50–250
Phosphoric acid	150–200	40–80	200–11,000
Molten carbonate	650	60–80	2,000+
Solid oxide	800–1,000+	60	100

are yet cheap/efficient enough to widely replace traditional ways of generating power, such as coal- and natural gas-fired, hydroelectric, or nuclear power plants. Fuel cells are currently being tested and marketed for the replacement of traditional internal combustion engines in automobiles. The high efficiencies and low emissions of fuel cells are extremely intriguing, but problems with emission-free production, and safe storage of hydrogen gas remain the primary stumbling blocks for widespread incorporation of this technology.

Alkaline fuel cells have been used the longest, since the 1960s by NASA for space shuttles. In fact, this application illustrates the utility of fuel cells. Hydrogen and oxygen gases are used to power the fuel cell, which powered the electrical components of the space shuttle. Water, the only byproduct of the reaction, was used as onboard drinking water for the crew. Although AFCs are the most inexpensive

to produce and have some of the highest efficiencies, they require high-purity oxygen to prevent catalyst poisoning by carbon dioxide. PEMFC designs also suffer from catalyst poisoning. The presence of small concentrations of CO (>1 ppm) in the reformate of fuels drastically alters the performance of the anodic catalyst (*e.g.*, Pt, Pt/Ru).

In this section, we will consider SOFCs, the most relevant to our discussion of crystal structures. These ceramic-based fuel cells are perhaps best suited for large-scale stationary power generators that could provide electricity for entire cities. This is a consequence of its high operating temperature, often greater than $1,000°C$. In addition to the primary electricity generated from the electrodes within the fuel cell, the steam byproduct may be used to turn turbines, generating secondary electricity. The SOFC can operate on most any hydrocarbon fuel, as well as hydrogen gas:

(58) $H_2 + O^{2-} \rightarrow H_2O + 2 \ e^-$ (at anode)

(59) $1/2 \ O_2 + 2 \ e^- \rightarrow \ O^{2-}$ (at cathode)
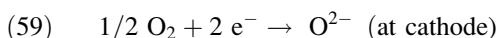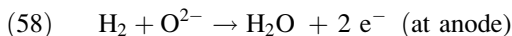
The electrochemical reactions occurring within a SOFC are shown in Eqs. 58 and 59. The anode consists of a porous mixture of a Ni or Co catalyst on yttria-stabilized zirconia. Such a mixture of metal and ceramic is referred to as a *cermet*. The zirconia acts to inhibit grain growth of the catalyst particles of nickel or cobalt and protects against thermal expansion. The cathode is generally a Sr-doped $LaMnO_3$ perovskite. The Sr dopant provides for oxygen transfer to the cathode–electrolyte interface.

Figure 2.101 shows a variety of stacked cell designs employed by SOFCs. Since an individual fuel cell produces a low voltage (typically <1 V), a number of cells are connected in series forming a fuel cell *stack*. An interconnect comprising a high-density material is used between the repeating {anode–electrolyte–cathode} units of the stack.

The electrolyte in a SOFC must have the following characteristics:
1. High oxide conductivity
2. Stability in both oxidizing and reducing environments
3. Chemical compatibility with other cell components
4. High density to prevent mixing of fuel and oxidant gases
5. Desirable thermal expansion properties, to prevent cracking of the fuel cell at high temperatures

One such material that satisfies all of the above requirements is yttrium-stabilized ZrO_2. In a SOFC, the electrolyte must allow oxide-ion transport between the anode and cathode. In its high-temperature cubic form, zirconia is not able to conduct oxide ions. That is, there are no suitable interstitial sites in the lattice to trap oxide ions. However, when a lower valent metal oxide such as Y_2O_3 (*i.e.*, Y^{3+}) is substituted for ZrO_2 (*i.e.*, Zr^{4+}), a vacancy is created in the unit cell of the extended lattice (Figure 2.96). This site is able to accept an O^{2-} ion generated at the cathode, and deliver it to the anode where it is transformed to H_2O. As illustrated in Figure 2.102, the oxide ion is transferred among adjacent zirconia unit cells en
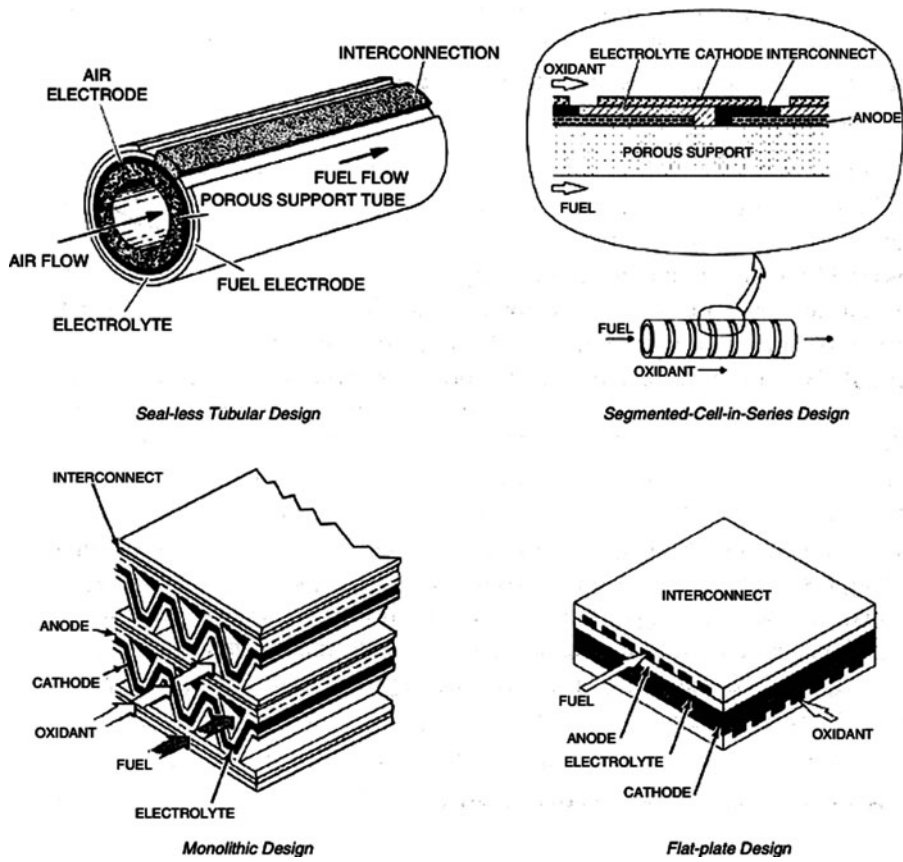
Figure 2.101. Types of solid oxide fuel cell (SOFC) designs. Reproduced with permission from *Electronic Materials Chemistry*, Bernhard Pogge, H. ed., Marcel Dekker: New York. Copyright 1996 Taylor & Francis.
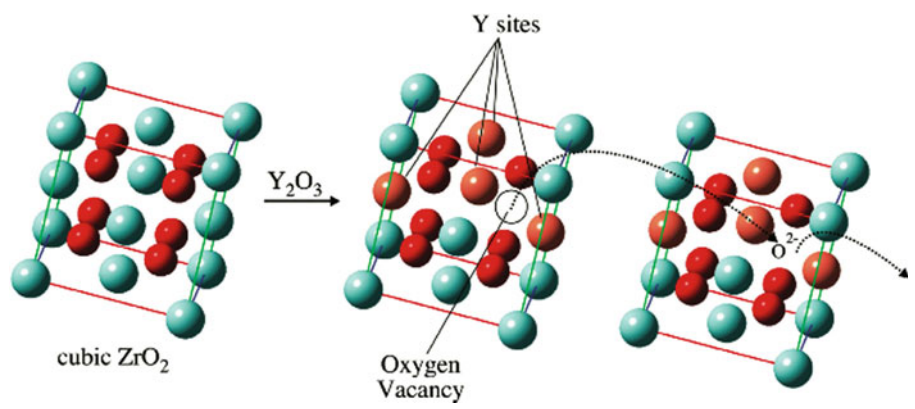

Figure 2.102. Comparison of unit cells of cubic zirconia and yttrium stabilized zirconia (YSZ), showing transport of oxide ions through a lattice via vacant sites in neighboring YSZ unit cells.

route from the cathode to anode compartments of the fuel cell. By contrast, the "holes" created by Y^{3+} substitution may be envisioned to move in the opposite direction, from the anode to cathode.

References and Notes

[1] Zallen, R. *The Physics of Amorphous Solids*, John Wiley and Sons: New York. 1983.

[2] Note: there is no empirical evidence that supports the flow of glass over time. That is, there is no analogous glass thickening observed in ancient Roman or Egyptian objects, no degradation in the optical performance of antique telescopes/microscopes, and no change in physical properties of prehistoric artifacts (*e.g.*, dulling of obsidian swords).

[3] Note: electrons in an s-orbital have a finite probability of being found at the nucleus. As the principal quantum number increases, the s-orbitals become more diffuse, leading to electrons being found at distances further from the nucleus. With less attraction toward the nucleus, these electrons are able to orbit the nucleus at speeds approaching the speed of light. When objects move at such high speeds, an increase in relativistic mass occurs, whereby the s-electrons behave as though they were more massive than electrons moving at slower speeds. This mass increase causes the orbiting electrons to be slightly contracted toward the nucleus, decreasing their availability to participate in chemical reactions.

[4] Schroers, J.; Johnson, W. L. "History Dependent Crystallization of $Zr_{41}Ti_{14}Cu_{12}Ni_{10}Be_{23}$ Melts" *J. Appl. Phys.* **2000**, *88*(1), 44–48, and references therein. More information may be obtained from http://www.liquidmetal.com.

[5] For example, see: Dera, P.; Lavina, B.; Borkowski, L. A.; Prakapenka, V. B.; Sutton, S. R.; Rivers, M. L.; Downs, R. T.; Boctor, N. Z.; Prewitt, C. T. *Geophys. Res. Lett.* **2008**, *35*, L10301.

[6] (a) Malone, B. D.; Sau, J. D.; Cohen, M. L. *Phys. Rev. B* **2008**, *78*, 161202, and references therein. (b) Pfrommer, B. G.; Cote, M.; Louie, S. G.; Cohen, M. L. *Phys. Rev. B* **1997**, *56*, 6662, and references therein.

[7] There is an ongoing debate whether the term "pseudopolymorph" should be abandoned, instead designating these compounds as "solvates". Two viewpoints may be found at: (a) Bernstein, J. *Cryst. Growth Design* **2005**, *5*, 1661. (b) Nangia, A. *Cryst. Growth Design* **2006**, *6*, 2.

[8] For a nice presentation regarding the thermal characterization of polymorphs, and the implications of polymorphism toward drug design, see: http://www.usp.org/pdf/EN/meetings/asMeetingIndia/2008Session1track3.pdf

[9] For example, see: Perrillat, J. P.; Daniel, I.; Lardeaux, J. M.; Cardon, H. *J. Petrology* **2003**, *44*, 773. May be found online at: http://petrology.oxfordjournals.org/cgi/content/full/44/4/773

[10] (a) For instance, the high-pressure polymorphism of silica is described in: Teter, D. M.; Hemley, R. J. *Phys. Rev. Lett.* **1998**, *80*, 2145; also available online: http://people.gl.ciw.edu/hemley/192TeterPRL 1998.pdf. (b) McMillan, P. F.; Wilson, M.; Daisenberger, D.; Machon, D. *Nature Mater.* **2005**, *4*, 680.

[11] Note: the Miller indices for the (211) plane may also be visualized by extending the unit cell beyond a cell volume of 1 cubic unit. For instance, equivalent planes would also pass through (2,0,0), (0,4,0), and (0,0,4), as well as other extended coordinates. For the (001) plane, the zeroes indicate that the plane does not intercept either the *a* or *b* axes.

[12] Cullity, B. D. *Elements of X-ray Diffraction*, 2nd ed., Addison-Wesley: Reading, Massachusetts, 1978.

[13] For a comprehensive list of SiC physical properties, see: http://www.ioffe.ru/SVA/NSM/Semicond/SiC/bandstr.html#Band

[14] For more details about the structure and applications of SiC, see: http://www.ifm.liu.se/matephys/new_page/research/sic/index.html

[15] Note: CdCl$_2$ also exists as a hexagonal lattice, analogous to CdI$_2$.

[16] This is the first of five rules that govern the geometric stability of ionic packing, as proposed by Nobel Laureate Linus Pauling (*J. Am. Chem. Soc.* **1929**, *51*, 1010). For more details, see: http://positron. physik.uni-halle.de/talks/CERAMIC1.pdf

[17] (a) Honle, W. *J. Solid State Chem.* **1983**, *49*, 157. (b) Perrin, et al. *Acta Crystallogr.* **1983**, *C39*, 415.

[18] For a recent discovery of a safer cathode alternative, LiFeO$_4$, see: Kang, B.; Ceder, G. *Nature* **2009**, *458*, 190. Information regarding a proposed intercalation mechanism for LiFeO$_4$ may be found in: Delmas, C.; Maccario, M.; Croguennec, L.; Le Cras, F.; Weill, F. *Nature Materials* **2008**, *7,* 665. For a recent method to study the thermal stability of a variety of oxide cathode materials for Li-ion battery applications, see: Wang, L.; Maxisch, T.; Ceder, G. *Chem. Mater.* **2007**, *19*, 543.

[19] Qi-Hui, W. *Chinese Phys. Lett.* **2006**, *23*, 2202.

[20] For example, see: Ferracin, L. C. et al. *Solid State Ionics* **2002***, 130*, 215.

[21] Willard, M. A.; Nakamura, Y.; Laughlin, D. E.; McHenry, M. E. *J. Am. Ceram. Soc.* **1999**, *82*, 3342.

[22] Nakamura, Y.; Smith, P. A.; Laughlin, D. E.; De Graef, M.; McHenry, M. E. *IEEE Trans. Magn.* **1995**, *31*, 4154.

[23] http://www.me.psu.edu/sommer/me445/ntcnotes.pdf

[24] (a) Jansen, M.; Letschert, H. P. *Nature* **2002**, *404*, 980. (b) Kasahara, A.; Nukumizu, K.; Hitoki, G.; Takata, T.; Kondo, J. N.; Hara, M.;Kobayashi, H.; Domen, K. *J. Phys. Chem. A* **2002**, *106*, 6750. (c) Hitoki, G.; Takata, T.; Kondo, J. N.; Hara, M.; Kobayashi, H.; Domen, K. *Chem. Commun.* **2002**, 1698.

[25] Pena, M. A.; Fierro, J. L. G. *Chem. Rev.* **2001**, *101*, 1981.

[26] (a) Honle, W. *J. Solid State Chem.* **1983**, *49*, 157. (b) Perrin, et al. *Acta Crystallogr.* **1983**, *C39*, 415.

[27] A nice updated website for past/recent superconductor discoveries is found at http://superconductors. org/type2.htm

[28] For example, see: (a) Emery, V. J.; Kivelson, S. A.; Tranquada, J. M. *Proc. Natl. Acad. Sci.* **1999**, *96*, 8814. (b) J. M. Tranquada, H. Woo, T. G. Perring, H. Goka, G. D. Gu, G. Xu, M. Fujita and K. Yamada *Nature* **2004**, *429*, 534. (c) Lee, K. H.; Hoffmann, R. *J. Phys. Chem. A* **2006**, *110*, 609. (d) http://www. nature.com/nature/journal/v440/n7088/edsumm/e060427-09.html

[29] For instance, see: (a) Lanzara, A.; Bogdanov, P. V.; Zhou, X. J.; Kellar, S. A.; Feng, D. L.; Lu, E. D.; Yoshida, T.; Eisaki, H.; Fujimori, A.; Kishio, K.; Shimoyama, J. -I.; Noda, T.; Uchida, S.; Hussain, Z.; Shen, Z. -X. *Nature* **2001**, *412*, 510. (b) Shchetkin, I. S.; Osmanov, T. S. *Powder Metall. Metal Ceram.* **1993**, *32*, 1068. (c) Abd-Shukor, R. *Solid State Commun.* **2007**, *142*, 587.

[30] One model used to explain superconductivity in YBCO is the reduction of unstable Cu^{3+} sites by redox reactions initiated by electrons passing through the solid in adjacent planes. As an electron passes by a Cu^{3+} ion, it causes an electron to be injected from a neighboring Cu^{2+} ion resulting in a lattice distortion, & hole propagation in the opposite direction. This concept is illustrated at: http:// www.chm.bris.ac.uk/webprojects2000/igrant/hightctheory.html

[31] Note: there are two ways to account for charge neutrality in p-type superconductors. First, La$_{2-x}$Sr$_x$CuO$_4$ may be formally written as: La$_{2-x}$Sr$_x$Cu$_{1-x}$$^{2+}Cu_x$$^{3+}O_4$ where one Cu^{3+} (or a Cu^{2+} with a trapped hole, Cu^{2+}(h$^+$)) forms for each Sr^{2+} added. Alternatively, the formula may be written as La$_{2-x}$Sr$_x$Cu^{2+}O$_{4-(x/2)}$, where one oxygen vacancy is formed for every two Sr^{2+} ions added to the lattice.

[32] For example, see: (a) Wojdet, J. C.; Moreira, I.; Illas, F. *J. Am. Chem. Soc.* **2009**, *131*, 906. (b) Kamihara, Y.; Watanabe, T.; Hirano, M.; Hosono, H. *J. Am. Chem. Soc.* **2008**, *130*, 3296.

[33] A recent issue of the New Journal of Physics was devoted to discoveries related to iron-based HTS: http://www.iop.org/EJ/abstract/1367-2630/11/2/025003

[34] Note: the most promising processing method for YBCO applications involves deposition onto a flexible metal tape coated with buffering metal oxides. Crystal-plane alignment can be introduced into the metal tape itself (via the RABiTS process) or a textured ceramic buffer layer can be deposited on an untextured alloy substrate (the IBAD process). Subsequent oxide layers prevent diffusion of the metal from the tape into the superconductor while transferring the template for texturing the superconducting layer.

[35] For a comprehensive review of recent HTS wire installation projects, and DoE goals related to HTS-based electrical applications, see: http://www.energetics.com/supercon07/agenda.html

[36] Note: there are precedents for crystals with five-fold rotation axes. These crystals are known as quasicrystals, since they exhibit long-range orientational order but are not consistent with lattice translations. For example, see: Shechtman, D.; Blech, I.; Gratias, D.; Cahn, J. W. *Phys. Rev. Lett.* **1984**, *53*, 1951. Another nice online summary of quasicrystals is: http://www.tau.ac.il/~ronlif/quasi-crystals.html.

[37] Note: the *d* notation indicates a diamond glide plane, found in diamond or zinc blende extended crystal structures. Whereas glide planes are found in many inorganic-based crystals, screw axes are found predominantly in protein structures.

[38] Note: scattering from the nucleus does not contribute to coherent scattering due to its relatively large mass, precluding its oscillation from the impinging of incident X-rays.

[39] Note: the cosine of angle ϕ is simply the x component of a unit vector after it is rotated by ϕ around a unit circle. If the vector is rotated at some constant speed, then its x-value will trace out a cosine wave as a function of time, with amplitude of vector length. Waves of different wavelengths or periods would result in the vectors rotating at different speeds; however, X-ray crystallography uses mono-chromatic photons of a single wavelength.

[40] An excellent summary of crystallography and systematic absences is given by: http://xrayweb.chem.ou.edu/notes/symmetry.html#absence

[41] (a) http://shelx.uni-ac.gwdg.de/tutorial/english/shelxs.htm; (b) http://www.lks.physik.uni-erlangen.de/diffraction/

[42] Note: another way to state this is that for a single crystal, only a few lattice planes will be oriented at their Bragg angle at any one time.

[43] (a) Yasuda, K.; Ohta, M. *J. Dental Res.* **1982**, *61*, 473. (b) Uzuka, T.; Kanzawa, Y.; Yasuda, K. *J. Dent. Res.* **1981**, *60*, 883.

[44] For instance, see: Mukoseev, A. G.; Shabashov, V. A.; Pilugin, V. P.; Sagaradze, V. V. *Nanostruct. Mater.* **1998**, *10*, 273.

[45] For example, see: http://xrayweb.chem.ou.edu/notes/twin.html

[46] For example, see: Lakes, R. S. *Science* 1987, *235,* 1038.

[47] http://www.ntcresearch.org/pdf-rpts/Bref0606/M04-GT21-06e.pdf

[48] The yield point for metals with gradual elastic–plastic transitions is constructed by drawing a straight line parallel to the elastic portion of the stress vs. strain curve at a specific strain offset, usually 0.002. The intersection of that line and the stress vs. strain curve gives rise to the yield strength, σ_y, of the material.

[49] Garlick, G. D.; Kamb, W. B. *J. Geol. Educ.* **1991**, 39, 398.

[50] For example, see: Fritsch, E.; Massi, L.; Rossman, G. R.; Hainschwang, T.; Jobic, S.; Dessapt, R., found online at: http://www.aigsthailand.com/(A(vlNwUMqNyQEkAAAAMzQ3Mjc5MzItNDR-kYy00NjIzLWEyY2YtNTg3YWM4M2EyYjlj2Mm3M88VUzWx_4m4U5KodgkCri41))/FieldTrips-Detail.aspx?tID=185&type=Publications&AspxAutoDetectCookieSupport=1

[51] Note: for a thorough treatment of crystal field theory, see Cotton, F. A.. Wilkinson, G.; Murillo, C. A.; Bochmann, M. *Advanced Inorganic Chemistry*, 6th ed., Wiley: New York, 1999.

[52] Note: the ground-state atomic term symbol for Cr^{3+} is ^4F, which splits into $^4T_2$, $^4T_1$ and $^4A_2$ for an octahedral transition metal complex. For more information regarding term symbol notation and absorption spectra for transition metal complexes, see: Shriver et al. *Inorganic Chemistry*, 4th ed., W. H. Freeman: New York, 2006. http://www.scribd.com/doc/6672586/Electronic-Spectroscopy-1

[53] Note: excited electrons give off their energy via infrared emission and thermal interactions with the corundum crystal lattice, referred to as electron–phonon (lattice vibrations) interactions.

[54] For an explanation of the electronic transitions underlying ruby lasers, as well as tunable lasers such as alexandrite, Ti:sapphire, and Nd:YAG, see: Thyagarajan, K. *Lasers, Theory and Applications*, Plenum Press: New York, 1981.

[55] See Shriver et al. *Inorganic Chemistry*, 4th ed., W. H. Freeman: New York, 2006 for more details re LMCT and MLCT processes.

[56] For more information regarding the trichroism of iolite and its use as a "Viking compass", see: http://www.nordskip.com/iolite.html

[57] Note: the Pauli exclusion principle states that each electron must possess a different set of four quantum numbers; that is, two electrons housed in the same orbital (identical n, l, m_l) must be of opposite spin ($m_s = \pm 1/2$).

[58] Note: the work function is the solid-state analogy of *ionization energy*, defined as removing the outermost electron from a gaseous atom. In general, the work function is *ca.* 1/2 the value of the ionization energy of its corresponding gaseous atoms.

[59] (a) Reif, F. *Fundamentals of Statistical and Thermal Physics*. McGraw–Hill: New York, 1965. (b) Blakemore, J. S. *Semiconductor Statistics*. Dover: Canada, 2002.

[60] Note: for AC current, the velocity would be identical to DC, but the electrons would travel back/forth, resulting in a much smaller drift velocity. A nice explanation of the speed of electricity may be found online at: http://www.radioelectronicschool.net/files/downloads/howfast.pdf

[61] Kittel, C. *Introduction to Solid State Physics*, 8th ed., Wiley: New York, 2004.

[62] For a recent review, see Cheetham, A. K.; Mellot, C. F. *Chem. Mater.* **1997**, *9*, 2269. It should be noted that the hydrolytic condensation of trifunctional organosilicon monomers (*e.g.*, $RSiCl_3$ or $RSi(OMe)_3$) results in polyhedral oligomeric silsesquioxanes (POSS) – see: http://www.azonano.com/details.asp?ArticleID=1342#_POSSTM_Polymers_Polymerization/Gr. These structures represent the smallest forms of silica, often being denoted as "molecular silica". Since particle diameters range from 0.07 to 3 nm, these are important architectures for nanoapplications (*e.g.*, see http://www.reade.com/Products/Polymeric/poss.html

[63] Note: a supercritical fluid has intermediate properties of liquid and gas. Typically, the alcogel is placed in an autoclave filled with ethanol. The system is pressurized to 750–850 psi with CO_2 and cooled to 5–10°C. Liquid CO_2 is then flushed through the vessel until all the ethanol has been removed from the vessel and from within the gels. When the gels are ethanol-free, the vessel is heated to a temperature above the critical temperature of CO_2 (31°C). As the vessel is heated, the pressure of the system rises. The pressure of CO_2 is carefully monitored to maintain a pressure slightly above the critical pressure of CO_2 (1050 psi). The system is held at these conditions for a short time, followed by the slow, controlled release of CO_2 to ambient pressure. The length of time required for this process is dependent on the thickness of the gels; this process may last anywhere from 12 h to 6 days.

[64] For a recent review on the synthesis, properties, and applications of aerogels see: Pierre, A. C.; Pajonk, G. M. "Chemistry of Aerogels and Their Applications", *Chem. Rev.* **2002**, *102*, 4243.

[65] Note: the γ-Al_2O_3 crystal structure is best described as a defect spinel structure comprised of a $2 \times 2 \times 2$ fcc array of oxide ions with 21/3 aluminum ions divided over the octahedral and tetrahedral interstices. By contrast, α-Al_2O_3 is an HCP array of O^{2-}, with Al^{3+} in 2/3 of the octahedral sites. For thermal transformations of alumina, see: Stumpf, H. C.; Russell, A. S.; Newsome, J. W.; Tucker, C. M. *Ind. Eng. Chem.* **1950**, *42*, 1398.

[66] For a comprehensive database of zeolite structures refer to: http://www.iza-structure.org/databases/

[67] For a recent review of applications for zeolite thin films, see: Lew, C. M.; Cai, R.; Yan, Y. *Acc. Chem. Res.* **2009**, ASAP.

[68] For comprehensive building models for zeolite frameworks, see: http://www.iza-structure.org/databases/ModelBuilding/Introduction.pdf

[69] For a review of applications for mesoporous zeolites, see: Corma, A. *Chem. Rev.* **1997**, *97*, 2373.

[70] For a comprehensive review of hydrothermal methods used to synthesize zeolites, see: Cundy, C. S.; Cox, P. A. *Chem. Rev.* **2003**, *103*, 663. A laboratory protocol for the synthesis and characterization of the ZSM-5 zeolite may be found online at: http://materials.binghamton.edu/labs/zeolite/zeolite.html

[71] For F-based zeolite syntheses, see: (a) Koller, H.; Wolker, A.; Eckert, H.; Panz, C.; Behrens, P. *Angew. Chem. Int. Ed. Engl.* **1997**, *36*, 2823. (b) Koller, H.; Wolker, A.; Villaescusa, L. A.; Daz-Cabanas, M. J.; Valencia, S.; Camblor, M. A. *J. Am. Chem. Soc.* **1999**, *121*, 3368.

[72] Comyns, A. E. *Focus on Catalysts* **2009**, *4*, 1.

[73] For more information regarding the mechanism for glass formation, see: Royall, C. P.; Williams, S. R.; Ohtsuka, T.; Tanaka, H. *Nature Mater.* **2008**, *7*, 556.

[74] Note: it should be noted that glass is not 100% transparent; that is, some incident light is reflected - even in glass that is free from dopant or other inclusion impurities.

[75] Note: in addition to scattering processes, a better rationale for the transparency of glass is due to its electronic *band structure*, in which the HOMO/LUMO gap is too large to absorb visible light.

[76] It should be known that other oxides are capable of glass network formation, such as B_2O_3, GeO_2, P_2O_5, As_2O_5, As_2O_3, Sb_2O_3, and to a limited degree V_2O_5, ZrO_2 and Bi_2O_3. The oxides of Te, Mo, W, Bi, Ba, Nd, Ti, Zn, Pb, Al, Th and Be are known as conditional glass formers. These may be included in varying concentrations, but will not on their own, yield a glass. These, and other oxides that will not form a glass (including Sc, La, Y, Sn, Ga, In, Mg, Li, Sr, Cd, Rb, Hg, and Cs) are used as network modifiers, to vary the melt viscosity and afford varying properties to the glass.

[77] For more information regarding other crystalline forms, see: Douglas, B. E.; Ho, S. -M. *Structure and Chemistry of Crystalline Solids*, Springer: New York, 2006.

[78] Note: this is a useful exploitation of the freezing-point depression *collligative property*, as taught in introductory physical chemistry (*e.g.*, adding salt to icy roads in the winter).

[79] *The Complete Book on Glass and Ceramics Technology*, NIIR Board of Consultants and Engineers, Asia Pacific Business Press, Inc., 2005.

[80] Some remaining stock of safe, weakly radioactive glass items such as ceramic plates, ore, marbles, etc. may still be acquired online from http://www.unitednuclear.com/

[81] For more details on the history, properties, and fabrication of fiber optics, see: Glass, A. M.; DiGiovanni, D. J.; Strasser, T. A.; Stentz, A. J.; Slusher, R. E.; White, A. E.; Kortan, A. R.; Eggleton, B. J. *Bell Labs Techn. J.* **2000**, Jan. - March, 168.

[82] http://en-us.transitions.com/

[83] For example, see: Armistead, W. H.; Stookey, S. D. *Science* **1964**, *144*, 15.

[84] For example, see: Morse, D. L. *Inorg. Chem.* **1981**, *20*, 777, and references therein.

[85] Richardson, T. J.; Slack, J. L.; Armitage, R. D.; Kostecki, R.; Farangis, B.; Rubin, M. D.; *Appl. Phys. Lett.* **2001,** *78*, 3047.

[86] Asphalt is a black, sticky, viscous liquid that is obtained from crude petroleum. It comprises almost entirely a form of tar called bitumen. The structure of asphalt is actually a colloidal suspension, with small particulates called asphaltenes dispersed through the petroleum matrix. More environmentally friendly aqueous-based asphalt emulsions are currently being used for road repair applications.

[87] For more details regarding the role of C4AF in the hardening mechanisms of Portland cement, see: Meller, N.; Hall, C.; Jupe, A. C.; Colston, S. L.; Jacques, S. D. M.; Barnes, P.; Phipps, J. *J. Mater. Chem.* **2004**, 14, 428, and references therein.

[88] A nice summary of ceramic processing is found online at: http://www.engr.sjsu.edu/~wrchung/images/MatE155/sp06/ceramicsprocessing.pdf

[89] Ratner, B. D.; Hoffman, A. S.; Schoen, F. J.; Lemons, J. E. *Biomaterials Science*, 2nd ed., Academic Press: New York, 2004.

[90] Aninwene, G. E.; Yao, C.; Webster, T. J. *Int. J. of Nanomed.* **2008**, *3*, 257.

[91] Klein, C. *Biomaterials.* **1990**, *11*, 509.

[92] LeGeros, R. Z.; LeGeros, J. P. *Adv. in Science and Technol.,* 49, 203.

Topics for Further Discussion

1. Considering that Si has the zinc blende crystal structure, draw the (111), (110), and (100) planes of Si. Place these planes in order of highest atomic density, from least to greatest. What impact would the structures of these planes have on their relative surface reactivities?

2. Show the relationship between 4_1 and 4_3 crystallographic point group operations.
3. A metal alloy consists of 5 at.% Au and 95 at.% Pt; calculate the composition in terms of wt%. How many atoms of gold will be present per cubic meter of the alloy?
4. What are the differences between amorphous and crystalline materials? Cite examples of each.
5. Prove that the theoretical packing densities for BCC, FCC, and HCP are 68%, 74%, and 74%, respectively.
6. Describe some techniques used to fabricate amorphous or crystalline materials.
7. What is the difference between point groups and space groups?
8. Is it possible to have a material that is both an ionic solid and a molecular solid? Explain your reasoning, and cite examples of such hybrids (if possible).
9. Consulting a Periodic Table and Table of Atomic Radii, what atoms would be suitable (a) interstitial dopants and (b) substitutional dopants within a Mn lattice? Show your calculations and rationale.
10. Using diagrams, determine whether (111) or (110) planes are more densely packed with atoms for FCC crystals.
11. Explain why the dislocation density of a single crystal is six times greater within 200 μm from the surface, relative to its bulk structure. Would a surface oxide layer induce more dislocations to form in a metal crystal, or insulate against dislocation formation? Explain.
12. Based on lattice parameters, explain why tetragonal, trigonal, and hexagonal crystals are often dichroic, whereas orthorhombic, monoclinic, and triclinic crystals may exhibit trichroism.
13. What are the benefits of fuel cells, as compared to batteries and other "standard" power sources such as fossil fuel power plants?
14. Why do acid-catalyzed and base-catalyzed sol-gel processes result in linear and branched metal oxides, respectively?
15. Describe the unit cell symmetry/centering and crystallographic symmetry operations (incl. translational operations such as glide planes and screw axes) for each of the following space groups: (a) P6$_3$/m, (b) Fd$\bar{3}$, (c) Imma, (d) P6mm, (e) Fddd, (f) P2$_1$/m.
16. For each of the crystallographic point groups represented in Q #15 above, determine whether the crystal is *piezoelectric* (change in voltage (ΔV) in response to a change in pressure) and/or *pyroelectric* (ΔV in response to a change in temperature). What are the governing symmetry elements that determine whether a crystal will exhibit these properties?
17. For each of the following: (1) indicate the positions of ALL symmetry elements, (2) list the coordinates of all points **within** the unit cell, and (3) determine the space group symbol.
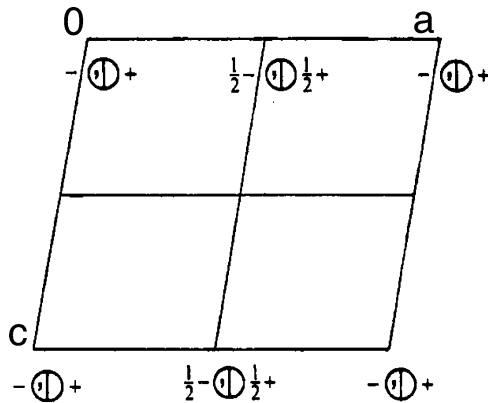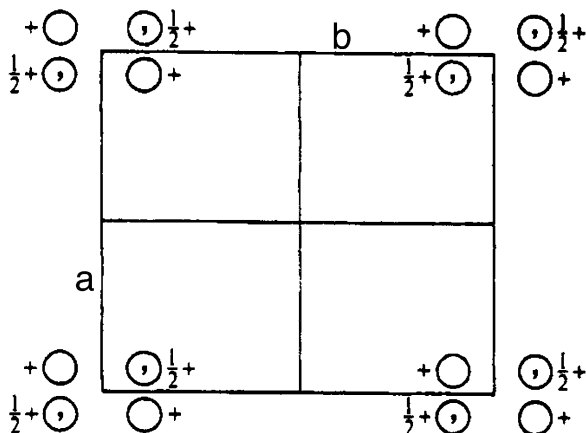
18. Provide precedents for sol-gel syntheses using tetramethoxysilane, with references. Describe the differences in experimental conditions and control over product morphology relative to using TEOS.

19. We have all seen cement trucks that have a distinctive rotating tank. Why is this constant rotation necessary, and what would happen if the tank stopped rotating?

20. Why are coarse and fine aggregates needed for the overall strength of concrete?

21. Explain why the reaction of C2S with hydroxides occurs much slower than the C3S/hydroxide reaction during cement hardening.

22. Suggest low- and high-temperature synthetic routes for AlN and BN ceramics.

23. How would you design smart glass-based intruder sensor, which would change color from clear to bright red?

24. What are 'chalcogenide glasses'? Describe some recent applications for these materials.

25. How would you design a smart glass windshield, which would self-repair itself after an automobile crash?

26. Ancient colored glasses contained nanoparticles of Au and Cu. How were these synthesized (*i.e.*, what metal salts were used, along with other experimental conditions required to yield nanosized metal clusters)?

27. Explain why borosilicate glass is transparent to visible radiation and quartz is transparent to both visible and UV radiation.

28. For metal oxide-based heterogeneous catalyst supports, describe the role of (1) surface hydroxyl groups (concentration and speciation) and (2) Lewis acidity of the metal center on the chemisorption of transition metal catalysts. Cite various examples of surface-bound M^0 and M^{n+} catalytic species.

29. Both homogeneous and heterogeneous catalysis offer distinct advantages and disadvantages. Though a particular system is usually designed to be either homo- or heterogeneous in nature, there is sometimes ambiguity regarding the exact nature of the active catalytic species. For instance, there may be leaching of the transition metal species into solution, which may also involve "release and capture" mechanisms. For a model system of your choosing (where leaching is a possibility), how would you unambiguously determine whether the active catalytic species was heterogeneous or homogeneous in nature?

30. For each of the following, determine the molecular and corresponding crystallographic point groups: (a) a piece of 8.5″ x 11″ paper (no lines), (b) staggered ferrocene, (c) eclipsed ferrocene, (d) hydrogen peroxide, (e) cyclopropane.

31. You are given a piece of golden-colored glass, and must add appropriate dopant(s) to yield a colorless material. What dopant(s) are likely present, and which would you add? Explain.

32. The lattice parameter of Ag is 0.4084 nm. Calculate the planar concentration (in units atoms/nm^2) of atoms on the planes {100}, {110} and {111}.

33. The lattice parameter of Ge is 0.5659 nm. Calculate the number of atoms per unit length, that is the linear atomic concentration (atoms per nm of length) along <100> and <110> directions.

34. γ-Al_2O_3, commonly used as a heterogeneous catalyst support, crystallizes in the Fd-3m space group. Describe the multiplicity and fractional coordinates of O and Al ions in the crystal lattice.

35. Predict and explain whether nonzero intensities for the (111) and (110) reflections will be observed from X-ray diffraction characterization of the following single crystals:
    (a) Barium sodium niobate: $Ba_{(4+x)}Na_{(2-2x)}Nb_{10}O_{30}$ (*J. Chem. Phys.* **1969**, *50*, 4352)
    (b) Hexathorium fluoride hydrate: $Th_6F_{24}H_2O$ (*Acta Cryst. B* **1979**, *35*, 1763)
    (c) Antimony gold yttrium: $Au_3Sb_4Y_3$ (*Acta Cryst. B* **1977**, *33*, 1579)
    (d) Ruthenium (III) chloride: $RuCl_3$ (*J. Chem. Soc. A* **1967**, 1038)

36. The intensities below were obtained from single-crystal X-ray diffraction (projection along (100)). Considering $P2_1/c$, Fd-3m, F-43m, Cmm2, $P6_3$/mmc, and Cmmm space groups, which would represent(s) the most likely description of this crystal? Explain.
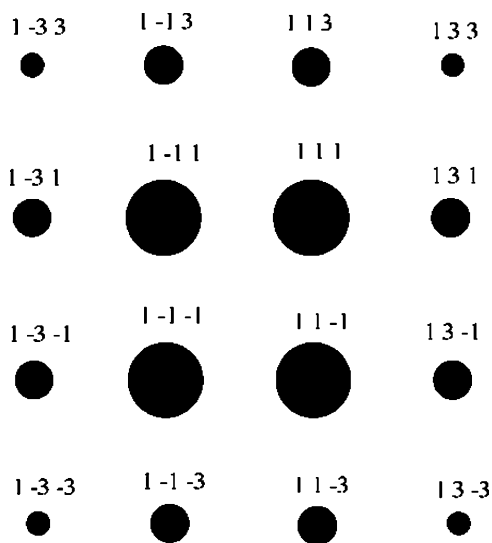
37. The following data was obtained from a YBCO bulk sample. Calculate the resistance for each trial given that a constant current of 100 mA was flowing through the sample. Using this data, determine the critical temperature for YBCO. How does this compare to the literature value?

Voltage	T (K)	Voltage	T (K)
0.0010370	118.2	0.008440	93.5
0.0010270	116.1	0.007830	93.2
0.0010600	114.8	0.006390	93
0.0010490	112.9	0.0005050	92.6
0.0010350	110.9	0.0003790	92.3
0.0010220	109.1	0.0002430	92.1
0.0010090	106.9	0.0000930	91.7
0.0010010	105	0.0000100	91.4
0.0009890	103.5	0.0000030	91
0.0009750	102.2	0.0000002	90.8
0.0009670	100	−0.0000002	90.1
0.0009510	97.9	−0.0000001	89.9
0.0009440	95.8	0.0000003	89.5
0.0009180	95	−0.0000001	88.8
0.0009110	94.3	0.0000001	88.5
0.0008920	93.8		

Further Reading

1. Pogge, H. B. *Electronic Materials Chemistry*, Marcel-Dekker: New York, 1996.
2. Glusker, J. P.; Lewis, M.; Rossi, M. *Crystal Structure Analysis for Chemists and Biologists*, VCH: New York, 1994.
3. Larminie, J.; Dicks, A. *Fuel Cell Systems Explained*, 2nd ed., Wiley: New York, 2003.
4. West, A. R. *Solid State Chemistry and Its Applications*, Wiley: New York, 1987.
5. West, A. R. *Basic Solid State Chemistry*, 2nd ed., Wiley: New York, 1999.
6. Moore, E.; Smart, L. *Solid State Chemistry: An Introduction*, 2nd ed., CRC Press: New York, 1996.
7. Hurd, C. M. *Electrons in Metals*, Wiley: New York, 1975.
8. Elliott, S. *The Physics and Chemistry of Solids*, Wiley: New York, 1998.